Rectennas for Wireless Energy Harvesting and Power Transfer

by

Sumin David Joseph

Thesis submitted in accordance with the requirements for the award of the dual degree of Doctor of Philosophy of the University of Liverpool, United Kingdom and National Tsing Hua University, Taiwan

March 2021

To my dear wife, parents and brother.

Acknowledgements

First of all, I thank GOD ALMIGHTY who has given me the mental and physical strength and confidence to do this work. This thesis would have not seen the light without the support and guidance of many people who are acknowledged here. I would like to express my deep gratitude to my supervisors, Professor Yi Huang and Professor Shawn. S. H. Hsu for offering me this opportunity. Their kind support, fruitful advice, critical discussions, and vast experience have motivated me during the whole time of my studies. I learned so much from them both academically and personally. Thank you for the invaluable comments and advice on my research as well as my life and career.

I would also like to thank Dr. Jiafeng Zhou for the generous support and academic guidance you have provided to me. I will always treasure your support, encouragement and guidance. I would also like to thank Dr. Chaoyun Song, Dr. Manoj Stanley, Dr. Ahmed Alieldin, Mr. Tianyuan Jia, Miss Wenzhang Zhang and Mr.Yeke Liu for their contributions and collaborations in editing the published papers of this research and for their friendly support. Thanks to all my friends and colleagues in the RF group of University of Liverpool, UK and National Tsing-Hua University, Taiwan for providing such a lovely and collaborative environment for research. I would like to thank CIC Hsinchu, Taiwan for providing me the opportunity to tape out and measure our designs. Special thanks to Mr. Mark Norman, Mr. John Gillmore, and Mr. Mark Burnley, who are technicians at electrical engineering workshop, University of Liverpool for their assistance in fabricating our designs.

Finally, thanks to my beloved wife, my parents and my brother for their invaluable support. This journey would not have been possible without their love and prayers.

Table of Contents

Table of Figures

Abstract

With the rapid advancement of the wireless technologies and demands of low-power electronic circuits for smart home, smart cities and IoT applications, various research trends have tended to investigate the feasibility of powering these circuits by harvesting RF energy from ambient electromagnetic space or by using dedicated RF sources. Recently, RF ambient energy harvesting and WPT technologies have gained much interest as a clean and renewable power source. However, the optimal design of a rectifying-antenna or rectenna, is still very challenging for deploying in real applications. A number of key issues and research problems have been identified for rectenna designs, such as the low conversion efficiency and strong nonlinearity under the ambient power conditions. Moreover, a clear distinction between rectennas for wireless energy harvesting (WEH) and wireless power transfer (WPT) are not significantly considered in the literatures while developing the rectennas for different applications. The purpose of this thesis is to present a comprehensive study into rectennas, aiming at overcoming the most challenging research problems of this topic. There are six main contributions from this PhD work, which can be divided into two main sections.

In the first section, three contributions are presented aimed to develop WEH rectennas. The design of broadband rectennas is exceptionally challenging due to the utilization of nonlinear elements of the rectifying circuit. Therefore, a low complexity novel broadband rectenna is initially proposed for WEH applications. The proposed rectenna consists of a novel broadband Yagi-Uda antenna and a transmission lines-based broadband rectifier. A novel three-stage impedance matching technique is utilized in the rectifier design to achieve high efficiency with a compact size. The proposed broadband rectifier outperforms other designs in bandwidth and conversion efficiency under similar operating conditions. Then, a novel dual-band rectenna is proposed for low power ambient energy harvesting. Most reported rectennas in the literature were designed for medium and high input power conditions. The proposed rectenna consists of a novel dipole antenna with folded stubs and a highly sensitive rectifier. Folded stubs are introduced in the dipole antenna for dual-mode operation. A novel single external inductor-based high sensitivity rectifier is also proposed. Based on the rectifier design, a dual-band high sensitivity rectifier is also proposed. This

rectenna design confirms the feasibility of harvesting RF power from low power ambient conditions. Thirdly, a novel RF energy harvester using combined harvesting topology to capture the ambient RF energy in 915-960 MHz, 1.8-2.7 GHz, and 3.4-3.7 GHz frequency bands is proposed. The proposed RF energy harvester utilised high sensitivity and high efficiency rectifiers for improving the performance. This design confirms the feasibility of capturing RF energy from a typical ambient environment for low power applications.

Rectennas for WPT applications are mainly presented in the second section. A novel communication rectenna solution is proposed to provide effective data and power transfer in wireless sensor nodes. Along with the ambient energy harvesting of conventional rectenna, the proposed design can also perform simultaneous wireless information and power transfer for facilitating uninterrupted power supply and data transfer of WSN nodes. A dual polarized 2×1 square patch antenna array and a multisection bended broadband monopole antenna are employed for SWIPT and AWEH, respectively. Thus, the proposed communication rectenna array with ambient energy harvesting can be a promising candidate for future wireless sensor nodes. Low breakdown voltage in commercial silicon Schottky diodes limits the conversion efficiency in the high-power region of conventional rectifiers. Therefore, a novel GaN Schottky diode-based microwave rectifier is proposed for high-power applications. A novel low loss impedance matching is utilised by exploiting the unavoidable inductance effects of bond wires used for providing the electrical connection between GaN chip and board. The proposed rectifier is better than the other published designs in terms of the high-power operation as well as the peak voltage and power. Conventional rectennas for WEH and WPT can only offer a limited DC power amount and typically do not have the rectenna's location knowledge. Thus, a novel duplexing rectenna with a harmonic feedback capability for efficient WPT applications with the antenna alignment is proposed. The duplexing rectenna can efficiently convert the incident RF power at 0.915 GHz to DC and also send a reasonable harmonic signal back to the RF transmitter at 1.83 GHz for tracking the position of rectenna to improve power transfer efficiency without the need of another antenna and transmitters. Thus, this complete WPT system based on a duplexing rectenna with feedback property is a very promising solution for future efficient WPT applications.

List of Publications

Journal Publications

[1] **S. D Joseph**, Y. Huang, S. Hsu, A. Alieldin and C. Song, "Second harmonic exploitation for high-efficiency wireless power transfer using duplexing rectenna," *IEEE Trans. Microw. Theory Techn.*, vol. 69, no. 1, pp. 482 - 494, Jan 2021.

[2] **S. D. Joseph**, Y. Huang, and S. Hsu, "Transmission lines-based impedance matching technique for broadband rectifier," *IEEE Access*, vol. 9, pp. 4665 - 4672, Jan 2021.

[3] **S. D. Joseph**, S. Hsu, A. Alieldin, C. Song, Y. Liu, and Y. Huang, "High-power wire bonded GaN rectifier for wireless power transmission," *IEEE Access*, vol. 8, pp. 82035 - 82041, May 2020.

[4] **S. D. Joseph**, Y. Huang, and S. Hsu, "A compact dual-mode dipole antenna with 47% bandwidth and stable omnidirectional radiation pattern," *IET Microw. Antennas Propag.*, submitted, Jun. 2021.

[5] C. Song, Y. Huang, P. Carter, J. Zhou, **S. D. Joseph**, and G. Li, "Novel compact and broadband frequency-selectable rectennas for a wide input-power and load impedance range," *IEEE Trans. Antennas Propag.*, vol. 66, no. 7, pp. 3306-3316, July 2018.

[6] W. Haoran, C. Li, Y. Liu, **S. D. Joseph**, Y. Huang, and S. Hsu, "Low turn-on voltage and high breakdown GAN Schottky barrier diodes for RF energy harvesting applications," *Jpn J Appl Phys*, vol. 59, no. SG, Feb 2020.

[7] M. Stanley, Y. Huang, H. Wang, H. Zhou, A. Alieldin and **S. D. Joseph**, "A capacitively coupled patch antenna array with high gain and wide coverage for 5g smartphone applications," *IEEE Access*, vol. 6, Aug. 2018.

[8] A. Alieldin, Y. Huang, M. Stanley, **S. D. Joseph**, and D. Lei, "A 5G MIMO antenna for broadcast and traffic communication topologies based on pseudo inverse synthesis," *IEEE Access*, vol. 6, pp. 65935-65944, 2018.

[9] A. Alieldin, Y. Huang, S. J. Boyes, M. Stanley, **S. D. Joseph**, Q. Hua and D. Lei, "A triple-band dual-polarized indoor base station antenna for 2G, 3G, 4G and Sub-6 GHz 5G applications," *IEEE Access*, vol. 6, pp. 49209-49216, Sep. 2018.

[10] A. Alieldin, Y. Huang, S. J. Boyes, M. Stanley, **S. D. Joseph**, and B. Al-Juboori, "A dual-broadband dual-polarized fylfot-shaped antenna for mobile base stations using MIMO overlapped antenna subarrays," *IEEE Access*, Sep. 2018.

Conference Publications

[1] **S.D. Joseph**, S. Hsu and Y. Huang, "Rectennas for wireless energy harvesting and power transfer," *Proc. RFIT 2021*, Taiwan (submitted).

[2] **S. D. Joseph**, Y. Huang, S. Hsu, M. Stanley, A. Alieldin and C. Song, "A novel duplexing antenna for feedback wireless power transfer," *Proc. EuCAP 2020*, Copenhagen, Denmark.

[3] **S. D. Joseph**, Y. Huang, S. Hsu, M. Stanley, A. Alieldin and C. Li, "A novel transmission line technique to realize broadband rectenna for WEH and WPT applications," *Proc.* AWPT 2019, Xian, China.

[4] **S. D. Joseph**, Y. Huang, S. Hsu, M. Stanley, A. Alieldin and C. Li, "A novel miniaturized broadband Yagi-Uda antenna with enhanced gain for wireless energy harvesting applications," *Proc. EuCAP 2019*, Krakow, Poland.

[5] **S. D. Joseph**, Y. Huang, S. Hsu, M. Stanley, and C. Song, "A novel dual-polarized millimeter-wave antenna array with harmonic rejection for wireless power transmission," *Proc. EuCAP 2018*, London, UK.

[6] **S. D. Joseph**, Y. Huang, A. Schuchinsky, R. Lebourgeois and L. Roussel, "Self-biased CPW circulator with low insertion loss," *Proc. IMWS-AMP 2020*, Suzhou, China.

[7] **S. D. Joseph**, R. Lebourgeois, Y. Huang, L. Roussel and A. Schuchinsky, "Low-loss hexaferrite self-biased microstrip and CPW circulators," *Proc. Thirteenth International Congress on Artificial Materials for Novel Wave Phenomena (Metamaterials) 2019*, Rome, Italy.

[8] C. Li, H. Wang, Y. Liu, **S. D. Joseph**, Y. Huang, and S. Hsu, "Low turn-on voltage and high breakdown GaN Schottky barrier diodes for RF energy harvesting applications," *Proc. Intl. Conf. on Solid State Devices and Materials* (SSDM), Nagoya, Sept. 2019.

[9] A. Alieldin, Y. Huang, M. Stanley, **S. D. Joseph**, T. Jia, F. Elhouni and Q. Xu, "A camouflage antenna array integrated with a streetlamp for 5G picocell base stations," *Proc. EuCAP 2019*, Krakow, Poland.

[10] A. Alieldin, Y. Huang, M. Stanley, and **S. D. Joseph**, "A circularly polarized circular antenna array for satellite TV reception," *Proc. EuMC 2018*, Madrid, 2018

[11] M. Stanley, Y. Huang, H. Wang, H. Zhou, A. Alieldin and **S. D. Joseph**, "A novel mm-wave phased array for 180-degree coverage for 5G smartphone applications," *Proc. EuCAP 2018*, London, UK.

[12] M. Stanley, Y. Huang, A. Alieldin, **S. D. Joseph**, C. Song and T. Jia, "A dual-band dual-polarised stacked patch antenna for 28 GHz and 39 GHz 5G millimetre-wave communication," *Proc. EuCAP 2019*, Krakow, Poland.

[13] M. Stanley, Y. Huang, H. Wang, H. Zhou, A. Alieldin and **S. D. Joseph**, "A transparent dual-polarised antenna array for 5G smartphone applications," *Proc. APS 2018*, Boston, USA

[14] M. Stanley, Y. Huang, H. Wang, H. Zhou, A. Alieldin and **S. D. Joseph**, "A novel mm-wave phased array antenna with 360-degree coverage for 5G smartphone applications," *Proc. UCMMT 2017*, Liverpool, UK.

Acronyms

5G	Fifth Generation
AC	Alternating Current
ADS	Advanced Design System
AR	Axial Ratio
AWEH	Ambient Wireless Energy Harvesting
BRF	Band-Reject Filter
CDMA	Code Division Multiple Access
CMOS	Complementary Metal-Oxide-Semiconductor
CP	Circular Polarization
CST	Computer Simulation Technology
CW	Continuous Wave
DC	Direct Current
DTV	Digital Television
EM	Electromagnetic
GPRS	General Packet Radio Service
GSM	Global System for Mobile communication
HB	Harmonic Balance
HILPB	High Intensity Laser Power Beam
HPBW	Half-Power Beam Width
HRCT	Hybrid Resistance Compression Technique

IEEE	Institute of Electrical and Electronics Engineers
IoT	Internet of Things
ISM	Industrial Scientific and Medical
JPL	Jet Propulsion Laboratory
LHCP	Left Hand Circular Polarization
LP	Linear Polarization
LSSP	Large Signal S-Parameter
LTE	Long Term Evolution
MIMO	Multiple Input Multiple Output
MINIX	Microwave Ionosphere Nonlinear Interaction
MPT	Microwave Power Transmission
MW	Modulated Wave
PCB	Printed Circuit Board
PIFA	Planar Inverted-F Antenna
RCN	Resistance Compression Network
RF	Radio Frequency
RFID	Radio-Frequency Identification
RHCP	Right Hand Circular Polarization
RX	Receiving Antenna
SISO	Single Input Single Output
SIW	Substrate Integrated Waveguide
SMS	Short Message Service

SNR	Signal to Noise Ratio
SPICE	Simulation Program with Integrated Circuit Emphasis
SPS	Solar Power Satellite Theory of Characteristic Modes
TM	Transverse Magnetic
UMTS	Universal Mobile Telecommunications System
USB	Universal Serial Bus
WEH	Wireless Energy Harvesting
Wi-Fi	Wireless Fidelity
WiMAX	World-wide Interoperability for Microwave Access
WLAN	Wireless Local Area Network
WPT	Wireless Power Transfer

Chapter 1. Introduction

For the past 150 years or so, humans have been heavily dependent on electricity to power everything from light bulbs to cars and to factories. With the rapid expansion of technical advancements and IoT systems, the number of connected devices that were in use worldwide exceeded 17 billion by 2018, with the number of IoT devices at 7 billion. IoT analytics research expects 34 billion global active devices connected to the internet in 2025, serving the global population as shown in Fig. 1.1 [1]. Following this expected growth in wireless devices, a need is also developing for an increased wireless sensor autonomy and small form factor [2]. The need for a long lifetime and small form factors of future wireless sensor nodes do not match up well with currently available battery technology [3]. Batteries typically have a limited operation time, and they have to be replaced or recharged to guarantee the operation of a network for a certain period. However, the procedure of battery replacement or recharging may create an undesired expenditure and sometimes is not practical or readily available (e.g., implant devices inside human bodies or for sensors embedded in building structures).

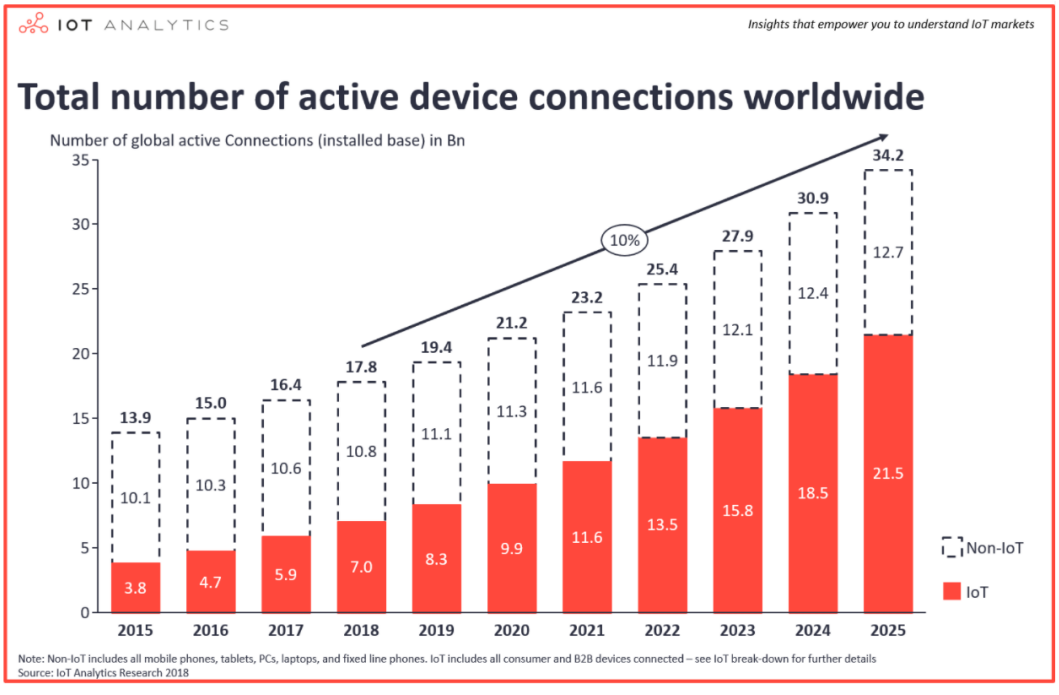

Fig. 1.1. Number of global active connections in billions [1].

Growing worldwide demand for energy and environmental impact associated with conventional energy sources may cause energy crisis in the next few decades. Fossil fuels such as coal and oil became gradually costly and scarce. The impacts of climate change are appearing now, but they will get worse. Therefore, it is necessary to develop new energy harvesting technologies that could reduce the demand for energy-related accessories such as batteries, cords, and power equipment for the coming decades. Using renewable energy to substitute traditional electric energy production could make a significant contribution to reducing environmental pollutions.

1.1. Ambient RF Wireless Energy Harvesting

Energy-harvesting technologies extracting energy from ambient power sources, such as vibration, heat, and electromagnetic waves, have recently attracted significant attention. Thus, numerous energy-harvesting systems, including energy-harvesting devices, topologies and circuitries, have been developed for self-sustainable standalone electronics. The commercialized energy harvesting systems are mostly based on solar [4] and wind energies since they can produce a tremendous amount of energy from nature. A solar panel can also operate in a hybrid mode in conjunction with other energy sources [5]. After the invention of the first silicon-based solar cell in the 1950s, photovoltaic technology has been well developed over the last 70 years. Physical properties (flexibility, durability, etc.) and electrical properties (efficiency, output voltage, etc.) also keep improving over time [7]. However, solar and wind-based energy harvesting systems require strict operating conditions, while their

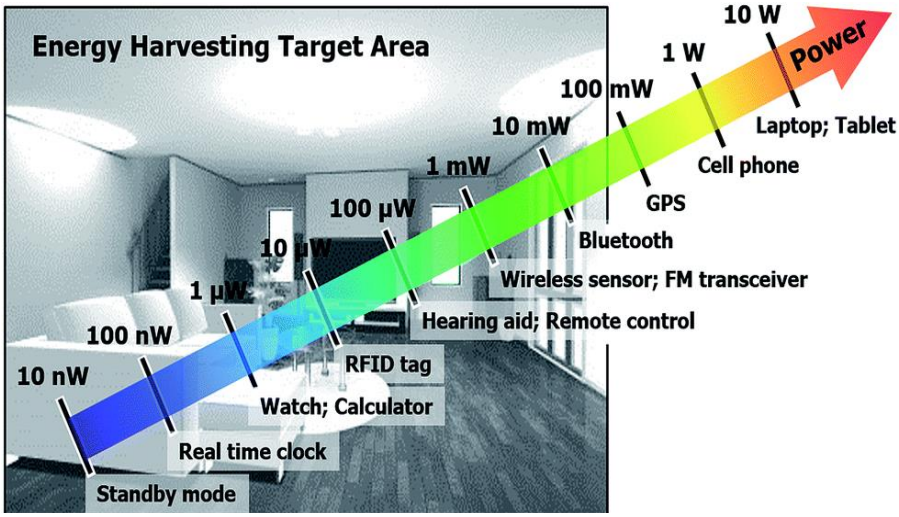

Fig. 1.2. Typical power required for potential applications [6].

performance depends heavily on weather and time. The thermal energy of the power source is also widely utilized. Using the advantage of thermoelectric effects such as the Seebeck effect or the Thomson effect, electrical power can be generated by exploiting the temperature difference in thermoelectric devices [8]. Typically, a thermoelectric generator provides an energy density of about 20–60 $\mu W/cm^2$ when it uses the human body as the thermal source at room temperature of 18^0C–25^0C [9]. The piezoelectric effect produces electrical voltages or currents from mechanical strains, such as vibration or deformation. Generally, piezoelectric-based energy harvesters keep creating power when there is a continuous mechanical motion, such as acoustic noises and wind. They sporadically generate power for intermittent strains, such as human action (walking, clicking a button, etc.). Typical output power density values of usual piezoelectric materials are around 250 $\mu W/cm^3$, but they can generate more power when a motion or deformation is intense [10].

An example of a typical hybrid energy-harvesting enabled wireless sensor platform is shown in Fig. 1.3 [11]. The electric energy can be captured from several ambient energy sources such as thermal, solar, vibration and RF/EM, and then stored in energy storage devices, such as a battery or a supercapacitor. A power management unit (PMU) optimizes the collected power level by matching and optimizing the duty cycle effectively. The lifetime of the primary power sources (such as a battery) can be extended by introducing energy-harvesting systems that effectively recharge the storage element. While the primary power source can also be removed when there is sufficient energy to drive the whole system for a truly standalone ("battery-less") autonomous operation.

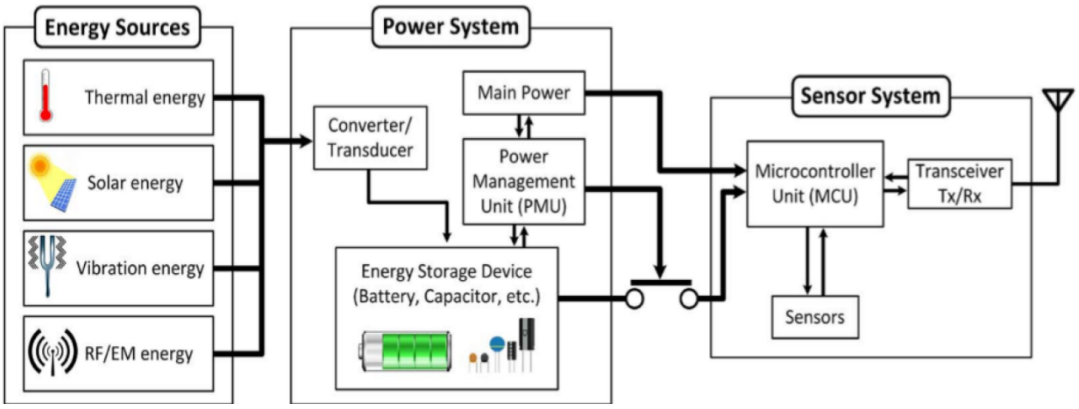

Fig. 1.3. Hybrid energy-harvesting enabled wireless sensor platform [11].

Among the multiple ambient energy sources, the wireless energy-harvesting technology has noticeably grown recently due to the predominance of wireless signals, especially after the technical advancements in the 21st century [12], [13]. With the growth of mobile cellular networks, Wi-Fi-enabled applications, and TV-based entertainment, the power density of ambient electromagnetic fields is dramatically increasing, enabling the RF powered applications. In [11], the harvested power by different ambient energy sources was compared and suggested potential applications. It was found that the energy captured from RF sources showed the lowest power density ranged from 0.001 to 0.1 $\mu W/cm^2$. Ambient RF power are mainly from bands such as DTV, GSM 900 MTx, GSM 900 BTx, GSM 1800 MTx, GSM 1800 BTx, 3G MTx ,3G BTx, Wi-Fi. and the average power densities are 0.89, 0.45, 36, 0.5, 84, 0.46, 12, 0.18 nW/cm^2 respectively [11]. Now, it can only be applied in some low power applications and sensors that consume very little energy. However, a larger amount of total available power in the range of 10-100 μW can be harvested by utilising a high efficiency harvester. To utilize the harvested power of a RF rectenna, a PMU with a dc–dc boost converter is needed since the output voltage from the rectenna is normally lower than the usable voltage level (e.g.,1.8 or 3 V). Hence, commercial PMUs such as BQ25504 (from Texas Instrument) can be utilised [14]. It has a low cold-start voltage and quiescent current of 0.33 V and 330 nA. The output voltage can be regulated to 3.3 V for the battery charging and other load applications.

A unique benefit of RF energy compared to solar and wind energy harvesting is that the ambient electromagnetic power density is available irrespective of the weather and environmental conditions (even though the power has fluctuations due to weather conditions). Thus, the RF energy harvesting system can work well in most cases. For example, only the energy from EM waves can be harvested at an indoor office environment during the night (where solar and wind energy is not available). With the upcoming new technology wave of smart home, smart cities and Internet of Things (IoT), this feature does make a lot of sense because most electronic devices and sensors used for these applications are of low power consumption and likely to be implemented for locations inside a building [15], [16]. With the aid of RF energy harvesting, these low power sensors and devices could become self-sustainable and eliminate the need for a battery replacement to save maintenance costs. From a long-term perspective, reducing the demand for batteries could also help with environmental protection.

1.2. Wireless Power Transfer

Wireless power transfer (WPT, wireless energy transmission, or electromagnetic power transfer) is the transfer of electrical power from a transmitter to a receiver in the form of electromagnetic energy, without the use of conductors like wires or cables across an intervening space, where it is converted back to an electric current and then used. Wireless transmission is used to power electronics devices when interconnecting wires are difficult, dangerous, or impossible. Maxwell's equations introduced the fundamental theory of WPT in 1864. Nikola Tesla is the one who started experiments to deliver electrical energy without conducting wires at the end of the 19th century [17]. But his experiments failed due to the limited technological advancements in that period. William C. Brown pioneered the rectenna concept and performed successful microwave power transmission in the 1960s [18]. Since then, significant research has been conducted on rectennas for energy harvesting applications. An efficient WPT via strongly coupled magnetic resonances at 9.9 MHz was proposed by Andre. Kurs's group from MIT (Massachusetts Institute of Technology) of the USA in 2007 [19]. It was a breakthrough for companies to develop resonant coupling WPT for commercial needs.

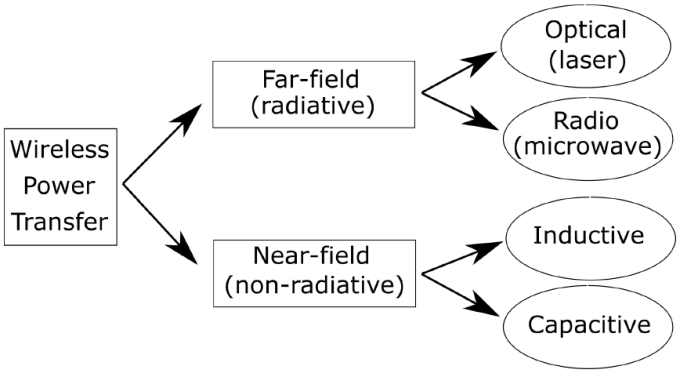

Fig. 1.4. Classification of wireless power transfer techniques.

Wireless power techniques can be mainly divided into two categories, non-radiative (near field) and radiative (far-field). The main difference between the two is that the non-radiative methods are coupling-based while the radiative are radio frequency (RF)-based, as shown in Fig. 1.4. Near field non-radiative techniques can be broadly divided into the inductive coupling, and capacitive coupling. In far-field, techniques can be transferred as a laser beam or as a radio frequency wave.

1.2.1. Non-radiative WPT

Near field non radiative techniques can be broadly divided into inductive coupling and capacitive coupling.

1.2.1.1. Inductive Coupling

In inductive wireless power transfer (IWPT), power is transferred between primary (transmitter) and secondary (receiver) coils of wire by a magnetic field [20]. Generally, with respect to free space wavelength, the dimensions of the coil are small at the frequency of power transfer. Similarly, while considering the wavelength λ, the two coils are close enough and the distance between the coils is usually smaller than $2D^2/\lambda$, where D is the coil diameter. By Ampere's law, an alternating current (AC) through the primary coil (L1) creates an oscillating magnetic field (B). The magnetic field passes through the secondary coil (L2), where it induces an alternating EMF (voltage) by Faraday's law of induction. The induced EMF results in alternating current may either drive the load directly or be rectified to direct current (DC) by a rectifier in the receiver, which drives the load. This type of non-radiative power transfer has several advantages: its non-radiative energy does not harm any living beings [21]; it has low power wastage; it does not interfere with radio waves; and it offers relatively high efficiency through highly resonant strong coupling. But the main disadvantage is that it can only work in the close proximity to the transmitter such as induction stovetops, industrial heaters, electric toothbrush and razor etc. Moreover, the number of variables in the coupling such as coil alignment, coupling factor with distance, coil design variations and mounting platforms etc makes the optimization difficult. In recent inductive systems, resonant inductive coupling is used for improving the performance by using resonant circuits. This can achieve high efficiencies at greater distances than non-resonant inductive coupling such as portable devices and electric vehicles.

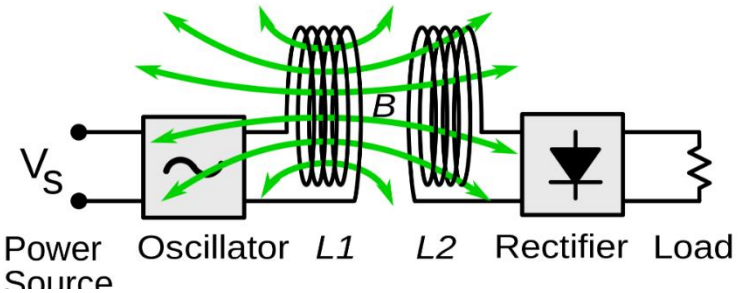

Fig. 1.5. Inductive wireless power transfer.

1.2.1.2. Capacitive Coupling

Capacitive wireless power transfer (CWPT) is a useful and essential alternative to the conventional inductive power transfer (IWPT), that has been highly researched in recent years due to its low-cost capacitive interfaces and simplicity [22]. Both IWPT and CWPT are prevalent methods that function over a short range. However, IWPT has been most frequently used to operate at various power loads and in a range of several meters. In [19], a group of researchers at the Massachusetts Institute of Technology demonstrated a resonant inductive coupling by transmitting 60 W power to a lamp placed 2 m from the transmitter with an efficiency of 40%. In contrast, CWPT uses electric field coupling, which is sustainable in kW level applications and produces lower electromagnetic interference with its reduced size, making it a highly feasible charging solution for battery-powered devices [23]. Based on CWPT's principle, both the transmitter and receiver are formed with a pair of parallel conductive plates. A supply current charges the plates at the transmitter's end while the plates on the receiving end are charged with the transmitter's opposite polarity. Thus, the voltage on the secondary side is generated between the plates. However, existing CWPT applications have the same limitations as regular capacitors where the coupling capacitance is restricted by the available area, as is the air gap between the conductors. Additionally, the medium between the plates also has a considerable effect on the capacitance. The CWPT circuit is presented in Fig. 1.6. One of the main advantages of using CWPT over IWPT is that the losses caused by eddy current are negligible. In CWPT, an inductive coil is not required to transmit power; therefore, the losses caused by eddy current only appears on the wires connecting the inverter and charging plates. The operating frequency at which the power is transmitted between the transmitter and receiver plates is considerably lower than the operating frequency

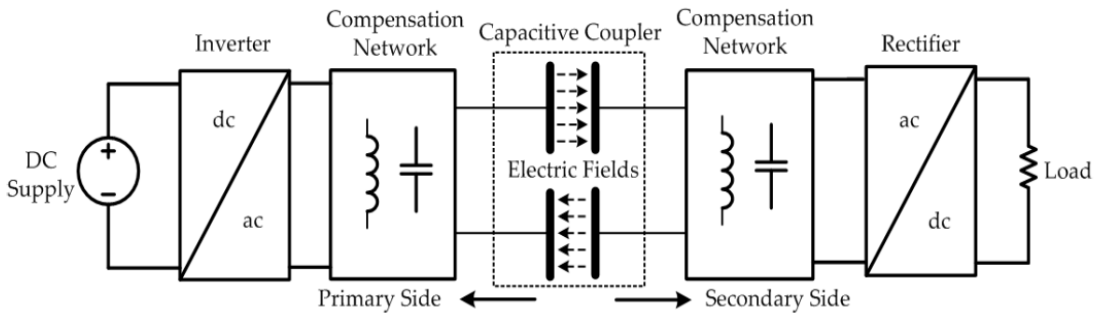

Fig. 1.6. Capacitive wireless power transfer.

of an IWPT system [24]. Higher charging efficiencies can be achieved by adding inductors that alter the operating frequency and duty cycle to accommodate higher capacitance. Applications of CWPT include EV charging, low-power integrated circuits, biomedical devices and mobile device chargers.

1.2.2. Radiative WPT

In far field or radiative techniques, power is transferred by beams of electromagnetic radiation, like microwaves or laser beams. These techniques can transport energy with longer distances but must be directed to the receiver. Recommended applications for this category are solar power satellites and wireless powered drone aircrafts.

1.2.2.1. Microwave Wireless Power Transfer (MWPT)

Microwave wireless power transfer (MWPT) is considered the most efficient far-field technique capable of transmitting power over multiple km range via microwave radiation. Initial microwave WPT was deployed in 1858 at Raytheon. MWPT system converts direct current (DC) into microwaves using a microwave generator, which is then passed through coax to the wave-guide adapter to isolate the wave generator and avoid detuning the selected frequency. Tuners and the directional couplers are used to distinguish the waves as per the propagation directions which are then transmitted directly from the transmitting antenna targeted towards the receiver antenna. Upon receiving the signal, it is then passed through a low pass filter (LPF) and the received microwave power is converted back into electrical energy. Even though 2.45GHz is practically proven to be the highest efficient frequency with efficiency over 95% to be used in MWPT [25], 5.8GHz, 8.5GHz, 10GHz and 35GHz are also used with reasonable efficiencies for MWPT. Moreover, MWPT efficiency strongly depends on the microwave generator and the rectenna used to transmit the power from the source to target. The MWPT is used to send energy on large distances. However, to enable the transmission, the transmitter must see the receiver [26]. The direction of the transmitter focus must be on the receiver at any time of the transmission. The main concern of using microwaves is safety since high-power microwaves presents a serious threat to the human body [27]. The main applications of microwave WPT are the unmanned ground vehicle (UGV), space missions, and solar power satellites (SPS).

1.2.2.2. Laser Power Transmission

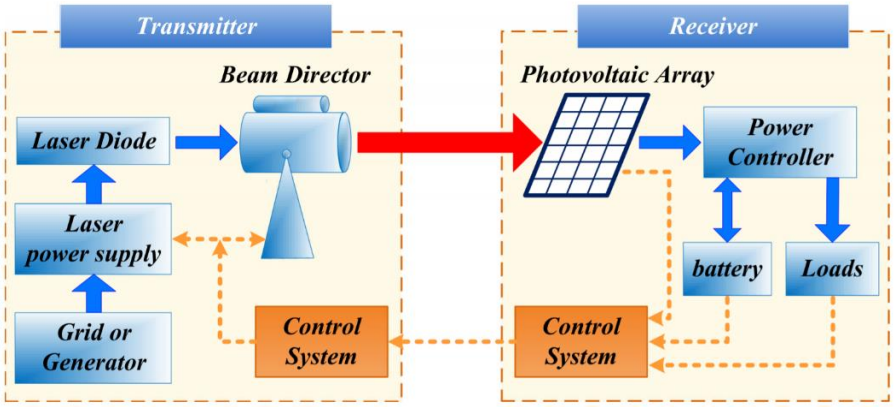

Fig. 1.7. Block diagram of laser power transmission.

Laser power transmission (LPT) is one of the most encouraging technologies in the long-range wireless power transfer field. LPT investigation has been driven by the desire to remotely power unmanned aerial vehicles, satellites, and other mobile electric facilities. But, the low overall efficiency is the primary issue that restricts the high-intensity laser power beam (HILPB) system. LPT technology is based on the concept of the photoelectric effect proposed in 1965 [28]. Later on, NASA's first successful demonstration of laser-powered aircraft flight was performed in 2003 [29]. The 500-W laser power beam manually tracked the aircraft's flight path at 15 m range, resulting in a laser power of 40 W to the PV array and 7 W of power to the motor to support flight for 15 min. After that, several attempts on LPT were carried out by Kinki University [30], Laser Motive [31], Beijing Institute of Technology [32] and Russia's Rocket and Space Corporation [33]. The LPT technology is still under advancement; most of the HILPB systems only can transmit several tens of watts across several hundred meters with comparably low efficiency and is far from its practical implementation. For the HILPB system to become a feasible option for practical wireless power transfer, each system's component must ensure sufficient high efficiency to provide high end-to-end system efficiency. The transmitter of the system converts power from a common source (battery, generator, or grid) into a monochromatic beam of light via a laser. This laser beam is then shaped with optics and directed via a beam director to the remote PV receiver. While in the receiver, specialized PV cells matched to the laser wavelength and beam intensity convert the laser light back into electricity to charge a battery, run a motor, or do other work.

1.3. Research Motivation

In recent years, wireless energy harvesting and power transfer have relished a rapid growth. Rectifying-antennas (also known as rectennas) are the critical element for RF energy harvesting systems. It was motivated by the idea of wireless power transfer via radio waves, raised by Tesla in 1890s, and first experimentally demonstrated by W. C. Brown in 1960s. Traditionally, the rectennas were developed with the purpose of long-distance microwave power transmission. Although much research has been conducted on rectennas' design, there is a continuous demand for finding new rectenna designs to meet the current and future wireless applications. Moreover, a clear distinction between rectennas for WEH and WPT are not significantly considered while developing the rectennas for different applications.

Most reported rectennas were designed for a single and narrow frequency band and optimized for a fixed incident power level and load impedance. These designs incident power levels were usually higher than 10 mW (up to several kilowatts). However, the ambient EM fields are of quite low power density, typically below 10 nW/cm^2[34]. The detailed EM power in the RF frequency bands is depicted in Chapter 2 (Fig. 2.13). The ambient RF power is distributed over a pretty wide frequency band, from about 88 MHz to 5 GHz. For ambient RF energy harvesting applications, most of the conventional rectenna will not work. Therefore, to increase the harvested power in such a low power ambient environment, there is a need for developing rectennas that cover a wide frequency band (to match with the ambient signal spectrum) and good power conversion efficiency at the ambient power levels. The design of broadband rectennas is exceptionally challenging due to the utilization of nonlinear elements (diodes) of the rectifying circuit. Unlike a passive antenna system (only as a function of frequency), the rectifier's impedance varies as a function of frequency, power, and load impedance (since the nonlinear device does not have a linear relationship between the current and voltage) [35]. Such a rectifying-antenna can be viewed as a nonlinear system. Therefore, it is hard to achieve a good conversion efficiency and impedance matching performance over a wide frequency band under the ambient power conditions.

Conventional WPT and WEH rectifier usually utilize Si-based Schottky diodes for rectification. Low breakdown voltage in silicon Schottky diodes limits the conversion

efficiency in the high-power region. High RF (radio frequency) input power results in large voltage and current swings in Schottky diodes. This triggers a breakdown in the metal-semiconductor junction and can permanently damage a diode. Consequently, Si Schottky diode-based rectifiers usually operate below watt-level input power. To prevent the breakdown in low-power capability diodes for realizing high-power rectifiers, power divider circuits are utilized to split the high input power into several diode circuits [36]. However, these approaches introduce additional size and losses, as well as increase circuit complexity.

As the WPT system employs intentional power from the transmitter, it can be possible to use a dedicated RF source's advantage. Conventional rectennas for WEH and WPT can only offer a limited DC power amount and typically do not have the rectenna's location knowledge. Several researchers proposed antenna arrays with beam steering capabilities to direct the microwave energy beam towards the desired rectenna and enhance the incident power level [37]. As the antenna array is typically used for high gain performance, the radiation is very directive. Thus, a slight misalignment can lead to an increased fall in energy conversion efficiency and output DC power. Thus, a technique to estimate the location to enhance the WPT is very much required.

The aforementioned problems are the major challenging issues that would restrict rectennas' application in practical energy harvesting systems and wireless sensor platforms. Besides, the design process of broadband rectennas usually is quite complicated. Thus, the structure of reported rectennas was relatively complex, increasing the cost and loss of the design. This feature could also limit the commercialization of RF energy harvesting systems since the cost of such a system using broadband rectennas could be higher than that of other commercial energy harvesting devices. The aim of this work is to overcome the aforementioned research challenges and problems. The objectives of the research in this thesis are:

- To develop a method of reducing the complexity of broadband rectennas so that the cost of the rectenna system can be significantly reduced. The broadband rectifier should be able to capture RF energy from a broad bandwidth.

- To develop a rectenna that has the ability to harvest RF energy from low ambient power conditions. The rectenna should be able to demonstrate high sensitivity for real life applications.
- To develop a RF energy harvester that can capture maximum available DC power. The rectenna should be able to capture RF energy in a typical indoor ambient environment (thus suitable for IoT and smart home applications).
- To develop a communication rectenna that has the ability to harvest RF energy from a dedicated RF source and ambient conditions. Moreover, the rectenna should be able to perform the wireless data transfer for WSN applications.
- To develop a microwave rectifier that exhibits a good performance in the high-power region and can withstand watts of input power before reaching the breakdown limit. The aim is to have a high efficiency performance with a small footprint and making it suitable for high-power applications like future unmanned intelligent devices and WPT in space applications.
- To develop a WPT rectenna that has the ability to provide a feedback to guide the radiation pattern of the transmitter antenna array. The rectenna should be able to form a closed-loop system by providing its location information for efficient WPT applications.

1.4. Organization of the Thesis

This thesis consists of nine chapters that mainly focus on design, optimization, and measurement of novel rectennas with improved efficiency, a reduced nonlinear effect, and a much-simplified structure for the target WPT and WEH applications. The structure of the thesis is organized as follows.

Chapter 1 introduces the background of this work, including the motivation and objectives of the research in this thesis.

Chapter 2 is an overview of the development of WPT and WEH technologies, with a detailed literature review of the state-of-art in rectenna designs for these applications. The conventional rectennas for high power WPT, recent rectennas for low power WEH and some techniques to improve the rectenna performance are discussed in separate sections.

Chapter 3 introduces a novel broadband rectenna design for WEH applications. The proposed rectenna consists of a novel broadband Yagi-Uda antenna and a transmission lines-based broadband rectifier. A highly compact antenna is proposed using curved reflectors and meandered dipoles and directors. A novel three-stage impedance matching technique is utilized in the rectifier design to achieve high efficiency with a compact size. This broadband rectifier exhibits high conversion efficiency performance over a wide bandwidth.

Chapter 4 introduces a novel dual-band high sensitivity rectenna for ambient WEH. The proposed rectenna utilised a dipole antenna with folded stubs for dual mode operation. A single inductor matched high sensitivity rectifier is also proposed. This design confirms the feasibility of ambient energy harvesting by demonstrating high conversion efficiency at low input power levels.

Chapter 5 presents a novel RF harvester for ambient low power energy harvesting applications. This design utilised a combined harvesting approach in which five antenna elements with dual-band and wide band characteristic are utilised to capture energy from 915-960 MHz, 1.8-2.7 GHz, and 3.4-3.7 GHz frequency bands. The proposed RF energy harvester utilised high sensitivity and high efficiency rectifiers for improving the performance. This design confirms the possibility of capturing high DC output power from indoor ambient RF environment.

Chapter 6 introduces a novel communication rectenna solution to provide efficient data and power transfer in wireless sensor nodes. With the ambient energy harvesting of conventional rectenna, the proposed design can also perform simultaneous wireless information and power transfer for facilitating uninterrupted power supply and data transfer of WSN nodes. A dual polarized 2×1 square patch antenna array and a multisection bended broadband monopole antenna are employed for SWIPT and AWEH, respectively. Thus, the proposed communication rectenna array with ambient energy harvesting can be a promising candidate for future wireless sensor nodes.

Chapter 7 introduces a novel GaN Schottky diode-based microwave rectifier for high-power applications. A novel low loss impedance matching is utilised by exploiting the unavoidable inductance effects of bond wires used for providing the electrical connection between GaN chip and board. This rectifier design confirms the feasibility of high-power operation and demonstrated high output voltage and power.

Chapter 8 presents a first-of-its-kind duplexing rectenna with a harmonic feedback capability for efficient WPT applications. Duplexing rectenna can efficiently convert the incident RF power at 0.915 GHz to DC and also send a reasonable harmonic signal back to the RF transmitter at 1.83 GHz for tracking the position of rectenna to improve power transfer efficiency without the need of another antenna and transmitters. Experimental demonstration of rectenna alignment for optimum power transfer is performed by determining the maximum received feedback power. This rectenna with feedback property is a very promising solution for future efficient WPT applications.

Chapter 9 draws the conclusions of this research work and some thoughts for the future work.

References

[1] "IoT analytics. State of the IoT 2018: Number of IoT devices now at 7B – Market accelerating," [Online]. Available: *https://iot-analytics.com/state-of-the-iot-update-q1-q2-2018-number-of-iot-devices-now-7b/.*

[2] Fierce electronics: "Wireless sensor use is expanding in industrial applications," [Online]. Available: *https://www.fierceelectronics.com/components/wireless-sensor-use-expanding-industrial-applications/.*

[3] R. Vullers, R. Schaijk, H. Visser, J. Penders, and C. Hoof, "Energy harvesting for autonomous wireless sensor networks," *IEEE Solid-State Circuits Mag.,* pp. 29-38, 2010.

[4] P. Jaffe and J. McSpadden, ''Energy conversion and transmission module for space solar power,'' *Proc. IEEE*, vol. 101, no. 6, pp. 1424–1437, Jun. 2013.

[5] A. Collado and A. Georgiadis, ''Conformal hybrid solar and electromagnetic (EM) energy harvesting rectenna,'' *IEEE Trans. Circuits Syst. I, Reg. Papers*, vol. 60, no. 8, pp. 2225–2234, Aug. 2013.

[6] R. Arai, S. Furukawa, N. Sato, and T. Yasuda, ''Organic energy harvesting devices achieving power conversion efficiencies over 20% under ambient indoor lighting,'' *J. Mater. Chem. A*, vol. 7, no. 35, pp. 20187–20192, 2019.

[7] B. Gregg and M. Hanna, ''Comparing organic to inorganic photovoltaic cells: Theory, experiment, simulation,'' *J. Appl. Phys.,* vol. 93, no. 6, pp. 3605–3614, Mar. 2003.

[8] G. Mahan, B. Sales, and J. Sharp, ‘‘Thermoelectric materials: New approaches to an old problem,’’ *Phys. Today*, vol. 50, no. 3, pp. 42–47, Mar. 1997.

[9] V. Leonov, ‘‘Thermoelectric energy harvesting of human body heat for wearable sensors,’’ *IEEE Sensors J.*, vol. 13, no. 6, pp. 2284–2291, Jun. 2013.

[10] H. S. Kim, J. -H. Kim, and J. Kim, ‘‘A review of piezoelectric energy harvesting based on vibration,’’ *Int. J. Precision Eng. Manuf.*, vol. 12, no. 6, pp. 1129–1141, Dec. 2011.

[11] S. Kim et al., “Ambient RF energy-harvesting technologies for self-sustainable standalone wireless sensor platforms,” *Proc. IEEE*, vol. 102, no. 11, pp. 1649–1666, Nov. 2014.

[12] H. Visser and R. Vullers, ‘‘RF energy harvesting and transport for wireless sensor network applications: Principles and requirements,’’ *Proc. IEEE*, vol. 101, no. 6, pp. 1410–1423, Jun. 2013.

[13] Gigaom. “Energy harvesting chips: The next big thing for a connected world,’’ [Online]. Available: *https://gigaom.com/2013/11/21/energy-harvesting-chips-the-next-big-thing-for-aconnected- world/.*

[14] Texas instruments. “BQ25504 Ultra-Low Power Boost Converter with Battery Management for Energy Harvester | Nano-Power Management,’’ [Online]. Available: *https://www.ti.com/product/BQ25504*

[15] S. Catarinucci, *et al*., “An IoT-aware architecture for smart healthcare systems,” *IEEE Internet Things J.*, vol. 2, No. 6, pp. 515-526, Mar. 2015.

[16] A. Zanella, N. Bui, A. Castellani, L. Vangelista and M. Zorzi, “Internet of Things for Smart Cities,” *IEEE Internet Things J.*, vol. 1, no. 1, pp. 22-32, Feb. 2014.

[17] N. Tesla, “The transmission of electrical energy without wires,” *Elect. World Eng*., vol. 1, 1904.

[18] W. C. Brown, “The history of the development of the rectenna,” *Solar Power Satell. Microw. Power Transmiss. Reception,* Washington, DC, USA, Tech. Rep. NASA CP-2141, 1980, pp. 271–280.

[19] A. Kurs, A. Karalis, R. Moffatt, J. D. Joannopoulos, P. Fisher and M. Soljačić, “Wireless power transfer via strongly coupled magnetic resonances,” *Science*, vol. 317, no. 5834, pp. 83-86, July 2007.

[20] N. Shinohara, “Power without wires,” *IEEE Microw. Mag*., vol. 12, no. 7, pp.

64–73, Dec. 2011.

[21] T. Hiramatsu, X. Huang, M. Kato, T. Imura, and Y. Hori, "Wireless charging power control for HESS through receiver side voltage control," *Proc. IEEE Appl. Power Electron. Conf.*, 2015, pp. 1614–1619.

[22] J. Dai and D. C. Ludois, ''A survey of wireless power transfer and a critical comparison of inductive and capacitive coupling for small gap applications,'' *IEEE Trans. Power Electron*., vol. 30, no. 11, pp. 6017–6029, Nov. 2015.

[23] F. Lu, H. Zhang, H. Hofmann, and C. Mi, "A double-sided LCLC-compensated capacitive power transfer system for electric vehicle charging," *IEEE Trans. Power Electron*., vol. 30, no. 11, pp. 6011–6014, 2015.

[24] F. Lu, H. Zhang, H. Health, and C. C. Mi, "An inductive and capacitive combined wireless power transfer system with LC-compensated topology," *IEEE Trans. Power Electron*., vol. 31, no. 12, pp. 8471–8482, Dec. 2016.

[25] Z. Harouni, L. Cirio, L. Osman, A. Gharsallah, and O. Picon, "A dual circularly polarized 2.45-GHz rectenna for wireless power transmission," *IEEE Antennas Wireless Propag. Lett*., vol. 10, pp. 306–309, 2011.

[26] X. Yang, W. Geyi, and H. Sun, ''Optimum design of wireless power transmission system using microstrip patch antenna arrays,'' *IEEE Antennas Wireless Propag. Lett*., vol. 16, pp. 1824–1827, 2017.

[27] A. Ahmad, M. S. Alam, and R. Chabaan, ''A comprehensive review of wireless charging technologies for electric vehicles,'' *IEEE Trans. Transport. Electrific*., vol. 4, no. 1, pp. 38–63, Mar. 2018.

[28] W. S. Jones, L. L. Morgan, J. B. Forsyth, and J. P. Skratt, "Laser power conversion system analysis, volume 2," *Lockheed Missiles Space Corp*., Palo Alto, CA, USA, 1979.

[29] D. E. Raible, "High intensity laser power beaming for wireless power transmission," Master's Thesis, *Dept. Elect. Comput. Eng.*, Cleveland State University, Cleveland, OH, USA, May 2008.

[30] N. Kawashima and K. Takeda, "Laser energy transmission for a wireless energy supply to robots," *Proc. Symp. Automat. Robot. Construction*, 2005, pp. 373–380.

[31] "AUVSI: Laser Motive, Lockheed demonstrate real-world laser power," 2012. [Online]. Available: *https://www.flightglobal.com/news/articles/auvsi-*

lasermotive-lockheed demonstrate-real-world-laser-375166/

[32] T. He, *et al*., "High-power high-efficiency laser power transmission at 100m using optimized multi-cell GaAs converter," *Chin. Phys. Lett*, vol. 31, no. 10, pp. 1042031–1042035, 2014.

[33] K. Jin and W. Zhou, "Wireless Laser Power Transmission: A Review of Recent Progress," *IEEE Trans. Power Electron*., vol. 34, no. 4, pp. 3842-3859, April 2019.

[34] M. Pinuela, P. D. Mitcheson, and S. Lucyszyn, "Ambient RF energy harvesting in urban and semi-urban environments," *IEEE Trans. Microw. Theory Techn*., vol. 61, no. 7, pp. 2715–2726, Jul. 2013.

[35] C. Song, *et al*., "A Novel Six-Band Dual CP Rectenna Using Improved Impedance Matching Technique for Ambient RF Energy Harvesting," *IEEE Trans. Antennas Propag*., vol. 64, no. 7, pp. 3160-3171, July 2016

[36] Y. Xu and R. G. Bosisio, "Design of Multiway Power Divider by Using Stepped-Impedance Transformers," *IEEE Trans. Microw. Theory Techn.*, vol. 60, no. 9, pp. 2781-2790, Sept. 2012.

[37] S. Ladan, A. B. Guntupalli, and W. Ke, "A high-efficiency 24 GHz rectenna development towards millimeter-wave energy harvesting and wireless power transmission," *IEEE Trans. Circuits Syst. I Reg. Papers*, vol. 61, no. 12, pp. 3358-3366, Dec. 2014.

Chapter 2. Literature Review

The history of wireless power transfer, the introductory phase of research that commenced during the early 18th century and the most recent development in the field of WPT are presented in Section 2.1. This discussion is further backed up with various existing WPT techniques that are prominently in use, including the far and near-field techniques. This chapter also outlines, a considerable amount of theoretical background which are based on areas where WPT applications are already in use. WPT has entered the mainstream with few impressive demonstrations despite the gaps between exhibiting the technology viability and commercialisation, this will shape the future of consumer electronics. In the second part of this chapter, advancements in rectenna design for ambient RF WPT and WEH are outlined. This section covers the various aspects of rectenna design for different applications. A detailed discussion of existing rectenna designs for WPT and WEH are also included in this chapter.

2.1. History of Wireless Power Transfer

The initially reported WPT experiment dates back to 1819 by Danish physicist and chemist H.C. Oersted [1]. Oersted discovered that the electric current through an electric wire generates a magnetic field around the conductor. Following Oersted's fundamental discovery, notable findings like Ampere's Force Law, Biot-Savart's Law following Faraday's Law of electromagnetic induction were established, highlighting the connection between magnetism and electric current. In 1864, J.C. Maxwell detailed how magnetic and electric field are generated and affected by each other and mathematically defined them via Maxwell's equations. Later in 1873, his electricity and magnetism theory and his other research efforts during his time in Cambridge were unified into a publication "A Treatise on Electricity and Magnetism" [2]. His study concluded that the same force regulates electricity and magnetism. This historic progress established the theoretical foundation of electromagnetism. After this, a major technical breakthrough appeared in 1888, which was the first experimentally

demonstrated existence of electromagnetic radiation by German scientist Heinrich Hertz, who successfully used a pair of oscillators to transfer electrical power through a small gap between the coils [3]. This experiment was a significant development being the first ever practical observation of the electromagnetic radiation's existence, confirming Maxwell's predictions. A series of experiments based on electromagnetic radiation was further conducted by Nikola Tesla (the father of alternating current (AC) electricity), spending a great deal of time and capital. The primary focus of Tesla's study was to develop a technique that transfers electrical energy over a large distance, eliminating electrical wires. In 1893, he successfully transmits high-frequency current over a short distance using a single wire as a conductor [4]. This was followed by another breakthrough in 1899, when he transmitted 108V of high-frequency electric power to turn on Geissler tubes across the stage [5]. He developed the famous "Tesla coil" which was resonated at 150 kHz and fed with 300 kW of low-frequency power obtained from the Colorado Springs Electric Company [6]. He became the first person to conduct experiments of WPT based on microwave technology. In 1901, Tesla completed his famous Wardenclyffe Tower, which was designed to transmit electricity through the ionosphere over a considerable distance [7]. A picture of Tesla's experiment is depicted in Fig. 2.1 and Fig. 2.2 shows the Wardenclyffe Tower. But the project was later shut down due to low efficiency, hazardous concerns and a lack of

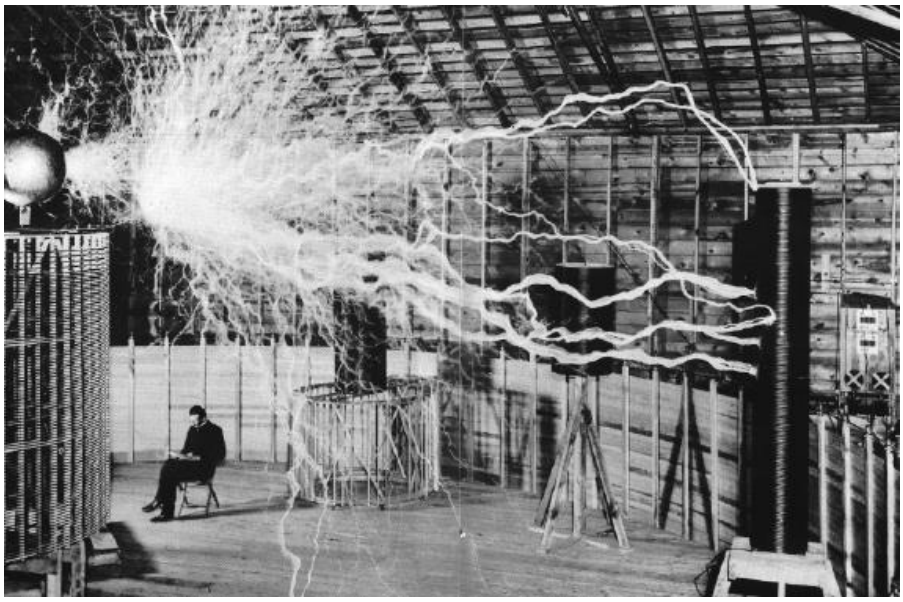

Fig. 2.1. Tesla's experiment of power transfer via radio waves using tesla coil [9].

Fig. 2.2. Wardenclyffe Tower located in Shoreham, New York, 1904 [10]

funding caused by a breakthrough made by an Italian researcher, Marconi, who was able to successfully transmit a radio signal across the Atlantic Ocean [8].

In the 1920s and 1930s, magnetrons were developed to convert the electricity to microwaves, enabling wireless power transmission over large distances [11]. The development of radar in World War II accelerated the antennas and microwave generation technologies. But, at that period, the absence of a device or a method to convert the microwave power back into DC power obstructed WPT development. It was more than a decade after World War II that the development of WPT was almost neglected. In 1964, W.C. Brown, who specialised in the magnetron principle, proposed WPT via microwave during a demonstration during which he also discovered a methodology that converts the incident microwaves back into DC power via a rectenna. As shown in Fig. 2.3, he demonstrated the first wireless-powered aircraft, a model helicopter powered by microwaves beamed from the ground [12]. This experiment confirmed the practicality of microwave powered applications thus stimulated the research interest on this topic during the 1970s and 80s. Since the

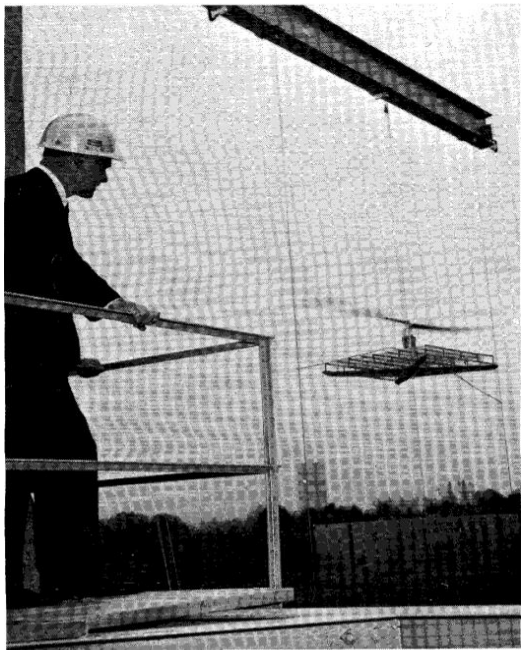

Fig. 2.3. W. C. Brown's microwave-powered helicopter, 1964 [12].

development of rectenna, numerous attempts have been made to achieve high power transmission over a long distance. The experiments were carried out mostly performed by Canadian and Japanese research institutes. In 1975, Brown, Richard Dickinson and his team performed the most extensive microwave power transmission (MPT) demonstration at the Venus Site of the JPL Goldstone Facility. They transmitted a 450-kW power using a 2.388 GHz parabolic antenna (with a diameter of 26 m). They received the power using a rectenna array (with a size of 3.4 m × 7.2 m) across a distance of 1 mile. The rectified DC power was 30 kW with a rectifying efficiency of 82.5% [13]. Another inspiring work in MPT research in the 1970s and 80s was to develop a solar power satellite (SPS), which was formed in 1968 by Peter Glaser [14]. The satellite would harvest energy from the sunlight using solar cells and transmit it down to Earth as microwaves to huge rectennas, converting it to electrical energy on the electric power grid. In 1980, Canada proposed a program to develop a long endurance high altitude platform called the Stationary High-Altitude Relay Program (SHARP) [15]. The platform was to be the first unmanned, fuel-less, lightweight airplane powered remotely by microwaves, thereby providing the ability to stay afloat for long periods. In 1992, Japan launched the Microwave lifted airplane experiment (MILAX), a driving demonstration of an airplane model using microwave power

Fig. 2.4. MILAX experiment [16].

Fig. 2.5. SSP concept

transmission [16]. The experiment was the first attempt to focus and power the moving target using an electronically scanned phased array to keep the 2.411-GHz signal as shown in Fig. 2.4. Two charge-coupled device (CCD) cameras determined the airplane's outline and passing the location to a computer which scanned the array to the proper location. The transmitting array was located on a sports utility vehicle which was also in motion during the tests. Several innovations in portable electronics (laptops, mobile phones, sensors etc) emerged during the late 1990s, due to that development of semiconductors led to far better and cheaper consumer electronics, after having competed primarily through performance which was measured by the energy consumption at the time. All approaches were pretty fruitless where the devices

Fig. 2.6. Massachusetts research group demonstrating inductive near-field coupling [18].

actually did not have a permanent power source and therefore a power source such as a battery was required. The battery offers a limited power source with shorter lifetime, hence the necessity for a low power inductive based wireless power transfer was raised. In 2000, NASA MSFC conducted the SSP Scientific Exploratory Research and Technology (SERT) program and broadened the scientific community's involvement and resulted in successful demonstrations on a variety of system level components [17].

In the same period, the near-field non-radiative coupling-based power transfer was not widely studied and therefore progressed slowly. In 2007, Massachusetts Institute of Technology physicist Marin Soljacic and his colleagues conducted an experiment to demonstrate the inductive near-field coupling of power from a primary ac-excited coil to an awaiting secondary coil located 2 m away. A 60-W light bulb attached to the secondary coil was successfully lit [18]. A picture of the demonstration of this

Fig. 2.7. Mophie 3-in-1 charger [20].

experiment is given in Fig. 2.6. As a result of this breakthrough, a wireless power consortium (WPC) was established in 2008 to develop standards regarding wireless charging of mobile devices [19]. They found the "Qi" standard for inductive coupling WPT in December 2010. Fig. 2.7 shows a Mophie 3-in-1 charger, for charging multiple devices simultaneously.

2.2. Overview of Rectennas Studies

2.2.1. Rectennas for High Power WPT

William. C. Brown was a pioneer in developing the first 2.45-GHz rectennas that included the basic circuit components still evident in today's rectenna designs. Motivated by Brown's experiment of ground-to-ground microwave power transmission, the development of rectenna in the 1990s focused on high power WPT systems used for SPS and MPT applications [21]-[29]. T. W. Yoo and K. Chang developed the first 35 GHz rectenna with an incident power of 60 mW and maximum conversion efficiency of 35% [21]. In 1992, a closed form equation was suggested for investigating the performance of rectenna diode's RF to DC power conversion efficiency [22]. The block diagram of rectenna used in this design is given in Fig. 2.8. The rectifying circuit consists of a single diode shunt-connected across the transmission lines. The low pass filter inserted between the antenna and rectifying circuit was designed to bypass the fundamental frequency and reject the higher-order harmonics generated from the nonlinear rectifying circuit. The higher order harmonics from rectifying diode may reradiate through the antenna and it can cause reduction in conversion efficiency. A 5.8 GHz high efficiency rectenna was designed for 50 mW input power and achieved a maximum conversion efficiency of 82% [26]. A dual-band rectenna was reported in [29] that had two resonant frequencies at 2.4 and 5.8 GHz, respectively. As shown in Fig. 2.9, two dipole antennas were connected to a series of band-stop filters coupled to a Schottky barrier diode. This design's conversion

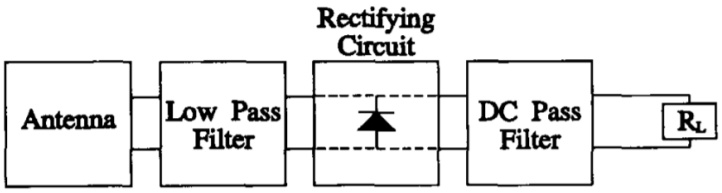

Fig. 2.8. Block diagram of rectenna [22].

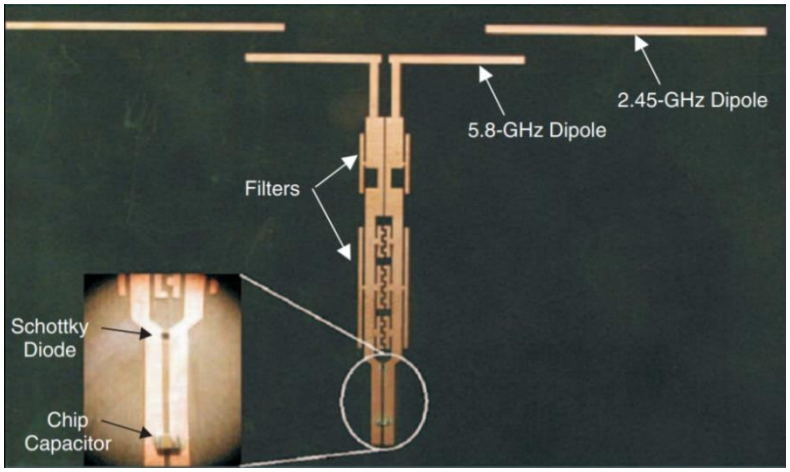

Fig. 2.9. Dual-band rectenna operating at 2.4 and 5.8 GHz [29].

efficiency was up to 84% when the input power to the rectifier was 80 mW. It was revealed that the filters for harmonic rejection utilized in this design were critical to increase the conversion efficiency. The reason for such improvements was that the low-pass filter blocked the higher-order harmonic signals generated by the rectifier to prevent the re-radiation of these signals by the antenna. In the meantime, these signals were partially rectified by the diodes. Therefore, the rectified DC power (around 20% of the total power) of these signals was delivered to the load. In general, the overall conversion efficiency of the rectifier can be improved by about 5 – 10% with the aid of such a harmonic rejection feature.

In the same period, a few rectenna arrays were reported to improve the antenna's RF power and increase the output power delivered to the load. Some examples of such rectenna arrays are depicted in Fig. 2.10. In [30], a very large rectenna array was reported with a size of 3.2 m × 3.6 m. It had 256 sub-array elements formed by 2.45 GHz circular microstrip patch receiving antennas. The RF-DC conversion efficiency of this rectenna array was about 64% at 2.5 W power. A high-efficiency C-band rectenna array was reported in 2003 [31]. Rectenna array utilized circularly polarised antennas with a high realized gain of 11 dB and a better than 1 dB axial ratio with a fractional bandwidth of 4.7%. A high conversion efficiency of 81% was achieved at 5.71 GHz and utilized a CPS band-reject filter (BRF) to suppress the re-radiated harmonics by about 19 dB. Similar work was presented in [32] and shown in Fig. 2.11(a). In order to avoid the polarization mismatch problems associated with LP polarization, a CP feature was adopted in this design. It achieved a conversion efficiency of more than 73% with an input power of 10 mW.

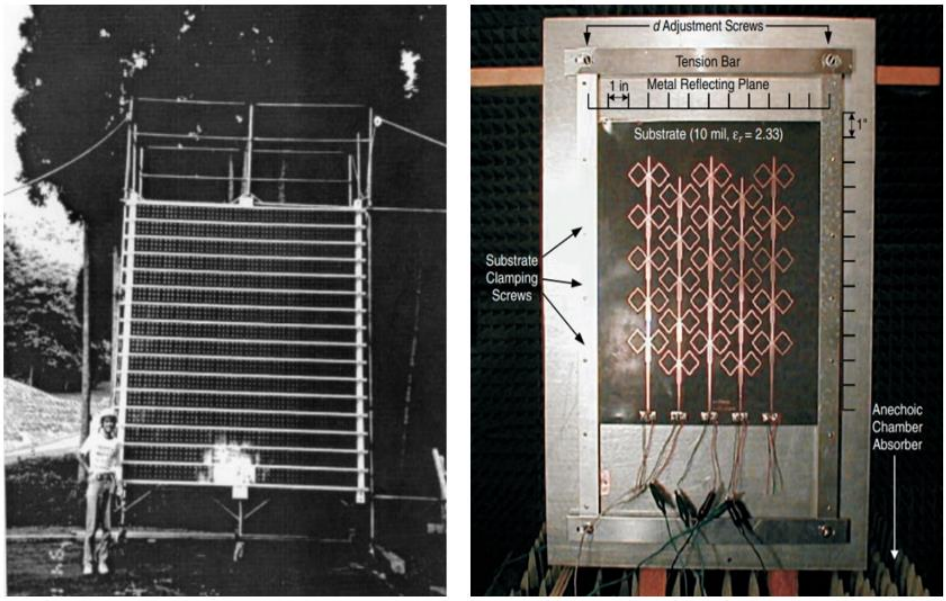

Fig. 2.10. (a) Rectenna array with 256 elements reported in [30] (b) C-band circularly polarized rectenna array [31].

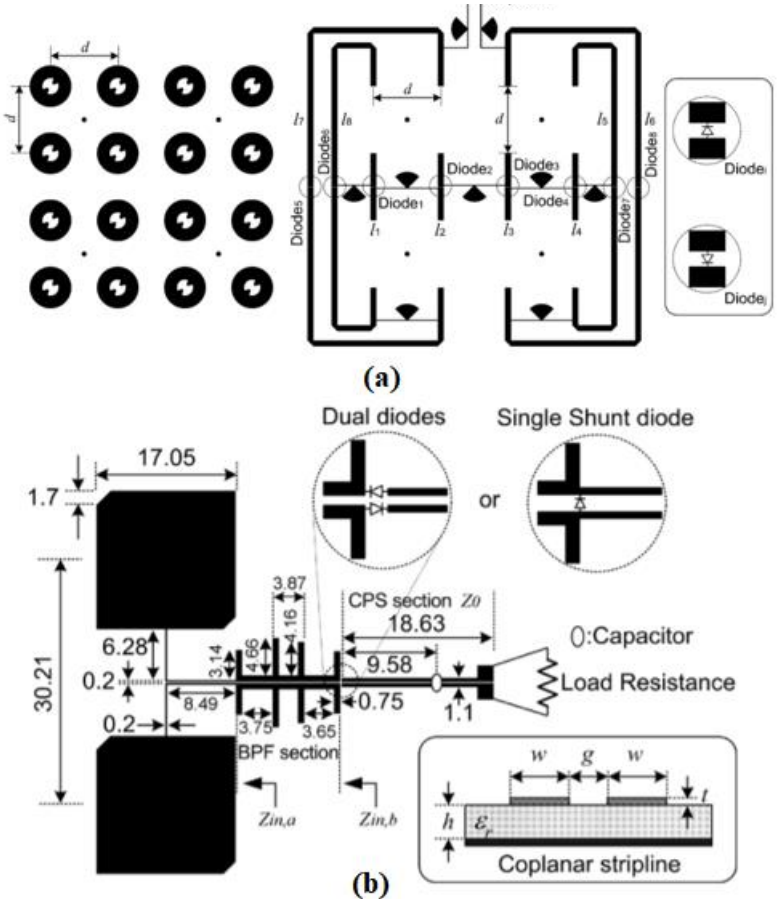

Fig. 2.11. (a) 5.8 GHz circularly polarized rectenna array [32] (b) circularly polarized retrodirective rectenna arrays.

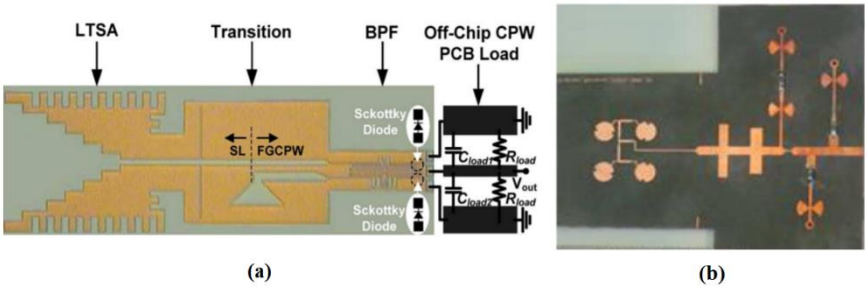

Fig. 2.12. (a) Dual-band rectenna operating at 35 and 94 GHz (b) 24 GHz rectenna.

In [34], circularly polarized retrodirective rectenna arrays, including a 2 × 2 array and a 4 × 4 array was introduced as shown in Fig. 2.11 (b). A proximity-coupled microstrip ring antenna was used as the retrodirective rectenna array element, automatically blocking harmonic signals up to the third order from reradiating by the rectifying circuit. The retrodirective rectenna array can automatically track the incoming power source signals and is less sensitive to the power incident angle variations, i.e., main-beam alignment deviation. Circularly polarized rectennas or rectenna arrays with harmonic rejection were demonstrated to have good performance for WPT applications [35]-[41], since the loss due to the polarization mismatch between the transmitting antenna and receiving rectenna can be removed and the reradiation of harmonic signals generated from the rectifier can be avoided as well. Such rectennas have demonstrated to achieve very high conversion efficiency (e.g., more than 80%), but most of them are a single band design and optimized for relatively high input powers (e.g., from 10 mW to 10 W).

At the National Central University (Jhongli, Taiwan) in 2010, researchers designed the dual-band rectenna shown in Fig. 2.12 (a). For an incident power density of 30 mW/cm^2, this rectenna achieves 53% and 37% conversion efficiencies at 35 and 94 GHz, respectively. The linear tapered slot antenna has gains of 7.4 and 6.5 dBi at 35 and 94 GHz. The total rectenna size is 2.9 mm^2 [42]. In [43], a high-efficiency 24 GHz rectenna was fabricated. The maximum conversion efficiency of 24% and a maximum output DC voltage of 0.6 V was observed at a power density of 10 mW/cm^2 at 24 GHz. Also, it was found that most designs reported in the literature were optimized for a specific operating condition such as a fixed input power level and a fixed load resistance. This will limit the practicality of such rectenna designs used in real-world applications since the operating condition for different applications is normally quite

different. Up to now, there are no good enough methods to design a rectenna that can harvest RF energy with high conversion efficiency from low ambient RF power levels (-35 to -20 dBm) over a broad bandwidth.

2.2.2. Rectennas for Low Power Energy Harvesting

With the rapid development of the consumer communication market, an increasing number of RF base stations for communications have been gradually mapped worldwide to ensure a wide network coverage. This vast growth in RF energy motivated the idea of ambient RF energy harvesting (also known as wireless energy harvesting) in recent years (after 2000). From the data reported in 2012 [44], there have been about 12 million cellular base stations deployed globally, and each station radiates around 4 W isotropic power. Moreover, according to [45], Wi-Fi-enabled consumer electronic devices have reached a number of 4000 million by the year of 2014 and more than 6800 million SIM cards were detected being in use [46]. Therefore, it is evident that there has been a significant amount of RF powers broadcasted into the air through various sources (such as radio, DTV, Wi-Fi and mobile phones). It is very attractive that if these RF powers can be harvested from the ambient environment and used by the low power devices related to the IoT as mentioned in Chapter 1. However, the ambient powers are distributed over a relatively wide frequency band, from 200 MHz to 3 GHz. In contrast, the power level at each band is normally low. A report of ambient RF power measurements was published in 2013 [47]. An example of the power spectrum is shown in Fig. 2.13 for typical ambient

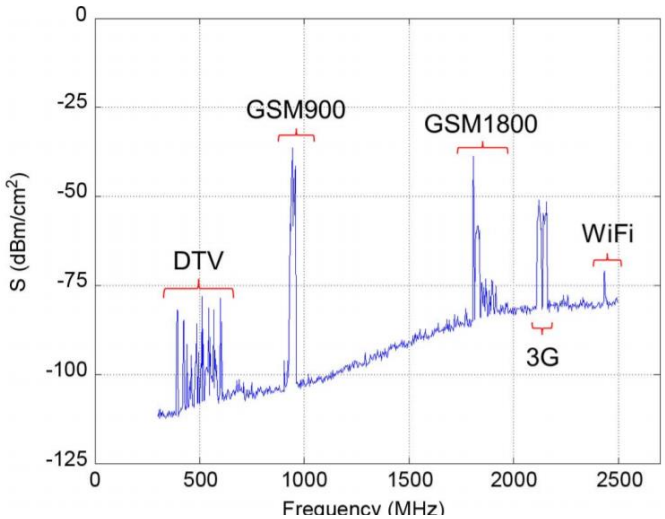

Fig. 2.13. An example of ambient power spectrum [47].

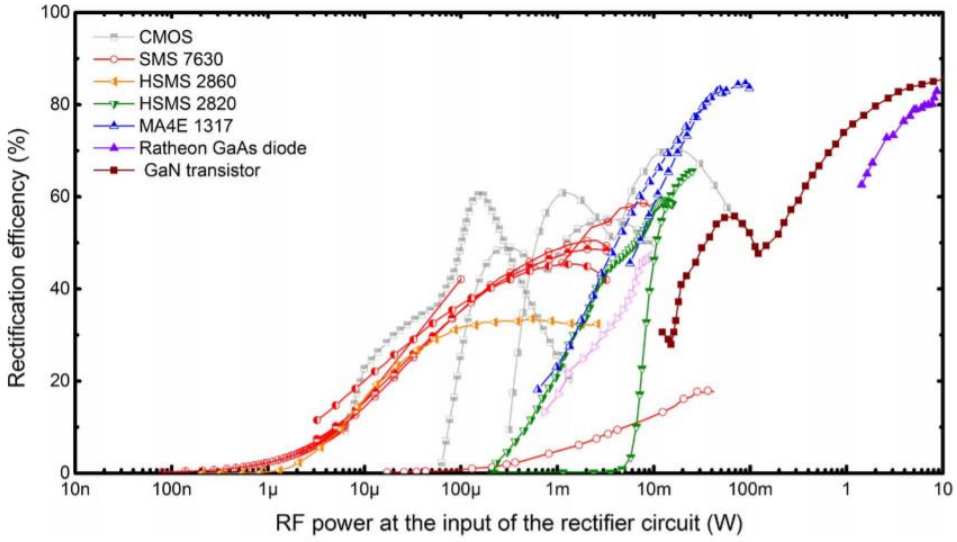

Fig. 2.14. Performance of microwave rectifiers with different rectifying diodes [48].

environments. It is shown that the ambient RF power densities over the broadband are generally below -30 dBm/cm^2. Thus, the rectenna designs discussed in Section 2.2.1 are not suitable for energy harvesting application due to their very high input power levels.

Numerous research efforts have been reported on low power ambient energy harvesting [48]-[65]. Rectifying elements are crucial elements which determine the performance of the rectifier. It is necessary to select diodes with low power consumption for low power AWEH. Even though it has only a negligible effect on high power WPT applications, it adversely affects the performance of low power AWEH. In [48], researchers compared the performance of different diodes typically used for rectenna designs. The best conversion efficiency curve achieved by each single diode is shown in Fig. 2.14. It is found that only a few diodes (e.g., SMS7630 from Skyworks) can work well at the ambient power levels (typically from -50 to -10 dBm). Most conventional diodes have nearly 0% efficiency when the input power is smaller than 1 mW. This is due to the high forward bias voltage and considerable series resistance created by these diodes with conventional semiconductor configuration. For low power WEH applications, diodes with low $\omega R_s C_j$ (where R_s is the series resistance and C_j is the junction capacitance of the diode) works well with high conversion efficiency. However, diodes with high breakdown voltage and high current carrying capabilities are suitable for WPT applications.

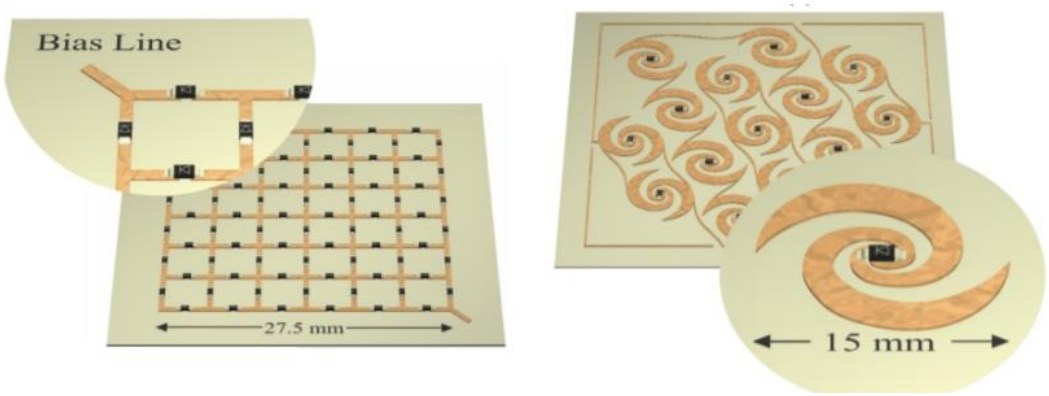

Fig. 2.15. Broadband rectenna arrays from the University of Colorado at Boulder [49].

In 2001, researchers from the University of Colorado at Boulder (Boulder, CO, USA) designed two broadband rectenna arrays, as shown in Fig. 2.15, for ambient RF power harvesting [49]. It was the first work to use rectenna for harvesting RF energy in areas where RF radiated power densities are comparably high. The first is a grid rectenna array operating from 4.5 to 8 GHz, and the second is a spiral rectenna operating from 8.5 to 15 GHz. The grid array had a maximum efficiency of 35% at 5.7 GHz for an incident CP power density of 7.78 mW/cm^2. The spiral array used alternating RHCP and LHCP spirals to achieve a maximum efficiency of 45% at 10.7 GHz for 1.56 mW/cm^2. Even though the rectenna has broad bandwidth and can capture arbitrarily polarized incident waves, it cannot be used to harvest abundant ambient energy such as DTV, Wi-Fi and mobile phones as the operating bandwidth was above 4.5 GHz.

A dual-polarized rectenna operating at 2.4 GHz for energy harvesting was reported in [50]. The rectenna achieved a maximum conversion efficiency of 38.2% at an ambient power density of 1.5 μW/cm^2. However, it was revealed that the harvested

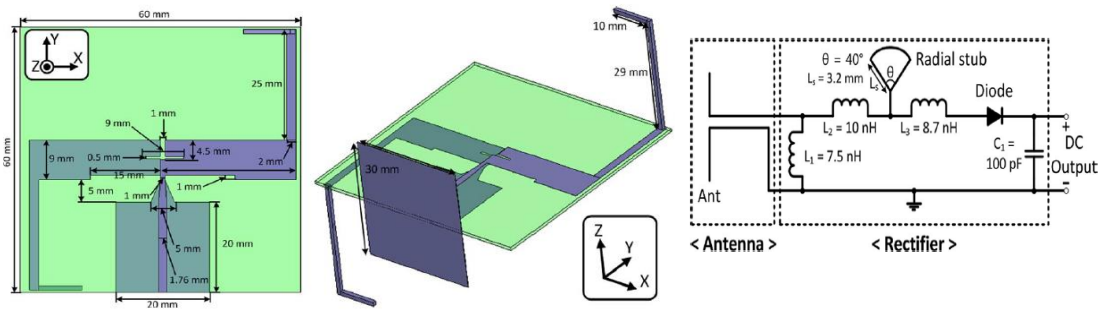

Fig. 2.16. (a) Folded dipole dual-band rectenna (b) Schematic of the dual-band rectifier [55]

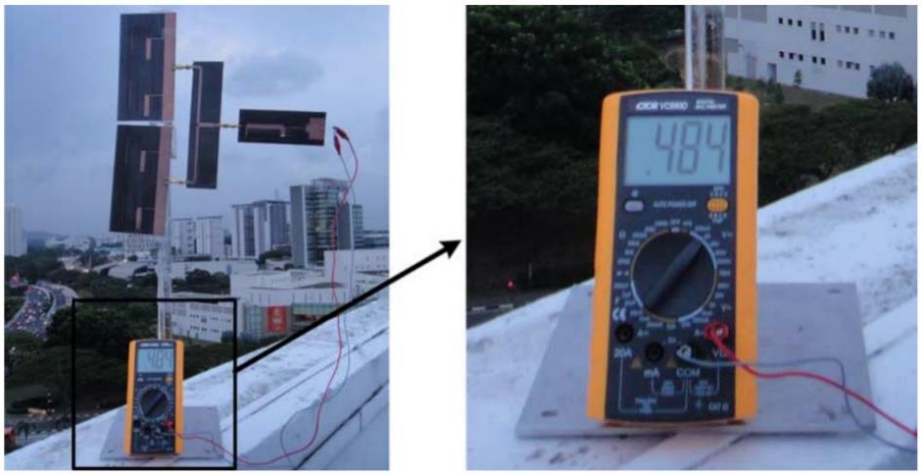

Fig. 2.17. Dual-band rectenna based on broadband Yagi antenna array [57]

power from a single band using such a rectenna was very low (less than 1 μW) and therefore not acceptable for most applications [51]-[53]. For increasing the harvested power from the rectenna, some dual-band rectennas were presented in [54]-[56]. In [55], a dual-band folded dipole rectenna operating at 0.915 and 2.45 GHz was reported with a conversion efficiency of 37% and 30% respectively as shown in Fig. 2.16. This design was optimised for a load resistor value of 2.2 kΩ and an input power of -9 dBm. Similarly, a dual-band rectenna based on broadband Yagi antenna array was reported in [57]. This rectenna covered 1.85 and 2.15 GHz bands for energy harvesting from the ambient GSM1800 and UMTS2100 signals. The structure of this design is given in Fig. 2.17. This rectenna reported a conversion efficiency of 40% and an output voltage of 400-mV across a 5 kΩ load resistor. It was revealed that the output power from a dual-band rectenna was much higher than that from a single band one. Therefore, the conversion efficiency and output power can be significantly improved by extending the rectenna's operating frequency band. However, because of the rectifying circuits' strong nonlinearity, the rectifier's impedance typically varies with the frequency over a range of values. The design of multiband or broadband rectennas covering more than three bands is exceptionally difficult.

A broadband design intended to cover a frequency band from 0.9 to 2.5 GHz was reported in [58]. But the conversion efficiency over the broad frequency band was lower than 8% which confirmed the challenges of broadband rectenna designs. In [59], a multiband stacked RF harvester was introduced to improve the overall efficiency of multiband rectennas. As shown in Fig. 2.18 (a), the overall conversion efficiency was

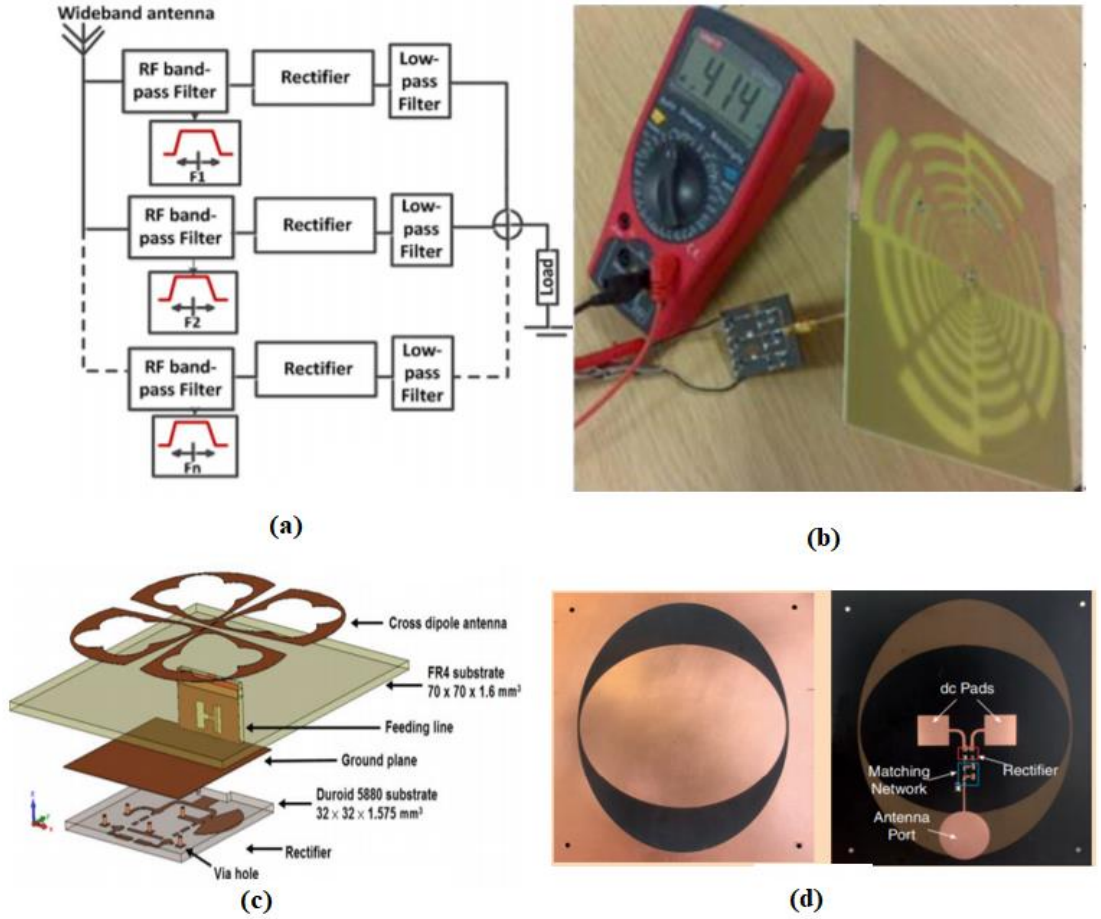

Fig. 2.18. Broadband and multiband rectennas (a) stacked RF rectifier [59], (b) six band rectenna [60], (c) broadband cross-dipole rectenna [61] and (d) broadband slot rectenna [62].

improved by using a stacked rectifier array structure where each circuit branch was optimized for a particular frequency band. The maximum efficiency of this design was up to 50% when the input power level was -15 dBm. A six-band dual circular polarization (CP) rectenna for ambient radio frequency (RF) energy harvesting was introduced in [60]. An annular ring structure antenna was employed in the design to harvest energy of 6 frequency bands from 0.55 to 2.5 GHz as shown in Fig. 2.18(b). A novel broadband rectenna for ambient wireless energy harvesting over the frequency band from 1.8 to 2.5 GHz was presented in [61]. This rectenna utilised a dual-polarized cross-dipole antenna with harmonic rejection property for reception. Rectenna reported a conversion efficiency of 55% with an input power of −10 dBm to the rectifier. However, the rectenna structure was complex and difficult to fabricate. A WEH for commercial telephony frequencies in the UHF band was introduced in [62]

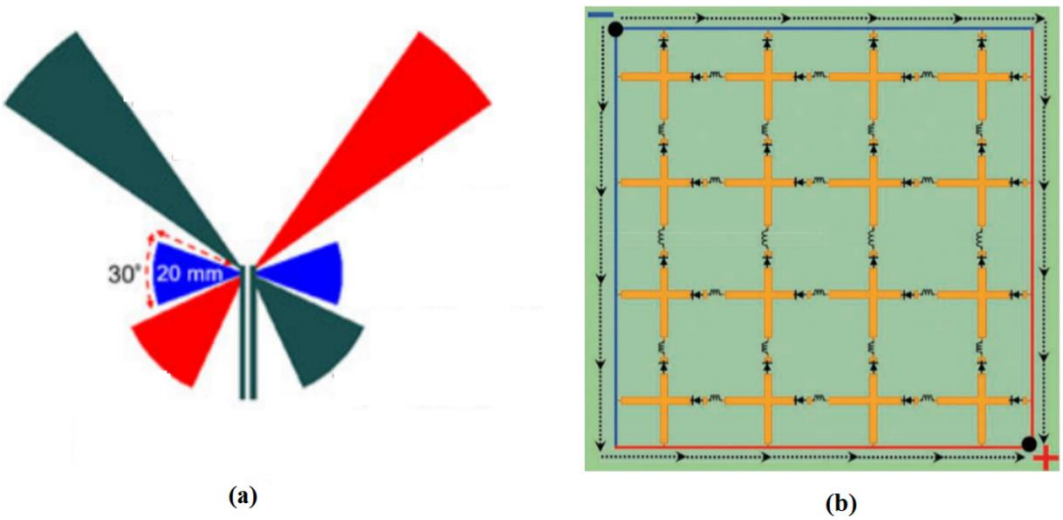

Fig. 2.19. Conjugate matched rectennas (a) off-center-fed dipole antenna [64], (b) a 4 × 4 WEH cross-dipole surface [65].

as shown in Fig. 2.18(d). Rectenna system achieved a high conversion efficiency of about 50% at 2 $\mu W/cm^2$.

As the input impedance of the rectifying diode is highly capacitive and, therefore, needs an inductive antenna to directly conjugate the impedance. High-impedance inductive antennas have been extensively used in RFID tags due to the chips' capacitive impedance [63]. Thus, a similar approach can be utilized to design an AWEH antenna to directly conjugate the rectifier's impedance. In [64], an off-center-fed dipole antenna as shown in Fig. 2.19, with relatively high input impedance was complex conjugate matched to the rectifier. An energy harvesting surface designed for electromagnetic energy harvesting and wireless power transfer consisting of an array of cross-dipole metallic elements was presented in [65]. Fig. 2.19 (b) shows the image of the WEH cross dipole surface.

2.3. Summary

In this chapter, the history of power transmission by radio waves and significant achievements in RF wireless power technologies has been reviewed. Due to the technological advancements in the recent times, the world's energy demands has been continuously increasing, and the various supplies of energy remain constrained. It has been clearly shown that the investigation of rectennas is of immense importance to the modern industry and it will still be a hot research topic for the coming decades.

The studies of rectennas for WPT and WEH applications have been highlighted and discussed in detail in Section 2.2. It was observed that a clear distinction between WPT and WEH rectennas was not considered in the majority of existing research in the literature. Difficulty in designing broadband rectennas was also clearly observed in the literature. However, most of the existing WEH rectennas did not have a good capability of dealing with the nonlinear effect of the system, which limits the application of such rectennas used in practice. In WPT applications, the advantages of having a dedicated RF source were not completely utilised. The information presented in this chapter is useful to gain a better understanding on the state of art in rectenna designs and meanwhile identify the research challenges and problems for us to overcome in this work.

References

[1] Bern Dibner, "*Oersted and the discovery of electromagnetism*," New York, Blaisdell, 1962.

[2] J. C. Maxwell, "*A Treatise on Electricity and Magnetism*," Clarendon press, 1873.

[3] Baird, Davis, Hughes, R.I.G. and Nordmann, Alfred eds. *Heinrich Hertz: Classical Physicist, Modern Philosopher*. New York, 1998.

[4] A. S. Marincic, "Nikola tesla and the wireless transmission of energy," *IEEE Trans. Power App. Syst*., vol. PAS-101, no. 10, pp. 4064–4068, Oct. 1982.

[5] C. K. Lee, W. X. Zhong, and S. Y. Hui, "Recent progress in Mid-Range wireless power transfer," *Proc. IEEE Energy Convers. Cong. Expo*., 2012, pp. 3819–3824.

[6] N. Tesla, "Apparatus for transmitting electrical energy," U.S. Patent 1 119 732, Dec. 1914.

[7] M. Cheney, R. Uth, J. Glenn, *Tesla, Master of Lightning*, Barnes & Noble Publishing, 1999.

[8] S. C. Nambiar and M. Manteghi. "A simple wireless power transfer scheme for implanted devices", *Proc. 2014 United States Nat. Committee of URSI Nat. Radio Science Meeting* (USNC-URSI NRSM). 2014, pp. 1–1.

[9] Tesla coil, from Wikipedia *https://en.wikipedia.org/wiki/Tesla_coil#cite_note-36*.

[10] M. Cheney, Tesla: "*Man, Out of Time*," Englewood Cliffs, NJ, USA: Prentice-Hall, 1981.

[11] H. Boot and J. Randafl, "Historical notes on the cavity magnetron," *IEEE Trans. Electron. Devices*, vol. ED-23, no. 7, July 1976.

[12] W. C. Brown, "The history of power transmission by radio waves," *IEEE Trans. Microw. Theory Techn.,* vol. 32, no. 9, pp. 1230–1242, Sep. 1984.

[13] B. Strassner and K. Chang, "Microwave power transmission: Historical milestones and system components," *Proc. IEEE*, vol. 101, no. 6, pp. 1379–1396, Jun. 2013.

[14] P. Glaser, "Power from the Sun: Its future," *Science*, vol. 162, pp. 857–861, 1968.

[15] J. Schlesak, A. Alden, and T. Ohno, ''SHARP rectenna and low altitude flight trials,'' *Proc. IEEE Global Telecommun. Conf.,* New Orleans, LA, USA, Dec. 2–5, 1985.

[16] Y. Fujino, T. Ito, N. Kaya, H. Matsumoto, K. Kawabata, H. Sawada, and T. Onodera, ''A rectenna for MILAX,'' *Proc. Wireless Power Transm. Conf*., Feb. 1993, pp. 273–277.

[17] J. M. Mcspadden and J. C. Mankins, ''Summary of recent results from NASA's Space Solar Power (SSP) programs and the current capabilities of microwave WPT technology,'' *IEEE Microw. Mag*., vol. 3, no. 4, pp. 46–57, Dec. 2002.

[18] A. Kurs et.al., "Wireless power transfer via strongly coupled magnetic resonances," *Science,* vol. 317, pp. 83–86, 2007.

[19] "Welcome to the wireless power consortium, home of wireless charging," [Online]. Available: *http://www.wirelesspower consortium.com/*

[20] "This Mophie wireless charger is probably the closest thing to Airpower that Apple will ever sell," [Online]. Available: *https://www.theverge.com /2019/8/9/20798422/apple-mophie-dual-3-in-1-wireless-charging-padairpower.*

[21] T. Yoo and K. Chang, "A 35 GHz integrated circuit rectifying antenna with 33 percent efficiency," *Electron. Lett*., vol. 27, no. 23, p. 2117, Nov. 1991.

[22] T. Yoo and K. Chang, "Theoretical and experimental development of 10 and 35 GHz rectennas," *IEEE Trans. Microwave Theory Tech*., vol. 40, pp. 1259–1266, June 1992.

[23] J. O. McSpadden, T. Yoo, and K. Chang, "Theoretical and experimental

investigation of a rectenna element for microwave power transmission," *IEEE Trans. Microwave Theory Tech.,* vol. 40, pp. 2359–2366, Dec. 1992.

[24] T. East, "A self-steering array for the SHARP microwave-powered aircraft," *IEEE Trans. Antennas Propag*., vol. 40, no. 12, pp. 1565–1567, Dec. 1992.

[25] P. Koert and J. T. Cha, "Millimeter wave technology for space power beaming," *IEEE Trans. Microw. Theory Tech*., vol. 40, no. 6, pp. 1251–1258, Jun. 1992.

[26] J. O. McSpadden, F. Lu, and K. Chang, "Design and experiments of a high-conversion efficiency 5.8-GHz rectenna," *IEEE Trans. Microw. Theory Techn*., vol. 46, no. 12, pp. 2053–2060, Dec. 1998.

[27] A. Alden and T. Ohno, "Single fore plane high power rectenna," *Electron. Lett*., vol. 28, no. 11, pp. 1072–1073, May 1992.

[28] Y.-H. Suh, C. Wang, and K. Chang, "Circularly polarized truncated corner square patch microstrip rectenna for wireless power transmission," *Electron. Lett*., vol. 36, pp. 600–602, Mar. 2000.

[29] Y.-H. Suh and K. Chang, "A high-efficiency dual-frequency rectenna for 2.45- and 5.8- GHz wireless power transmission," *IEEE Trans. Microw. Theory Techn*., vol. 50, no. 7, pp. 1784–1789, Jul. 2002.

[30] N. Shinohara and H. Matsumoto, "Experimental study of large rectenna array for microwave energy transmission," *IEEE Trans. Microw. Theory Techn*., vol. 46, No. 3, pp.261- 268, Mar. 1998.

[31] B. Strassner and K. Chang, "Highly efficient C-band circularly polarized rectifying antenna array for wireless microwave power transmission," *IEEE Trans. Antennas Propag.,* vol. 51, No. 6, pp.1347-1356, Jun. 2003.

[32] Y.-J. Ren and K. Chang, "5.8-GHz circularly polarized dual-diode rectenna and rectenna array for microwave power transmission," *IEEE Trans. Microw. Theory Techn*., vol. 54, no. 4, pp. 1495–1502, Jun. 2006.

[33] J. A. Hagerty, F. B. Helmbrecht, W. H. McCalpin, R. Zane, and Z. B. Popovic, "Recycling ambient microwave energy with broad-band rectenna arrays," *IEEE Trans. Microw. Theory Techn*., vol. 52, no. 3, pp. 1014–1024, Mar. 2004.

[34] Y. Ren and K. Chang, "New 5.8-GHz circularly polarized retrodirective rectenna arrays for wireless power transmission," *IEEE Trans. Microw. Theory Techn* vol. 54, no. 7, pp. 2970-2976, July 2006.

[35] M. Ali, G. Yang, and R. Dougal, "A new circularly polarized rectenna for

wireless power transmission and data communication," *IEEE Antennas Wireless Propag. Lett*., vol. 4, pp. 205– 208, 2005.

[36] C. Chin, Q. Xue, and C. Chan, "Design of a 5.8-GHz rectenna incorporating a new patch antenna," *IEEE Antennas Wireless Propag. Lett.,* vol. 4, pp. 175–178, 2005.

[37] Z. Harouni, L. Osman, and A. Gharsallah, "Efficient 2.45 GHz CPW patch antenna including harmonic rejecting device for wireless power transmission," in *Proc. Int. Multi-Conf. Syst. Signals and Devices*, 2011, pp. 1–3.

[38] M. Ali, G. Yang, and R. Dougal, "Miniature circularly polarized rectenna with reduced out of band harmonics," *IEEE Antennas and Wireless Propagat. Lett.,* vol. 5, no. 1, pp. 107–110, 2006.

[39] Y.-J. Ren and K. Chang, "5.8-GHz circularly polarized dual-diode rectenna and rectenna array for microwave power transmission," *IEEE Trans. Microw. Theory Techn.,* vol. 54, no. 4, pp. 1495–1502, Jun. 2006.

[40] T.-c. Yo, C.-m. Lee, C.-m. Hsu, and C.-h. Luo, "Compact circularly polarized rectenna with unbalanced circular slots," *IEEE Trans. Antennas Propag*., vol. 56, no. 3, pp. 882–886, Mar. 2008.

[41] Z. K. Ma, and G. A. E. Vandenbosch, "Wideband harmonic rejection filtenna for wireless power transfer," *IEEE Trans. Antennas Propag*., vol. 62, no. 1, pp. 371–377, Oct. 2013.

[42] H. Chiou and I. Chen, "High-Efficiency Dual-Band On-Chip Rectenna for 35- and 94-GHz Wireless Power Transmission in 0.13-um CMOS Technology," *IEEE Trans. Microw. Theory Techn.*, vol. 58, no. 12, pp. 3598-3606, Dec. 2010.

[43] S. Ladan, A. B. Guntupalli and K. Wu, "A High-Efficiency 24 GHz Rectenna Development Towards Millimeter-Wave Energy Harvesting and Wireless Power Transmission," *IEEE Trans. Circuits Syst. I Regul. Pap*., vol. 61, no. 12, pp. 3358-3366, Dec. 2014.

[44] D. Mavrakis, ''Small Cell Market Status December 2012,'' London, U.K., 2012.

[45] D. Watkins, Embedded WLAN (Wi-Fi) CE Devices: Global Market Forecast. Boston, MA, USA: Strategy Analytics, 2014.

[46] B. Sanou, ''ICT Facts and Figures,'' International Telecommunication Union, Geneva Switzerland, 2013

[47] M. Pinuela, P. D. Mitcheson, and S. Lucyszyn, "Ambient RF energy harvesting

in urban and semi-urban environments," *IEEE Trans. Microw. Theory Techn*., vol. 61, no. 7, pp. 2715–2726, Jul. 2013.

[48] S. Hemour, Y. P. Zhao, C. H. P. Lorenz, D. Houssameddine, Y. S. Gui, C.m. Hu, and K. Wu, "Towards low-power high-efficiency RF and microwave energy harvesting," *IEEE Trans. Microw. Theory Tech*., vol. 62, no. 4, pp. 965–976, Feb. 2014.

[49] J. Hagerty and Z. Popovic´, ''An experimental and theoretical characterization of a broadband arbitrarily-polarized rectenna array,'' *IEEE MTT-S Int. Microwave Symp. Dig*., Phoenix, AZ, USA, May 2001, pp. 1855–1858.

[50] A. Georgiadis, G. Andia-Vera, and A. Collado, "Rectenna design and optimization using reciprocity theory and harmonic balance analysis for electromagnetic (EM) energy harvesting," *IEEE Antennas Wireless Propag. Lett*., vol. 9, pp. 444–446, May 2010.

[51] N. Zhu, R. W. Ziolkowski, and H. Xin, "Electrically small GPS L1 rectennas," *IEEE Antennas Wireless Propag. Lett*., vol. 10, pp. 935–938, 2011.

[52] U. Olgun, et al., "Investigation of rectenna array configurations for enhanced RF power harvesting," *IEEE Antenna Wireless Propag. Lett*., vol. 10, pp. 262–265, 2011.

[53] H. Takhedmit, et al., "Compact and efficient 2.45 GHz circularly polarised shorted ring slot rectenna," *Electron. Lett*., vol. 48, no. 5, pp. 253–254, 2012.

[54] K. Niotaki, et al., "A compact dual-band rectenna using slot-loaded dual-band folded dipole antenna," *IEEE Antennas Wireless Propag. Lett*., vol. 12, pp. 1634–1637, Dec. 2013.

[55] E. Falkenstein, ''Characterization and design of a low-power wireless power delivery system,'' Ph.D. dissertation, Dept. Electr., Comput. Energy Eng., Univ. Colorado Boulder, Boulder, CO, USA, Jan. 2012.

[56] E. Falkenstein, M. Roberg, and Z. Popovic, ''Low-power wireless power delivery,'' *IEEE Trans. Microw. Theory Tech*., vol. 60, no. 7, pp. 2277–2286, Jul. 2012.

[57] H. Sun, Y.-x. Guo, M. He and Z. Zhong, "A dual-band rectenna using broadband Yagi antenna array for ambient RF power harvesting," *IEEE Antennas and Wireless Propag. Lett*., vol. 12, pp. 918–921, 2013.

[58] A. Collado and A. Georgiadis, ''Conformal hybrid solar and electromagnetic

(EM) energy harvesting rectenna," *IEEE Trans. Circuits Syst. I, Reg. Papers*, vol. 60, no. 8, pp. 2225–2234, Aug. 2013.

[59] V. Kuhn, C. Lahuec, F. Seguin, and C. Person, "A multi-band stacked RF energy harvester with RF-to-DC efficiency up to 84%," *IEEE Trans. Microw. Theory Techn*., vol. 63, no. 5, pp. 1768–1778, May 2015.

[60] C. Song, Y. Huang, J. Zhou, J. Zhang, S. Yuan and P. Carter, "A High-Efficiency Broadband Rectenna for Ambient Wireless Energy Harvesting," *IEEE Trans. Antennas Propag*., vol. 63, no. 8, pp. 3486-3495, Aug. 2015.

[61] C. Song, *et al*., "A Novel Six-Band Dual CP Rectenna Using Improved Impedance Matching Technique for Ambient RF Energy Harvesting," *IEEE Trans. Antennas Propag*., vol. 64, no. 7, pp. 3160-3171, July 2016

[62] V. Palazzi, M. D. Prete, and M. Fantuzzi, "Scavenging for energy: A rectenna design for wireless energy harvesting in UHF mobile telephony bands*," IEEE Microw. Mag*., vol. 18, no. 1, pp. 91–99, Feb. 2017

[63] G. Marrocco, "The art of UHF RFID antenna design: Impedance-matching and size reduction techniques," *IEEE Antennas Propag. Mag*., vol. 50, no. 1, pp. 66–79, 2008.

[64] C. Song, *et al.*, "Matching network elimination in broadband rectennas for high-efficiency wireless power transfer and energy harvesting," *IEEE Trans. Ind. Electron*., vol. 64, no. 5, pp. 3950–3961, May 2017.

[65] A. Z. Ashoor and O. M. Ramahi, "Polarization-independent cross-dipole energy harvesting surface," *IEEE Trans. Microw. Theory Techn*., vol. 67, no. 3, pp. 1130–1137, 2019.

Chapter 3. Broadband Rectenna for Wireless Energy Harvesting Applications

The previous chapter concluded the lack of highly efficient and simple broadband rectenna designs for harvesting energy from wide RF spectra (UK GSM-1800/4G, 3G/UMTS-2100, and WLAN-2.4 GHz). In this chapter, a novel broadband Yagi-Uda antenna and a transmission lines-based broadband rectifier are proposed and discussed. Initially, a novel miniaturized constant high gain broadband Yagi-Uda antenna is designed for wireless energy harvesting applications. The proposed antenna consists of two meandered dipoles connected using feed lines serves as the radiating element for realizing the broadband. A highly compact antenna is realized using curved reflectors and meandered dipoles and director. To maintain constant enhanced gain throughout the band, the reflector is designed to provide better performance at lower frequencies and to improve the front to back ratio. The meandered director is optimized for gain enhancement at higher frequencies. The operational principles of the antenna are studied, and the final design is optimised, fabricated, and tested. Then, a high-efficiency compact broadband rectifier is developed for WEH. A novel three-stage impedance matching technique is utilized in a broadband rectifier design to achieve high conversion efficiency with a compact size. In the rectifier, a low loss impedance matching technique is initiated by employing a linearly tapered transmission line for controlling the impedance curve at the required input power level, followed by two stages to make a circular impedance curve for wideband impedance matching. Finally, rectenna evaluation is performed after combining broadband antenna and rectifier. The proposed broadband rectenna proves to be an excellent candidate for WEH applications. One journal paper '*Transmission lines-based impedance matching technique for broadband rectifier'* has been published in *IEEE ACCESS* and two conference papers were presented in *EuCAP 2018* and *AWPT 2019* based on this work.

3.1. Introduction

Several literatures demonstrated the possibility of utilizing the power from various radio frequency (RF) transmitters including, FM, TV, cellular, and Wi-Fi systems to operate low-power electronics [1]-[3]. However, the complex propagation settings, broadcasting schedules and changing demands of these transmissions result in variable nature of the time-/space-varying ambient RF power. Thus, it is necessary to harvest RF energy from a large frequency spectrum to ensure the required power for various real-life applications [4], [5]. Broadband or multiband rectennas are therefore needed as shown in Fig. 3.1.

The rest of the chapter is organized as follows: Section 3.2 introduces a novel miniaturised broadband antenna design. A broadband rectifier with transmission lines-based matching technique is discussed in Section 3.3. The experimental results of the rectenna are presented in Section 3.4. Finally, a summary is drawn in Section 3.5.

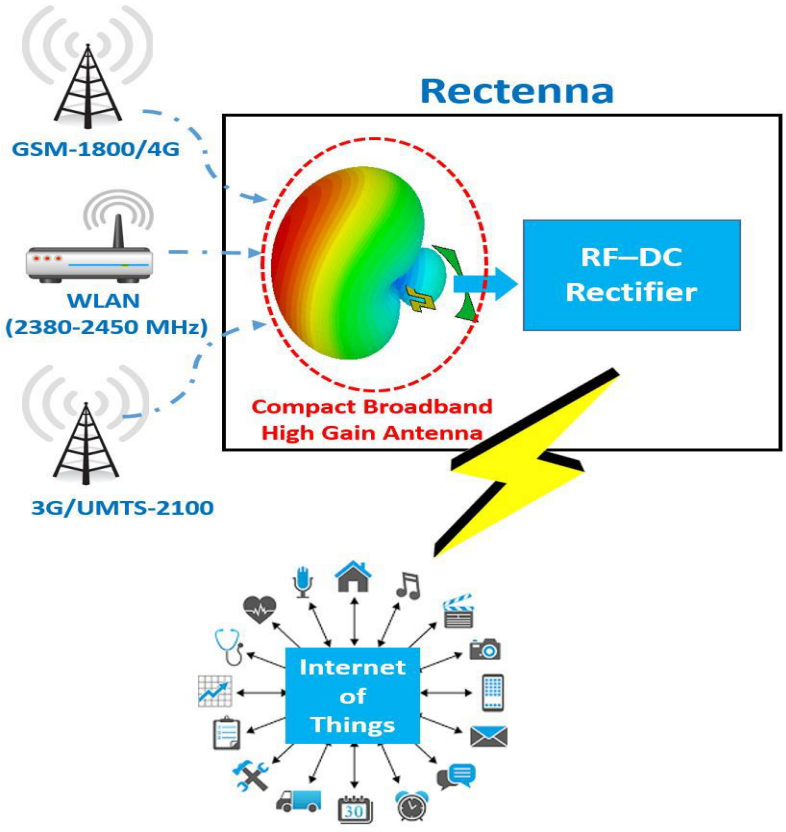

Fig. 3.1. Rectenna to harvest energy for IoT devices

3.2. Miniaturized Broadband Yagi Uda Antenna

3.2.1. Introduction

Yagi-Uda antenna is a prominent candidate for wireless energy harvesting (WEH) and wireless power transfer (WPT) rectennas. With the increasing demand of various portable devices, the planar printed antennas have drawn lots of attention from the academia and industry for its ease of fabrication, small size, and ease of integration with microwave circuit components compared to waveguide based antenna technology [5]. Although for WEH, we normally do not want high gain antennas, in some cases (e.g., the direction for incoming waves is known), we do prefer to use a directional antenna. A lot of progress has been made in the research of the Yagi-Uda antenna, in terms of its gain, front to back ratio, bandwidth and dimension. It is worth mentioning that there is always a trade-off between these factors as shown in Fig. 3.2. Quasi-Yagi antennas (QYAs) have been widely used as high performance broadband unidirectional antennas because of their simple structure and broad bandwidth [6]. But the moderate gain is an important limiting factor of quasi-Yagi antennas. In [7], a wideband quasi-Yagi antenna with a 70 % bandwidth using a microstrip-to-coplanar

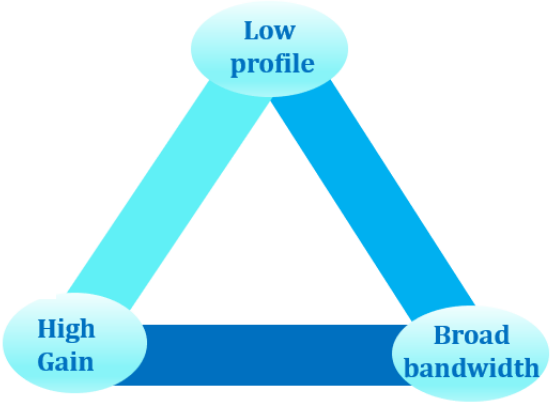

Fig. 3.2. Trade-off between antenna factors

stripline balun is presented. However, it can realize a peak gain of only 4 dBi. Yagi-Uda with meandered driver dipoles are employed in [8], to reduce the size of the antenna. Even though meandered elements shrink the overall size of the antenna, but it degrades the bandwidth and front-back ratio. A large concave parabolic reflector is used for improving the front to back ratio and to reduce the antenna size, but it reduces the bandwidth (only 5.8%) considerably with a larger antenna footprint [9]. A high

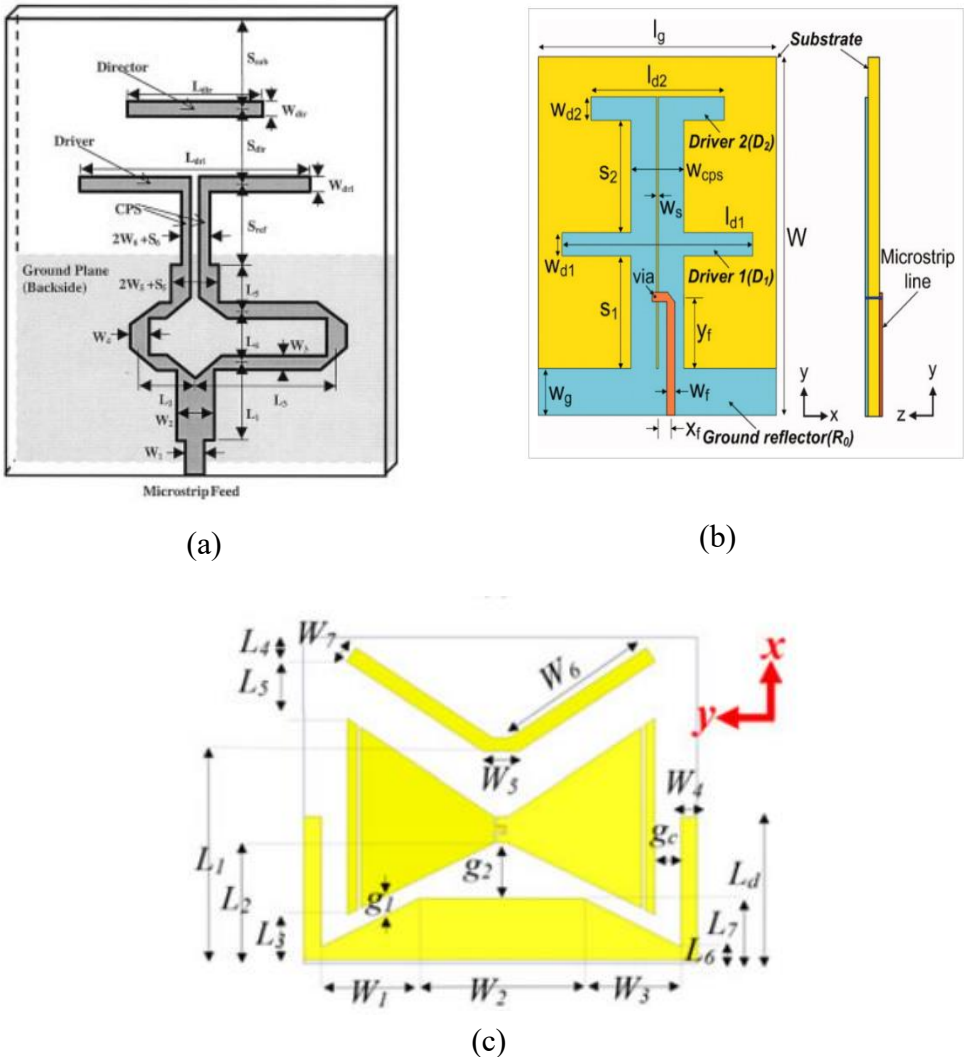

Fig. 3.3. Broadband Yagi-Uda antennas in literatures (a) Planar quasi-Yagi antenna [6] (b) series-fed two dipole array antenna [11] (c) Yagi antenna with capacitively coupled reflector [12]

directivity is realized in [10] by implementing a Yagi-Uda antenna with 11 patches. 10 dBi directivity is achieved with the aid of 8 director patches. However, the antenna has a large overall dimension of 150 mm × 90 mm at 5 GHz.

3.2.2. Design and Principle

The proposed antenna consists of a curved reflector, two meandered dipole elements and a single stage meandered director as shown in Fig. 3.4. A curved reflector is placed in the bottom layer instead of rectangular strip reflector in Yagi-Uda antenna, to enhance the gain and the front to back ratio. Two arms of meandered driven dipoles (D1 and D2) are solely responsible for the broadband performance of the antenna. The

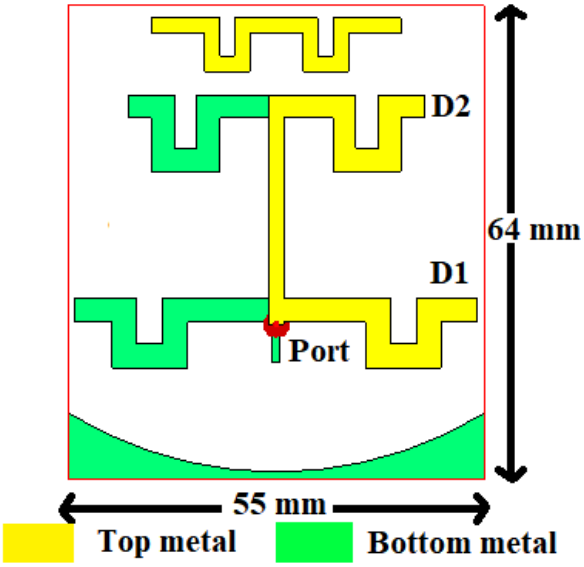

Fig. 3.4. Proposed broadband Yagi-Uda antenna

meandered shape helps to make the antenna compact. Both the meandered dipoles have one arm on the top and the other arm on the bottom metal layer of the substrate. Dipole D1 with 85 mm length ($\lambda_{low}/2$) is responsible for the lower frequencies (f_{low} = 1.8 GHz). In order to cover the higher frequencies (f_{high} = 2.4 GHz), dipole D2 with a length of 62 mm ($\lambda_{high}/2$) is also used. Two feeding strip lines are used in the top and bottom layer to connect the dipoles together. Bottom strip line length is extended to the reflector side to achieve proper impedance matching. The width of the feeding strip lines is adjusted to obtain the required bandwidth. The proposed design is 55 mm × 64 mm. FR-4 material of 1.6 mm thickness with a relative dielectric constant 4.4 and tangential loss of 0.02 substrate for printed circuit board. The inner conductor of the coaxial probe feed extends from the bottom layer of dipole D1 through the PCB top layer, which connects to the other arm of dipole D1. Meandered director is placed in the top layer to enhance the radiation pattern. Director can also be placed in the bottom layer. Initially, a microstrip line feeding through the edge of the substrate was intended. Therefore, a reflector is placed in the bottom layer in order to ease the microstrip line feeding through top layer. Later, the feeding method changed to coaxial, but the reflector position is not altered. A broadband Yagi-Uda antenna with constant enhanced gain is difficult to achieve. For the proper operation of a Yagi-Uda antenna, the spacing between the reflector and the driver, and between the driver and the director, should be in the range of 0.15−0.4 λ_0 for the antenna to be better matched to

50 Ω and have high-efficiency values. Similarly, the reflector length should be more than λ/2 (5% longer than the driven element). However, it is difficult to design a broadband antenna with a reflector which is suitable for the whole 1.65 to 2.5 GHz band. Thus, the curved reflector length and spacing between D1 and reflector are optimized for low-frequency gain enhancement i.e., in accordance with dipole D1. The spacing between the reflector and D1 is reduced to $0.12\lambda_{low}$, for shrinking the size of the antenna. It is quite remarkable that the actual length of dipole D1 is higher than that of reflector's length. Combination of the curved reflector and meandered dipole can reduce the overall size considerably. Fig. 3.5 shows the current distribution in antenna structure at 1.8 GHz and 2.4 GHz. It can be observed that there is no current flow in dipole D2 and director at 1.8 GHz. In addition to that, the presence of current distribution can be analysed in the curved reflector. So, the presence of curved reflector

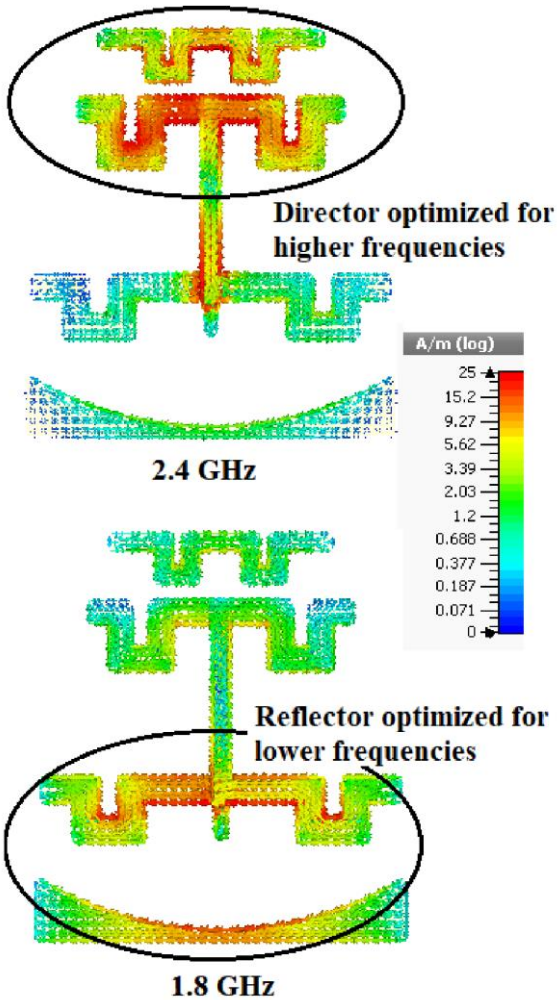

Fig. 3.5. Current distribution of antenna at 2.4 GHz (f_{high}) and 1.8 GHz (f_{low}).

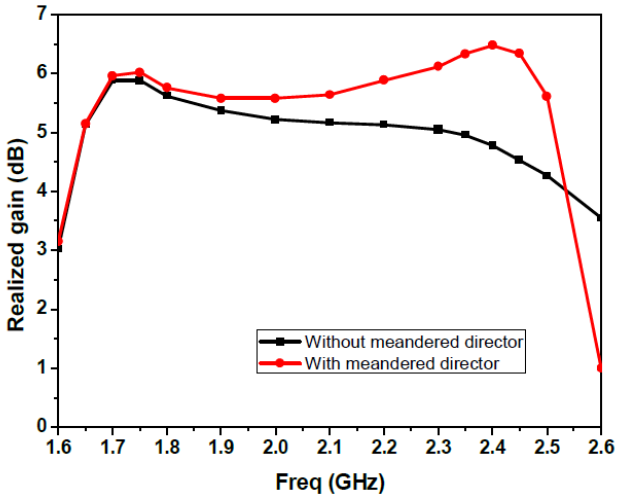

Fig. 3.6. Realized gain of the antenna with and without director.

and spacing between dipole D1 and reflector aids to enhance the performance at lower frequencies. A single stage meandered director is used in this design to improve the directive capability of the radiation pattern. Moreover, to achieve a high constant gain throughout the bandwidth, it is necessary to enhance the performance at higher frequencies. Therefore, the length of the meandered director is $0.4\lambda_{high}$, designed in accordance with dipole D2. The spacing between the D2 and director is reduced to $0.1\lambda_{high}$, for reducing the antenna size. The capacitive effect of the meandered director and the inductive effect of reflector is properly optimized for impedance matching and making the antenna compact. Fig. 3.6. illustrates the enhanced gain performance of the broadband antenna with and without the director. At higher frequencies, the realized gain is dropped considerably in antenna without the director. But the presence of meandered director increases the gain in higher frequencies successfully. Realized gain at 2.4 GHz is improved from 4.78 dB to 6.48 dB by the addition of director, which is designed by considering D2 as the radiating element.

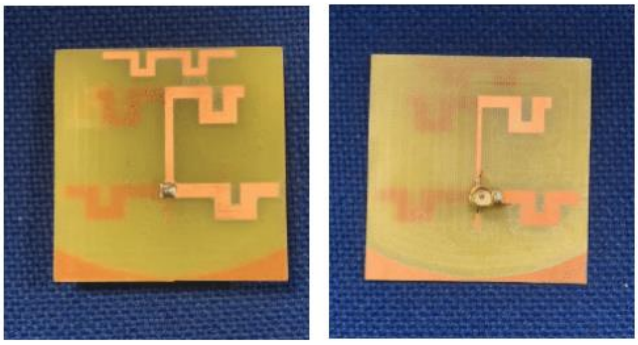

Fig. 3.7. Fabricated prototype of broadband antenna.

3.2.3. Antenna Performance

The broadband antenna was fabricated and tested for its performance. Fig. 3.7 shows the fabricated prototype of the broadband antenna. The simulated and measured reflection coefficient of the antenna is shown in Fig. 3.8. It can be observed that more than 10 dB return loss has been achieved over is 920 MHz from 1.65 GHz to 2.57 GHz (43.6%).

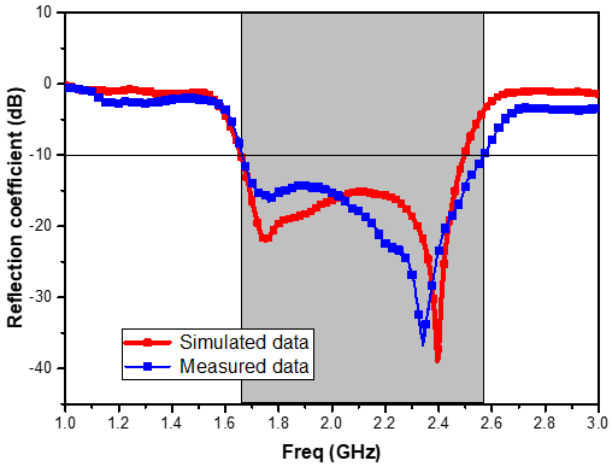

Fig. 3.8. Simulated and measured reflection coefficient of broadband antenna.

The two resonant frequencies f_{low} and f_{high} can be clearly observed in Fig. 3.8. The radiation patterns and realized gain of the broadband antenna are measured in an anechoic chamber as in Fig. 3.9. The radiation pattern of the broadband antenna at different frequencies is shown in Fig. 3.10. The simulated and measured radiation patterns are in close agreement. Fig. 3.11 illustrates the simulated and measured realized gain of the fabricated antenna. The broadband antenna has a worst-case realized gain of 5 dBi throughout the band.

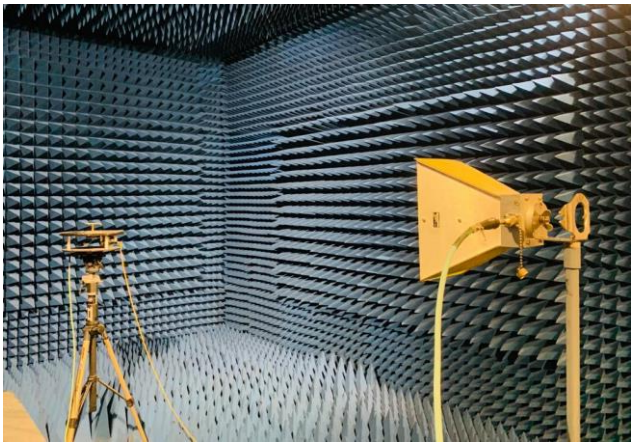

Fig. 3.9. Realized gain measurement setup in anechoic chamber.

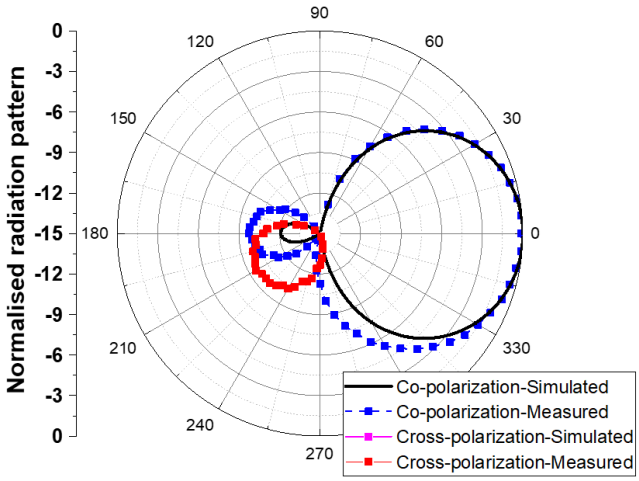

1.7 GHz

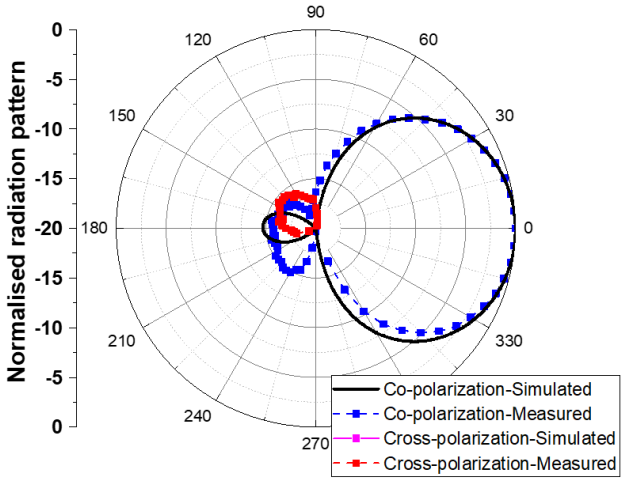

2.2 GHz

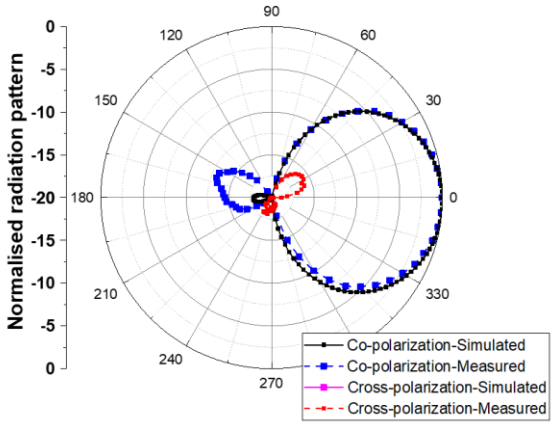

2.5 GHz

Fig. 3.10. Simulated and measured radiation pattern of broadband antenna

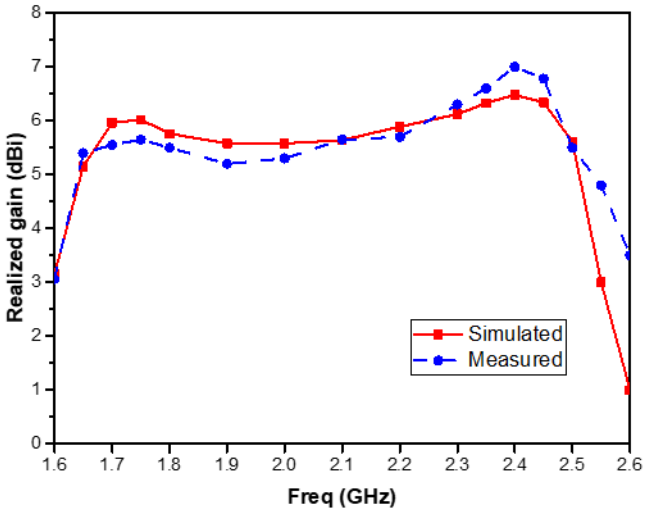

Fig. 3.11. Simulated and measured realized gain of broadband antenna

In order to evaluate the performance of the proposed antenna, it is compared with the other Yagi-Uda antennas. The important parameters are the bandwidth, directivity, and overall size of the antenna. Even though there exist several Yagi-Uda antenna designs, only the broadband Yagi-Uda designs operating in similar frequency bands and comparable sizes are chosen for a fair comparison (designs with broadband baluns are not considered). Compared to [12], proposed antenna has an area reduction of 37% and around 31% increase in bandwidth. The proposed antenna has comparable size with [13] but it has only 4.6% whereas the proposed antenna has a bandwidth of 43.6%. Similarly, it has an increase in 2 dBi gain and 70% size reduction, as compared to [14]. The proposed antenna has the smallest size, good bandwidth and high directivity compared to other designs, making it suitable for energy harvesting applications.

Table 3.1 Comparison of proposed antenna and other broadband Yagi-Uda designs

Ref-Year	**[11]-2012**	**[13]-2017**	**[14]-2019**	**[15]-2017**	**This work**
Frequency bandwidth (GHz)	1.7-2.8 (48%)	2.27-2.58 (12.7%)	2.4-2.515 (4.6%)	2.12-3.37 (45%)	**1.65-2.57 (43.6%)**
Substrate Dielectric constant	FR4 4.4	Rogers 2.55	Rogers 2.2	FR4 4.4	**FR4 4.4**
Director stages	-	1	1	1	**1**
Realized gain (dBi)	6	6	8.2	4.5	**5 - 7**
Antenna Size	$0.72\lambda_0 \times 0.82\ \lambda_0$	$0.53\lambda_0 \times 0.49\lambda_0$	$0.47\lambda_0 \times 0.36\lambda_0$	$1.1\lambda_0 \times 0.50\lambda_0$	**55×64×1.6 ($0.37\lambda_0$ x $0.44\lambda_0$)**

3.3. Transmission Lines-Based Impedance Matching Technique

Due to the non-linearity of diodes, also the varying input impedance with both the input power and the operating frequency making the broadband matching difficult, the RF to DC conversion efficiency reduces considerably in broadband rectennas compared to narrow band rectennas. There are only few broadband rectennas reported with good conversion efficiencies [16],[17]. To address this problem, several approaches (such as the resistance compression network, stacked RF harvester and the resistance-controlled DC–DC converter) have been reported for realizing high performance broadband or multiband rectennas [18]-[21]. Resistance compression networks (RCNs) are introduced to reduce the sensitivity and nonlinearity of rectennas. Moreover, the large variation of load impedance can be compressed using this technique which results in a smaller variation of the input impedance [18]. A broadband rectifier based on a branch-line coupler was presented in [19]. Even though the coupler added an insertion loss of 0.9 dB and took up a reasonably large circuit area, a fractional bandwidth of 21.5% was realized. A non-uniform transmission line-based octave band rectifier exhibited a broad bandwidth ranging from 470 to 860 MHz at 10 dBm input power with efficiency over 60% [20]. In [21], a compact broadband rectifier with efficiency over 30% from 870 MHz to 2.5 GHz was presented based on two cascaded L-section reactive elements. The rectifier achieved a wide bandwidth by introducing several lumped elements for impedance matching. Source-pull simulation was used in [22], to find the optimum load impedance for realizing a 58% fractional bandwidth (FBW) with more than 50% efficiency. Most of the previously proposed broadband rectifiers not only demand complex matching procedures but also reduce the efficiency because of the loss introduced by the circuit components. Thus, more efforts are required to develop a highly efficient, robust, flexible, and simple broadband rectifier for wireless energy harvesting applications.

In this design, a broadband rectifier is realized by employing a novel transmission lines-based impedance matching technique. In this proposed rectifier, a voltage doubler topology is combined with a tapered line; a short circuit stub and a pair of

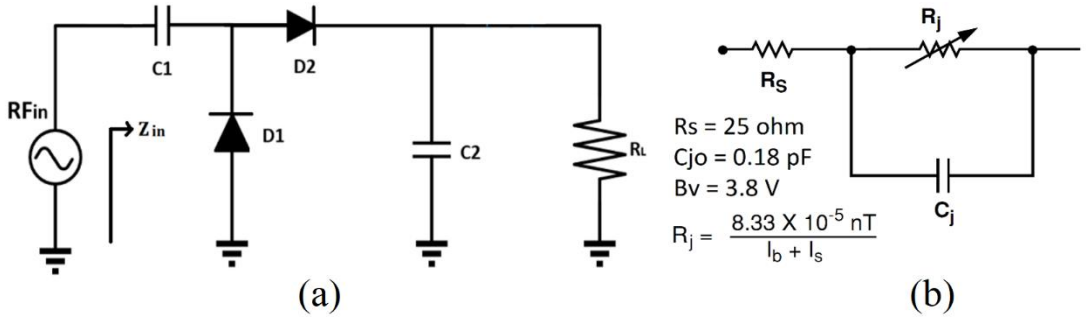

Fig. 3.12. (a) Schematic diagram of reference voltage doubler (b) Equivalent circuit of HSMS2850

open stubs are employed to widen the frequency bandwidth and maintain high efficiency. The detailed design procedure and theoretical analysis are presented in Section 3.3.1. Measured results of the fabricated rectifier and analysis of its performance are addressed in Section 3.3.2. Comparison of the proposed rectifier performance with other broadband designs is made in the end of this section.

3.3.1. Proposed Broadband Rectifier Design

Schottky diodes are key elements for the rectification of RF signals in WEH and WPT scenarios because of their fast-switching properties and low threshold voltage [23]. But the capacitive nature of Schottky diodes imposes difficulties in impedance matching. Adopting complex circuits with lumped elements to realize broadband matching results in the reduction of power conversion efficiency. Different topologies with the diodes are introduced for implementing broadband rectifiers. The single series topology has the advantage of low biasing requirement, but the low breakdown voltage limits the power handling capabilities, which will be harmful for the broadband performance [24]. Moreover, this topology can only provide a narrow bandwidth. To improve the power handling capabilities, multi-diode rectifiers such as charge pump rectifiers with two or more diodes can be used [25]. But it affects the performance at low input voltage due to the loss factor and also increases the complexity. In this design, a voltage doubler configuration with two diodes is selected which offers the benefit to maintain a minimum circuit complexity while achieves low-power performance.

Fig. 3.12 (a) shows the schematic diagram of a typical voltage doubler configuration. The rectifier consists of capacitors *C1* and *C2* which have the function of storing the energy rectified by the rectifying elements *D1* and *D2*. Schottky diodes HSMS 2850 from Avago have been selected in this voltage doubler rectifier design due to their low

threshold voltage and junction capacitance [26]. The equivalent circuit of an HSMS 2850 is shown in Fig. 3.12 (b). The rectifier is designed to operate from f_l = 1.0 to f_h = 2.6 GHz (to cover the UK GSM-1800/4G, 3G/UMTS-2100, and WLAN-2.4 GHz bands) with a load impedance of 1 kΩ. The vital factor for the design of a broadband rectifier is the impedance matching circuit. Due to the nonlinearity of the rectifier, the input impedance Z_{in} depends on the operating frequency range f_{req}, input power P_{in}, load resistor R_L and the nonlinear impedance of the diode Z_d.

$$Z_{in} = f(f_{req}, P_{in}, R_L, Z_d) \tag{3.1}$$

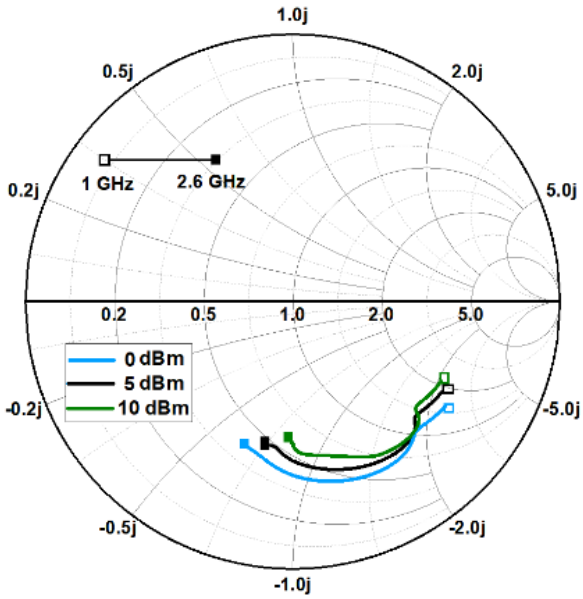

Fig. 3.13. Input impedance Z_{in} of reference voltage doubler at different input power levels.

Fig. 3.13 shows the input impedance Z_{in} of the reference doubler design over the frequency band f_l to f_h at three different power levels by using the Harmonic Balance (HB) simulation in Advanced Design System (ADS). It can be observed that the rectifier has a large capacitance over the entire operating band. The sharp change in diode impedance with frequency is mainly due to the rapidly varying capacitive reactance of the diode. The effect of series resistance on the capacitance is significant at higher frequencies when the capacitance decreases rapidly with frequency. Furthermore, the low input power levels appear to be more difficult to match than the high input power levels. For easy analysis, we define the mid frequency of the operating frequency band as $f_m = (f_l + f_h)/2$. At f_l, f_m and f_h, the diode input impedance of reference design at a 5

dBm input power level (P_{in}) can be observed as $Z_{in}(f_l)$ = 105.7 – 115.5j Ω, $Z_{in}(f_m)$ = 39.50 – 83.4j Ω and $Z_{in}(f_h)$ = 30.16 – 42.75j Ω.

To overcome the losses due to the lumped elements in complex broadband impedance matching circuits and to maintain a high efficiency performance, a novel transmission

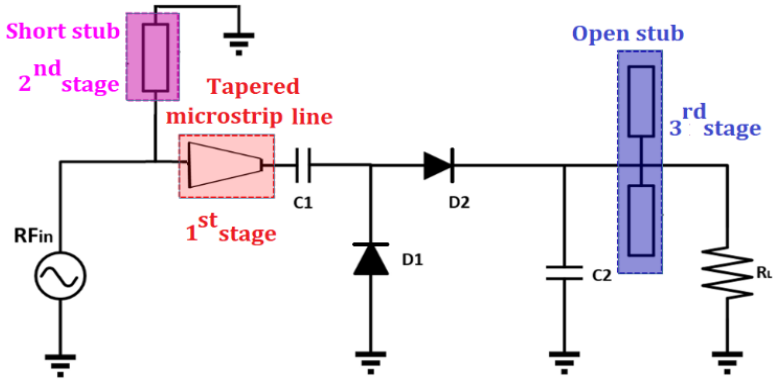

Fig. 3.14. Schematic of the proposed broadband rectifier.

lines-based impedance matching technique is introduced. Fig. 3.14 shows the schematic diagram of the proposed broadband rectifier comprising of the three-stage matching process. Impedance matching is achieved by employing the three-stage process which consists of a tapered microstrip line, a short circuit stub and a pair of open stubs in DC pass filter. The proposed rectifier is suitable for a wide range of operating frequencies and load impedances.

3.3.1.1. Design of the 1st Stage

A linearly tapered microstrip line is utilized in the 1st stage of broadband realization. A tapered microstrip line is intended to make input impedance symmetric with respect to the real axis (resistance axis) and to maintain the mid frequency $Z_{in1}(f_m) \approx 25$ Ω. Instead of having a stepped impedance transformer, the linearly tapered impedance transformer helps to improve the bandwidth. Fig. 3.15(a) shows a linearly tapered transmission line connecting to a source with an impedance of Z_0 at the input and connecting to Z_L at the output. Considering a multisection tapered transmission line is made up of many small sections of length Δl as in Fig. 3.15(b), the incremental reflection coefficient can be expressed as

$$\Delta\Gamma = \left|\frac{((Z+\Delta Z)-Z)}{((Z+\Delta Z)+Z)}\right| \approx \frac{\Delta Z}{2Z} \tag{3.2}$$

In order to reduce the reflections, it is required to consider a very small Δl. As $\Delta l \rightarrow 0$, the exact differential can be estimated as in [27]

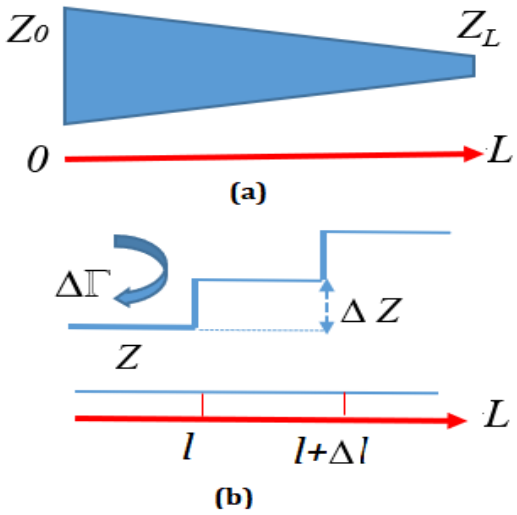

Fig. 3.15. (a) Linearly tapered transmission line (b) Model of an incremental impedance step.

$$d\Gamma = \frac{d(ln\,(Z/Z_0))dZ}{2dZ} \tag{3.3}$$

The total reflection coefficient at $l = 0$ by combining all the partial reflections with their appropriate phase shifts.

$$\Gamma(\theta) = \frac{1}{2}\int_0^L e^{-j2\beta l}\,\frac{d(ln\,(Z/Z_0))dl}{dl} \tag{3.4}$$

The length of the tapered line is determined by minimizing the reflection coefficient at the input, $\Gamma(\theta)$. Fig. 3.16 shows the input impedance Z_{in1} after the 1st stage over 1.0

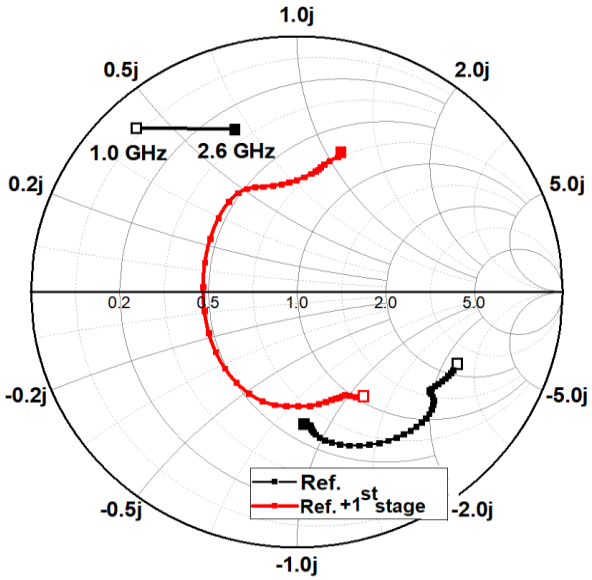

Fig. 3.16. Input impedance Z_{in1} after the 1st stage design at P_{in} = 5 dBm

to 2.6 GHz at P_{in} = 5 dBm. As observed, the imaginary part of input impedance is odd symmetrical with $Z_{in1}(f_m)$ around 25 Ω achieved by the 1st stage of impedance matching. At f_l, f_m, and f_h, the diode input impedance after the 1st stage at P_{in} = 5 dBm can be observed as $Z_{in1}(f_l)$ = 50 – 52.9j Ω, $Z_{in1}(f_m)$ = 24.5 Ω, and $Z_{in1}(f_h)$ = 35 + 52.8j Ω. It can be observed that the reactance part of $Z_{in1}(f_l)$, and $Z_{in1}(f_h)$ are approximately conjugate.

$$X_{in1}(f_l) \approx -X_{in1}(f_h) \tag{3.5}$$

3.3.1.2. Design of the 2nd Stage

A short circuit shunt stub with the characteristic impedance Z_s and electrical length θ_s is added in the 2nd stage to cancel out the imaginary part of $Z_{in1}(f_l)$ and $Z_{in1}(f_h)$, making the real part nearly constant. The input admittance of short circuit shunt stub can be represented as

$$Y_s(f) = \frac{1}{jZ_s tan\theta_s(f)} \tag{3.6}$$

Proper width and length of shunt stub can be employed to make the imaginary part at f_l and f_h close to zero.

$$Imag(Y_{in1}(f_l)) = -(Imag(Y_{in1}(f_h))) = -jB \tag{3.7}$$

Therefore,

$$Y_s(f_l) = \frac{1}{jZ_s tan\theta_s(f)} = jB \tag{3.8}$$

$$Y_s(f_h) = \frac{1}{jZ_s tank\theta_s(f)} = -jB \tag{3.9}$$

By combining (3.8) and (3.9), the short circuit shunt stub dimensions can be derived as

$$\theta_s = \frac{\pi}{(1+k)} \tag{3.10}$$

$$Z_s = \frac{1}{B\ tan(K\theta_s)} \tag{3.11}$$

Thus, the characteristic impedance Z_s and electrical length θ_s of the short circuit shunt stub can be estimated. In this design, a length of 25 mm and a width of 0.8 mm are utilized after careful ADS simulation. Fig. 3.17 shows the input impedance Z_{in2} after the 2nd stage over 1.0 to 2.6 GHz at P_{in} = 5 dBm. It clearly reveals the circular

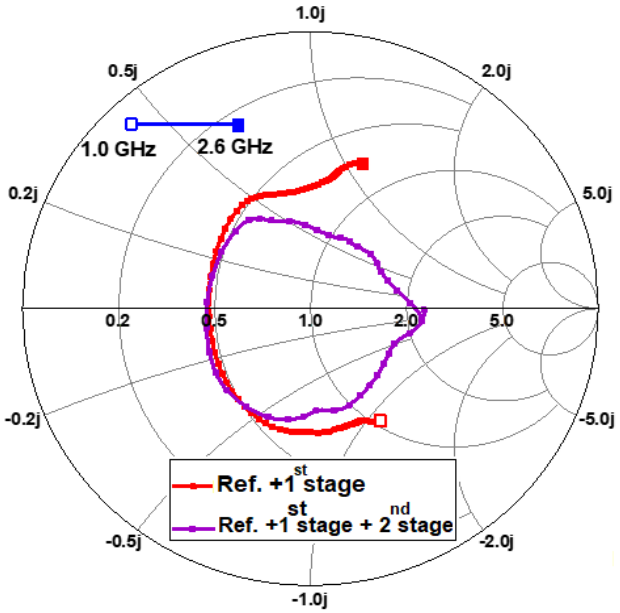

Fig. 3.17. Input impedance Z_{in2} after the 2nd stage design at P_{in} = 5 dBm.

impedance curve obtained after 2nd stage impedance matching. Moreover, the reactance part of $Z_{in2}(f_l)$ and $Z_{in2}(f_h)$ approaches zero as intended.

$$X_{in2}(f_l) \approx -X_{in2}(f_h) \approx 0 \tag{3.12}$$

3.3.1.3. Design of the 3rd Stage

A broad stopband DC-pass filter is required at the output of the rectifier to choke the RF signals within a wide frequency range. In conventional rectenna design, a DC pass filter is employed to acquire a ripple free DC signal by suppressing the fundamental and harmonic frequencies from the rectified output. Even though a large value of capacitor (typically higher than 100 pF) can be utilized with R_L for realizing

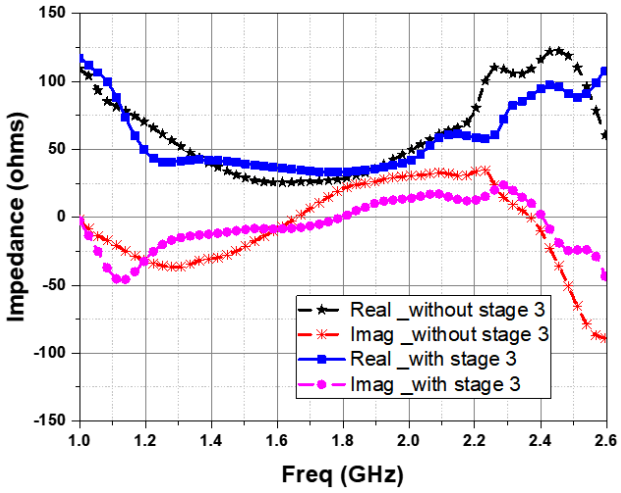

Fig. 3.18. Real and imaginary parts of input impedance Z_{in3} with and without the 3rd stage design.

the output low-pass filter, the equivalent series resistance (ESR) of a large capacitor results in power losses, reduced efficiency, and instability of power supplies and regulators circuits. Thus, parallel connection of small capacitors is utilized to reduce the effective ESR in addition to reducing the ripple voltage and allows the circuit to handle higher currents with less losses [28]. In [29], open stubs are utilized to substitute shunt-to-ground capacitor to produce additional transmission zero in each transmission path to improve the required stopband level. Therefore, a combination of open stubs and a small shunt capacitor are introduced for enhancing the stop band and to realize a ripple free DC voltage in this design. Additionally, the open stubs are also helpful to improve the impedance matching by fine tuning of the stub dimensions.

In the 2nd stage, a constant reflection coefficient circle is achieved with a VSWR

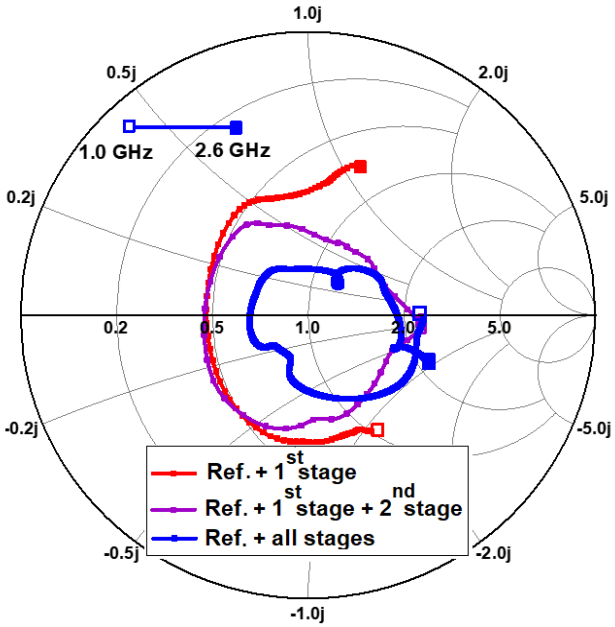

Fig. 3. 19. Input impedance Z_{in3} after the 3rd stage design at P_{in} = 5 dBm.

value of around 2. For high RF-DC efficiency performance, it is necessary to shrink the impedance curve close to 50 Ω. As the DC-pass capacitor C2 is having a low value of 22 pF, a pair of open circuit shunt stubs are utilized to perform the fine-tuning of rectifier impedance and to achieve high output DC power. Open stubs and the length of transmission lines in DC pass filter are tuned with capacitor C2 to reduce the ripples in output DC voltage and to ensure the required rectifier impedance. The value of capacitor C2 is optimized after evaluating the effect of transmission lines using layout cosimulation in ADS Momentum. Fig. 3.18 shows the real and imaginary parts of the rectifier impedance in with and without adding stage 3. The imaginary part of

impedance crosses 0 Ω three times as expected (at f_l, f_h and f_m). It can be observed that the open stubs help to make the real part close to 50 Ω and the imaginary part more constant about 0 Ω in the desired band. Fig. 3.19 shows the input impedance Z_{in3} after the 3rd stage over 1.0 to 2.6 GHz at P_{in} = 5 dBm.

Following the three-stage process, a broadband rectifier is designed. Layout level simulations are performed using electromagnetic (EM) simulator Momentum in ADS. Fig. 3.20 shows the layout of the proposed rectifier and the parameters are summarized in Table 3.2. Capacitors C1 and C2 are from Murata with model numbers GRM0335C2A101GA01 and GRM0335C2A220JA01. The simulated reflection coefficients at three input power levels are shown in Fig. 3.21. It can be observed that at 10 dBm input power, the simulated return loss is better than 10 dB over a 1640 MHz bandwidth from 1.23 to 2.87 GHz. The reflection coefficient is better than -10 dB for a wide bandwidth at the desired input power levels. At high input powers, the impedance matching performance is comparably better than that of low power levels.

Table 3.2. Parameters of the proposed rectifier

Parameter	Value (mm)	Parameter	Value (mm)
W11	0.5	L11	10
W12	1.2	L21	7
W21	0.8	L22	12.5
W31	0.4	L23	5.5
L31	2.6	Ls	3

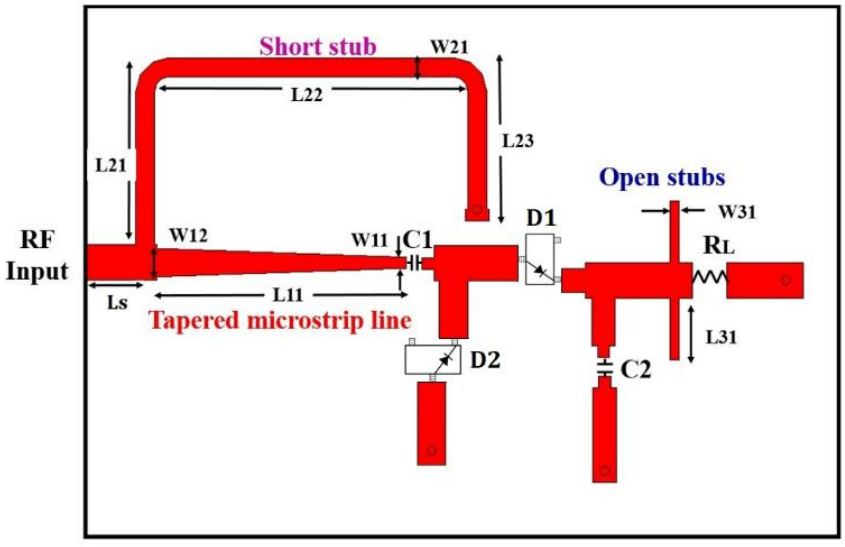

Fig. 3.20. Layout of the proposed broadband rectifier.

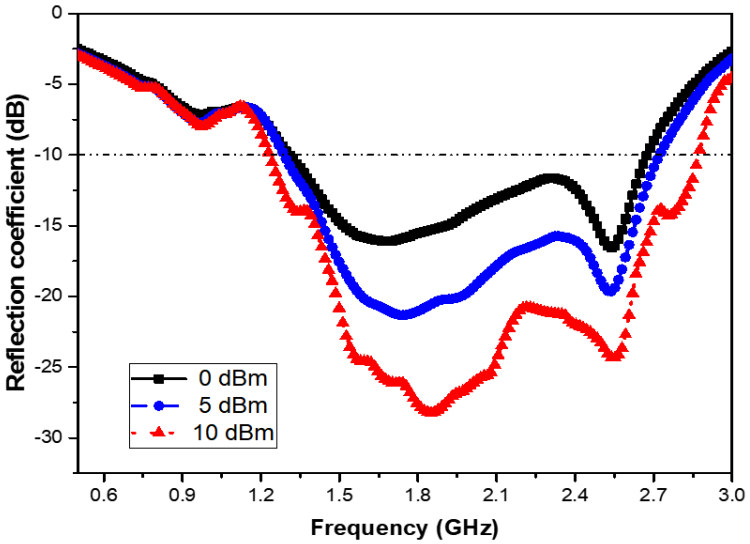

Fig. 3.21. Simulated reflection coefficients of broadband rectifier at three input power levels.

3.3.2. Broadband Rectifier Performance

The proposed broadband rectifier was fabricated for experimental validation on a Rogers 4350B material of 1.52 mm thickness with a relative permittivity of 3.48. Initially, the reflection coefficient of the rectifier was evaluated using a VNA. In Fig. 3.22, the measured reflection coefficient at 0 dBm input power with different load values are shown. At 520 Ω, the measured 1.3 GHz bandwidth ranges from 1.2 to 2.5 GHz which corresponds to a fractional frequency bandwidth of 70%. Even though, the upper limit crosses -10 dB at 2.5 GHz, reflection coefficient is around -9 dB till 2.75 GHz. For higher load values, the impedance bandwidth decreases.

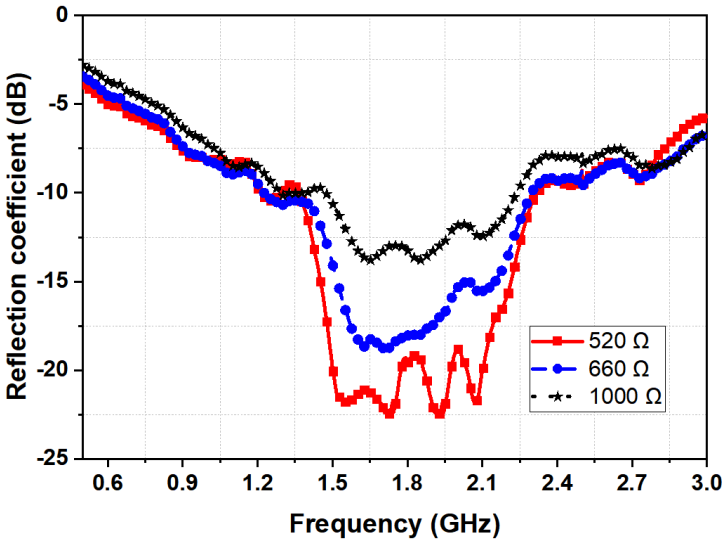

Fig. 3.22. Reflection coefficients of the broadband rectifier at different load resistors.

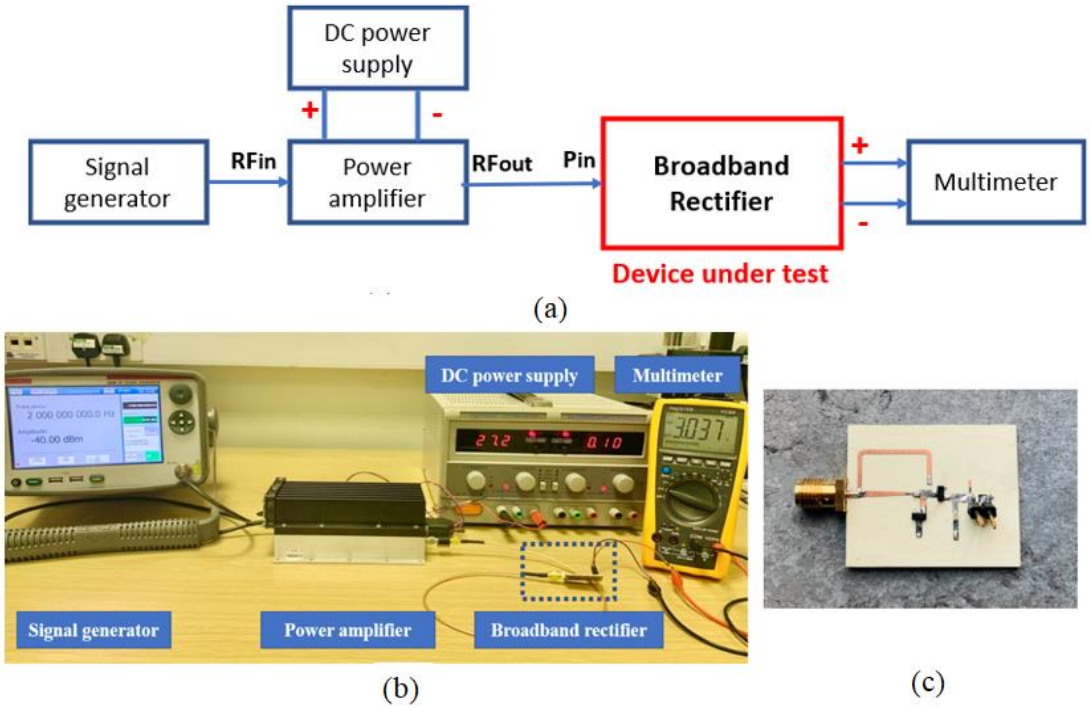

Fig. 3.23. Measurement of broadband rectifier (a) block diagram (b) measurement set up (c) fabricated rectifier.

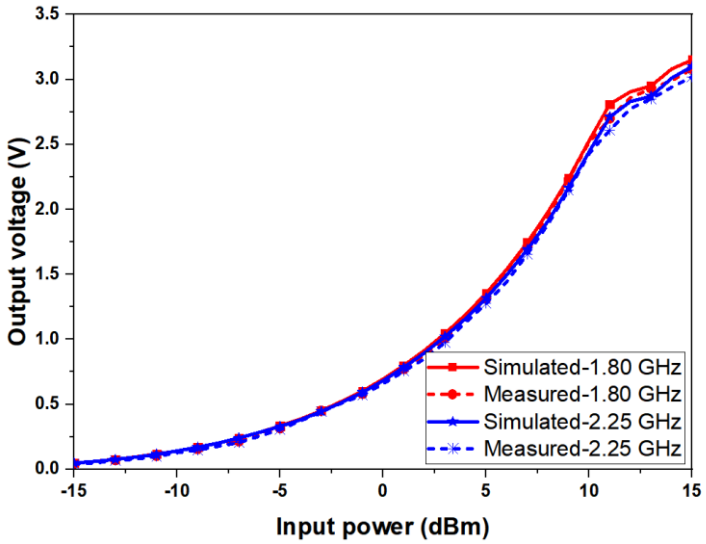

Fig. 3.24. Output voltage versus input power.

The power conversion efficiency of the fabricated rectifier is evaluated using the measurement setup shown in Fig. 3.23. A Keithley 2920 RF signal generator with an output power up to 13 dBm was utilized to generate the RF signal at 1 to 3 GHz. A 40 dB gain GaN power amplifier was employed to amplify the signal for the testing of broadband rectifier. To protect the signal generator from any power surge and reflections, a 3-dB attenuator was connected between the signal generator and power

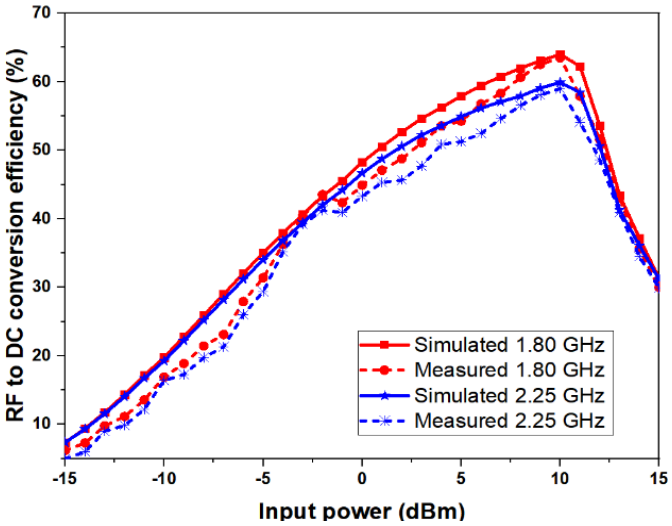

Fig. 3.26. RF to DC conversion efficiency versus input power.

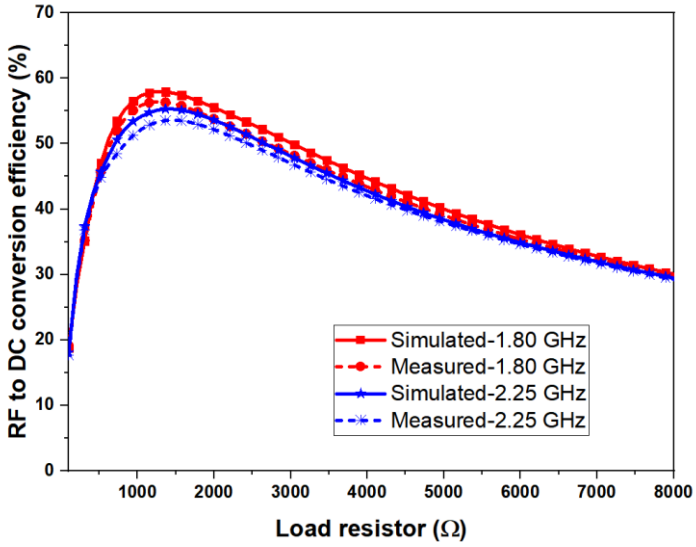

Fig. 3.25. RF to DC conversion efficiency versus load resistor at an input power of 5 dBm

amplifier. For analyzing and estimating the signal power from the power amplifier, a Keithley signal analyzer together with a 20 dB attenuator is utilized. A digital multimeter is used to measure the output voltage across the R_L resistor. The measurement setup is appropriately calibrated considering all device losses to provide the most reliable results. Initially, output voltage is measured at 1.8 and 2.25 GHz by varying the input power from -15 to 15 dBm as shown in Fig. 3.24. It can be observed that maximum output voltage of 3.1 V is measured at 1.8 GHz. Simulated and measured values are in close agreement. The RF-to-DC conversion efficiency (η) of a microwave rectifier is calculated as the ratio of the rectified DC output power to the incident RF power, it can be expressed as

$$\eta = {V_{out}^2}/{(R_L P_{in})} \times 100\% \quad (3.13)$$

where P_{in} is the input power and V_{out} is the DC output voltage across the load resistor R_L of the microwave rectifier. Fig. 3.25 shows the simulated and measured conversion efficiencies of the proposed microwave rectifier at 1.8 and 2.25 GHz as a function of input power. A maximum efficiency of 65% is achieved at 1.8 GHz with 10 dBm input power. Fig. 3.26 depicts that the proposed rectifier has a relatively stable efficiency over a wide circuit load range from 300 to 8000 Ω. This shows that the proposed rectifier could be integrated with different load devices. For analyzing the broadband performance of the rectifier, the RF-to-DC conversion efficiency is measured at an input power level of 5 dBm and 10 dBm as shown in Fig. 3.27 by varying the frequencies from 0.6 to 3 GHz. It can be observed that a peak efficiency of 58% is obtained at 1.8 GHz by 5 dBm input power. The conversion efficiency is higher than 50 % for a fractional bandwidth (FBW) of 74% from 1.12 to 2.43 GHz at 5 dBm input power. At 10 dBm, the conversion efficiency is higher than 50 % from 0.97 to 2.55 GHz (FBW = 90%).

In order to evaluate the performance of the proposed rectifier, it is compared with other similar broadband rectifiers in Table 3.3. The important parameters are the operational bandwidth, efficiency, input power, and size. It can be concluded that our transmission line-based impedance matching design achieves high conversion efficiency over a wide frequency band. More specifically, a fractional bandwidth

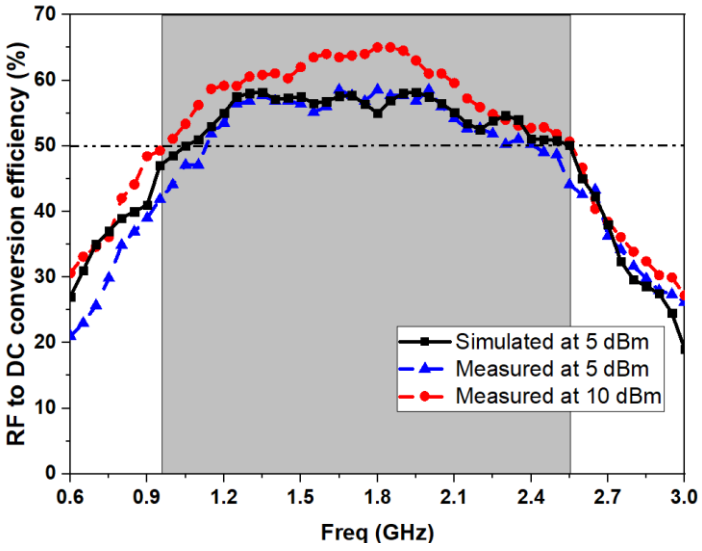

Fig. 3.27. RF to DC conversion efficiency versus frequency at an input power of 5 and 10 dBm.

(FBW) of 74% is achieved at 5 dBm and 90% at 10 dBm input power which is the highest among all the designs under comparison. Furthermore, our design has the smallest overall dimension 24×36 mm^2 (electrical size is 0.14 $\boldsymbol{\lambda}$× 0.21 $\boldsymbol{\lambda}$). Therefore, the proposed rectifier is very much suitable for energy harvesting applications due to its small footprint and high energy conversion efficiency performance over a wide bandwidth at low input power.

Table 3.3. Comparison of the proposed broadband rectifier with other related designs

Ref. (year)	**Description**	**Efficiency in operating bandwidth at input power**			**Area ($\boldsymbol{\lambda^2}$)**
		FBW (GHz)	**η (%)**	**Input power (dBm)**	
[30] (2019)	Dual-stub matching network	2.2-2.7 (20.4%)	>50	5	N.A.
[31] (2019)	Multi-stage matching, and a DC-pass filter	1.75-3.2 (58.5%)	>50	10	0.29 ×0.31
[32] (2018)	Two-Stage Matching Network	1.5-2.3 (42.1%)	>50	5.5	N.A.
[33] (2018)	Non-uniform transmission line matching	0.45-0.86 (67%)	>50	10	0.22 ×0.31
[34] (2020)	Microstrip line matching of shunt rectifier	2-3.3 (45%)	>50	4	0.16 ×0.27
This work	**3-stage matching technique**	**1.12-2.43 (74%) 0.97-2.55 (90 %)**	**>50 >50**	**5 10**	**0.14 ×0.21**

3.4. Rectenna Evaluation

The rectenna is fabricated, and its performance over free space transmissionis evaluated. The experimental setup is illustrated in Fig. 3.28. During the experiment, an RF power source is connected to a standard horn antenna, which is performed as the transmitter. The RF energy from power source at LTE band is carried by a continuous wave. The designed rectenna is aligned and placed at a distance of 1 m away from the transmitter, which is the far-field distance determined by

$$R = \frac{2D^2}{\lambda} \tag{3.14}$$

where R is the far-field distance, λ is the wavelength of the operating frequency, and d is the largest dimension of the antenna. The RF to DC conversion efficiency is the most critical parameter to evaluate the performance of the proposed rectenna, which is estimated by

$$\eta = \frac{V_{DC}^2}{R_L P_r} \tag{3.15}$$

$$P_r = \left(\frac{\lambda}{4\pi R}\right)^2 G_r G_t P_t \tag{3.16}$$

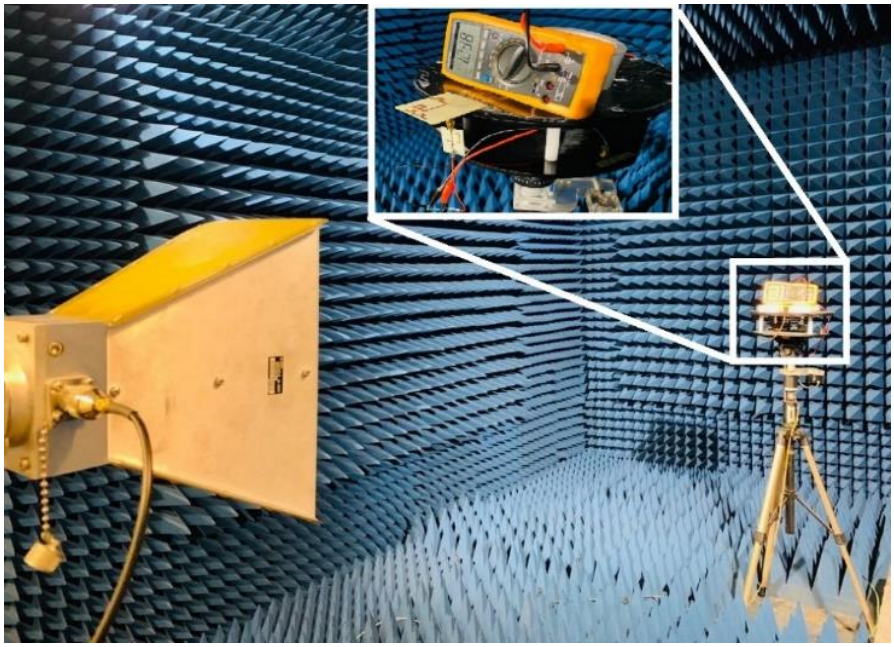

Fig. 3.28. Measurement setup of rectenna conversion efficiency

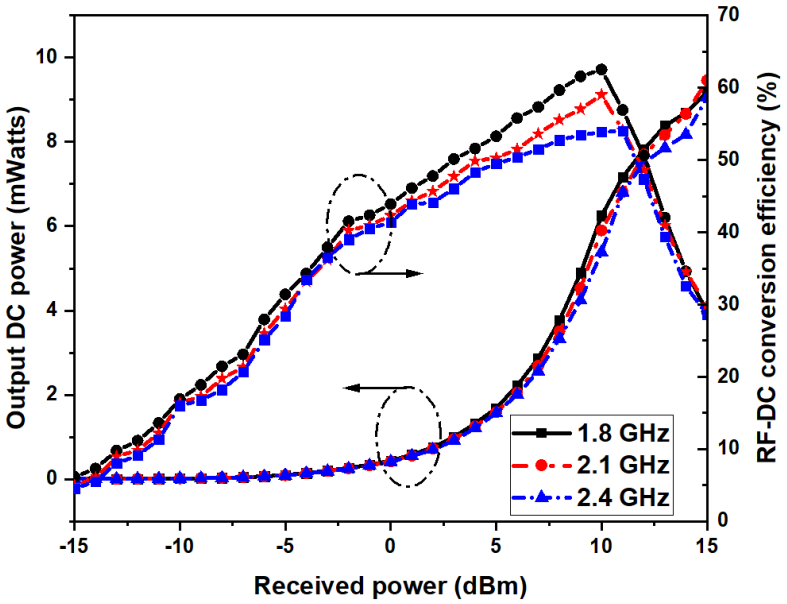

Fig. 3.29. Output DC power and RF to DC conversion efficiency versus received power

and where η is the RF to DC conversion efficiency, V_{DC} is the measured output voltage of the load, R_L is the load resistance, and P_r is the received power of rectenna, G_r and G_t are the realized gain of the designed antenna and the transmitter, and Pt is the transmitting power of the horn antenna. Fig. 3.29 shows the measured conversion efficiency and output DC power of the rectenna as a function of received power at different frequencies in the operating band. It is noted that the maximum efficiency of 63% is obtained at 1.8 GHz and 60% at 2.1 GHz at an input power of 10 dBm. It can be also seen that the efficiency is over 50% with an input power of 5 dBm at all three frequencies.

3.5. Summary

In this chapter, two broadband rectenna related studies for wireless energy harvesting applications have been proposed. In the first design, a novel enhanced gain broadband Yagi-Uda antenna has been designed. Two meandered dipoles are connected using feed lines was properly optimized for broadband operation. Curved reflectors and meandered dipoles are also utilized for improving the gain. Antenna achieved a bandwidth of 920 MHz ranging from 1.65 to 2.57 GHz and having the worst-case directivity of 5 dBi throughout the bandwidth. In the second design, we proposed a novel three-stage transmission lines-based impedance matching technique

to achieve a broadband rectifier with excellent RF - DC conversion efficiency. A circular impedance curve has been realized by utilizing a tapered microstrip line, short circuit shunt stub and open stubs. The fabricated broadband rectifier achieved a conversion efficiency of more than 50% at a 5 dBm input power level over a wide bandwidth of 1.12-2.43 GHz (FBW = 74%). In addition, the rectifier has more than 50% efficiency from 0.97-2.55 GHz (FBW = 90%) at an input power of 10 dBm, which is the highest bandwidth reported under this condition to the best of our knowledge. The proposed transmission lines-based impedance matching design has superior performance in terms of its wide bandwidth and compactness making it suitable for realizing broadband rectifier for WEH and WPT applications. The proposed rectenna has the ability to harvest RF energy from a large spectrum of 1.12 – 2.43 GHz with reasonably high conversion efficiency of more than 50% at a 5 dBm input power level.

References

[1] S. Kim *et al*., "Ambient RF energy-harvesting technologies for self-sustainable standalone wireless sensor platforms," *Proc. IEEE*, vol. 102, no. 11, pp. 1649-1666, Nov. 2014.

[2] R. J. Vyas, B. B. Cook, Y. Kawahara, and M. M. Tentzeris, "E-WEHP: A battery less embedded sensor-platform wirelessly powered from ambient digital-TV signals," *IEEE Trans. Microw. Theory Techn.*, vol. 61, no. 6, pp. 2491–2505, Jun. 2013.

[3] C. Song, Y. Huang, J. Zhou, J. Zhang, S. Yuan, and P. Carter, "A high-efficiency broadband rectenna for ambient wireless energy harvesting," *IEEE Trans. Antennas Propag.,* vol. 63, no. 8, pp. 3486-3495, Aug. 2015.

[4] V. Palazzi *et al*., "A novel ultra-lightweight multiband rectenna on paper for RF energy harvesting in the next generation LTE bands," *IEEE Trans. Microw. Theory Techn*., vol. 66, no. 1, pp. 366–379, Jan. 2018.

[5] W.R. Deal, Y. Qian, T. Itoh and V. Radisc, "Planar Integrated Antenna Technology," *Microw. J*., Jul. 1999.

[6] N. Kaneda, W. R. Deal, Y. Qian, R. Waterhouse and T. Itoh, "A broadband planar quasi-Yagi antenna," *IEEE Trans. Antennas Propag*., vol. 50, no. 8, pp. 1158-1160, Aug. 2002.

[7] P. T. Nguyen, A. Abbosh and S. Crozier, "Wideband and compact quasi-Yagi antenna integrated with balun of microstrip to slotline transitions," *Electron. Lett.*, vol. 49, no. 2, pp. 88-89, Jan. 2013.

[8] P. V. Nikitin and K. V. S. Rao, "Compact Yagi antenna for handheld UHF RFID reader," *Proc. IEEE Int. Symp. Antenna and Propagation*, Jul. 2010.

[9] H. C. Huang, J. C. Lu, and P. Hsu, "A planar Yagi–Uda antenna with a meandered driven dipole and a concave parabolic reflector," *Proc. Asia-Pacific Microw. Conf.,* pp. 995–998, Dec. 2010.

[10] M. Bemani and S. Nikmehr, "A novel wide-band microstrip yagi-uda array antenna for WLAN applications," *Prog. Electromagn. Res.,* Vol. 16, 389–406, 2009.

[11] J. Yeo and J. I. Lee, "Broadband series-fed two dipole array antenna with an integrated balun for mobile communication applications," *Microwave. Opt. Technol. Lett*., vol. 54, no. 9, pp. 2166-2168, Sep. 2012.

[12] S. A. Rezaeieh, M. A. Antoniades and A. M. Abbosh, "Miniaturized Planar Yagi Antenna Utilizing Capacitively Coupled Folded Reflector," *IEEE Antennas Wirel. Propag. Lett*., vol. 16, pp. 1977-1980, 2017.

[13] Y. Luo, Q. Chu, and J. Bornemann, "A differential - fed Yagi - Uda antenna with enhanced bandwidth via addition of parasitic resonator," *Microw. Opt. Technol. Lett*., vol. 59, no. 1, pp. 156-159, Jan. 2017

[14] R. Chopra and G. Kumar, "Uniplanar Microstrip Antenna for Endfire Radiation," *IEEE Trans. Antennas Propag*., vol. 67, no. 5, pp. 3422-3426, May 2019.

[15] L. Lu, L. Shu, A. Denisov, L. Dongyu, C. Yangyang and T. Shuo, "A broadband and high gain yagi antenna with complex parabolic boundary reflector," *Proc. IEEE Int. Symp. Antenna and Propagation*, San Diego, CA, pp. 1785-1786, 2017.

[16] S. Chandravanshi, S. S. Sarma, and M. J. Akhtar, "Design of triple band differential rectenna for RF energy harvesting," *IEEE Trans. Antennas Propag*., vol. 66, no. 6, pp. 2716–2726, Jun. 2018.

[17] Kuhn, V., C. Lahuec, F. Seguin, and C. Person, "A multi-band stacked RF energy harvester with RF-to-DC e±ciency up to 84%," *IEEE Trans. Microw. Theory Techn*., Vol. 63, No. 5, 1768-1778, May 2015.

[18] T. W. Barton, J. M. Gordonson, and D. J. Perreault, "Transmission line

resistance compression networks and applications to wireless power transfer," *IEEE J. Emerging Sel. Topics Power Electron*., vol. 3, no. 1, pp. 252–260, Mar. 2015.

[19] X. Y. Zhang, Z.-X. Du, and Q. Xue, "High-efficiency broadband rectifier with wide ranges of input power and output load based on branchline coupler," *IEEE Trans. Circuits Syst. I, Reg. Papers*, vol. 64, no. 3, pp. 731–739, Mar. 2017.

[20] J. Kimionis, A. Collado, M. M. Tentzeris, and A. Georgiadis, "Octave and decade printed UWB rectifiers based on nonuniform transmission lines for energy harvesting," *IEEE Trans. Microw. Theory Techn*., vol. 65, no. 11, pp. 4326–4334, Nov. 2017

[21] M. M. Mansour, and H. Kanaya, "Compact and broadband RF rectifier with 1.5 octave bandwidth based on a simple pair of L-section matching network," *IEEE Microw. Wireless Compon. Lett.*,vol. 28, no. 4, pp. 335-337, april, 2018.

[22] H. Zhang and X. Zhu, "A broadband high efficiency rectifier for ambient RF energy harvesting," *Proc. IEEE MTT-S Int. Microw. Symp*., Tampa, FL, USA, pp. 1-3, Jun. 2014.

[23] C. Liu, F. Tan, and Q. He, "A novel single-diode microwave rectifier with a series band-stop structure," *IEEE Trans. Microw. Theory Techn*., vol. 65, no. 2, pp. 600–606, Feb. 2017.

[24] K. Fujimori, S.-I. Tamaru, K. Tsuruta, and S. Nogi, "The influences of diode parameters on conversion efficiency of RF-DC conversion circuit for wireless power transmission system," *Proc. Eur. Microw. Conf. (EuMC)*, pp. 57–60, Oct. 2011.

[25] H. Takhedmit *et al*., "A 2.45-GHz dual-diode RF-to-DC rectifier for rectenna applications," *Proc*. *Eur. Microw. Conf. (EuMC)*, pp. 37–40, Sep. 2010.

[26] C. R. Valenta and G. D. Durgin, "Harvesting wireless power: Survey of energy-harvester conversion efficiency in far-field wireless power transfer systems," *IEEE Microw. Mag*., vol. 15, no. 4, pp. 108-120, Jun. 2014.

[27] D. M. Pozar, *Microwave Engineering*, 4th ed., Wiley, Nov. 2011.

[28] K. S. Kumar*, Electric Circuits and Networks*. New Delhi, India: Pearson Edu., 2009.

[29] P. H. Deng, J. H. Guo, and W. C. Kuo, "New wilkinson power dividers based on compact stepped-impedance transmission lines and shunt open stubs," *Prog.*

Electromagn. Res., vol. 123, pp. 407–426, 2012.

[30] Y. Shi, Y. Fan, Y. Li, L. Yang, and M. Wang, "An efficient broadband slotted rectenna for wireless power transfer at LTE band," *IEEE Trans. Antennas Propag*., vol. 67, no. 2, pp. 814–822, Feb. 2019.

[31] P. Wu *et al*., "Compact high-efficiency broadband rectifier with multistage-transmission-line matching," *IEEE Trans. Circuits Syst. II, Exp. Briefs*, vol. 66, no. 8, pp. 1316–1320, Aug. 2019.

[32] Y. Wu, J. Wang, Y. Liu, and M. Li, "A novel wideband rectifier design with two-stage matching network for ambient wireless energy harvesting," *Proc. 2018 Prog. Electromagn. Res. Symp. (PIERS-Toyama)*, Toyama, 2018, pp. 1351-1354.

[33] P. Wu, S. Y. Huang, W. Zhou, and C. Liu, "One octave bandwidth rectifier with a frequency selective diode array," *IEEE Microw. Wireless Compon. Lett.,* vol. 28, no. 11, pp. 1008–1010, Nov. 2018.

[34] Z. He, and C. Liu, "A compact high-efficiency broadband rectifier with a wide dynamic range of input power for energy harvesting," *IEEE Microw. Wireless Compon. Lett*., vol. 30, no. 4, pp. 433–436, Apr. 2020.

Chapter 4. Highly Sensitive Dual-Band Rectenna

In this chapter, a novel highly sensitive dual-band rectenna is proposed for ambient WEH. This dual-band rectenna consists of a novel dual-band dipole antenna and a highly sensitive dual-band rectifier. The dual-mode dipole antenna with folded stubs is proposed for dual-band operation. By introducing these stubs in the dipole antenna, the effective electrical length for the third-order mode is increased, which shifts the third-harmonic frequency down and results in a dual-mode antenna with wideband or dual-band characteristics. The position and length of the stubs have been optimized to enhance the impedance matching. To validate the design, a prototype was fabricated and tested. A dual-band antenna is designed based on the dual mode dipole antenna. A highly sensitive rectifier is realized by using a single inductor-based impedance matching. Finally, the proposed highly sensitive dual-band rectenna is measured and observed a high conversion efficiency at low ambient power conditions. One journal paper '*A compact dual-mode dipole antenna with 47% bandwidth and stable omnidirectional radiation pattern'* has been submitted in *IET* and one conference paper submitted in *RFIT 2021* based on this work.

4.1. Introduction

Design of highly sensitive rectifiers is very challenging due to the finite threshold voltage and the parasitic elements of the diodes. To enhance the sensitivity, several low power rectifiers with low or zero threshold diodes have been reported. Some efforts have also been made to exploit the high functionality of the CMOS IC technology to control the threshold voltage, both statically [1] and dynamically [2]. In [3], an enhancement mode (E-mode) FET with nearly zero threshold voltage in FET rectifiers of amplifier-oriented design has also been shown to enhance the efficiency at -30 dBm. Nevertheless, several investigations are still focusing to improve the

performance of conventional Schottky barrier diodes-based rectifiers with finite threshold voltages [4]-[7]. For enhancing the output voltage, voltage multiplying rectifiers using multiple diodes are commonly used. However, the loss in the rectifier increases with the number of diodes and the low power operation degrades significantly. Therefore, it is better to use rectifier topologies with minimum diodes for low power ambient RF harvesting, even though the output voltage is low for practical applications. In the meantime, single-diode rectifiers can be combined with boost converters for enhancing the output voltage. For now, such conventional type rectifiers using commercially available Schottky Barrier Diodes (SBD) have shown significant improvement in the efficiency [8], [9]. Most of them are designed based on tuning the circuit parameters or impedances. Complex impedance networks can guarantee matching effectively with the cost of associated loss of impedance circuits. Therefore, a simple effective method to acquire low power rectification using commercially available SBDs with relatively large parasitic elements and finite threshold voltage is very much required.

4.1.1. Design of Highly Sensitive Rectifier

To design a high sensitivity rectifier, it is necessary to understand the input impedance of SBD diode at low input power. A Schottky barrier diode (SBD) from Skyworks SMS7630-079F, which is widely used for low-power rectifiers due to its low threshold voltage is carefully chosen [10]. Based on the datasheet, a nonlinear diode spice model with parasitic is used in the simulation. I_S = 5×10^{-6} A, R_S = 20 Ω, C_{j0} = 0.14 pF, V_j = 0.34 V, N = 1.04, M = 0.4 and B_V = 2 V, X_{ti} = 2, Tt = 10^{-11} sec. A packaged commercial diode can be depicted as shown in Fig. 4.1. For typical low power applications, the diode model is simulated at an input power of -30 dBm from0.5 to 5 GHz. A smith chart with the diode input impedance is shown in Fig. 4.2. It can be observed that the impedance of the rectifier is capacitive.

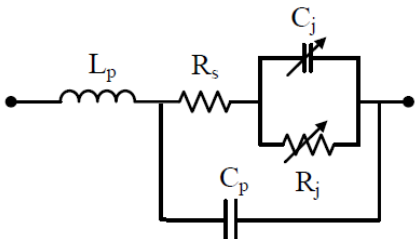

Fig. 4.1. Equivalent circuit of a commercial diode.

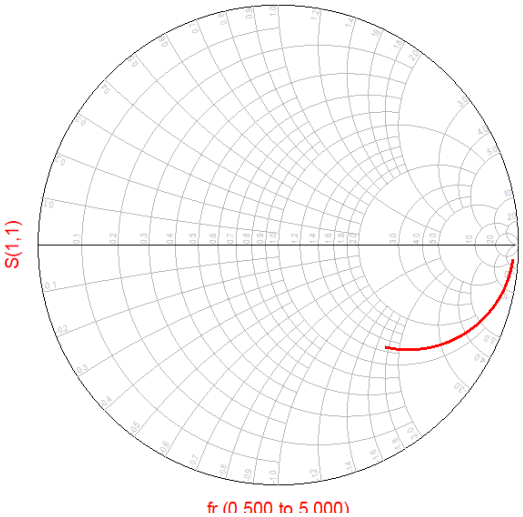

Fig. 4.2. Diode input impedance in smith chart

Capacitive input impedance primarily raised from the junction C_j and package C_p capacitances. Thus, in order to match the diode at a specific operating frequency, a single external inductor-based matching is proposed to compensate these capacitive effects. The inductor is intended to resonate with the zero-bias capacitors of the diode at the operating frequency. Moreover, this technique can provide good impedance matching and high bandwidth. Sensitivity of the rectifier can be significantly improved by reducing the losses in impedance matching by using only an inductor instead of complex matching circuits.

The proposed inductor matched series diode rectifier is shown in Fig. 4.3. Capacitor *C2* and load resistor R_L forms a low pass filter for removing the fundamental and harmonics. For analysing the performance of inductor-based resonant matching rectifier, a series diode rectifier operating at 0.915 GHz is designed. A load resistor of value 6 kΩ and a matching inductor of 82 nH are used in this rectifier. The inductor is from coilcraft 0402HP series with model number 0402HPH-82NXGLW.

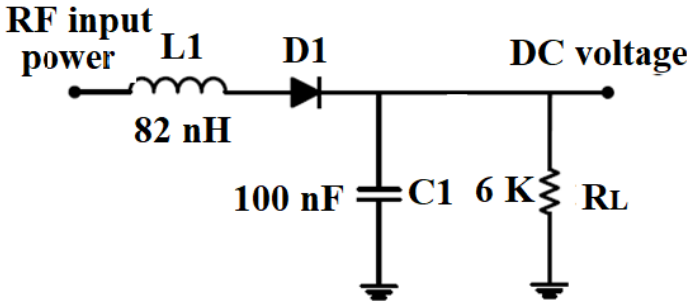

Fig. 4.3. Proposed 0.915 GHz highly sensitive rectifier

For evaluating the performance of single inductor matched high sensitivity rectifier, a prototype is fabricated on FR4 substrate with a thickness of 1.52 mm. Harmonic balance and LSSP simulations are carried out using ADS. A Keithley 2920 RF signal generator with an output power up to 13 dBm has been utilized to generate the RF signal at 0.915 GHz. A digital multimeter has been used to measure the output voltage across the R_L resistor. Fig. 4.4 shows the simulated and measured reflection coefficient of the inductor matched rectifier. The measured rectifier bandwidth extends from 0.89 GHz to 0.94 GHz. The input power to the rectifier has been varied from -45 to 0 dBm, to measure the DC voltage across the load resistor. The RF to DC conversion efficiency of a microwave rectifier is calculated as the ratio of the rectified DC output power to the input RF power, and it can be expressed as

$$\eta = \frac{V_{out}^2}{R_L P_{in}} \tag{4.1}$$

where P_{in} is the input power and V_{out} is the DC output voltage across the load resistor R_L of the microwave rectifier. Fig. 4.5(a) shows the simulated and measured conversion efficiencies of the proposed microwave rectifier as a function of input power. A maximum measured efficiency of 59% is achieved at -10 dBm. Conversion efficiencies of 13 and 54 % are measured at input power levels of -30 and -15 dBm,

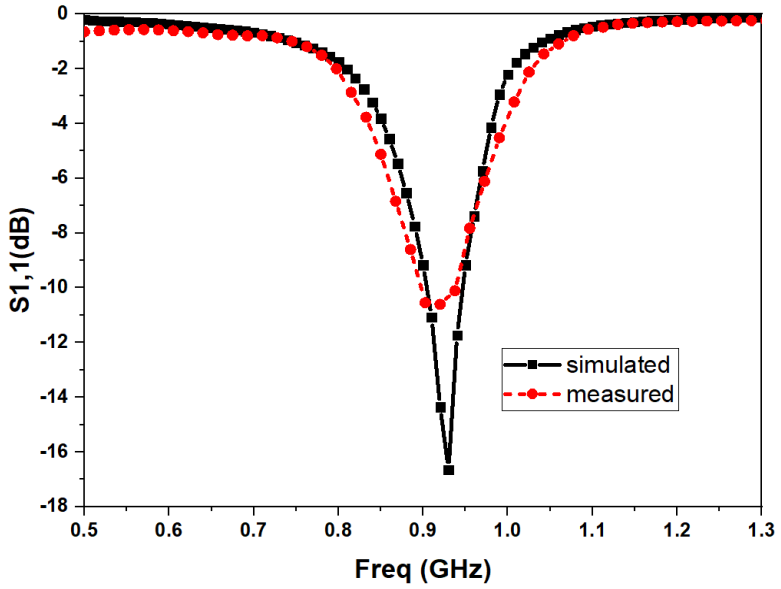

Fig. 4.4. Reflection coefficient of a 0.915 GHz rectifier

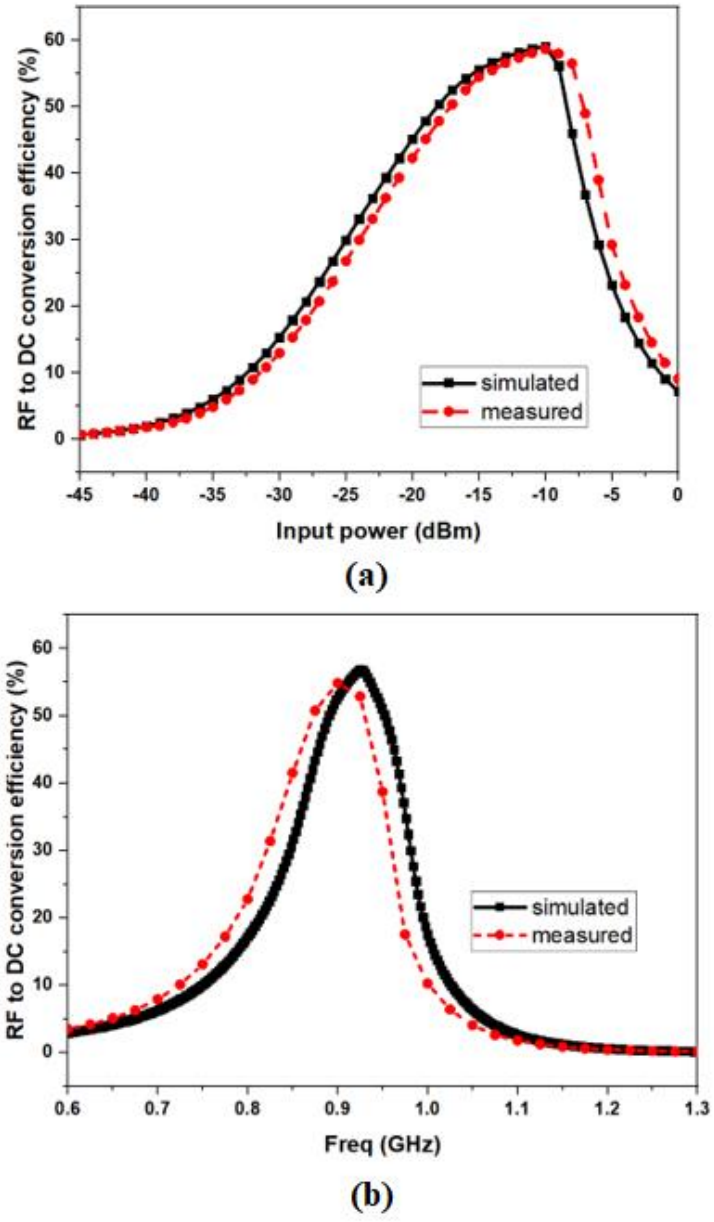

Fig. 4.5. RF to DC conversion efficiency versus (a)input power (b) frequency

respectively. A high sensitivity and efficiency performance can be clearly observed in single series at low input power (-40 to -10 dBm). Measured conversion efficiency has good agreement with simulated values. In order to evaluate the RF-DC conversion efficiency bandwidth at a -15 dBm input power level, the input frequency is varied from 0.6 to 1.3 GHz. Fig. 4.5(b) depicts the conversion efficiency as a function of frequency at -15 dBm input power. Conversion efficiency of more than 50% is achieved from 0.87 to 0.93 GHz.

4.2. Highly Sensitive Dual-Band Rectifier

Based on the discussed high sensitivity rectifier, a dual-band rectifier is designed to cover 0.915 GHz and 2.45 GHz for wireless energy harvesting. In Section 4.2.1, the design of dual-band rectifier is explained. The measured performance of the rectifier is studied in detail in Section 4.2.2.

4.2.1. Design of Dual-Band Rectifier

In order to cover the 0.915 GHz and 2.45 GHz ISM bands, the designed single inductor matched rectifier technique is utilised. As mentioned in the previous chapters, for dual-band operation RF stack approach is better for maximum DC output power and conversion efficiency. Hence, a parallel two branch rectifier is designed, in which the upper branch is responsible for 0.915 GHz and the lower branch for 2.45 GHz. A T-junction is utilised in the input side of the two branches. Complex bandpass filters and diplexers with more lumped elements are not considered in this design to reduce the losses associated with complex circuitry and lumped elements. Sensitivity of the rectifier can be significantly improved by using a single inductor in both branches and thus, only the inductor loss affects the performance instead of complex matching circuits and bandpass filters (diplexers). Fig. 4.6 shows the layout of the proposed dual-band high sensitivity rectifier.

A load resistor of 4 kΩ is used for this dual-band rectifier. A matched inductor of 68 nH is intended to resonate with the zero-bias capacitors of the diode at the 0.915 GHz with load resistor. Similarly, 13 nH inductor is utilised to rectify the 2.45 GHz

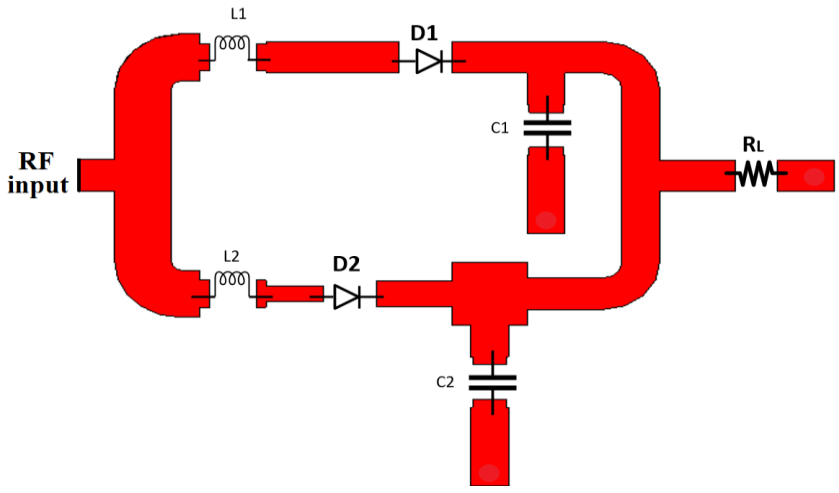

Fig. 4.6. Layout of dual-band rectifier

band. *C1* and *C2* are used for DC pass filter and has a value of 100 pF. High Q inductors are from Coil Craft 0402HP series with model number 0402HPH-68NXGLW and 0402HP-13NXGLW. Capacitors are from Murata with model number GRM0335C2A101GA01.The two-branch rectifier topology offers high performance in both frequency bands.

4.2.2. Performance of the Rectifier

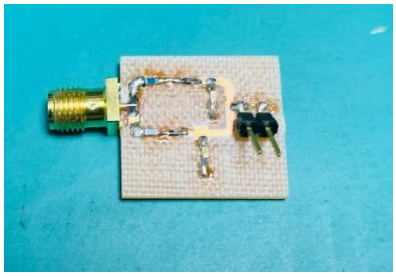

Fig. 4.7. Fabricated dual-band rectifier

The proposed dual-band rectifier was fabricated for experimental validation on a FR4 material of 1.52 mm thickness with a relative permittivity of 4.4 as shown in Fig. 4.7. Initially, the reflection coefficient of the rectifier was evaluated using a VNA. In Fig. 4.8, the simulated and measured reflection coefficient at 0 dBm input power is shown. It can be clearly observed that even though both bands have good impedance matching, the lower 0.915 GHz band has better reflection coefficient than the 2.45 GHz band. The measured rectifier bandwidth extends from 0.9 GHz to 0.97 GHz in the lower band and 2.37 GHz to 2.46 GHz in the upper band. The input power to the rectifier has been varied from -45 to 0 dBm, to measure the DC voltage across the load.

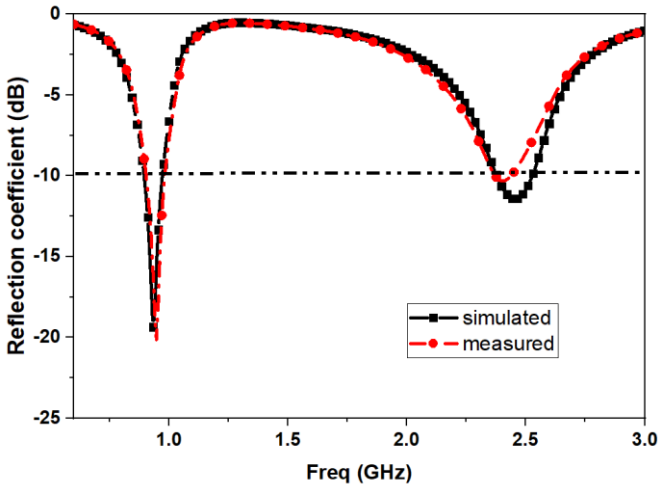

Fig. 4.8. Reflection coefficient of the dual-band rectifier

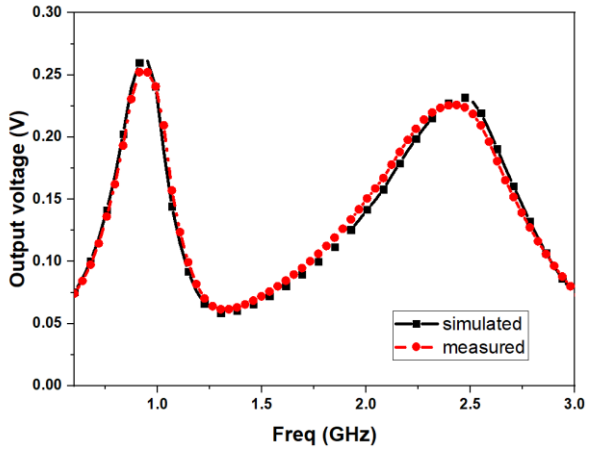

Fig. 4.10. Output voltage of the dual-band rectifier

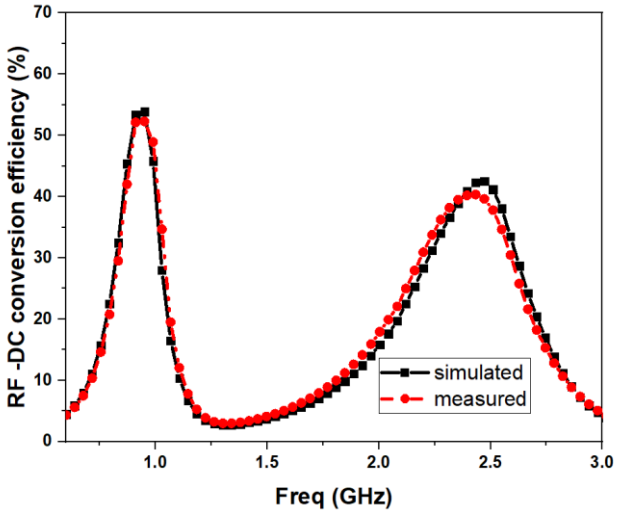

Fig. 4.9. RF to DC conversion efficiency of the dual-band rectifier

Fig. 4.9 shows the output voltage of the rectifier as a function of frequency at an input power of -15 dBm. Output voltage of 0.25V and 0.225 V are observed at 0.915 GHz and 2.4 GHz, respectively. RF to DC conversion efficiency of the rectifier as a function of operating frequency at -15dBm input power is shown in Fig. 4.10. Conversion efficiencies of more than 52% and 40% are obtained in the lower and upper bands, respectively. This demonstrates the feasibility of the proposed highly sensitive rectifier to capture RF energy from ambient environments.

4.3. Dual-Mode Dipole Antenna

With the rapid development of 5G technologies, the need of wideband antennas with stable omnidirectional radiation pattern over their operating frequency bands has

immensely increased [11]. Conventionally, antennas with frequency independent concept such as the spiral antennas and log-periodic antennas were widely used to achieve wide bandwidth [12]-[15]. But large size and design complexity of these antennas make them difficult to be realized. Patch antennas with different feeding techniques like slot coupling feeding [16], U-shaped slot feeding [17], and L-shaped probe feeding [18] have also been widely studied for large bandwidth. Though, in order to achieve omnidirectional radiation pattern, dipole antennas are usually selected due to its simple structure [18]-[21]. However, the high Q factor of thin wire dipoles results in narrow bandwidth [22]. Thus, several techniques were investigated to widen the bandwidth of dipole antennas. One widely used approach to achieve wide bandwidth is to use parasitic resonator loadings. Typically, split-ring resonators, dipoles, and loops have been employed to enhance the bandwidth of dipole antennas [23]-[26]. In [27], a wideband unidirectional antenna composed of a planar electric dipole and a shorted patch antenna is presented. By combining a pair of electric and magnetic dipoles, stable radiation patterns are realized over the entire operating band. This work has attracted broad attention and in-depth studies in wideband dipoles. In [28], a wide bandwidth dipole antenna is presented based on the mu-negative transmission line (MNG-TL). A wideband antenna with stable omnidirectional radiation pattern consisting of a dipole and parasitic loop has been investigated in [26]. Multiple dipoles with different lengths were also widely utilized for exciting multiple resonant frequencies [29]. But the additional resonators and periodic structures increase the overall size and complexity.

Another major approach to realize wideband performance in compact size is by employing mode compression methods [30]-[33]. In mode compression methods, multiple resonant modes are excited and compressed together to form the required wide bandwidth using loaded structures. In [30], the fifth-order mode of the compressed dipole has moved close to its third-order mode for broad bandwidth Moreover, the first mode and third mode are utilized and compressed in [31] and [32] to achieve more compact dipoles. Similar attempts were also demonstrated to be beneficial on slot antennas. In [33], a wideband antenna is introduced by exciting the multiple modes in a single slotline radiator. Stub slots are added along the main slot to excite dual-mode operation for wide bandwidth. Even though the above-mentioned

mode compressed designs have a high bandwidth, the unstable radiation patterns are restricting their applications.

Considering the above concerns, a dipole antenna loaded with folded stubs are proposed to realize broad bandwidth and stable omni directional radiation pattern. This antenna utilizes the first and third order resonances and compressed them to create a

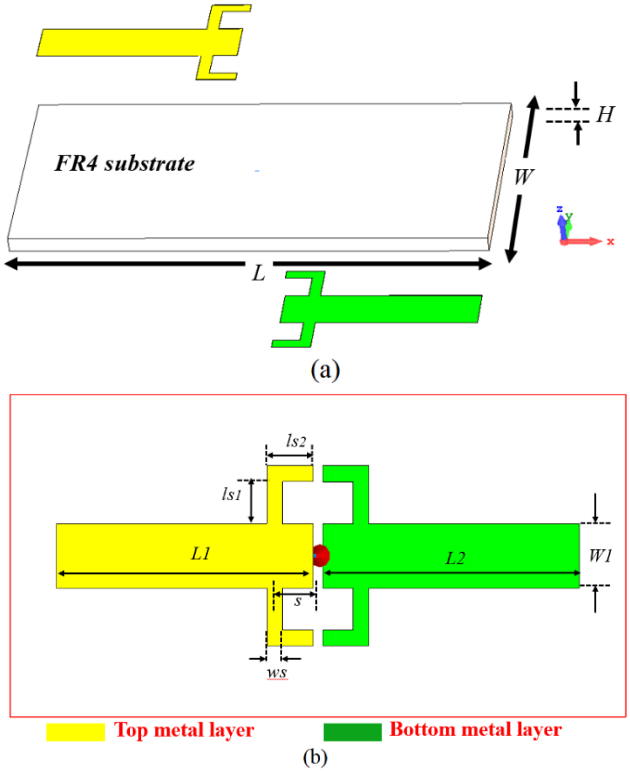

Fig. 4.11. Proposed dual mode antenna (a) perspective view (b) top view without substrate.

broadband. Section 4.3.1 explains the design and operation principle of the proposed dual mode dipole antenna with folded stubs. Section 4.3.2 describes the measurement results of the proposed folded stub loaded dipole. A comparison between this proposed design and other related dipole antenna designs are also addressed in this Section. Finally, conclusions are drawn in Section 4.3.3 emphasizing the achievements of this research and future work directions.

4.3.1. Dual-Mode Dipole Antenna Design

The geometry of the proposed dual mode dipole antenna is depicted in Fig. 4.11. The antenna is printed on a low cost FR4 substrate (relative dielectric permittivity ε_r = 4.3, loss tangent tan δ = 0.025) with a height of 1.52 mm and has an overall size of 40 × 20 mm^2. Each arm of the dipole is printed on top and bottom layers separately as

shown in Fig. 4.11. Folded stubs are loaded in both the dipole arms for shifting the third order mode and merging with the first order mode to achieve a wide bandwidth. All the physical dimensions of this antenna (after optimization to be discussed later) are tabulated in Table 4.1.

The design of dual-mode dipole antenna can be demonstrated using reference designs as seen in Fig. 4.12. In order to illustrate the working principle of this design, initially the resonances of a conventional dipole are examined. The Ref 1 half-wavelength dipole has a length of 34 mm and operating at 2.9 GHz. Fig. 4.13 shows the input impedances of the Ref 1 design. The first and third odd order modes can be seen at 2.9 GHz and 8.45 GHz, respectively. Fig. 4.14 (a) shows the radiation pattern of the conventional dipole at first and third order modes.

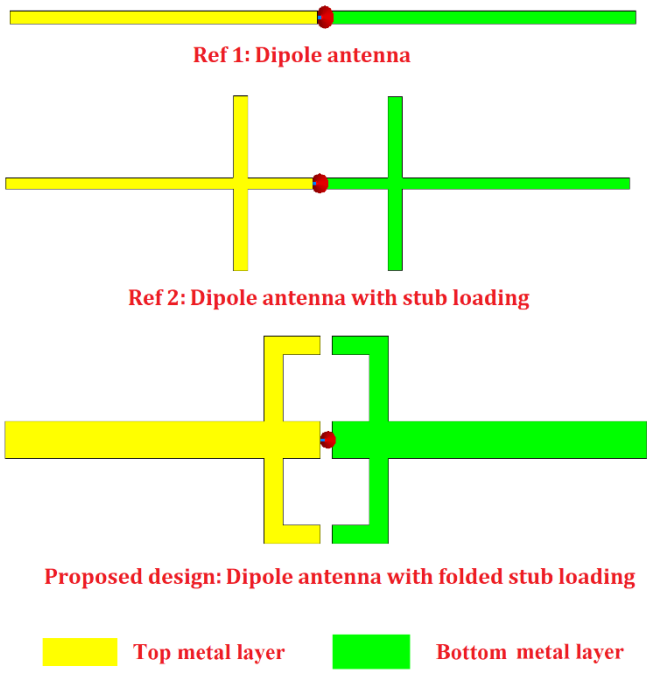

Fig. 4.12. Evolution of broadband dual mode dipole antenna.

Table 4.1. Parameters of the proposed antenna

Parameter	Value (mm)	Parameter	Value (mm)
L1	47.2	ls1	0.8
L2	17	ls2	0.5
W1	52	ws	1
S	43.3		

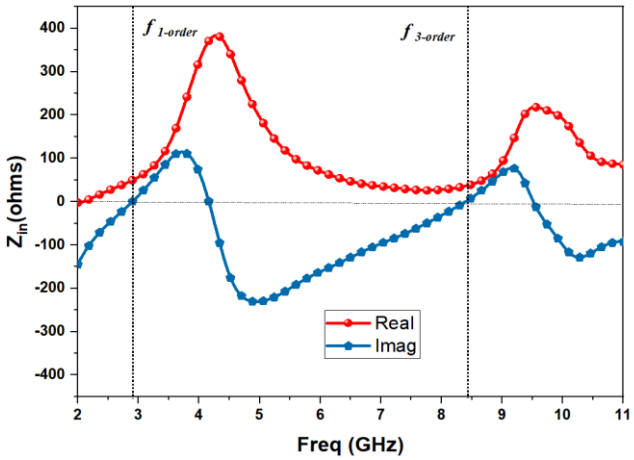

Fig. 4.13. Input impedance of Ref. 1 dipole antenna

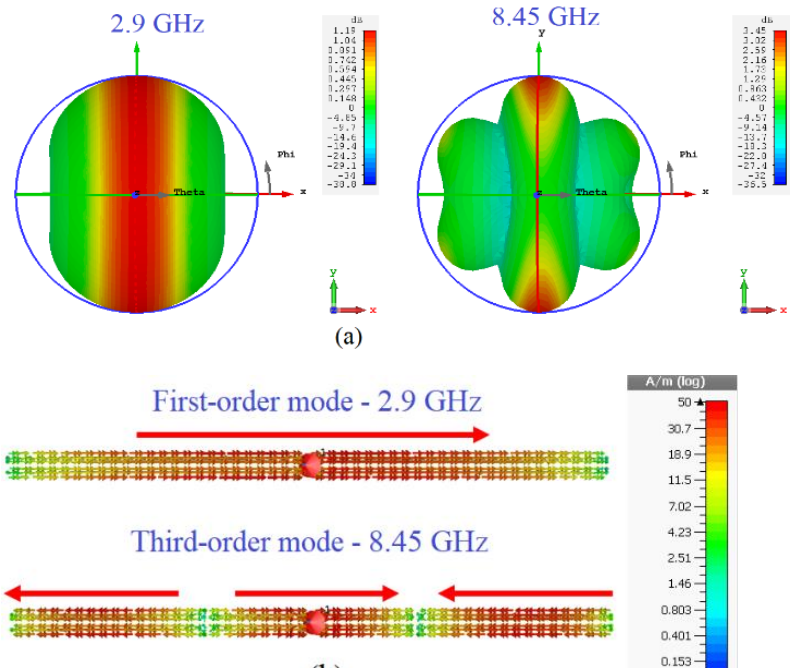

Fig. 4.14. (a) Simulated radiation pattern and (b) surface current distribution of Ref. 1 dipole antenna.

The presence of side lobes and unstable radiation patterns of third-order mode limits its applications. The difference in the radiation pattern of first and third-order modes is due to the difference in current distributions as shown in Fig. 4.14 (b). In order to achieve a wide bandwidth and stable omni directional radiation pattern, it is necessary to design some techniques to control the third order resonance. Thus, we have proposed a dipole antenna with stub loaded in both arms to control the third order resonance as in Ref 2 of Fig. 4.12. The main idea of this loading is to lengthen the third order mode of the dipole without affecting the first order mode and thereby can shift the third order resonance to a lower frequency. For analyzing the stub loaded dipole

antenna dimensions, the current distribution of the proposed stub loaded dipole antenna be depicted as in Fig. 4.15. The linear length of the Ref 1 can be represented as L i.e., nearly $0.5\lambda_1$ (λ_1 is the effective wavelength of dipole antenna). The electrical length of the new third order mode wavelength (λ_{3new}) is the sum of the length of the original third order mode (λ_3) and the length of the stubs. Thus,

$$\frac{3}{2}\lambda_3 + 4ls = \frac{3}{2}\lambda_{3new} \tag{4.2}$$

So, the length of the stub can be calculated as

$$4ls = \frac{3}{2}(\lambda_{3new} - \lambda_3) \tag{4.3}$$

$$ls = \frac{3}{8}(\lambda_{3new} - \lambda_3) \tag{4.4}$$

Similarly, the spacing S of the stub from the center of dipole can be estimated by equating the lengths of each section of third order mode.

$$(2ls + 2S) = \left(\frac{L}{2} - S + ls\right) = \frac{\lambda_{3new}}{2} \tag{4.5}$$

$$S = \frac{L}{2} + ls - \frac{\lambda_{3new}}{2} \tag{4.6}$$

To analyze the performance of stub loading in dipole antenna, Ref 2 is designed to shift the third order mode to 6 GHz. A sub length, ls of 4.25 mm and spacing S of 4.25 mm is estimated based on (4.4) and (4.6). Fig. 4.16 shows the input impedances of the Ref. 2 design. The third odd order mode is shifted from 8.45 GHz to 6 GHz, whereas

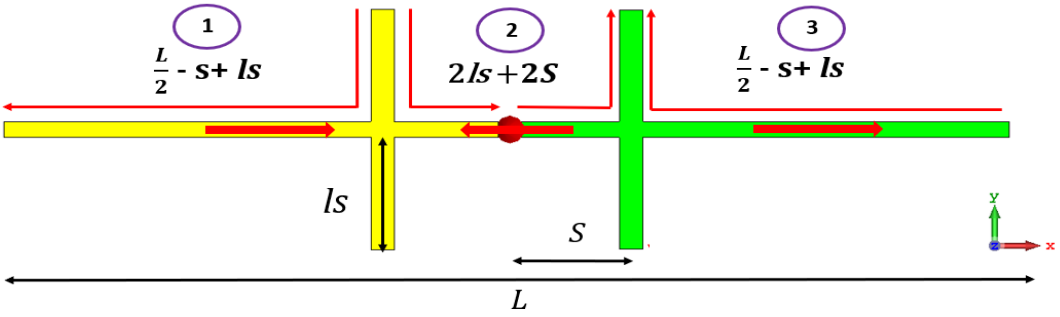

Fig. 4.15. Surface current distribution of Ref. 2 stub loaded dipole antenna.

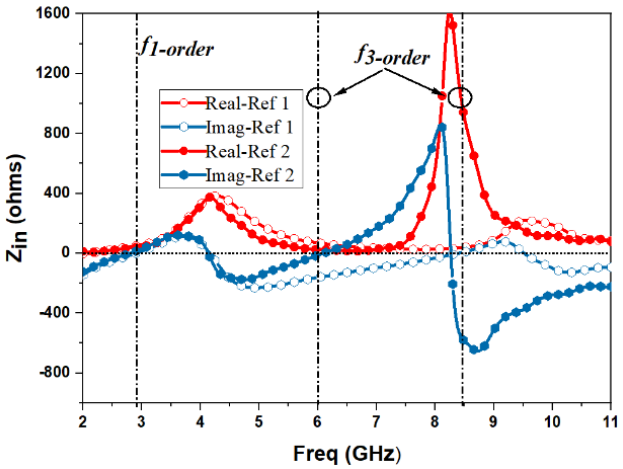

Fig. 4.16. Input impedance of Ref. 1 and Ref. 2 stub loaded dipole antennas.

the first order mode is still in 2.9 GHz. It can be observed that the input impedance increased in Ref 2 design as the third order resonance shifted to lower frequency (6 GHz). Fig. 4.17 (a) shows the radiation pattern of the Ref 2 design at first and third order modes. Grating lobes in the third-order mode is significantly reduced by shifting the resonance to 6 GHz by stub loading. Hence, the first and third order mode has

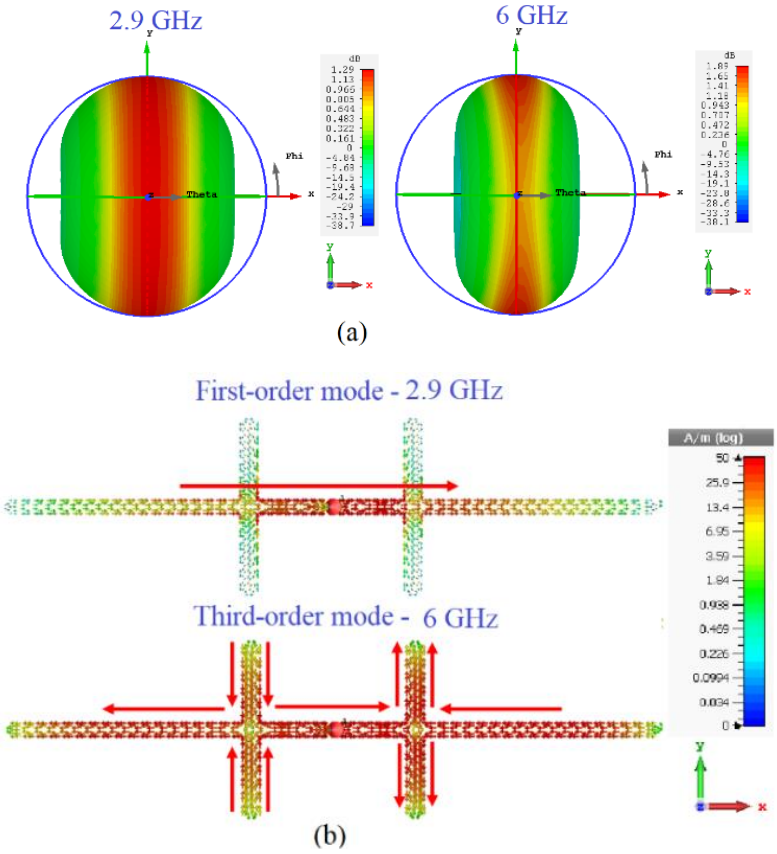

Fig. 4.17. (a) Simulated radiation pattern and (b) surface current distribution of Ref. 2 stub loaded dipole antenna.

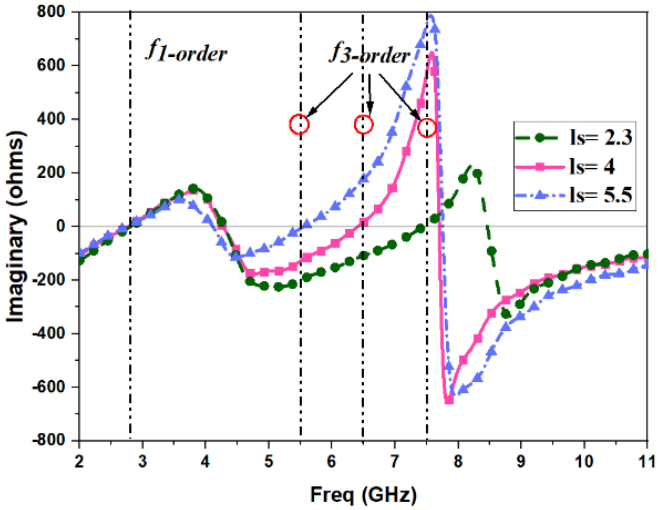

Fig. 4.18. Simulated input reactance of the Ref. 2 dipole for various ls

similar omnidirectional properties similar to dipole's half wave mode. To further reveal its principle, the current distributions of the two resonant modes of the proposed dipole antenna with stub loading are shown in Fig. 4.17. It can be clearly revealed that the dipole resonates at first-order mode and the current amplitude in the loaded stubs are negligibly small. Hence, the dipole is responsible for the radiation at 2.9 GHz. As the third-order mode in a dipole has a current distribution in which middle current direction is opposite to that on both sides. It can be seen from Fig. 4.17 (b) that the strong currents are present in the loaded stubs and it lengthened the current of the third order mode and hence, it can be concluded that the resonant frequency of third-order mode is decreased and shifted to 6 GHz. To provide a better understanding of the stub loaded antenna, a parametric study is conducted to investigate the resonance shift and dimensions of the stub. The effect of stub length and spacing from the center of the

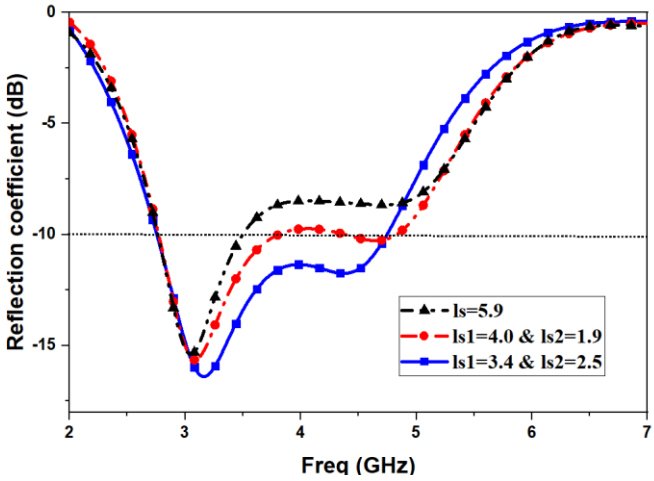

Fig. 4.19. Simulated reflection coefficients of the folded stub loaded dipole for various ls2

dipole as a function of input reactance is depicted in Fig. 4.18. It can be observed that as *ls* increases, the reactance null point of third-order mode decreases, while the first order mode remains unchanged. The spacing S from the dipole center decreased with increased stub length ls. The stub length ls and corresponding spacing S moved the third order resonance from 7.5 GHz to 5.5 GHz, as *ls* varied from 2.3 to 5.5 mm in Ref 2 design. For realizing the broadband antenna, it is necessary to shift the third order resonant frequency close to first order mode. A *ls* of 5.9 mm with a spacing *S* of 2 mm, is initially utilized as in Ref 2. But the impedance matching is not satisfactory at third order mode. Therefore, final proposed design utilized folded stub loading in order to improve the impedance matching through field coupling. Folded stub comprises of vertical and horizontal sections with lengths *ls1* and *ls2* as shown in Fig. 4.11. As the horizontal section length *ls2* increases, the resonant frequency of third order mode moves to 4.5 GHz and improves the impedance matching as shown in Fig. 4.19. Thus, a broadband antenna with a bandwidth of 1.8 GHz ranging from 2.95 GHz to 4.75 GHz (VSWR < 2) is realized by folded stub loading for shifting the third order mode close

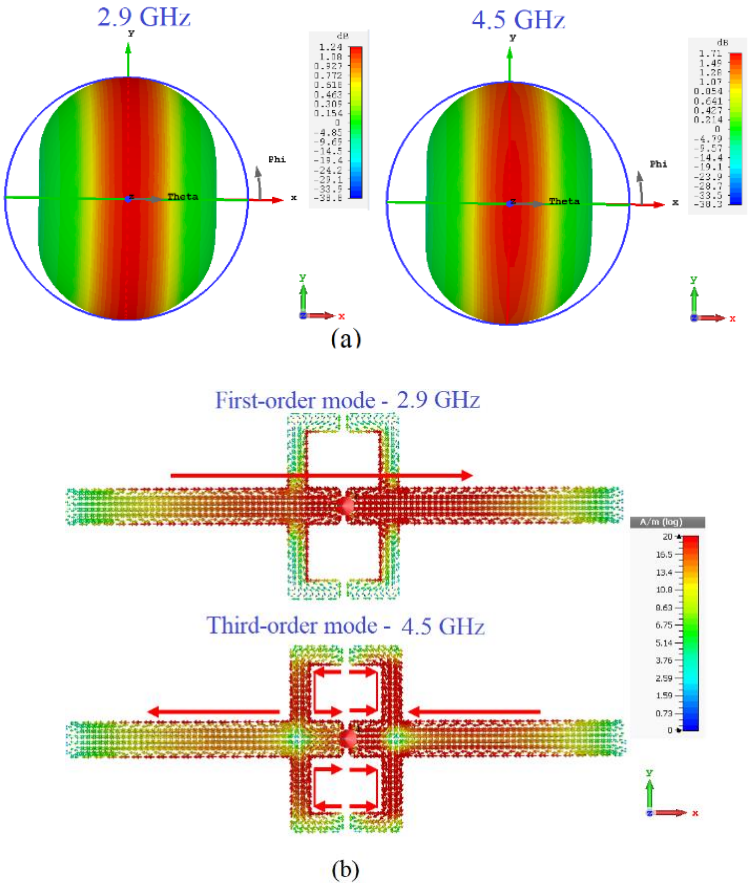

Fig. 4.20. (a) Simulated radiation pattern and (b) surface current distribution of the proposed folded stub loaded dipole antenna.

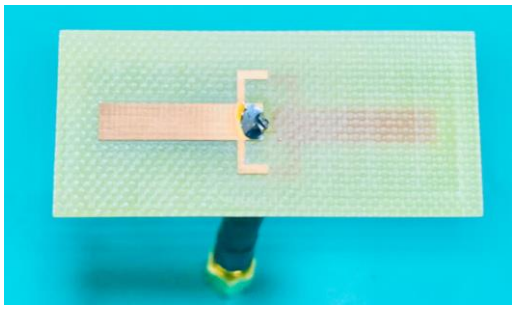

Fig. 4.21. Fabricated prototype of the fabricated broadband antenna.

to the first order mode. Fig. 4.20 (a) shows the radiation pattern of the proposed design at 2.95 GHz and 4.5 GHz. The first and third order modes of the proposed design has omnidirectional pattern similar to half wavelength dipole. The current distributions of the proposed antenna at two resonant frequencies, 2.9 and 4.5 GHz are shown in Fig. 4.20 (b). It can be seen that for the first resonance, the current is mainly distributed on the dipole i.e., half wavelength dipole in the first order mode. At 4.5 GHz, strong currents can be observed in folded stubs and the middle section of dipole has current in opposite direction that of both sides. Thus, it can be clearly revealed that the third order resonance is shifted from 8.45 GHz to 4.5 GHz.

4.3.2. Measurement Results and Validation

To verify the proposed design, a prototype of the proposed folded stub loaded dipole antenna was fabricated and measured. The prototype is shown in Fig. 4.21, which is fed by 50 Ω coaxial cable. As the proposed antenna is not having a balun in the design, an external ferrite choke balun is used in S11 measurement. However, the

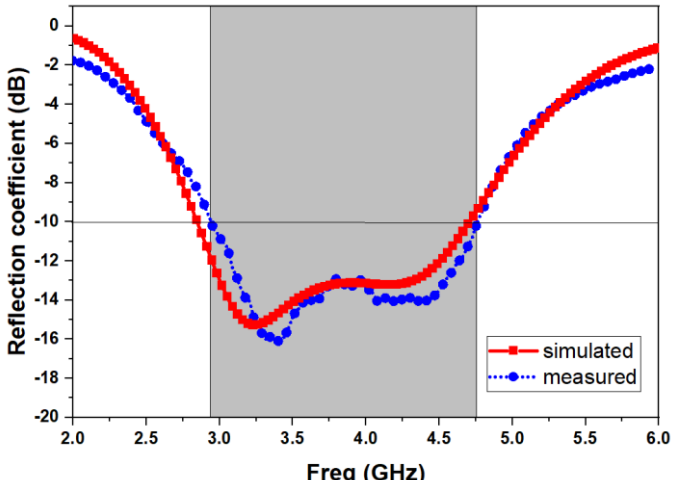

Fig. 4.22. Simulated and measured reflection coefficient of the proposed broadband antenna.

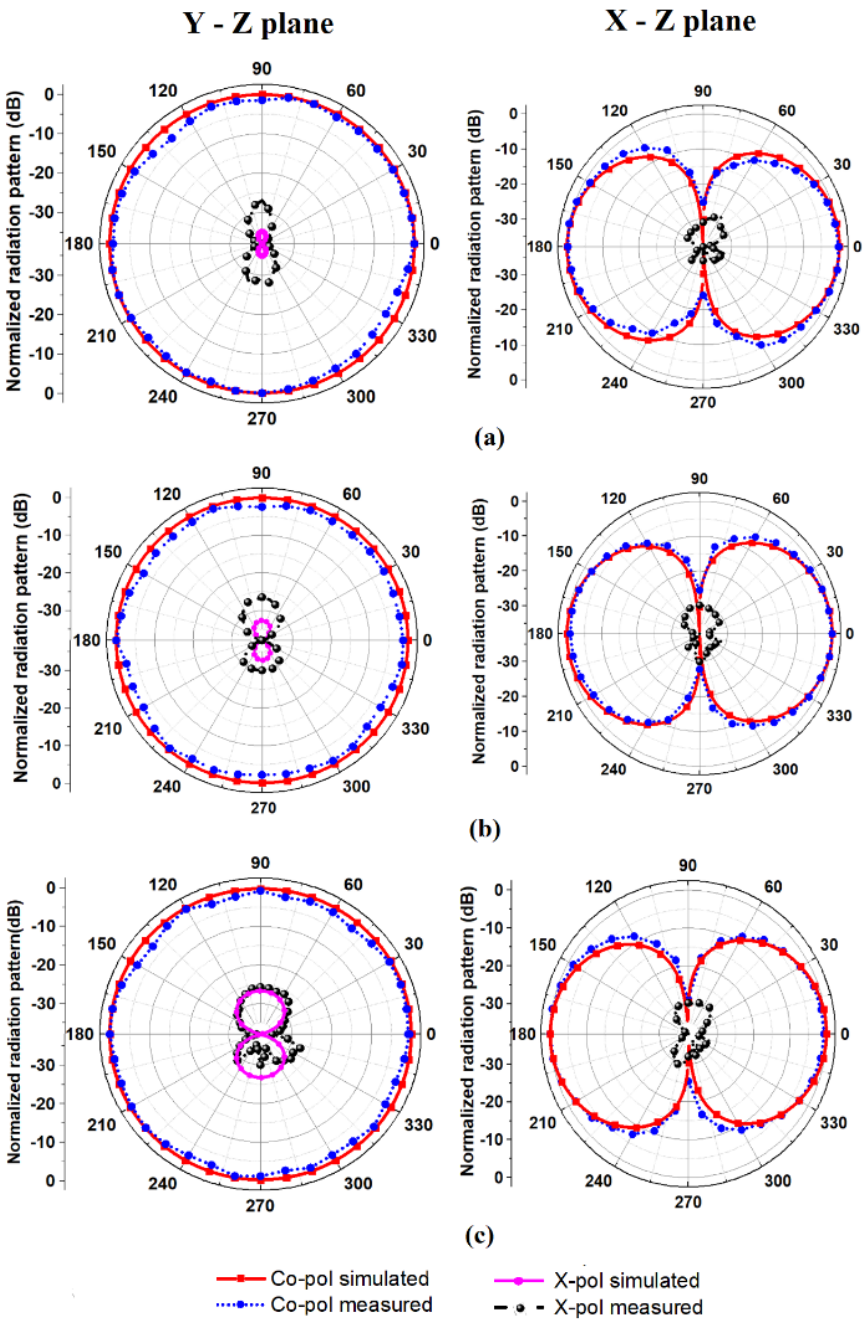

Fig. 4.23. Simulated and measured normalized radiation patterns of the proposed broadband antenna (a) 3.5 GHz (b) 4 GHz (c) 4.5 GHz.

proposed antenna achieved a similar performance with or without external balun. The reflection coefficient of the antenna is measured by using Anritsu 37369A VNA, while radiation patterns are obtained by performing a far field antenna measurement in an anechoic chamber. Fig. 4.22 shows the simulated and measured reflection coefficients. An impedance bandwidth of 1.8 GHz is achieved extending from 2.95 to 4.75 GHz (47%).

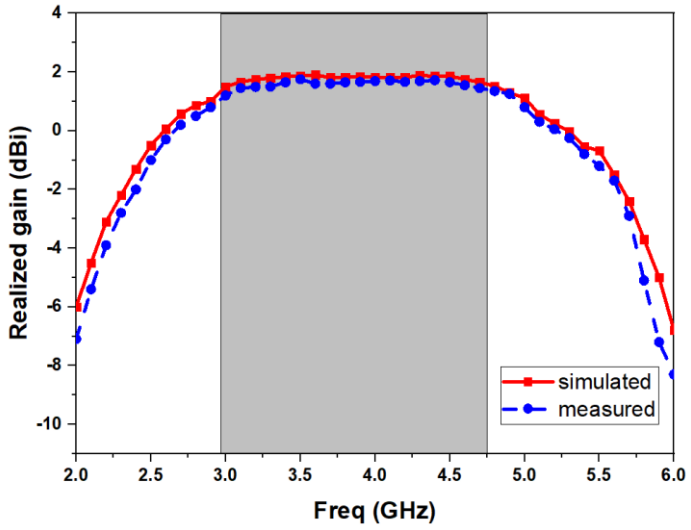

Fig. 4.24. Simulated and measured realized gain of the broadband antenna.

Fig. 4.23 shows the simulated and measured an 8-shaped radiation pattern in the XOZ-plane and omnidirectional pattern in the YOZ-plane in all 3 operating frequency bands. The simulated and measured patterns are in close agreement for both XOZ and YOZ planes. It can also be concluded that stable radiation patterns are achieved at both E-plane (XOZ-plane) and H-plane (YOZ-plane) across the entire operating frequency band. The realized gain of the fabricated prototype is shown in Fig. 4.24 as a function of operating frequency. Simulated and measured realized gain of the fabricated antenna is in close agreement. Gain of the antenna is relatively stable throughout the bandwidth and its value ranges between 1.5 to 2 dBi.

Table 4.2. Comparison among the proposed antennas with other dual-mode dipoles

Year-Ref.	**Description**	**Bandwidth (%)**	**Size ($\lambda_0 x \lambda_0$)**	**Radiation pattern**	**Gain**
2015- [33]	Slot line antenna with stub loading	31.5	1.32 × 1.32	Not stable	Varying gain
2017- [26]	Two resonators (Dipole + parasitic loop)	44.2	0.63 × 0.32	Nearly omnidirectional	Varying gain
2019- [30]	Dipole higher order with stub loading	11.2	1.04 × 0.83	Not stable	Constant gain
2020- [31]	Dipole with loop resonator	27.8	0.45 × 0.17	Nearly omnidirectional	Constant gain
Proposed design	**Dipole with folded stub loading**	**47**	**0.45 × 0.15**	**Stable omnidirectional**	**Constant gain**

Table 4.2 shows a comparison between our dipole antenna and related designs. Dual-mode dipole antennas with mode compression techniques are only considered for a fair comparison. Compared to previous designs, our design has a larger bandwidth with a smaller size. Moreover, the proposed design has stable omnidirectional radiation pattern and constant gain throughout the operating band. Thus, it is suitable for many 5G technologies.

4.4. Dual-Band Antenna for WEH

In this Section, based on the discussed dual mode dipole design, a dual-band antenna is proposed to cover 0.915 GHz and 2.45 GHz for wireless energy harvesting. In Section 4.4.1, the design of dual-band antenna is explained. The measured performance of the antenna is studied in detail in Section 4.4.2. Radiation pattern of the fabricated antenna is also discussed in this Section.

4.4.1. Design of Dual-Band Antenna

In order to cover the 0.915 GHz and 2.45 GHz ISM bands, initially a dipole antenna resonating at 0.915 GHz is designed. The half wavelength dipole at 0.915 GHz has an overall length of 120 mm and the third order mode can be observed at 2.95 GHz as shown in Fig. 4.25. The simulated radiation patterns of the dipole antenna at fundamental and harmonic modes are depicted in Fig. 4.26. It can be observed that the third order mode has high side lobes.

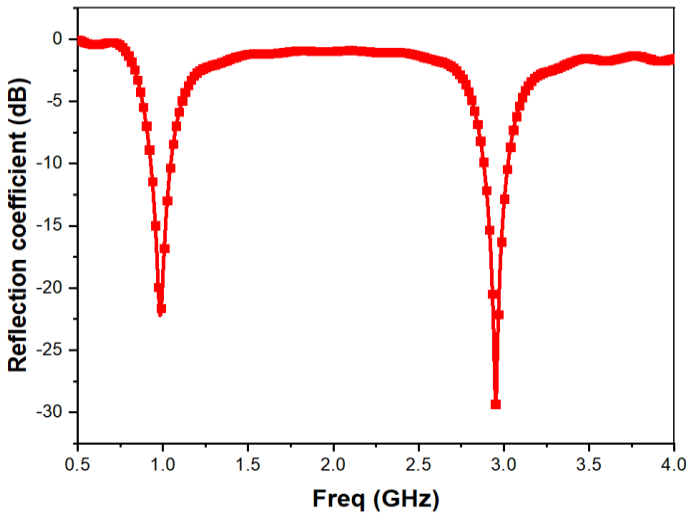

Fig. 4.25. Reflection coefficient of dipole antenna

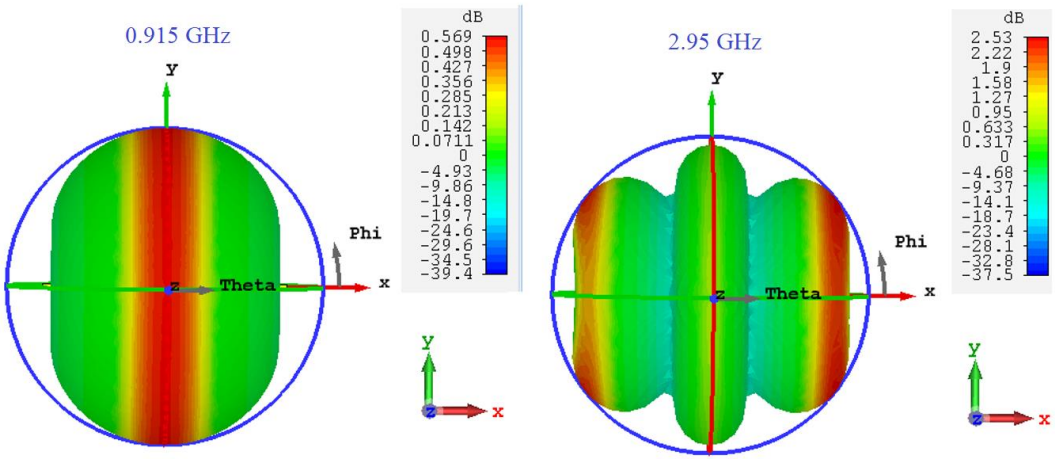

Fig. 4.26. Radiation pattern of dipole antenna at 0.915 and 2.95 GHz

For covering the 2.45 GHz ISM band, the proposed dual mode technique discussed in Section 4.3 is utilised. Folded stub resonators are introduced in the dipole design for shifting the third order mode. Based on the derived equations in (4.4) and (4.6), the length of the stub *ls* and position *S* are calculated as 12.5 mm and 21 mm, respectively. For easy prototype fabrication, the proposed dual-band dipole antenna arms are printed on both sides of FR4 substrate as shown in Fig. 4.27. Thus, the electrical length of the third order mode of the dipole is increased without disturbing the first order mode. The reflection coefficient of the proposed duad band dipole antenna with folded stubs is depicted in Fig. 4.28. It can be observed that the reflection coefficient of the fundamental is at 0.915 GHz for both conventional dipole and dipole antenna with folded stubs. However, as expected the third order mode is shifted from 2.95 GHz to 2.45 GHz by introducing the folded stubs with folded stubs. The radiation pattern of the first order and third order mode in the proposed dual-band antenna is shown in Fig.

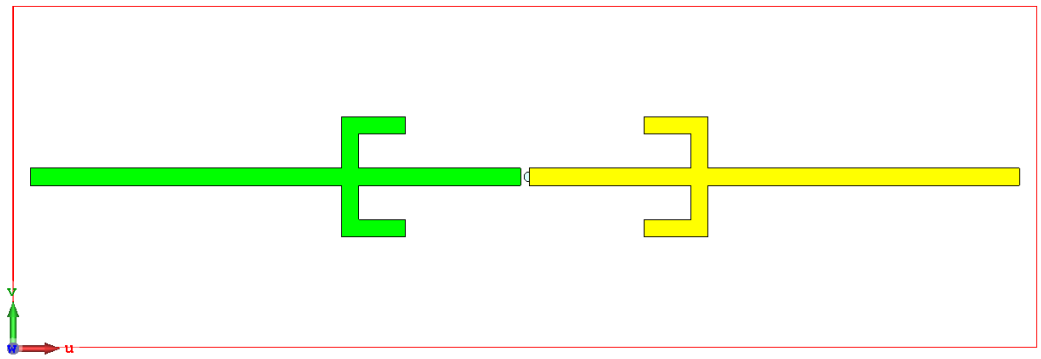

Fig. 4.27. Proposed dual-band dipole antenna

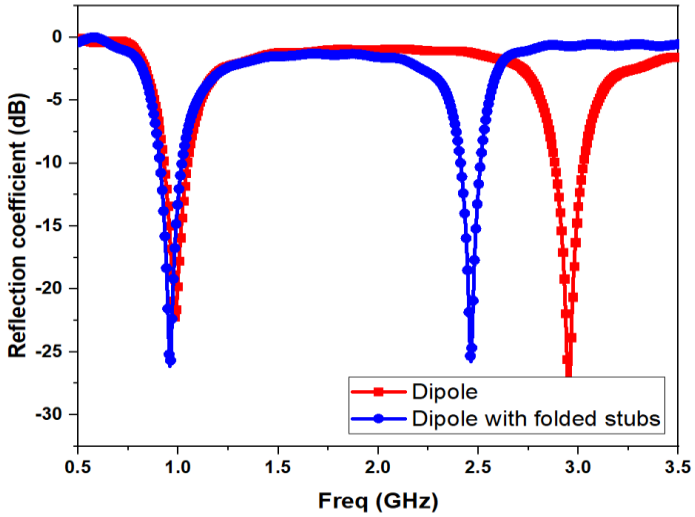

Fig. 4.28. Reflection coefficient of the proposed dual-band antenna

4.29 (a). Side lobes in the third order mode is significantly reduced by shifting the resonance to 6 GHz by stub loading. Hence, the first and third order mode has similar omnidirectional properties similar to dipole's half wave mode.

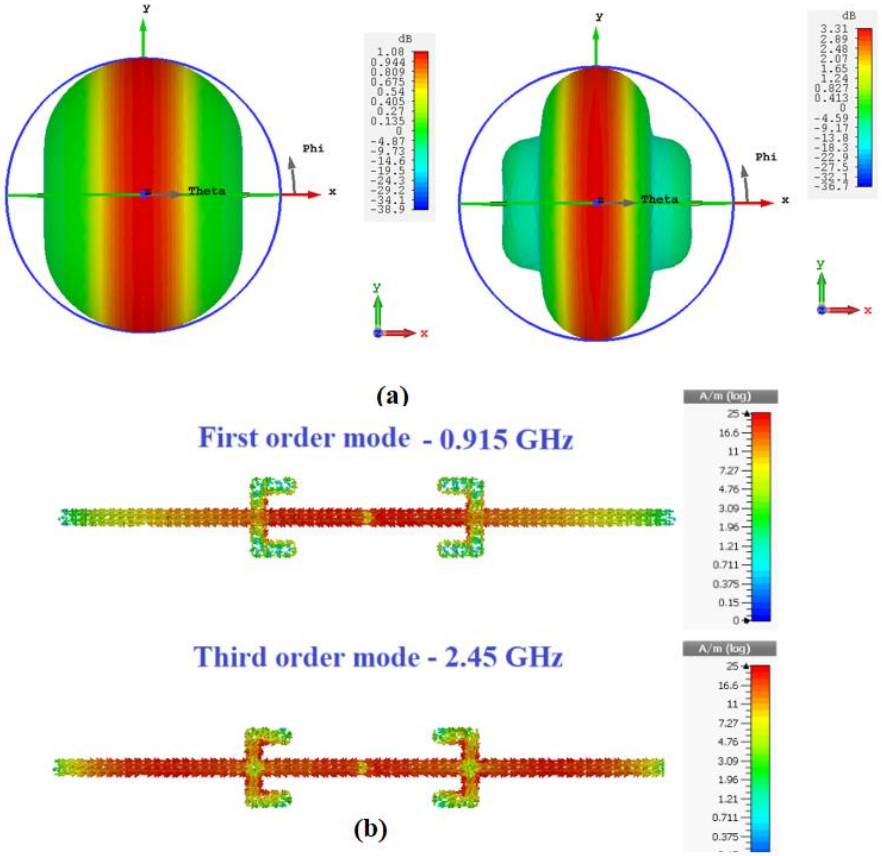

Fig. 4.29. (a) Simulated radiation pattern and (b) surface current distribution of the proposed folded stub loaded dipole antenna.

To further reveal its principle, the current distributions of the two resonant modes of the proposed dipole antenna with stub loading are shown in Fig. 4.29 (b). It can be clearly revealed that the dipole resonates initially at the first-order mode and the current amplitude in the loaded stubs are negligibly small. Hence, the dipole only is responsible for the radiation at 0.915 GHz. As the third-order mode in a dipole has a current distribution in which middle current direction is opposite to that on both sides. It can be seen from Fig. 4.29 (b) that the strong currents present in the loaded stubs and it lengthened the current of the third order mode and hence, it can be concluded that the resonant frequency of third-order mode is decreased and shifted to 2.45 GHz.

4.4.2. Dual-Band Dipole Antenna Evaluation

To verify the proposed dual-band folded stub loaded dipole antenna design, a prototype was fabricated and measured. The prototype is shown in Fig. 4.30, which is fed by 50 Ω coaxial cable. The reflection coefficient of the antenna is measured by using Anritsu 37369A VNA, while radiation patterns are obtained by performing a far field antenna measurement in an anechoic chamber. The measured reflection coefficient of the dual-band dipole antenna can be seen in Fig. 4.31. It can be seen that the simulated and measured data are in close agreement. The lower band has an impedance bandwidth of 171 MHz ranging from 0.844 to 1.015 GHz. In the upper band, a bandwidth of 105 MHz is achieved extending from 2.37 to 2.475 GHz. The measured radiation pattern of the antenna is shown in Fig. 4.32. An omnidirectional pattern in the YOZ-plane and almost near 8-shaped radiation pattern in the XOZ-plane in both frequency bands. The simulated and measured patterns are in close agreement for both XOZ and YOZ planes. The prototype measured a realized gain of 1 and 3 dB are achieved at 0.915 and 2.45 GHz, respectively.

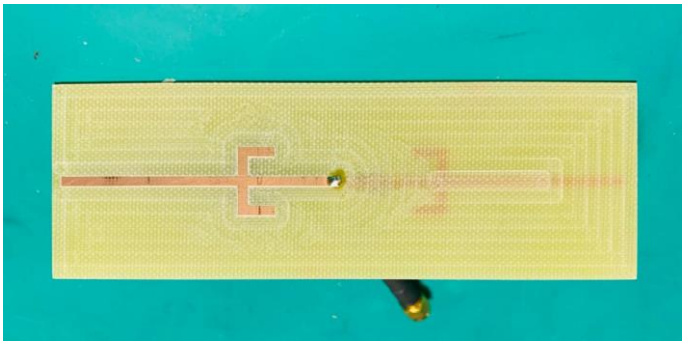

Fig. 4.30. Fabricated prototype of dual-band antenna

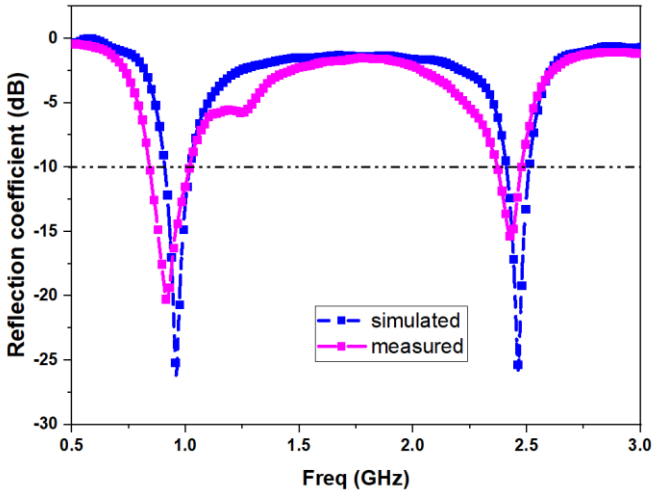

Fig. 4.31. Reflection coefficient of the dual-band antenna

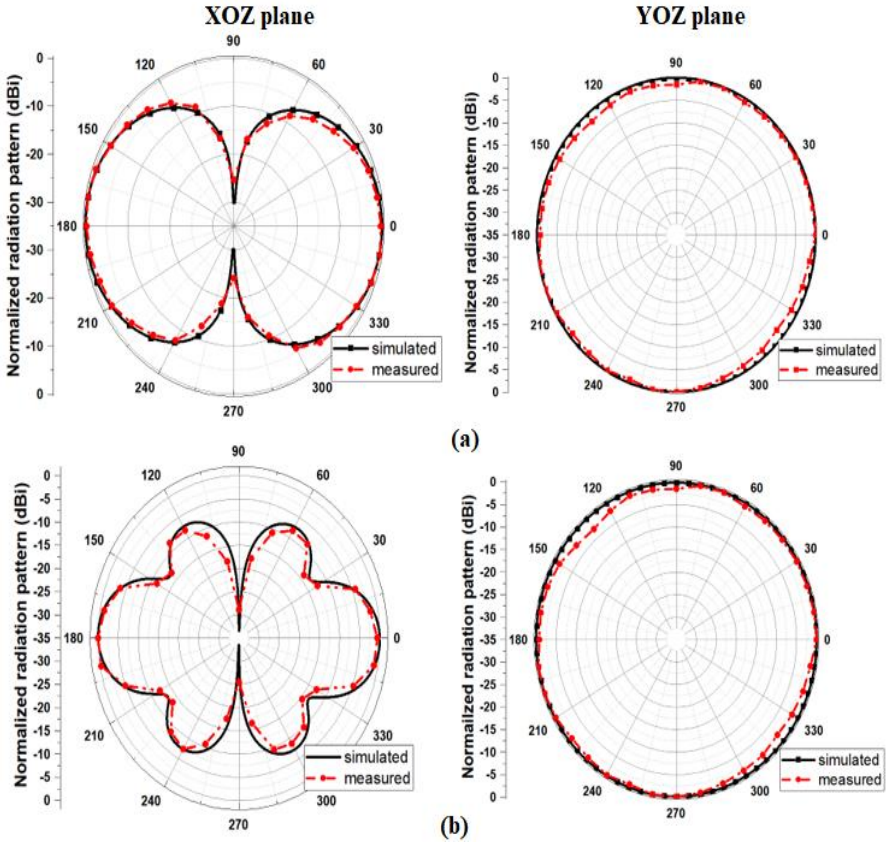

Fig. 4.32. Radiation pattern of the dual-band antenna (a) 0.915 GHz (b)2.45 GHz

4.5. Rectenna Evaluation

The rectifying circuit and the receiving antenna are connected together to form the highly sensitive rectenna as shown in Fig.4.33.

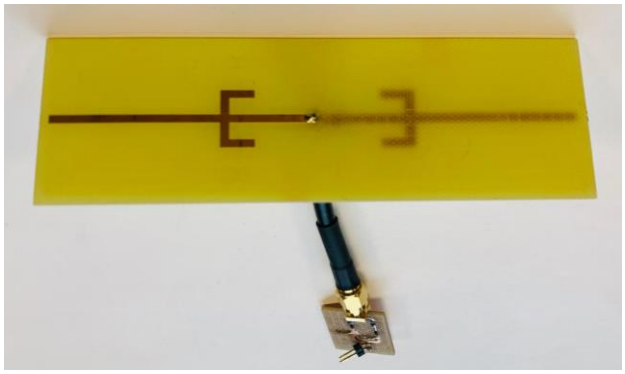

Fig. 4.33. Fabricated highly sensitive rectenna

The designed rectenna has been measured in an anechoic chamber which is illustrated in Fig.4.34. During the experiment, an RF power source is connected to a standard horn antenna, which acts as the transmitter. The RF energy from power source at LTE band is carried by a continuous wave. The designed rectenna is aligned and placed at a distance of 2 m away from the transmitter, which is the far-field distance determined by

$$R = \frac{2D^2}{\lambda} \tag{4.9}$$

where R is the far-field distance, λ is the wavelength of the operating frequency, and d is the largest dimension of the antenna. The RF to DC conversion efficiency is the most critical parameter to evaluate the performance of the proposed rectenna, which is estimated by

$$\eta = \frac{V_{DC}^2}{R_L P_r} \tag{4.10}$$

$$P_r = \left(\frac{\lambda}{4\pi R}\right)^2 G_r G_t P_t \tag{4.11}$$

and where η is the RF to DC conversion efficiency, V_{DC} is the measured output voltage of the load, R_L is the load resistance, and P_r is the received power of rectenna, G_r and

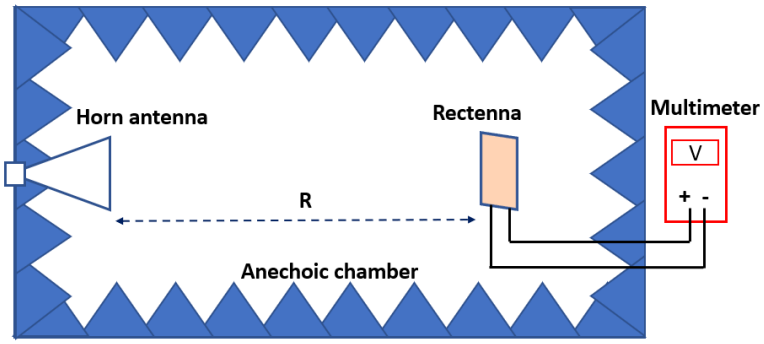

Fig. 4.34. Measurement setup for rectenna evaluation

G_t are the realized gain of the designed antenna and the transmitter, and P_t is the transmitting power of the horn antenna. Fig.4.35 shows the measured conversion efficiency and output voltage as a function of received power at different frequencies in the operating band. It is noted that the maximum efficiency of 67% is obtained at 0.915 GHz and 55% at 2.45 GHz at an input power of -7 dBm. A maximum output voltage of 0.88 V is measured at 0.915 GHz and 0.82 V at 2.45 GHz. It can be clearly observed that at typical low power of -15 dBm, the designed rectenna has high conversion efficiency of 52 % and 40 % respectively at 0.915 and 2.45 GHz, which is quite high sensitivity compared to literatures [4], [7].

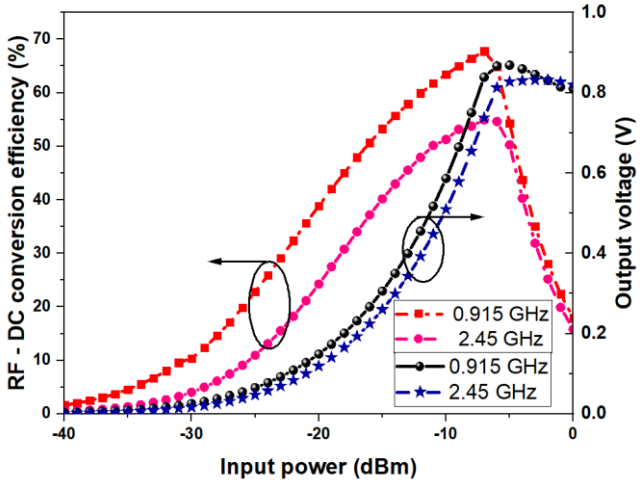

Fig. 4.35. Measured RF to DC conversion efficiency and output voltage of the rectenna

4.6. Summary

A novel dual-band rectenna has been proposed in this Chapter for very low input power conditions. This design utilised a dipole antenna with folded stubs and a high sensitivity rectifier. The dual-mode dipole antenna with folded stubs has achieved a stable omnidirectional radiation pattern over the entire operating band from 2.95 to 4.75 GHz. A dual-band antenna has been demonstrated to cover the 0.915 GHz and 2.45 GHz based on the proposed dual-mode technique. A single external inductor-based dual-band highly sensitive rectifier for very low power ambient energy harvesting has also proposed. Conversion efficiencies of more than 52% and 40% have been obtained in the lower and upper bands at -15 dBm input power. It was also shown that the rectenna prototype can provide high DC power in very low input power conditions.

References

[1] K. Kotani and T. Ito, "High efficiency CMOS rectifier circuit with self-Vth-cancellation and power regulation functions for UHF RFIDs," *Proc. ASSCC*, Nov. 2007.

[2] M. Stoopman, S. Keyrouz, H. j. Visser, K. Philips, and W. A. Serdijn, "Codesign of a rectifier and small loop antenna for highly sensitive energy haresters," *IEEE J. Solid State Circuits*, vol. 49, no. 3, pp. 622-634, Mar. 2014.

[3] R. Ishikawa, T. Yoshida, and K. Honjo, "A 2.4 GHz-band enhancement mode GaAs HEMT rectifier with 19% RF-to-DC efficiency for 1mW input power," *Proc. EUMW*, Paris, Oct. 2019.

[4] C. Song, Y. Huang, J. Zhou, Z. Sheng, and P. Carter, "A high efficiency broadband rectenna for ambient wireless energy harvesting," *IEEE Tans. Antennas Propag.*, vol. 63, no.8, pp.3486-3495, Aug. 2015.

[5] H. Sun, Y.-x. Guo, M. He and Z. Zhong, "A dual-band rectenna using broadband Yagi antenna array for ambient RF power harvesting," *IEEE Antennas and Wireless Propa. Lett.*, vol. 12, pp. 918–921, 2013.

[6] V. Kuhn, C. Lahuec, F. Seguin, and C. Person, "A multi-band stacked RF energy harvester with RF-to-DC efficiency up to 84%," *IEEE Trans. Microw. Theory Techn.,* vol. 63, no. 5, pp.1768–1778, May 2015.

[7] C K. Niotaki, A. Georgiadis, A. Collado, and J. S. Vardakas, "Dual-band resistance compression networks for improved rectifier performance," *IEEE Trans. Microw. Theory Techn.*, vol. 62, no. 12, pp. 3512 -3521, Dec. 2014.

[8] S.E. Adami, P. Proynov, G. S. Hilton, G.Yang, C. Zhang, D. Zhu, Y. Li, S. P. Beeby, I. J. Craddock, and B. H. Stark, "A flexible 2.45-GHz power harvesting wristband with net system output from -24.3 dBm of RF power," *IEEE Trans. Microw. Theory Techn*., vol. 66, no. 1, pp. 380–395, Jan. 2018.

[9] C. Song et al., "Matching network elimination in broadband rectennas for high-efficiency wireless power transfer and energy harvesting," *IEEE Trans. Ind. Electron.*, vol. 64, no. 5, pp. 3950–3961, 2017.

[10] *Surface Mount Mixer and Detector Schottky Diodes, Data Sheet*. Skyworks Solutions, Inc., Woburn, MA, USA, 2013.

[11] S. Kumar, A. S. Dixit, R. R. Malekar, H. D. Raut, and L. K. Shevada, "Fifth generation antennas: A comprehensive review of design and performance

enhancement techniques," *IEEE Access*., vol. 8, pp. 163568 - 163593, Sep. 2020.

[12] J. Dyson, "The characteristics and design of the conical log spiral antenna," *IEEE Trans. Antennas Propag*., vol. AP-13, no. 4, pp. 488–499, Apr. 1965.

[13] R. DuHamel and F. Ore, "Logarithmically periodic antenna designs," *Proc. IRE Int. Conv. Rec*., vol. 6. 1958, pp. 139–151.

[14] S. Choudhury, A. Mohan, and D. Guha, "A new printed log periodic antenna using SIW concept," *Proc. IEEE Indian Conf. Antennas Propag. (InCAP),* Hyderabad, India, Dec. 2018, pp. 1–3.

[15] J. Mruk, Z. Hongyu, M. Uhm, Y. Saito, and D. Filipovic, "Wideband mm-wave log-periodic antennas," *Proc. 3rd Eur. Conf. Antennas Propag*., Berlin, Germany, 2009, pp. 2584–2587.

[16] S. C. Gao, L. W. Li, M. S. Leong and T. S. Yeo, "Dual-polarized slot-coupled planar antenna with wide bandwidth", *IEEE Trans. Antennas Propag*., vol. 51, no. 3, pp. 441-448, Mar. 2003.

[17] K. F. Lee, K. M. Luk, K. F. Tong, S. M. Shum, T. Huynh, and R. Q. Lee, "Experimental and simulation studies of the coaxially fed U-slot rectangular patch antenna," *IEE Proc.-Microw., Antennas Propag.*, vol. 144, no. 5, pp. 354–358, Oct. 1997.

[18] C. L. Mak, K. M. Luk, K. F. Lee, and Y. L. Chow, "Experimental study of a microstrip patch antenna with an L-shaped probe," *IEEE Trans. Antennas Propag.*, vol. 48, no. 5, pp. 777–783, May 2000.

[19] S. Moghaddam, J. Yang, A. A. Glazunov, and A. U. Zaman, "A planar single-polarized ultra-wideband antenna element for millimeter-wave phased array," *Proc. Int. Symp. Antennas Propag. (ISAP)*, Busan, South Korea, 2018, pp. 1–2.

[20] A. A. Omar and Z. Shen, "Compact and wideband dipole antennas," *Proc. IEEE-APS Topical Conf. Antennas Propag. Wireless Commun. (APWC),* Granada, Spain, Sep. 2019, pp. 1–3.

[21] W. D. Ake, M. Pour, and A. Mehrabani, "Asymmetric half-bowtie antennas with tilted beam patterns," *IEEE Trans. Antennas Propag*., vol. 67, no. 2, pp. 738–744, Feb. 2019.

[22] G. Vandenbosch, "Reactive energies, impedance, and Q factor of radiating structures," *IEEE Trans. Antennas Propag*., vol. 58, no. 4, pp. 1112–1127, Apr. 2010.

[23] K. E. Kedze, H. Wang, and I. Park, "Compact broadband omnidirectional radiation pattern printed dipole antenna incorporated with split-ring resonators," *IEEE Access*, vol. 6, pp. 49537–49545, 2018.

[24] R. Wu and Q. X. Chu, "Resonator-loaded broadband antenna for LTE700/GSM850/GSM900 base stations," *IEEE Antennas Wireless Propag. Lett*., vol. 16, pp. 501–504, 2017.

[25] H.-T. Hsu and T.-J. Huang, "Generic dipole-based antenna-featuring dual-band and wideband modes of operation," *IET Microw., Antennas Propag*., vol. 6, no. 15, pp. 1623–1628, Dec. 2012.

[26] D. Wen, Y. Hao, H. Wang, and H. Zhou, "Design of a wideband antenna with stable omnidirectional radiation pattern using the theory of characteristic modes," *IEEE Trans. Antennas Propag*., vol. 65, no. 5, pp. 2671–2676, May 2017.

[27] K. M. Luk and H. Wong, "A new wideband unidirectional antenna element," *Int. J. Microw. Opt. Technol*., vol. 1, no. 1, pp. 2098–2101, Jul. 2006.

[28] K. Wei, Z. Zhang, Z. Feng, and M. F. Iskander, "A wideband MNG-TL dipole antenna with stable radiation patterns," *IEEE Trans. Antennas Propag*., vol. 61, no. 5, pp. 2418–2424, May 2013.

[29] Q. X. Chu and Y. Luo, "A broadband unidirectional multi-dipole antenna with very stable beamwidth," *IEEE Trans. Antennas Propag*., vol. 61, no. 5, pp. 2847–2852, May 2013.

[30] Y. Luo, Z. Chen, and K. Ma, "Enhanced bandwidth and directivity of a dual-mode compressed high-order mode stub-loaded dipole using characteristic mode analysis," *IEEE Trans. Antennas Propag*., vol. 67, no. 3, pp. 1922–1925, 2019.

[31] W. Zhang, Y. Li, Z. Zhou, and Z. Zhang, "Dual-mode compression of dipole antenna by loading electrically small loop resonator," *IEEE Trans. Antennas Propag*., vol. 68, no. 4, pp. 3243–3247, Apr 2020.

[32] W. J. Lu, L. Zhu, K. W. Tam, and H. B. Zhu, "Wideband dipole antenna using multi-mode resonance concept," *Int. J. Microw. Wireless Technol*., vol. 9, no. 2, pp. 365–371, Mar. 2017.

[33] W.-J. Lu and L. Zhu, "A novel wideband slotline antenna with dual resonances: Principle and design approach," *IEEE Antennas Wireless Propag. Lett*., vol. 14, pp. 795–798, 2015.

Chapter 5. High-Efficiency Compact RF Harvester

In this chapter, a novel RF energy harvester using combined harvesting topology for ambient WEH is presented. Five antenna elements are utilised in the harvester to capture RF energy from 900-960 MHz, 1.8-2.7 GHz, and 3.4-3.7 GHz frequency bands. The proposed RF energy harvester employed high sensitivity and high efficiency rectifiers for improving the performance. The RF output from dual-band or multiband antennas are fed to different RF branches and DC output from each RF branch is connected in parallel to increase the DC current. Finally, DC output from each rectenna is combined serially to produce maximum output DC voltage. The measured results show that the maximum harvested DC power of the rectenna indoor environments is 27.5 μW; it can therefore be applied to a range of low-power in wireless applications. Typical DC output power obtained from RF harvesters in the similar indoor conditions in literature is less than 20 μW [21], [22].

5.1. Introduction

To enable self-sustainability in IoT sensors, high amount of DC power in the range of micro to milliwatts is required [1]-[3]. Several single band rectennas have achieved high RF-DC conversion efficiencies of more than 80%; mostly at high input power levels (0 dBm [4], 5 dBm [5], 10 dBm [6]), 15 dBm [7], 18 dBm [8], and 20 dBm [9]). Typical, ambient RF energy available is in the range of -30 to -15 dBm., broadband rectennas operating at low input power levels suffers from low RF-DC conversion efficiency [10]-[16]. Most of these works utilized a single-port antenna and therefore, the spatial domain has not been efficiently exploited to maximize the harvested RF energy. Furthermore, in most instances the output of single port antenna fed to a multiband or broadband rectifier with cascaded matching network. The perfect matching on multiple frequencies necessitates high-order RF bandpass filters with

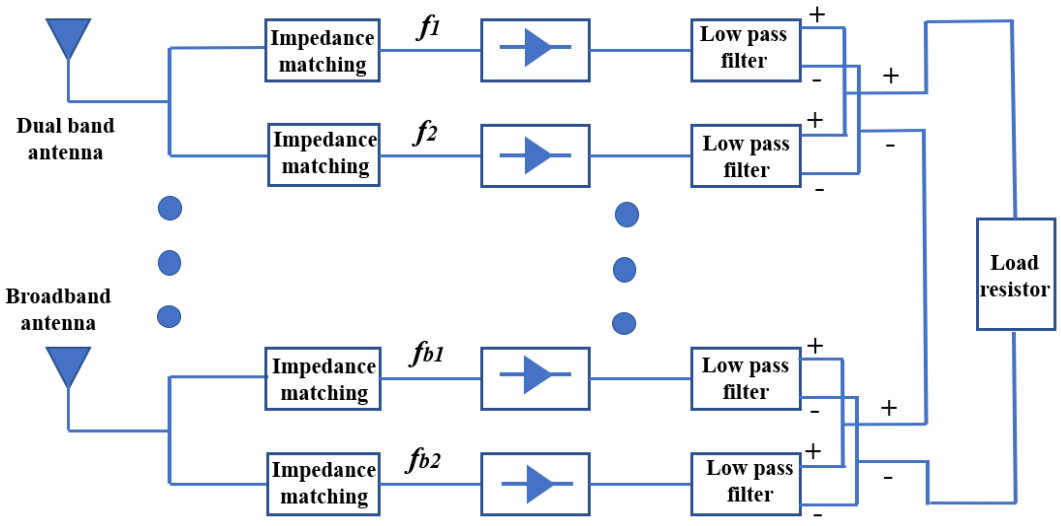

Fig. 5.1. Proposed hybrid combining RF harvester

large complexity. The performance of such harvesters is significantly degraded if the operating frequencies are slightly shifted from the optimal resonance frequency. Additionally, increasing the number of adaptive frequency bands significantly decreases the RF to DC efficiency. Thus, it is necessary to reduce the losses due to the filter components to achieve highly efficient RF harvester.

Several attempts have been made by researchers to develop rectenna arrays to accumulate ambient RF energy. But most designs were designed for a single operating frequency band although the overall dimension of arrays are large [17]. Rectenna arrays require the essential spacing gap between the array elements. e.g., half-wavelength, so that mutual coupling is small enough to be ignored and total RF power received by all the antenna elements is increased. For instance, RF energy harvesting rectenna arrays at Wi-Fi band are presented in [18] and [19]. In recent times, some attempts have been made to develop omnidirectional and multi-beam rectenna arrays in order to capture more energy from the randomly propagated wireless signals in multi-path ambient environments. However, these designs still have a limited frequency band coverage, and often of relatively high-profiles due to the spatial arrangements of the array. Different rectenna array architectures have been analysed in literature that aim to enhance the output DC power. Array rectennas typically use either RF combination of the antenna outputs or DC combination of multiple rectifier outputs. In RF combined array, as the RF power from multiple antennas combined and fed to a single rectifier, the RF to DC conversion efficiency reduces due to the losses

in the higher order filter. However, in the DC combined rectenna array, the received RF signal of each antenna element rectified prior to combining it at the DC output and it has a large complex structure. Therefore, in order to have a high sensitivity and high efficiency compact RF harvester, a novel topology of RF harvester is proposed as shown in Fig. 5.1. Instead of using an array of broadband antenna based rectenna array, in this combined harvesting topology several dual-band and broadband antennas are utilized to harvest RF energy from multiple bands from arbitrary polarizations and directions. RF output from dual-band or multiband antennas are fed to different RF branches (association of the RF bandpass filter, rectifying elements, and low-pass filter). DC output from each RF branch is connected in parallel to increase the DC current. Finally, DC output from each rectenna is combined serially to produce a maximum output DC voltage.

5.2. Antenna Design

For RF energy harvester design, antennas with high gain are not always preferred. High gain antennas are suitable if the position of transmitter and receiver antennas are known i.e., in wireless power transfer applications. Low gain antennas are preferred if the positions of source and receiving antenna are relatively uncertain in order to collect signals from various directions simultaneously. This is the case for ambient RF energy harvesting. Moreover, it is necessary to employ an antenna system with omnidirectional property and polarization insensitivity, to collect the ambient energy from incoming waves with arbitrary polarization and incident angles. As already

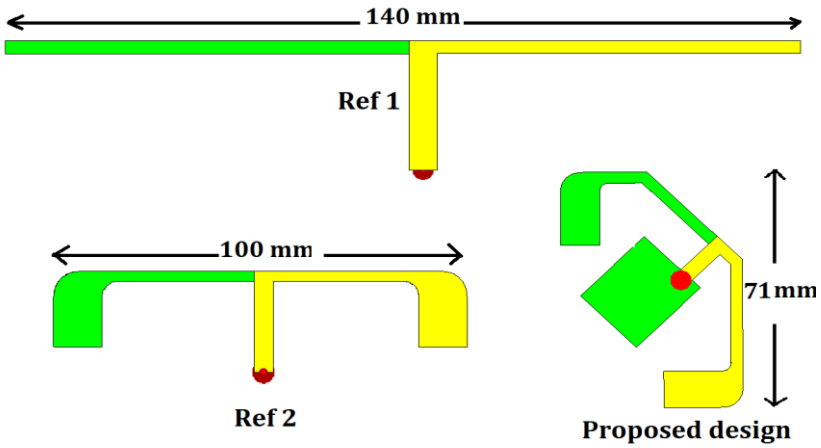

Fig. 5.2. Proposed dual-band antenna evolution

discussed, a single broadband antenna for covering all the required bands is not appropriate for extracting maximum possible output DC power. Therefore, multiple antennas with dual-band and broadband properties are combined in a small footprint for maximum efficiency with good isolation. Dual-band dipoles are utilized to cover the 900-960 MHz and 3.4-3.7 GHz. The proposed dual-band antenna is evolved from two reference antennas as shown in Fig. 5.2. A dipole antenna with a length of 140 mm resonating at 0.915 GHz is used as the initial design (Ref 1). Ref 1 antenna has the third resonance at 2.9 GHz. In order to reduce the overall length and to shift the third order resonance to 3.5 GHz, Ref 2 design is utilized. Ref 2 design is a dipole antenna with perpendicular arm having thicker width. For further enhancing the

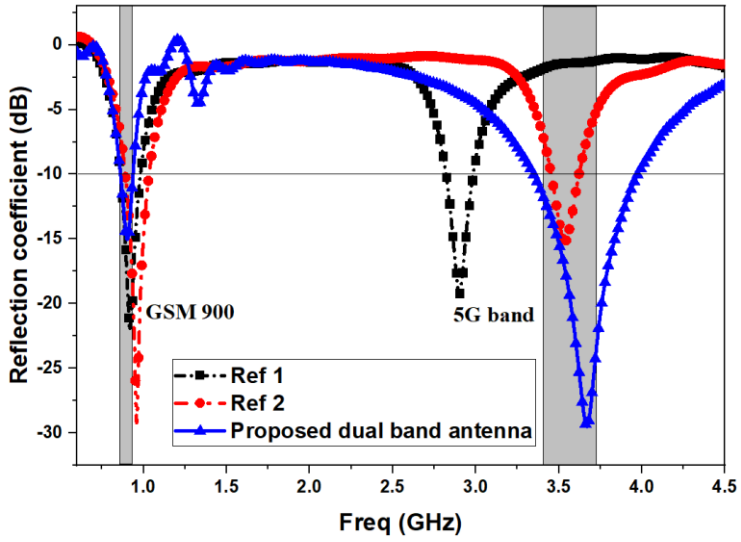

Fig. 5.4. Reflection coefficient of reference designs

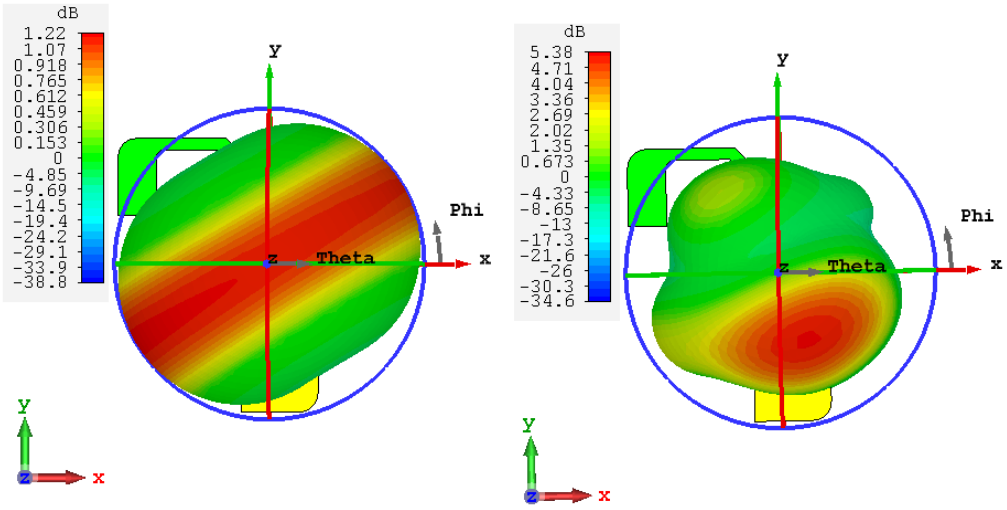

Fig. 5.3. Radiation pattern of dual-band antenna

bandwidth in the 5G band, arms of the proposed dual-band design are folded as in Fig. 5.2. This has also been done to maintain the simplicity and to reduce the overall length of the antenna. The reflection coefficient of the reference designs and dual-band antenna are depicted in Fig. 5.3. It can be observed that the proposed dipole antenna can cover the GSM 900 and 5G band. The 3-D radiation pattern of the proposed antenna at two operating frequencies are presented in Fig. 5.4.

For harvesting the RF energy from 1.8 to 2.7 GHz frequency bands, broadband monopole antennas are employed. Monopole antennas are selected based on their wide bandwidth and omnidirectional radiation pattern. Two broadband designs are employed in the RF harvester in order to keep the antennas in small footprint for

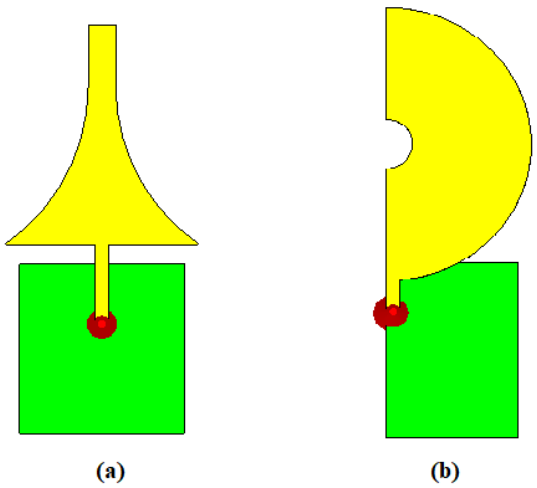

Fig. 5.5. Proposed monopole antennas (a) broadband 1 (b) broadband 2

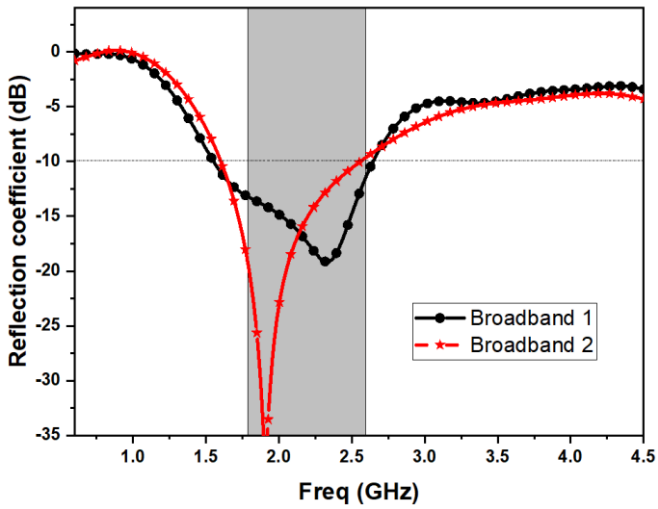

Fig. 5.6. Simulated reflection coefficient of broadband 1 and broadband 2 monopole antennas

extracting energy from all possible directions. A tapered broadband monopole antenna is utilized as the broadband 1 antenna as shown in Fig. 5.5 (a).

The spacing between ground plane and monopole radiator is optimized for achieving the required bandwidth. In order to minimize the size of the antenna and coupling with other antenna elements, edges of the monopole radiator are smoothly reduced to a smaller width at the top. Hemispherical monopole antenna as shown in Fig. 5.5 (b) is utilized as the broadband 2 design. The reflection coefficient of the proposed broadband antennas is depicted in Fig. 5.6. The simulated broadband 1 antenna has a bandwidth of 1.2 GHz ranging from 1.5 to 2.7 GHz and broadband 2 extends from 1.55 to 2.7 GHz. Therefore, both broadband designs can cover the GSM 1800, GSM 2100 and WLAN bands. The 3-D radiation pattern of the proposed broadband antennas at 1.8 GHz and 2.4 GHz are presented in Fig 5.7 and Fig. 5.8.

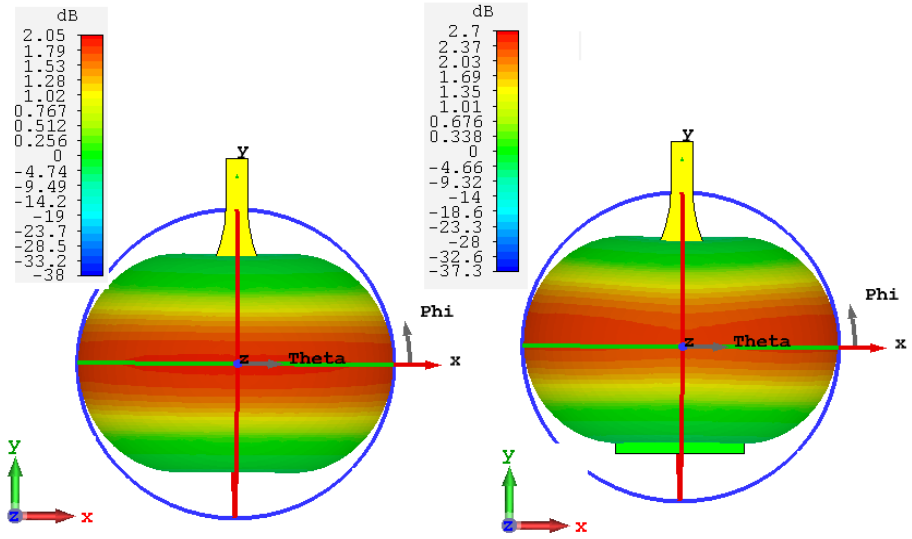

Fig. 5.7. 3-D radiation pattern of broadband 1 antenna

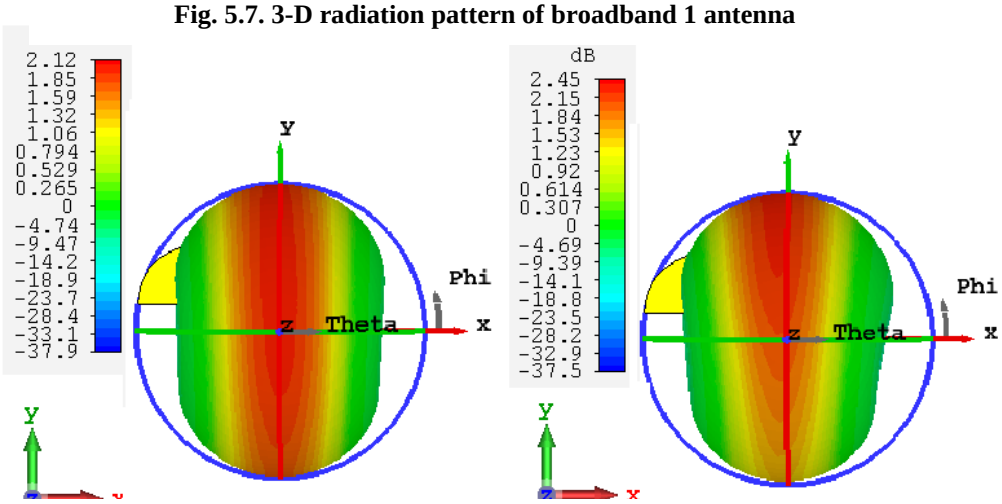

Fig. 5.8. 3-D radiation pattern of broadband 2 antenna

Each broadband antenna has an omnidirectional radiation pattern throughout the required bandwidth; thus, the antenna can receive incident signals from many different angles.

The proposed high sensitivity and high efficiency RF energy harvesting system comprises of five antenna elements to cover the ambient RF energy in 915-960 MHz, 1.8-2.7 GHz, and 3.4-3.7 GHz frequency bands as shown in Fig. 5.9. Antennas consists of 3 broadband monopoles and 2 dual-band dipoles (multiple bands together) to develop the polarization insensitive system. Thus, the harvester is able to receive RF

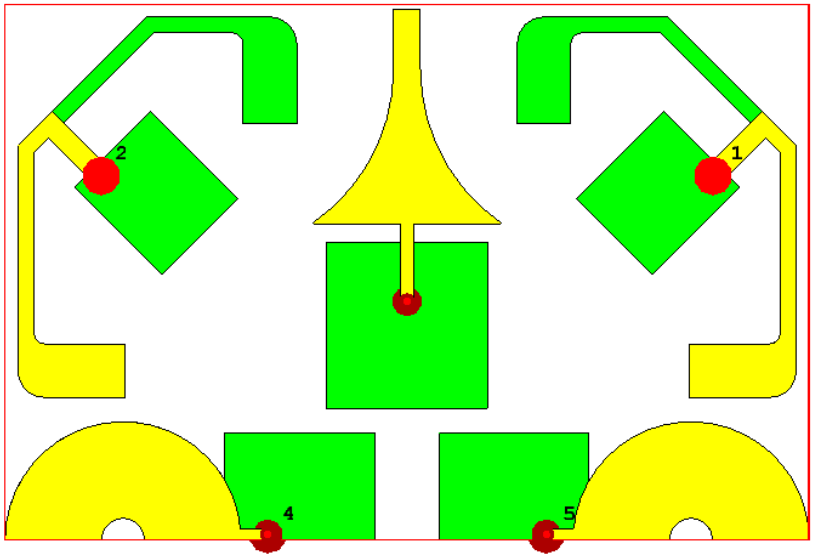

Fig. 5.10. Proposed RF harvester antennas

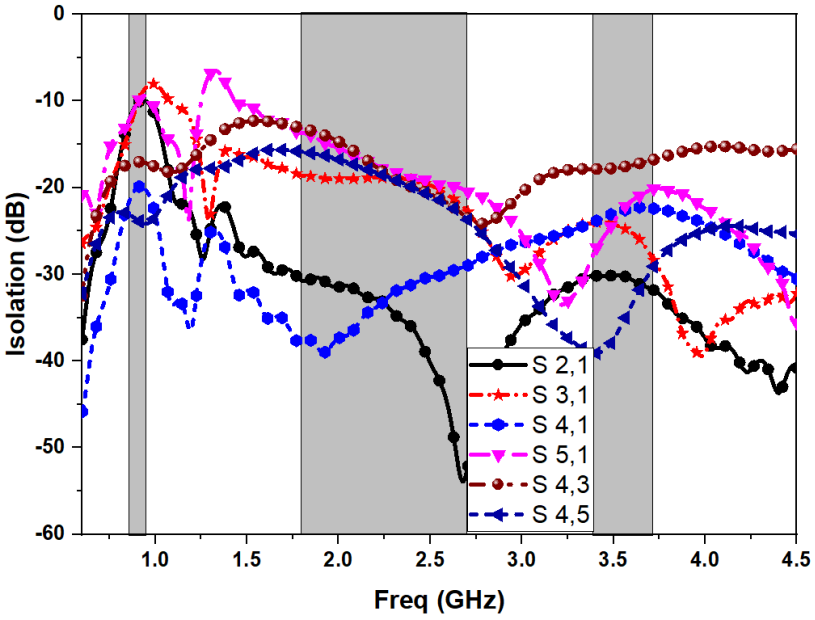

Fig. 5.9. Isolation of proposed RF harvester antennas

waves with arbitrary polarization and has demonstrated that the antenna is indeed dual polarization. The five-antenna system is printed on low loss Rogers 5880 substrate (relative dielectric permittivity $\varepsilon_r = 2.2$, loss tangent $\tan \delta = 0.0037$) with a height of 1.52 mm and has an overall size of 150 × 100 mm^2. The isolation of the antenna ports is shown in Fig. 5.10. It can be clearly observed that good isolation is achieved between the antenna ports in the small footprint. The fabricated prototype of the five-antenna system is shown in Fig. 5.11. The measured reflection coefficient of the antennas is shown in Fig. 5.12. It can be seen that the antennas can harvest the RF power from 0.915 GHz, 1.8-2.7 GHz, and 3.4-3.7 GHz irrespective of polarization and directions of the incoming waves.

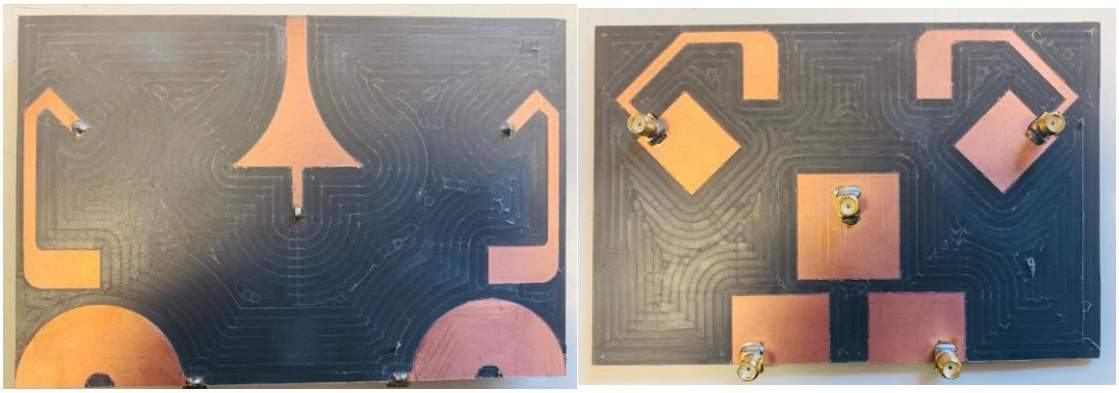

Fig. 5.12. Fabricated RF harvester antennas

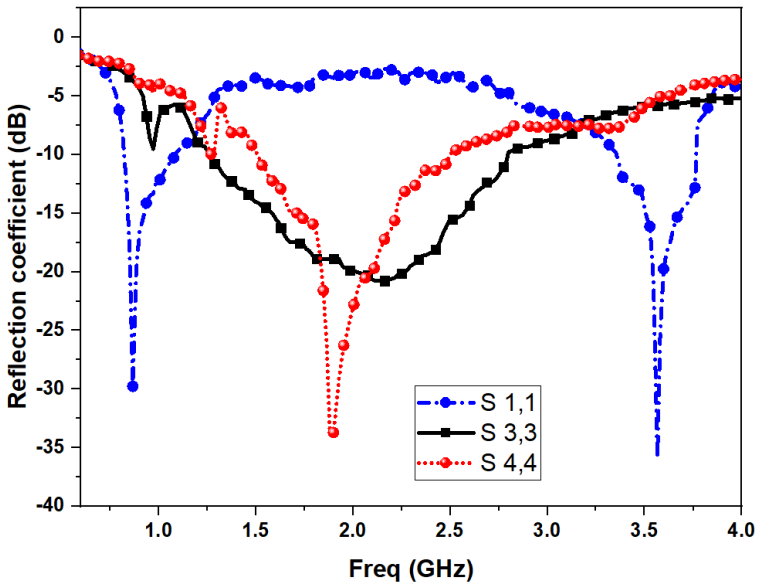

Fig. 5.11. Measured reflection coefficient of RF harvester antennas

5.3. Rectifier Design

Broadband RF rectifier topologies can be broadly divided into single branch and multiple branch impedance matching networks. In single branch technique, the signals received by the antenna over the frequency band of interest (from f_0 to f_N) can be delivered to the rectifier through the network. This topology has the advantage of low overall size, but the loss of the complete matching network is quite high due to the large number of cascaded circuit components, and it cannot effectively reject the higher order harmonics generated by the rectifier. Thus, it would be difficult to achieve a high efficiency rectenna that can cover different frequency bands using this method. To overcome the challenges in the single branch topology, multiple RF branch topology is used. This rectenna is designed with multi-branch separate matching networks and rectifiers, where each branch is matched to a particular operating frequency. Meanwhile, the output dc power of the whole circuit is combined at the DC output port. In this case, the loss of a single matching network can be reduced and the operating frequency of the rectenna can be extended by adding additional circuit branches. However, the multiple RF branches leads to a complex large design. Therefore, great care should be given in order to design a broadband RF harvester by considering the aforementioned topologies.

Another important factor affecting the sensitivity of rectifier is the choice of rectifying element and its configuration. Low series resistance and junction capacitance are very much needed to perform low input power rectification. Hence, sky work's SMS7630 has been selected for the broadband rectifier. Low threshold voltage of SMS7630 with high sensitivity performance at low input power levels, making it ideal for power harvesting applications. Basically, three widely used diode configurations for rectenna include the single diode, voltage doubler and Greinacher. A single diode is preferred when input power levels are very low, however it is difficult to withstand medium range power. Furthermore, single diode configuration can only provide low output voltage which is not enough to drive typical output applications. The ambient power levels normally range from low to medium intensity. Greinacher rectifier is used for applications involving higher power handling. Therefore, the

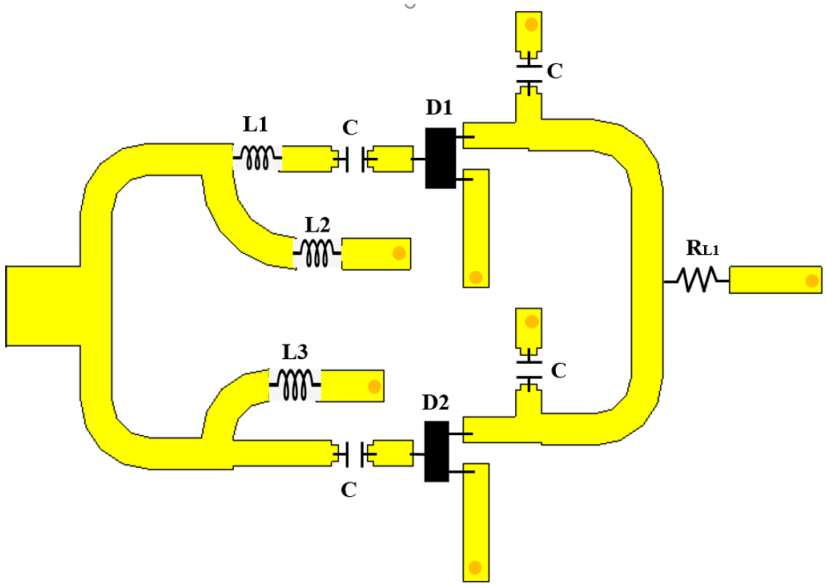

Fig. 5.13. Layout diagram of 1.8-2.7 GHz broad band rectifier

voltage doubler topology is chosen due to its high- power handling capability, low input voltage requirement (depending on the diode), and doubled output DC voltage. To improve the conversion efficiency and to reduce the non-linearity of the diode, several techniques are investigated like resistance compression networks (RCN), hybrid resistance compression technique (HRCT), broadband conjugate matching and impedance compression networks (ICN). The large variation of load impedance can be compressed using RCN and ICN techniques, which results in a smaller variation of the input impedance of the circuit. Thus, the RCN has been used in rectenna design to reduce the nonlinear effects when the loading condition is varying. But the performance of RCN heavily relies on the operating frequency of the network. Matching elimination by conjugate matching helps in reducing the losses associated with lumped matching circuit elements such as insertion loss and parasitic effects in rectifier circuits [20]. But broadband matching will be difficult due to conjugate matching at high impedances.

In order to cover the broad 1.8-2.7 GHz band, a two-branch rectifier is proposed as shown in Fig. 5.13. From literatures, it is concluded that stacked RF circuit's topology will be better for high efficiency performance in a broadband rectifier. Matching each RF circuit and optimizing it for a particular frequency of operation. For this rectifier, initially the two RF branches are matched to 1.9 and 2.4 GHz. As the diode-pair input impedance is capacitive in nature, an inductor-based matching is proposed to reduce

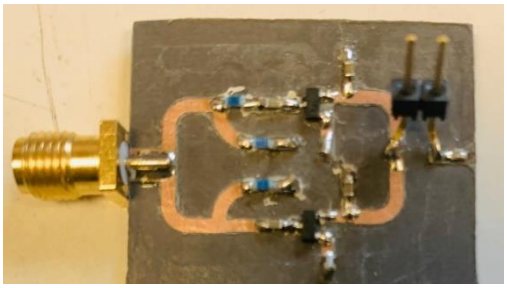

Fig. 5.15. Fabricated 1.8-2.7 GHz broad band rectifier

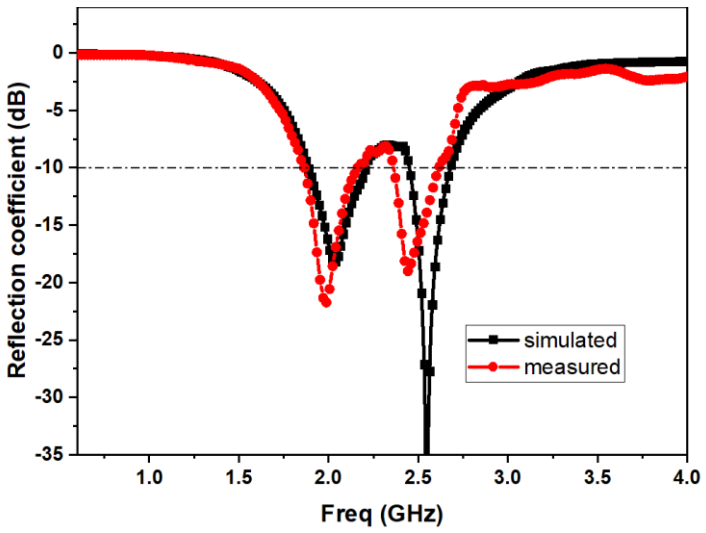

Fig. 5.14. Simulated and measured reflection coefficient of 1.8-2.7 GHz broadband rectifier

the losses in each RF branch. Depending upon the two frequencies to cover the 1.8-2.7 GHz band, two inductors L1 and L2 are used in the first branch and inductor L3 is used in the second branch for impedance matching. RF power in 1.8-2.7 GHz range is divided into two branches based on frequency, and then the DC power after rectification is combined together at the load resistor. Therefore, this rectifier itself performs a RF splitting in the beginning and DC combining at the end. The values and part numbers of the circuit components are given in Table 5.1. Fig. 5.14 depicts the fabricated 1.8-2.7 GHz broadband rectifier. Reflection coefficient of the proposed broadband rectifier at -15 dBm is shown in Fig. 5.15. It can be clearly observed that the rectifier covers the bandwidth of 1.8-2.7 GHz at a low input power of -15 dBm. Output voltage reached a peak voltage of 0.22V at -15 dBm input power with a load impedance of 4 kΩ. The RF to DC conversion efficiency bandwidth of the 1.8-2.7 GHz broadband rectifier is shown in Fig. 5.16. Conversion efficiency is higher than 27% from 1.8-2.7 GHz at -15 dBm input power. Thus, the 1.8-2.7 GHz broadband rectifier works efficiently with high sensitivity and efficiency.

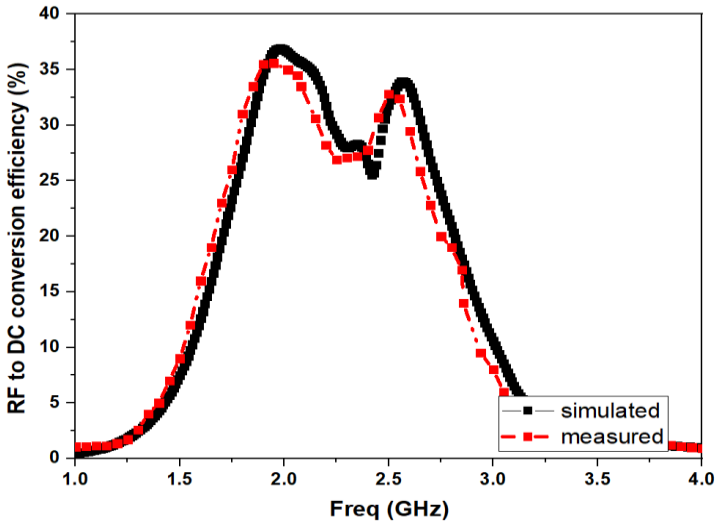

Fig. 5.16. RF to DC conversion efficiency of 1.8-2.7 GHz broadband rectifier

Table 5.1. Circuit components used in the rectifiers design

Component name	Nominal value	Part number and supplier
C	100 pF chip capacitor	GRM0335C2A101GA01, Murata
C1	1 pF chip capacitor	GRM0335C2A1R0CA01, Murata
L1	6.2 nH chip inductor	0402HP-6N2XJLW, Coilcraft
L2	4.7 nH chip inductor	0402HP-4N7XJLW, Coilcraft
L3	3.6 nH chip inductor	0402HP-3N6XJLW , Coilcraft
L4	36 nH chip inductor	0402HP-36NXJLW , Coilcraft

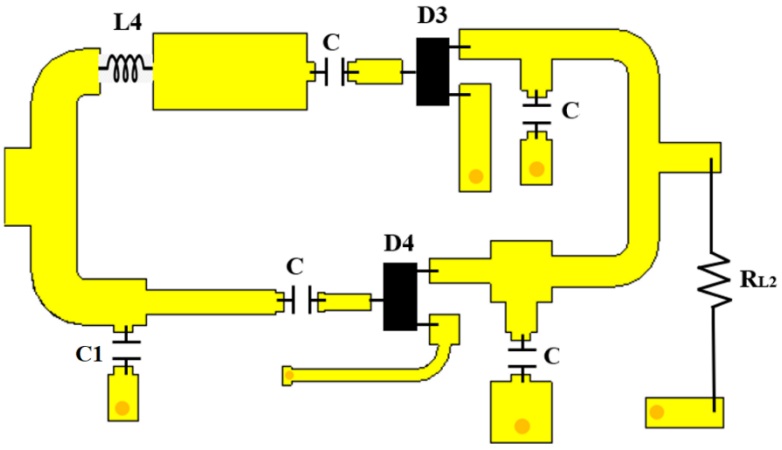

Fig. 5.17. Layout diagram of the dual-band rectifier

Fig. 5.18. Fabricated dual-band rectifier

For incorporating the rectification of 0.9-0.96 and 3.4-3.7 GHz frequency bands, a dual-band rectifier based on the voltage doubler topology is proposed as shown in Fig. 5.17. Initially, the two RF branches are matched to 0.93 and 3.5 GHz. An inductor-based matching is utilized for matching the 0.93 GHz, whereas a capacitor *C5* is shunt connected for matching the 3.5 GHz band. As the frequency becomes higher, the ωRC value also increases. Therefore, the performance of rectifier in low-input power region degrades in the 3.5 GHz band. Fig. 5.18 depicts the fabricated dual-band rectifier. The reflection coefficient of the fabricated dual-band rectifier at -15 dBm is shown in Fig. 5.19. It can be clearly observed that the rectifier covers the dual-bands at a low input power of -15 dBm. The RF to DC conversion efficiency bandwidth of the dual-band rectifier is shown in Fig. 5.20. Conversion efficiency is higher than 40 % at 0.915 GHz with an input power of -15 dBm. Output voltage reached a peak voltage of 0.235V at -15 dBm input power. In 3.4-3.7 GHz band, sensitivity is less than that of other bands as expected due to the high ωRC value. Conversion efficiency is higher than 25 % from 3.4 to 3.7 GHz at -15 dBm input power.

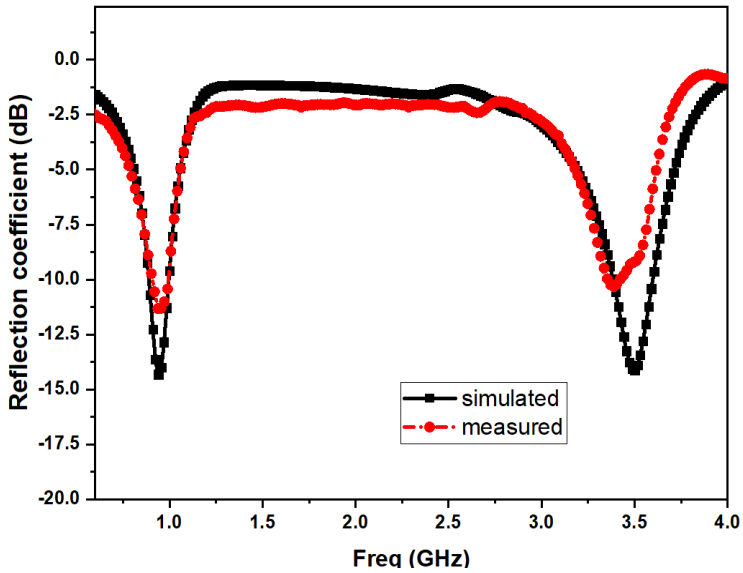

Fig. 5.19. Simulated and measured reflection coefficient of dual-band rectifier

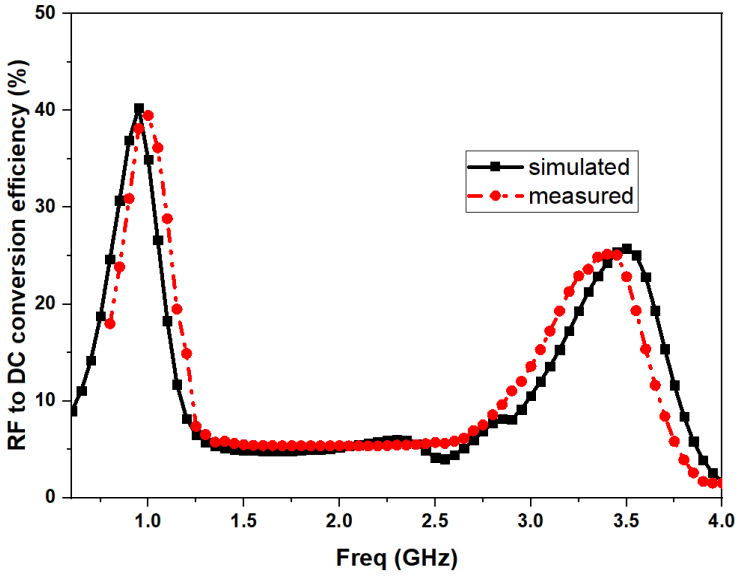

Fig. 5.20. RF to DC conversion efficiency of dual-band rectifier

5.4. RF Energy Harvester Measurement

The proposed ambient RF energy harvesting system was fabricated to verify our design, as shown in Fig. 5.21. In this proposed high voltage hybrid topology, outputs of all branches are DC combined in a series manner. It should be noted that connecting the rectifier DC outputs in series can increase the total voltage whereas parallel connection increases the DC current. High output voltage is an important necessity of ambient energy harvesting systems for providing enough voltage to drive typical applications under low input power conditions. Thus, in order to connect the outputs in series, the grounds are separated for isolating the DC.

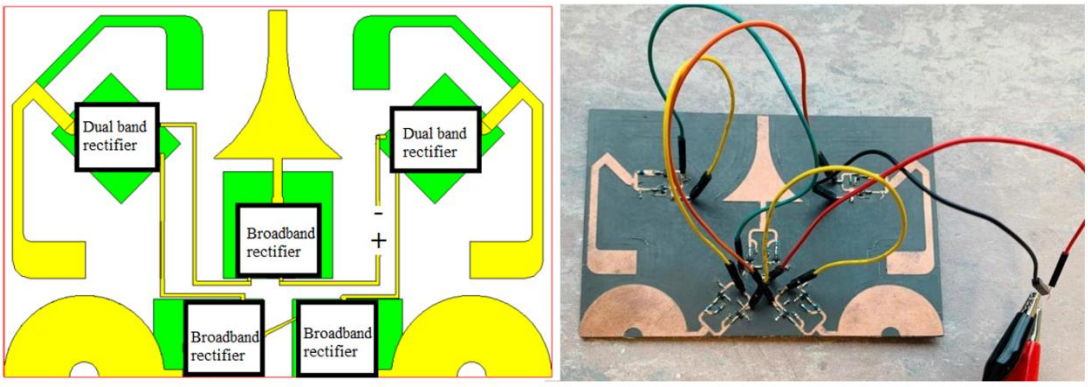

Fig. 5.21. RF energy harvester (a) Layout (b) Fabricated prototype

Even though the rectenna elements are different, all rectennas were initially designed to work with same load resistor and in similar input power conditions and all elements load resistance. Therefore, for maximum power output condition, the load impedance of the array is selected as $R_L = 5 \times R_{L0}$, where R_{L0} is the load impedance of a single element and n is the number of elements [35]. To demonstrate the capability of harvesting ambient RF energy, we test the proposed energy harvesting system in a typical indoor office environment with a relatively low ambient RF power density to conduct the measurement as shown in Fig. 5.22. The ambient power is mainly distributed at four frequency bands which are GSM 900, GSM-1800/4G, UMTS-2100/3G, and Wi-Fi. The input power level on each frequency band has an average value of −35 to −20 dBm. The ambient harvester measured an output voltage of 500 to 550 mV with a load resistor of 10 kΩ. Hence, the average measured output DC power is in the range of 27.5 μW. Typical DC output power obtained from RF harvesters in the similar indoor conditions in literature is less than 20 μW [21], [22]. Measured output power is considerably high compared to other RF harvesters discussed in the literature. Such output DC power can be stored to support low power and low duty-cycle devices, such as sensors in IoT. Therefore, our proposed RF energy harvesting system is a promising solution to overcome the challenge of battery recharging and replacement in IoT applications.

Fig. 5.22. RF energy harvester measured in indoor environment

5.5. Summary

A novel hybrid combining multiband RF harvester has been proposed for ambient WEH applications to overcome the challenge of battery recharging and replacement in IoT. The proposed harvester utilised five antenna elements with dual-band and multi band characteristics to capture RF energy from 0.9-0.96 GHz, 1.8-2.7 GHz and 3.4-3.7 GHz in all possible directions. Antenna elements are placed precisely in a compact area of 150 × 100 mm^2 with good isolation. Novel broadband and dual-band rectifiers have been proposed with high conversion efficiency at low power ambient conditions. The broadband rectifier achieved a peak conversion efficiency of 37% at an input power of -15 dBm. Conversion efficiencies of more than 40 % and 25% have been obtained at 0.91-0.96 GHz and 3.4-3.7 GHz frequency bands respectively with -15 dBm input power. The proposed RF harvester combined all DC outputs in a series manner to obtain a maximum output voltage. It was also shown that the prototype can provide output DC power up to 30 μW in a typical indoor ambient environment.

References

[1] Y. K. Tan and S. K. Panda, "Energy harvesting from hybrid indoor ambient light and thermal energy sources for enhanced performance of wireless sensor nodes," *IEEE Trans. Ind. Electron.,* vol. 58, no. 9, pp. 4424-4435, Sept. 2011.

[2] T. Hosseinimehr and A. Tabesh, "Magnetic field energy harvesting from ac lines for powering wireless sensor nodes in smart grids," *IEEE Trans. Ind. Electron*., vol. 63, no. 8, pp. 4947-4954, Aug. 2016.

[3] S. Kim *et al*., "Ambient RF energy-harvesting technologies for self-sustainable standalone wireless sensor platforms," *Proc. IEEE*, vol. 102, no. 11, pp. 1649–1666, Nov. 2014.

[4] B. Strassner and K. Chang, "5.8-GHz circularly polarized dual-rhombic-loop traveling-wave rectifying antenna for low power-density wireless power transmission applications," *IEEE Trans. Microw. Theory Tech.,* vol. 51, no. 5, pp. 1548–1553, 2003.

[5] Q. Awais, Y. Jin, H. T. Chattha, M. Jamil, H. Qiang, and B. A. Khawaja, "A compact rectenna system with high conversion efficiency for wireless energy

harvesting," *IEEE Access*, vol. 6, pp. 35 857–35 866, 2018.

[6] Y.-J. Ren and K. Chang, "5.8-GHz circularly polarized dual diode rectenna and rectenna array for microwave power transmission," *IEEE Trans. Microw. Theory Techn.*, vol. 54, no. 4, pp. 1495–1502, 2006.

[7] Y. Yang, L. Li, J. Li et al., "A circularly polarized rectenna array based on substrate integrated waveguide structure with harmonic suppression," *IEEE Antennas Wireless Propag. Lett*., vol. 17, no. 4, pp. 684–688, 2018.

[8] Y. Yang, J. Li, L. Li et al., "A 5.8 GHz circularly polarized rectenna with harmonic suppression and rectenna array for wireless power transfer," *IEEE Antennas Wireless Propag. Lett*., vol. 17, no. 7, pp. 1276–1280, 2018.

[9] X. Li, L. Yang, and L. Huang, "Novel design of 2.45-GHz rectenna element and array for wireless power transmission," *IEEE Access*, vol. 7, pp. 28356–28362, 2019.

[10] S. Chandravanshi, S. S. Sarma, and M. J. Akhtar, "Design of triple band differential rectenna for RF energy harvesting," *IEEE Trans. Antennas Propag.*, vol. 66, no. 6, pp. 2716–2726, 2018

[11] H. Sun, Y.-X. Guo, M. He, and Z. Zhong, "A dual-band rectenna using broadband Yagi antenna array for ambient RF power harvesting," *IEEE Antennas Wireless Propag. Lett.*, vol. 12, pp. 918–921, 2013.

[12] K. Niotaki, S. Kim, S. Jeong, A. Collado, A. Georgiadis, and M. M. Tentzeris, "A compact dual-band rectenna using slot-loaded dual-band folded dipole antenna," *IEEE Antennas Wireless Propag. Lett.*, vol. 12, pp. 1634–1637, 2013.

[13] S. Shen, C.-Y. Chiu, and R. D. Murch, "A broadband L-probe microstrip patch rectenna for ambient RF energy harvesting," *Proc. IEEE Int. Symp. Antennas Propag. USNC/URSI Nat. Radio Sci. Meeting*, 2017, pp. 2037– 2038.

[14] Z. Liu, Z. Zhong, and Y. Guo, "High-efficiency triple-band ambient RF energy harvesting for wireless body sensor network," *Proc. IEEE MTT-S Int. Microw. Workshop Ser. RF Wireless Techn. Biomed. Healthcare Appl.*, 2014, pp. 1–3.

[15] S. Chandravanshi, S. S. Sarma, and M. J. Akhtar, "Design of triple band differential rectenna for RF energy harvesting," *IEEE Trans. Antennas Propag.*, vol. 66, no. 6, pp. 2716–2726, Jun. 2018.

[16] V. Kuhn, C. Lahuec, F. Seguin, and C. Person, "A multi-band stacked rf energy harvester with RF-to-DC efficiency up to 84%," *IEEE Trans. Microw. Theory*

Techn., vol. 63, no. 5, pp. 1768–1778, 2015.

[17] S. Shen, Y. Zhang, C. Chiu and R. Murch, "An ambient RF energy harvesting system where the number of antenna ports is dependent on frequency," *IEEE Trans. Microw. Theory Techn*., vol. 67, no. 9, pp. 3821–3832, Sept. 2019.

[18] U. Olgun, C.-C. Chen, and J. L. Volakis, "Design of an efficient ambient WiFi energy harvesting system," *IET Microw. Antennas Propag*., vol. 6, no. 11, pp. 1200–1206, Nov. 2012.

[19] X. Zhang et al., "Two-dimensional MoS2-enabled flexible rectenna for Wi-Fi-band wireless energy harvesting," *Nature*, vol. 566, pp. 368–372, Jan. 2019.

[20] C. Song *et al*., "Matching network elimination in broadband rectennas for high-efficiency wireless power transfer and energy harvesting," *IEEE Trans. Ind. Electron*., vol. 64, no. 5, pp. 3950–3961, 2017.

[21] E. Vandelle, D. H. N. Bui, T. Vuong, G. Ardila, K. Wu and S. Hemour, "Harvesting ambient RF energy efficiently with optimal angular coverage," *IEEE Trans. Antennas Propag.,* vol. 67, no. 3, pp. 1862-1873, Mar. 2019.

[22] C. Song, P. Lu and S. Shen, "Highly Efficient Omnidirectional Integrated Multi-Band Wireless Energy Harvesters for Compact Sensor Nodes of Internet-of-Things," *IEEE Trans. Ind. Electron*., early access article, Jul. 2020.

.

Chapter 6. SWIPT Rectenna With AWEH Capability for WSN Nodes

A novel communication rectenna solution is introduced to provide effective data and power transfer in wireless sensor nodes. Along with the ambient energy harvesting of conventional rectenna, the proposed design can also perform simultaneous wireless information and power transfer for facilitating uninterrupted power supply and data transfer of WSN nodes. A dual polarized 2×1 square patch antenna array is designed to achieve high isolation and low cross polarization between the dual-polarized ports in order to guarantee low mutual interference between the communication and the rectifying ports. To minimize the overall size of the rectenna, a multisection bended broadband monopole antenna is designed to perform ambient energy harvesting from arbitrarily polarized incoming waves. Broadband antenna measured a broad bandwidth of 2.7 GHz extending from 1.5 to 4.2 GHz. Multibranch broadband rectifier is realized with a fractional bandwidth (FBW) of 85% (from 1.49 to 3.73 GHz) and power conversion efficiency of more than 50% at a 0 dBm input power level. $+45^0$ polarized patch antenna ports are RF combined to provide enough communication sensitivity and -45^0 polarized ports are utilized for WPT. Measured results shows that the communication port achieved a bandwidth of 200 MHz and an isolation better than 20 dB. The performance of communication port is verified with a 50 MHz OFDM signal. DC combined WPT array achieved a peak efficiency of 73.5% at 5.8 GHz with12 dBm CW input signal. Thus, the proposed communication rectenna array with ambient energy harvesting can be a promising candidate for future wireless sensor nodes.

6.1. Introduction

Available existing ambient RF energy is mostly distributed in the cellular band and WLAN band from hundreds of megahertz to 3 GHz (2G- GSM, 3G-UTMS, ISM-WiFi-2.4 GHz and 4G-LTE). Additionally, with the continuing popularization of 5G technology, the 5G-IMT band operating at around 3500 MHz is also an important power source [1]. Thus, due to the scattered distribution of multiple RF sources, it will be difficult to design rectenna with multiband antenna to cover all available channels. Moreover, the WEH receiver antenna need to maintain all polarization property to receive RF power from all possible directions [2]. However, the total available power from all possible ambient RF sources is low and it is difficult to meet the power demand of the WSN nodes. Therefore, it is necessary to employ an active power source for uninterrupted working of the WSN nodes [3].

One of the promising solutions is to use wireless power transfer (WPT) technology [4]. WPT enables remote replenishment of electric power to wireless devices in a long distance and avoids frequent replacement of battery, which makes wireless devices become more portable, self-sustainable, and longevity [5]. WPT uses a dedicated RF source for powering the WSN node wirelessly. However, if the receiver could redirect the RF energy and deliver it to terminal devices while exchanging information, the efficiency and power consumption of the wireless system can be significantly improved. With this regard, the idea of simultaneous wireless information and power

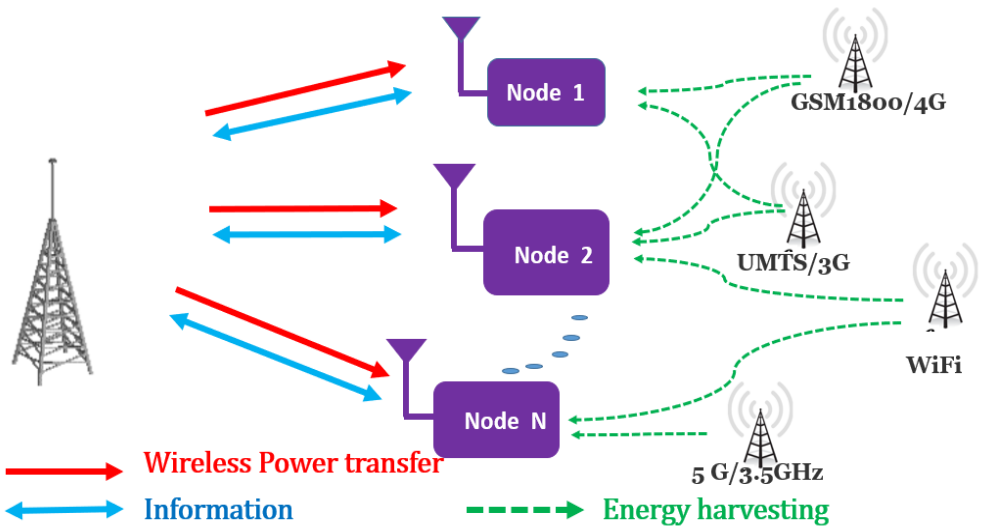

Fig. 6.1. Framework of simultaneous RF ambient WEH and directional WPT for power supply of wireless sensor network.

transfer (SWIPT) was proposed in [6], for performing the communication and power transfer simultaneously. Several literatures analyzed the correlation between the channel rate, channel capacity and energy efficiency in SWIPT [7],[8]. Different SWIPT schemes (power splitting, time splitting, separate receivers and antenna switching) and their integrations with various technologies have extensively been studied [9].

In this work, a novel rectenna to realize simultaneous wireless information and power transfer with ambient broadband energy harvesting is proposed. Fig. 6.1 illustrates the framework of wireless sensors nodes with power supply solution by WEH and SWIPT. Each WSN node must be able to not only harvest ambient RF energy but also perform simultaneous wireless information and power transfer for facilitating uninterrupted power supply and data transfer for WSN nodes. This proposed technology can be implemented to build reliable and convenient SWIPT systems for remotely charging various low- to medium-power devices such as WSN nodes and RFID tags. Radio frequency identification (RFID) is a solid, industrial example of simultaneous wireless information and power transfer (SWIPT). Design and performance of broadband antenna for WEH and square patch antenna for SWIPT are discussed in Section 6.2. Broadband rectifier design and performance for WEH is addressed in Section 6.3. Then, WPT rectifier is discussed in section 6.4. Section 6.5 illustrates the wireless power transmitting and receiving test and the analysis of the measured results to validate the practicality and reliability of the proposed rectenna.

6.2. Antenna Design

For ambient RF energy harvesting, a broadband antenna with omnidirectional radiation pattern is preferred whereas for directive WPT technology a narrowband directional radiation pattern is more suitable. Moreover, the ambient RF energy receiving antenna needs to maintain multi-polarization characteristics as much as possible. The proposed design has a monopole antenna and a 2×1 square patch antenna array as shown in Fig. 6.2. The monopole antenna has four sections with a tapered first section to realize the impedance matching for the broadband operation. The antenna is designed to operate from 1.8 to 4.48 GHz (to cover the U.K. GSM-1800/4G, 3G/UMTS-2100, WLAN 2380-2450 and 5G/3.2-4.2 GHz bands). To achieve multiple

polarization property in the designed monopole antenna, the antenna is bend into multiple sections. The radiating patch is fabricated on one side of the substrate and ground plane is fabricated on the other side. Two square patch antennas are utilized for simultaneous wireless information and power transfer at 5.8 GHz.

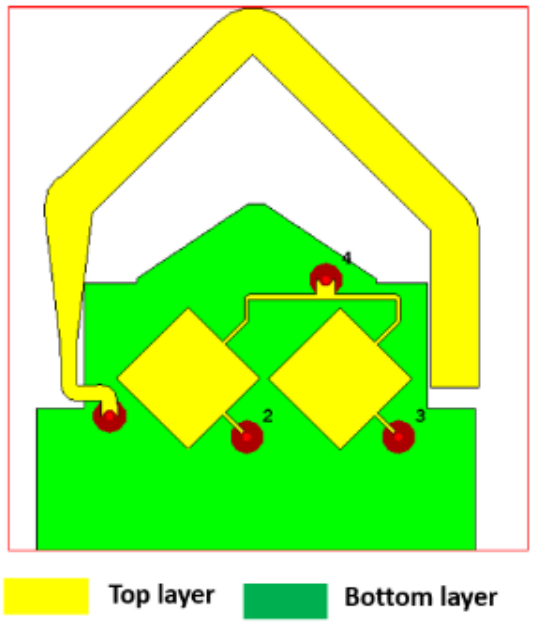

Fig. 6.2. Proposed antenna design

The square patches are placed close to the monopole antenna to minimize the overall footprint of the design. Two feeding lines are connected to the orthogonal edges of each patch antenna to excite the TM10 and TM01 modes. The square patch is rotated by 45^0 angles to provide symmetric shape and compactness to the overall design of rectenna. The patch antenna has -45^0 and $+45^0$ polarization angles. For

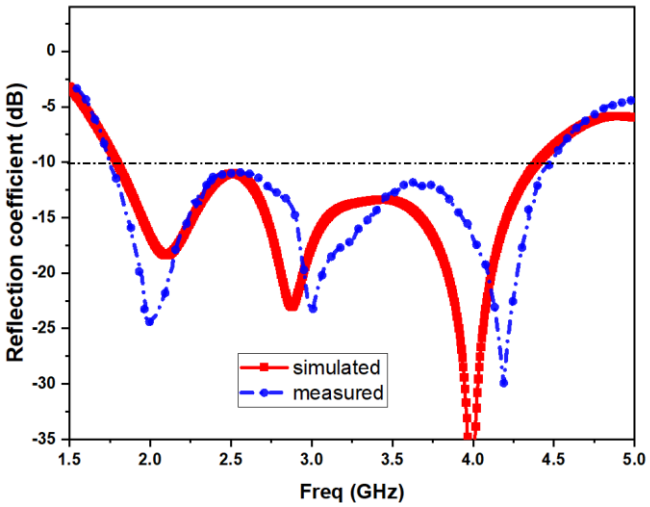

Fig. 6.3. Reflection coefficient of WEH monopole antenna

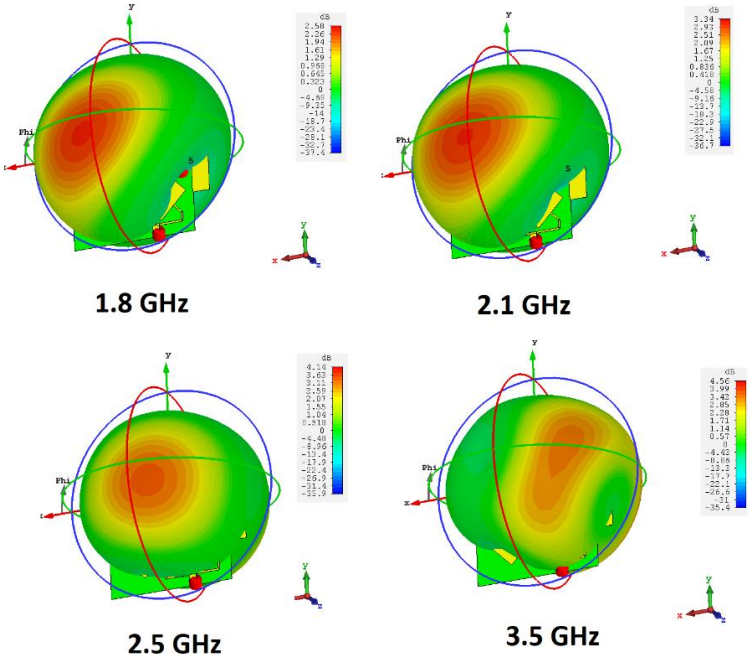

Fig. 6.4. 3-D radiation pattern of WEH monopole antenna

analyzing the performance of designed WEH and SWIPT antenna, the antenna is fabricated on Rogers 4350B substrate with the relative dielectric constant, ε_r = 3.48 and a loss tangent of 0.0037. As the receiver is equipped with 2 square patch antennas that receives information and power simultaneously from the transmitter antennas, the multipath effects needed to be consider in the signal processing stage of communication system. However, the scope of this work is limited to the rectenna system. A detailed study of the signal processing stage in a WIPT system is described

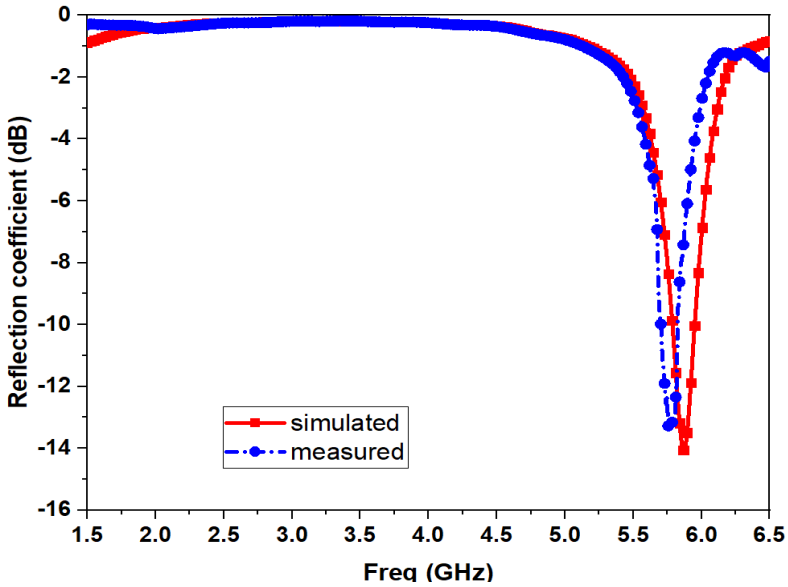

Fig. 6.5. Reflection coefficient of patch antenna

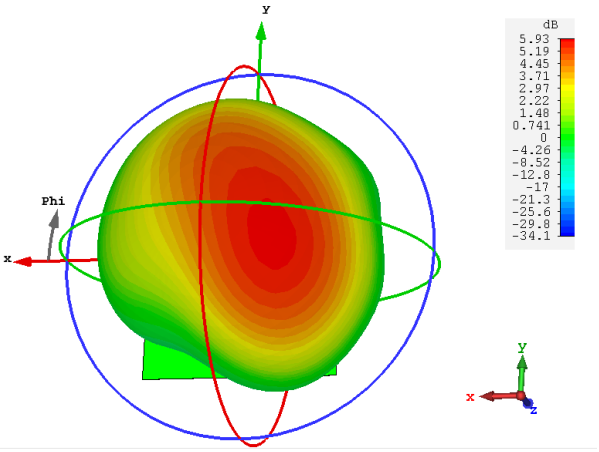

Fig. 6.6. 3-D radiation pattern of patch antenna

in [9]. Fig. 6.3 shows the measured and simulated reflection coefficient of the WEH antenna. The measured bandwidth of the antenna extends from 1.5 GHz to 4.2 GHz. Thus, it covers all required LTE and 5G frequency bands. 3-D radiation pattern of monopole antenna at different operating frequencies are shown in Fig. 6.4. Fig. 6.5 shows the simulated and measured reflection coefficient of square patch antenna. Patch antenna has a measured bandwidth of 200 MHz ranging from 5.72 to 5.92 GHz. The measured isolation S21 between two ports is higher than 20 dB within a broad bandwidth, implying very low interference between two ports. Monopole antenna has achieved a bidirectional radiation pattern with dual polarization throughout the bandwidth. Fig. 6.6 shows the radiation pattern of patch antenna. It can be observed that a unidirectional radiation pattern is obtained with a realized gain of 5.93 dBi.

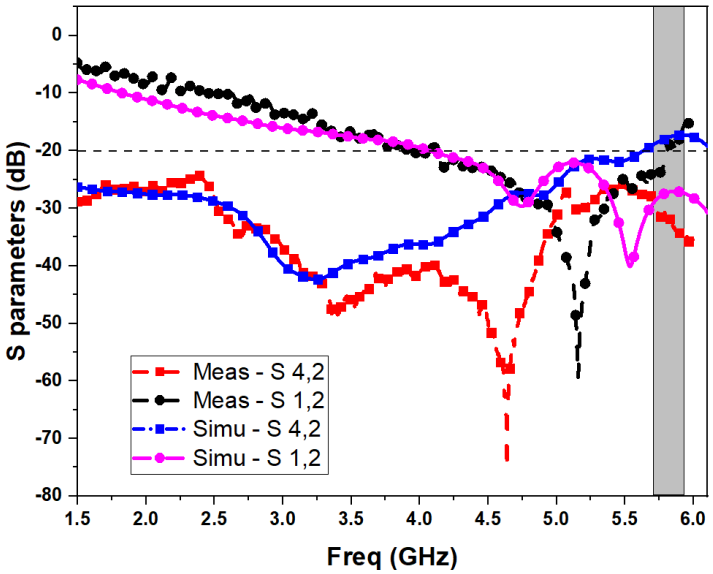

Fig. 6.7. S parameters of antenna.

6.3. Broadband Rectifier Design

A rectifying circuit is the crucial component in a wireless energy harvesting system. Several rectifier topologies are investigated in the literature such as single series, single shunt, voltage doubler and Greinacher rectifier [20]. Single series and shunt diode topologies have high sensitivity performance in low ambient power conditions. However, the limited power handling capability due to low breakdown voltage restricts the applications of these topologies. On the other hand, single band rectennas can achieve a high efficiency (more than 80%). In order to have a reasonable DC output power, it is necessary to harvest the distributed RF ambient energy from multiple frequency bands. Thus, multiband or broadband rectenna that can harvest ambient RF energy from different frequency bands simultaneously is of great importance. Due to the nonlinearity of the rectifying diodes, the input impedance of the circuit varies as a function of the frequency, input power level, and load impedance. Therefore, the multiband or broadband design is really critical. A good RF energy harvesting circuit should have broadband performance with high conversion efficiency at low input power levels. In order to have a high conversion efficiency, we must achieve a good impedance matching over a large bandwidth of frequency. Therefore, it is very difficult to reach a high efficiency with a single branch rectifier, especially when we consider the nonlinear behavior of diodes and the dependency between the input impedance of

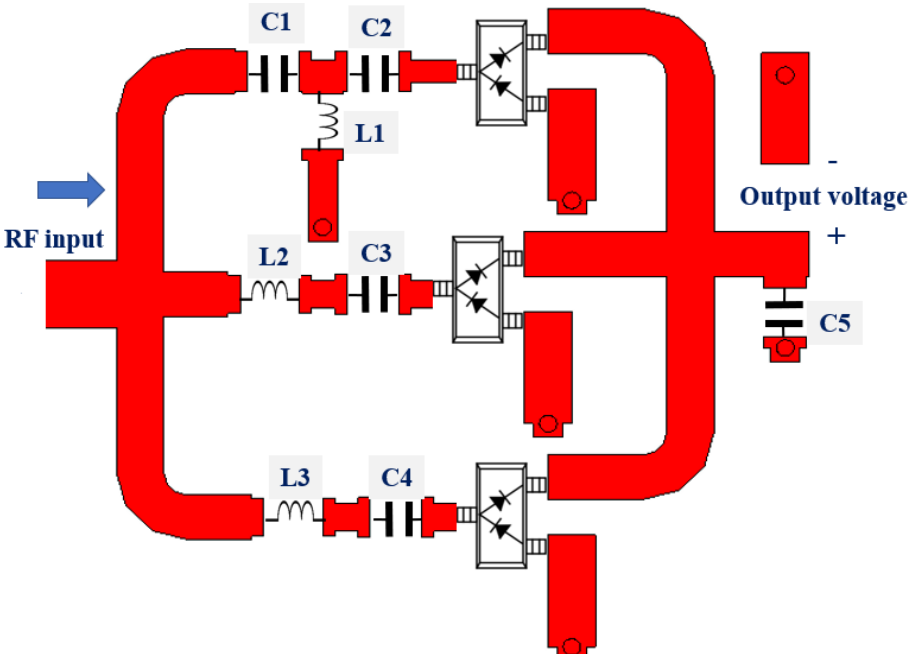

Fig. 6.8. Layout of broadband rectifier.

the rectifying circuit and frequency. Moreover, a single branch rectifier requires a complex filter with high associated loss for wideband impedance matching. Additionally, expanding the number of adaptive frequencies significantly reduces the RF to DC efficiency.

6.3.1. Design of Broadband Rectifier

Based on the aforementioned challenges, a RF stack approach is utilized to design the broadband rectifier. A proper choice of the diode is also important since itself could be a main source of loss and may affect the overall circuit performance. The Schottky diode SMS7630 is selected for the rectifier due to its low biasing voltage requirement for low power ambient input signal (forward bias voltage: 60–120 mV at 0.1 mA).

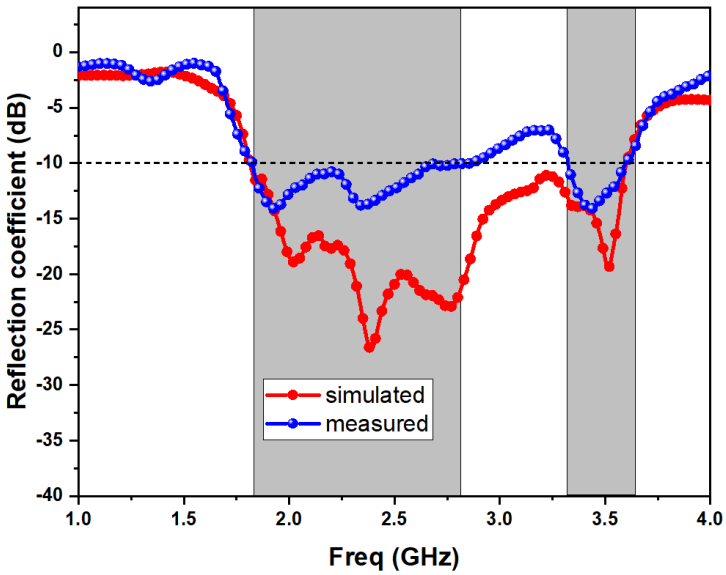

Fig. 6.9. Reflection coefficient of broadband rectifier

Table 6.1. Circuit components used in the rectifier design

Component name	Nominal value	Part number and supplier
C1	0.7 pF chip capacitor	GRM0335C2AR70BA01, Murata
C2, C3, C4, C5	100 pF chip capacitor	GRM0335C2A101GA01, Murata
L1	6.2 nH chip inductor	0402HP-6N2XJLW, Coilcraft
L2	5.1 nH chip inductor	0402HP-5N1XJLW, Coilcraft
L3	9.5 nH chip inductor	0402HP-9N5XJLW, Coilcraft

A nonlinear spice model with parasitic for the Schottky diode, provided by Skyworks Solutions Inc. [21], is used in the simulation. A voltage doubler topology is selected in each branch for higher efficiency and DC output voltage. In order to harvest RF energy from U.K. GSM-1800/4G, 3G/UMTS-2100, WLAN 2.45 GHz and 5G bands, a novel three branch broadband rectifier is proposed. The layout of the proposed rectifier is shown in Fig. 6.8. The lower branch has a single chip inductor *L3* for matching and aimed to get the RF branch match around 1.8 GHz. Similarly, an inductor *L2* is utilized in the middle RF branch and is aimed to get the circuit matched around 2.4 GHz. Thus, the impedance matching based on single inductor works by cancelling out the capacitive input impedance of Schottky rectifier. The losses associated with chip inductor is reasonably low compared to lossy complex filtering circuits. Hence, it can work well in low input power levels with high conversion efficiency. In the upper RF branch, a L type impedance network with a capacitor *C1* and shunt chip inductor *L1* is utilized to match the rectifier at 3.5 GHz. After the voltage doubler topology in each RF branch, the outputs are combined together in a parallel manner. A capacitor *C5* is then utilized as a low pass filter to bypass the harmonics and fundamental frequencies to ground. The four chip capacitors are selected as 100 pF. The chip capacitors and inductors are modelled using S-parameter files provided by Murata and Coil craft. Table 6.1 shows the circuit components used in the broadband rectifier. The harmonic balance simulation of ADS is employed to optimize the matching network at low input power levels (-30 to 0 dBm). An accurate

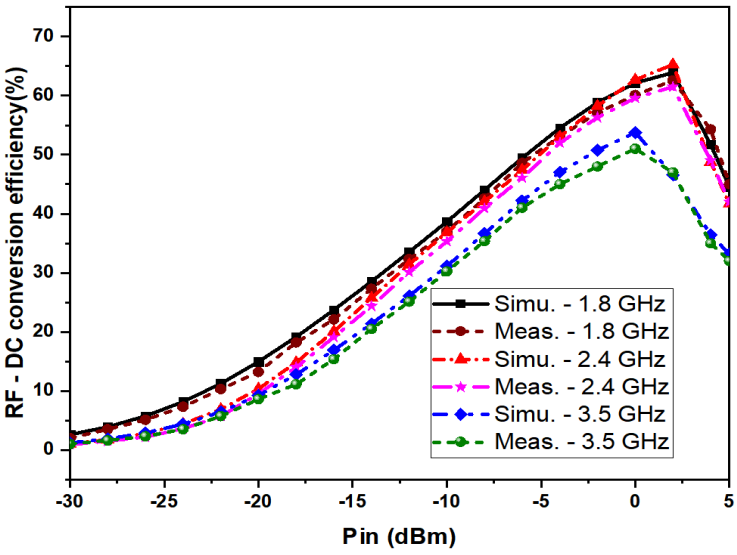

Fig. 6.10. RF to DC conversion efficiency of the broadband rectifier

EM tuning was also used to optimize the parameters of the matching network. A prototype is fabricated for evaluating the performance. Fig. 6.9 shows the simulated and measured reflection coefficient of the broadband rectifier. It can be observed that the bandwidth of antenna clearly covered all the required bands. Fig. 6.10 shows the simulated and measured RF to DC conversion efficiency of the broadband rectifier at 1.8, 2.4 and 3.5 GHz by varying the input power from -15 to 15 dBm. Peak efficiencies of 63%, 62% and 52% are achieved at 1.8, 2.4 and 3.5 GHz, respectively. Higher efficiencies are obtained at lower frequencies compared to 3.5 GHz as expected due to the low ωRC value at lower frequencies.

Fig. 6.11 shows the simulated and measured RF to DC conversion efficiency of the broadband rectifier as a function of operating frequency. It can be observed that conversion efficiency of more than 50% is achieved at 1.49-3.72 GHz bandwidth with an input power of 0 dBm. Therefore, this proposed broadband rectifier is well suited for low power ambient power conditions.

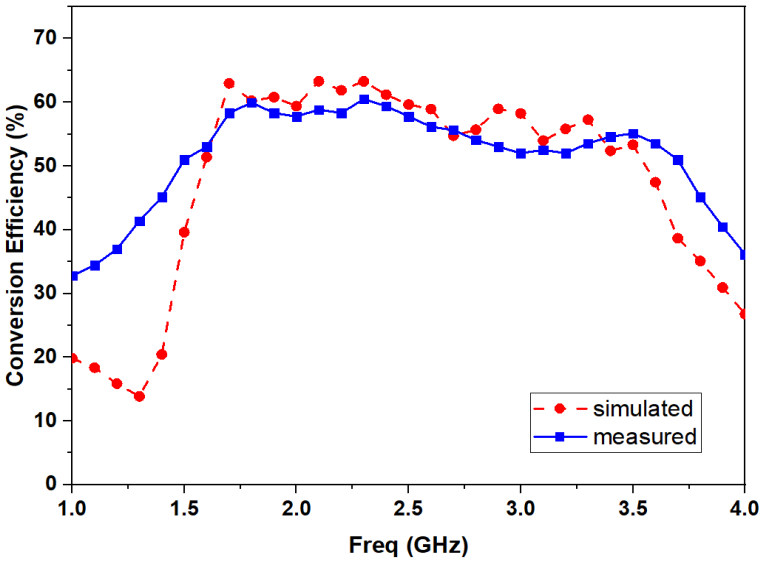

Fig. 6.11. RF to DC conversion efficiency of the broadband rectifier as a function of frequency

6.4. WPT Rectifier

A single shunt diode topology is adopted for proposed WPT rectifier in order to reduce the energy losses in rectifier and to reduce the circuit components as shown in Fig. 6.12. As the WPT system receives energy from a dedicated RF source, a narrowband rectifier at 5.8 GHz is designed with high conversion efficiency at high input power levels, typically above 0 dBm. HSMS 2860 diode is utilized as the

rectifying element for this design. It has high reverse breakdown voltage and low power loss, which is favourable for high power rectifying.The equivalent parameters of the diode are built-in turn-on voltage Vbi = 0.3 V, series resistance Rs = 6 Ω, zero-biased junction capacitance Cj0 = 0.18 pF, and reverse breakdown voltage Vbr = 7 V. Typically, RF power is initially passed through a matching network for delivering the maximum power. In this designed WPT rectifier, matching network is eliminated for reducing the losses associated with the impedance matching circuits. The negative half cycle of the wave is rectified by the shunt diode D1 and the energy is stored in C1. C2 along with load resistor RL acts as a DC pass filter to suppress the ripples from the rectified voltage.

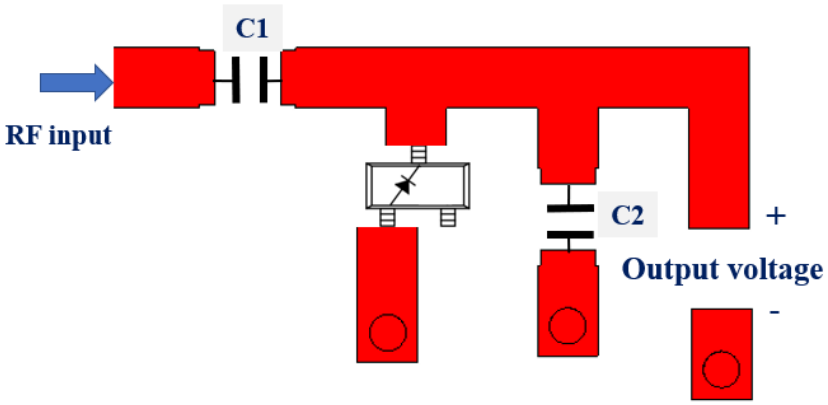

Fig. 6.12. Layout of proposed WPT rectifier

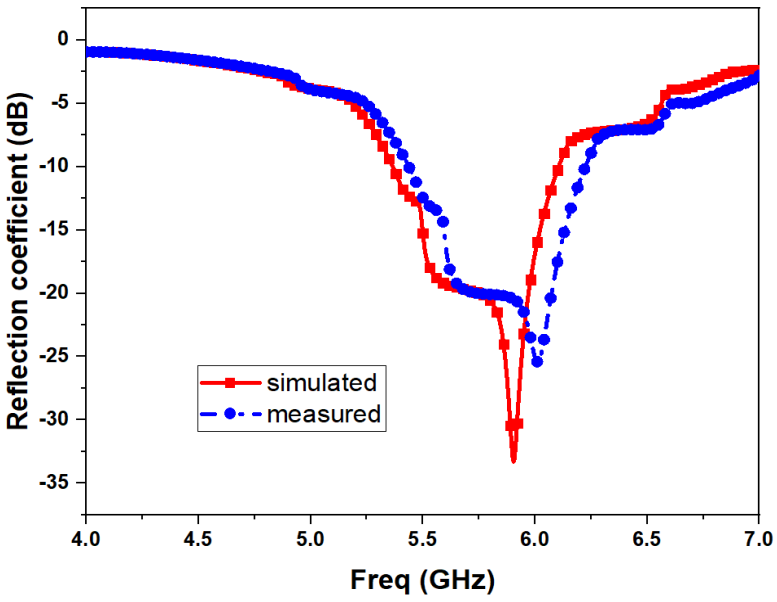

Fig. 6.13. Reflection coefficient of the WPT rectifier

For experimental validation of the WPT rectifier, a prototype is fabricated on a Rogers 4350B material of 1.52 mm thickness with a permittivity of 3.48. Initially, the reflection coefficient of the rectifier is evaluated using a VNA. In Fig. 6.13, the measured reflection coefficient at 0 dBm input power is shown. The rectifier has an measured impedance bandwidth of 0.78 GHz ranging from 5.44 to 6.22 GHz. For evaluating the RF-DC conversion efficiency, a Keithley 2920 RF signal generator with an output power up to 13 dBm has been utilized to generate the RF signal at 5.8 GHz. A digital multimeter has been used to measure the output voltage across the R_L resistor. Fig. 6.14 shows the simulated and measured RF to DC conversion efficiency (η) of the WPT rectifier. A maximum efficiency of 73.5% is achieved at an input power of 9 dBm.

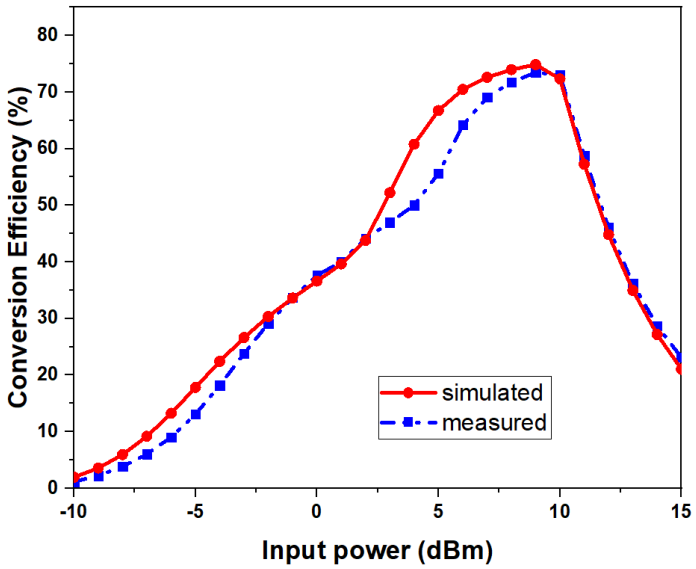

Fig. 6.14. RF to DC conversion efficiency of the WPT rectifier

6.4.1. Parallel DC Combining

In this design, two WPT rectifiers are connected to each square patch antenna. The output DC power of the proposed WPT rectenna array is parallelly combined (current combination), as shown in Fig. 6.16. The equivalent linear model of the single-rectenna element is shown in Fig. 6.15(a). Using that equivalent circuit, an analytical model of parallel rectenna array can be represented as in Fig. 6.16(b). The output power of single rectenna can be defined as

$$P_0 = \frac{V_{D0\times R_{L0}}^2}{(R_{D0}+R_{L0})^2} \quad (6.1)$$

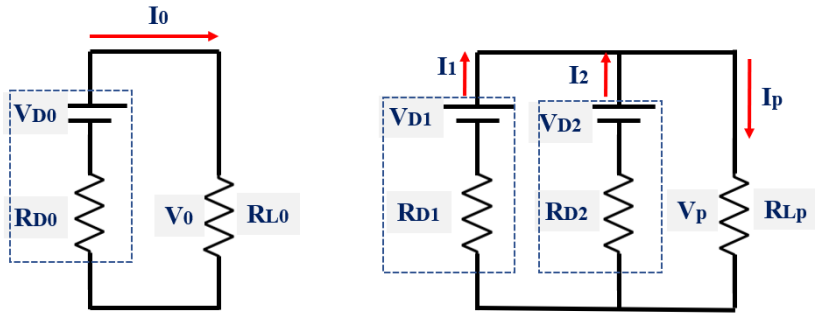

Fig. 6.17. Equivalent linear model of the single-rectenna

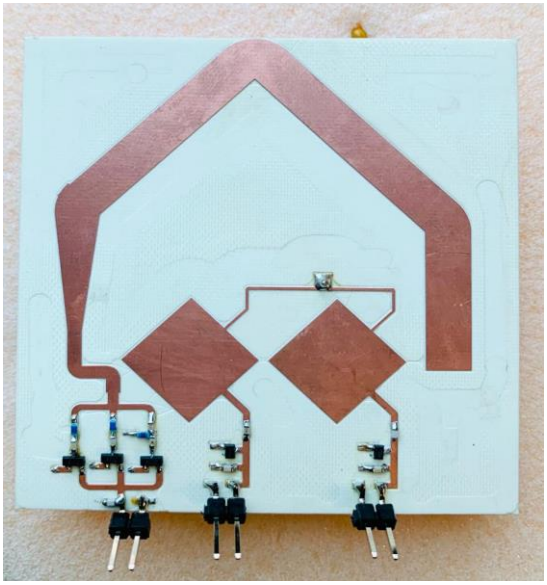

Fig. 6.15. Fabricated SWIPT and AWEH rectenna

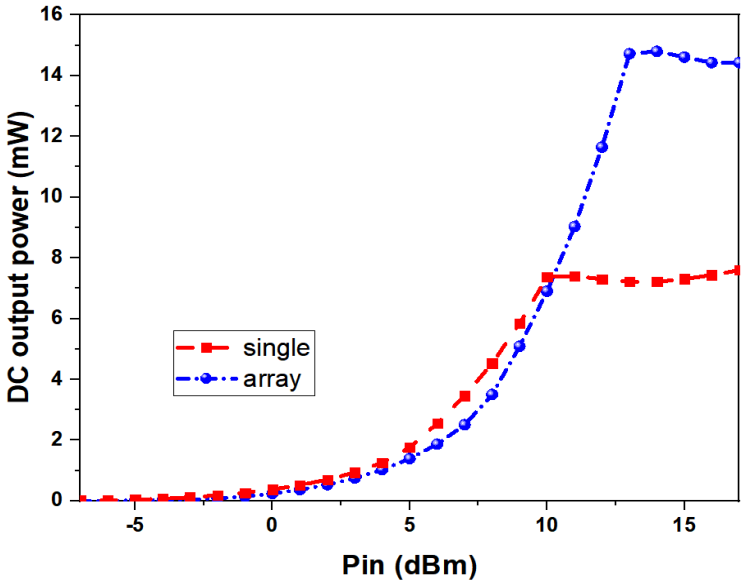

Fig. 6.16. DC output power measured at the output of single rectifier and DC array

Similarly, the output power of parallel DC combined rectenna array can be written as

$$P_p = I_p \times V_p = \frac{(V_{D1}+V_{D2})^2 \times R_{L0}}{2\times(R_{D0}+R_{L0})^2} \quad (6.2)$$

If all rectenna elements are identical, for the maximum power output condition, the load impedance of the array should be

$$R_{LP} = \frac{R_{L0}}{2} \quad (6.3)$$

This parallel DC combining can increase the output DC current. A load resistor value of 500Ω is utilized in this parallel combined array. Fig. 6.17 shows the DC output power measured at the output of single rectifier and parallel combined array. It can be observed that the DC output power is almost double than that of single at an input power of 12 dBm. Fig. 6.18 shows the RF -DC conversion efficiency of the DC array. Parallel combined DC array achieved a maximum efficiency of 73.5% at an input power of 12 dBm.

6.5. Communication Rectenna Array

The SWIPT capability of the communication rectenna array has been verified. The experimental setup of the simultaneous wireless information and power transfer of the proposed rectenna system is shown in Fig. 6.19. The signal sources for generating CW and modulated signals are the same as those used for the reciter measurement. A 5.8 GHz dual polarized patch antenna is used as the transmitting antenna. An OFDM signal with a 20 MHz bandwidth centered at 5.8 GHz is utilised as the transmitted

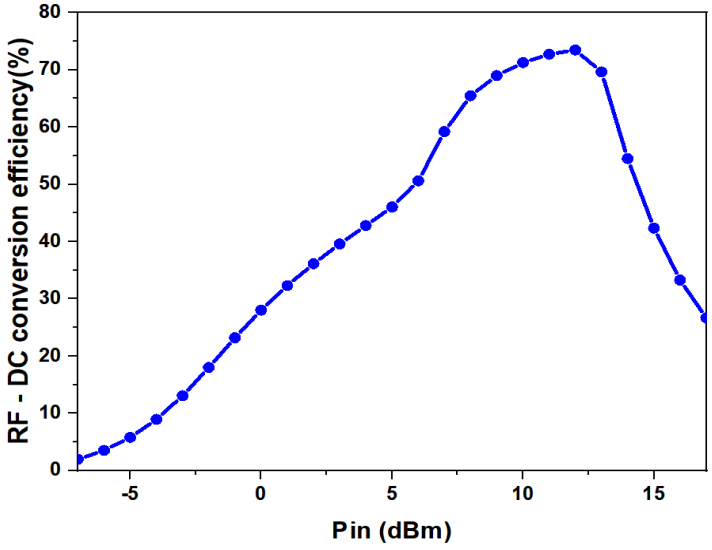

Fig. 6.18. RF to DC conversion efficiency of the DC combining.

signal as shown in Fig.6.20(a). To verify the ability of communication, received signal is captured from the communication port and is measured using the spectrum analyzer R&S-FSQ26, as shown in Fig. 6.20(b). Comparing to the transmitted signal in Fig. 6.20 (a), which is generated by the signal source, we note a relatively good agreement between the two signals, which means the communication function can also be performed using the proposed rectenna. This proposed rectenna with SWIPT property can use as standalone WSN nodes.

Fig. 6.19. Experimental setup

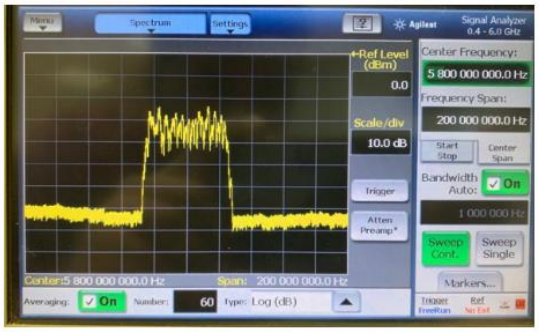

(a)

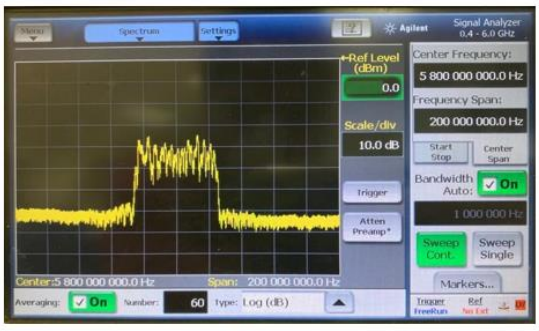

(b)

Fig. 6.20. (a) Transmitted signal (b) Received signal

6.6. Summary

A novel communication rectenna array has been proposed in this chapter for effective data and power transfer in WSN applications. In this proposed rectenna, a dual polarized 2×1 square patch antenna array has been employed to perform simultaneous wireless information and data transfer. For incorporating ambient energy harvesting in limited footprint, a multisection bended broadband monopole antenna has also been introduced. The measured 2.7 GHz bandwidth of monopole antenna extended from 1.5 to 4.2 GHz covering 2G/3G/4G/5G communication bands and ISM-2.4 GHz. Broadband rectifier has been achieved a conversion efficiency of more than 50 % from 1.49 to 3.73 GHz at an input power level of 0 dBm. Meanwhile, the communication port of the rectenna has measured 200 MHz bandwidth with good isolation (better than 20 dB) and the communication ability has been verified using a 50MHz OFDM at 5.8 GHz. The WPT rectifiers are DC combined and achieved a peak efficiency of 73.5% at an input power of 12 dBm. Thus, the proposed compact communication rectenna array with ambient energy harvesting can be an excellent candidate for future IoT and WSN applications.

References

[1] P. Zhang, H. Yi, H. Liu, H. Yang, G. Zhou and L. Li, “Back-to-Back Microstrip Antenna Design for Broadband Wide-Angle RF Energy Harvesting and Dedicated Wireless Power Transfer,” *IEEE Access*, vol. 8, pp. 126868-126875, 2020.

[2] C. Song, Y. Huang, P. Carter, J. Zhou, S. Yuan, Q. Xu, and M. Kod, “A novel six-band dual CP rectenna using improved impedance matching technique for ambient RF energy harvesting,” *IEEE Trans. Antennas Propag.*, vol. 64, no. 7, pp. 3160–3171, Jul. 2016.

[3] Y. K. Tan and S. K. Panda, “Energy harvesting from hybrid indoor ambient light and thermal energy sources for enhanced performance of wireless sensor nodes,” *IEEE Trans. Ind. Electron*., vol. 58, no. 9, pp. 4424-4435, Sep. 2011.

[4] N. B. Carvalho et al., “Wireless power transmission: R&D activities within Europe,” *IEEE Trans. Microw. Theory Techn*., vol. 62, no. 4, pp. 1031-1045, Apr. 2014.

[5] B. Strassner and K. Chang, “Microwave power transmission: Historical milestones and system components,” *Proc. IEEE*, vol. 101, no. 6, pp. 1379-1396, Jun. 2013.

[6] L. R. Varshney, “Transporting information and energy simultaneously,” *Proc. IEEE Int. Symp. Inf. Theory*, Toronto, ON, Canada, Jul. 2008, pp. 1612-1616.

[7] L. Liu, R. Zhang, and K.-C. Chua, “Wireless information transfer with opportunistic energy harvesting,” *IEEE Trans. Wireless Commun.*, vol. 12, no. 1, pp. 288-300, Jan. 2013.

[8] O. Ozel, K. Tutuncuoglu, J. Yang, S. Ulukus, and A. Yener, “Transmission with energy harvesting nodes in fading wireless channels: Optimal policies,” *IEEE J. Sel. Areas Commun.*, vol. 29, no. 8, pp. 1732-1743, Sep. 2011.

[9] B. Clerckx, R. Zhang, R. Schober, D. W. K. Ng, D. I. Kim and H. V. Poor, “Fundamentals of Wireless Information and Power Transfer: From RF Energy Harvester Models to Signal and System Designs,” *IEEE J. Sel. Areas Commun.*, vol. 37, no. 1, pp. 4-33, Jan. 2019.

[10] J. P. Curty, N. Joehl, F. Krummenacher, C. Dehollain and M. J. Declercq, “A model for u-power rectifier analysis and design,” *IEEE Trans. Circuits Syst.*, vol. 52, no. 12, pp. 2771-2779, Dec. 2005.

[11] *Surface Mount Mixer and Detector Schottky Diodes Data Sheet*, 2013.

Chapter 7. High-Power Wire Bonded GaN Rectifier for Wireless Power Transmission

A novel wire bonded GaN rectifier for high-power wireless power transfer (WPT) applications is proposed. The low breakdown voltage in silicon Schottky diodes limits the high-power operations of microwave rectifier. The proposed microwave rectifier consists of a high breakdown voltage GaN rectifying element for high-power operation and a novel low loss impedance matching technique for high efficiency performance. Wire bonding method is adopted to provide electrical connection between GaN chip and board which induces undesirable inductance. In order to realize high efficiency performance, an impedance matching network is proposed to exploit the unavoidable inductance along with a single shunt capacitor, resulting in a low loss matching circuit to achieve a compact high-power rectifier. The fabricated GaN rectifier exhibits a good performance in the high-power region and can withstand up to 39 dBm input power before reaching the breakdown limit at the operating frequency of 0.915 GHz and load resistance of 100 Ω. It has a compact size and exhibits high efficiency performance in high-power region (achieved a maximum efficiency of 61.2% at 39 dBm), making it suitable for high-power applications like future unmanned intelligent devices and WPT applications. One journal paper '*High-power wire bonded GaN rectifier for wireless power transmission'* has been published in *IEEE ACCESS* based on this work.

7.1. Introduction

Forthcoming unmanned and intelligent devices demand a wireless power technique to supply actuators or wireless sensors [1]. Input power required for these electronic devices is in the range of watts instead of micro and milliwatts for IoT sensors. Power transmission for low power IoT sensors (-20 to 20 dBm) are extensively studied and demonstrated in literatures using Si and GaAs commercial Schottky diodes [2]. But

very few studies have been reported on the WPT for high-power applications. Therefore, in order to ensure the reliability of high-power WPT and to handle large quantity of power, a high-power microwave rectifier is an essential circuit element. Conversion efficiency in high-power region is restricted by the low breakdown voltage in silicon Schottky diodes [3].

In order to prevent the breakdown in low-power capability diodes for realizing high-power rectifiers, power divider circuits are utilized to split the high input power into several diode circuits [4]. In [5], a stepped impedance transformer and coupled lines are employed to develop a planar Wilkinson power divider. However, these circuits based on transmission lines are complex in structure and large in size. To solve the low breakdown voltage problem of the Schottky diodes in the zero-bias and full-wave bridge rectifiers, the one-to-four series-dividing transformer and parallel-dividing transformer for impedance matching and power dividing were employed in [6]. Diode arrays were also used to increase the power capacity of microwave rectifiers [7]. However, these approaches introduce additional size and losses, as well as increase circuit complexity.

In this chapter, a GaN Schottky diode based high-power microwave rectifier is proposed. High current carrying ability of GaN is utilized to realize the rectifier. A GaN HEMT is turned to a Schottky diode by shorting the source and drain to make the cathode and gate as the anode. Circuit model of GaN diode is estimated for better simulation of the rectifier. A shunt diode topology is adopted in this high-power rectifier to achieve maximum efficiency. Impedance matching is achieved in this rectifier by using a single shunt capacitor along with the bond-wire interconnects. The length of interconnects is properly designed to attain the impedance matching with minimum number of lumped elements, to minimize the losses. Due to the low loss rectifying element and efficient impedance matching technique, the high-power GaN rectifier achieves a peak efficiency of 61.2 % at 39 dBm. Maximum output voltage of 24.5 V is observed at 0.915 GHz with an input power of 40 dBm.

The organization of this chapter is as follows. The rectifying element selection, wire bonding interconnects and the rectifier design are presented in Section 7.2. The proposed high-power rectifier performance is illustrated and discussed in Section 7.3. Comparison with related high-power rectifiers is also presented in this section. Finally, conclusions are drawn in Section 7.4.

7.2. Rectifier Design

7.2.1. Rectifying Element Selection

The difficulty in development of high-power rectifier is the limitations of the performance of the rectifying element. A high breakdown voltage and current carrying capabilities of the rectifying element are necessary factors in the design of a high-power rectifier.

Table 7.1. Parameters of commercially available Schottky diodes

Diode (Company)	Technology	Breakdown voltage (V)
HSMS2862 (Avago)	Si	7
DMK2790 (Skyworks)	GaAs	4
MA4E1317(MACOM)	GaAs	7
HSMS270B (Avago)	Si	15

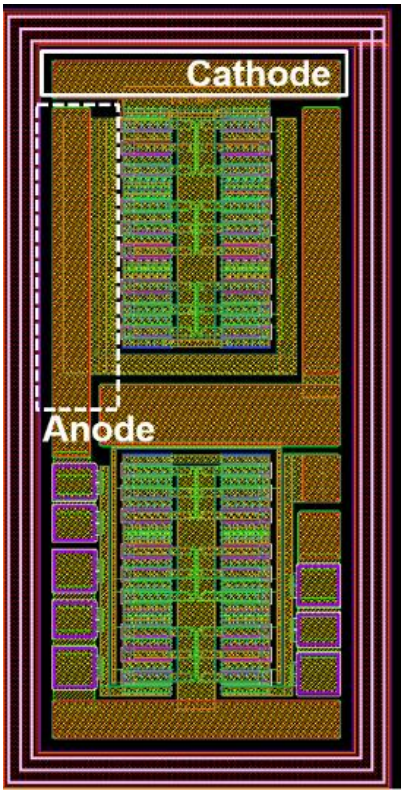

Fig. 7.1. Layout of GaN HEMT

Parameters of commercially available diodes are summarized in Table 7.1 for comparison. It can be observed that Si and GaAs based commercially available diodes have low reverse breakdown voltage (⩽15 V) and power capabilities, which limits their applicability in high-power applications. A promising solution to design the high-power rectifier is to use GaN technology. GaN has attracted much attention as a material suitable for operating at microwave frequencies due to the high-power and high conversion efficiency of high-power amplifiers (HPAs) and rectifiers [8]. Properties like wide bandgap, high electron saturation velocity, high critical electric field, and high carrier density in 2-D electron gas (2DEG) channel in the device and high breakdown voltage making it suitable for wireless power transmission applications [9]. GaN Schottky barrier diode is better suited than Si and GaAs Schottky diodes for increasing the handling power of the high-power wireless transmission.

Based on the above-mentioned properties, a GaN HEMT is proposed for wireless power transfer application. A Schottky barrier diode is implemented by shorting the source and drain of the HEMT to serve as the cathode. Layout of the GaN HEMT is shown in Fig. 7.1. To design the rectifier circuit, the GaN Schottky diode is measured individually to achieve the diode model for ADS simulation. I-V (current-voltage) and C-V (capacitance-voltage) measurements are carried out and curve fitting is performed for estimating the diode parameters. Circuit model of the GaN diode is shown in Fig. 7.2. Major differences between HEMT based GaN diode and Si diodes can be observed in breakdown voltage. The measured breakdown voltage of the GaN diode *Bv* is 76 V, which makes it suitable for high-power applications. Due to the large bandgap of GaN material, forward voltage *Vf* is observed as 1.1 V. Instead of using GaN, a low forward voltage of Si Schottky diodes with similar series resistance and breakdown voltage can

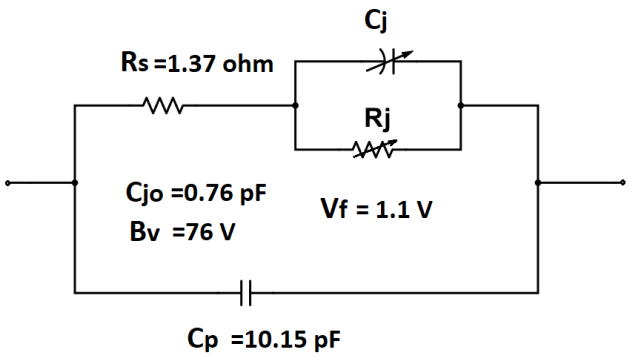

Fig. 7.2. Circuit model of GaN Schottky diode.

only perform well at low frequencies. Due to the larger size of the pads in the GaN chip, the parasitic elements have high values. However, proper impedance matching can cancel out the reactive parasitic elements of the physical diode without affecting the rectifying efficiency.

7.2.2. Wire Bonding Interconnects

For realizing a high-power and high efficiency rectifier, it is necessary to eliminate the packaging losses of the semiconductor devices. Therefore, a chip on board method is adopted in this design by directly using the GaN chip in the rectifier circuit. Chip on board method helps to eliminate the packaging of semiconductor devices and thus, the final product can be more compact, lighter, and less costly.

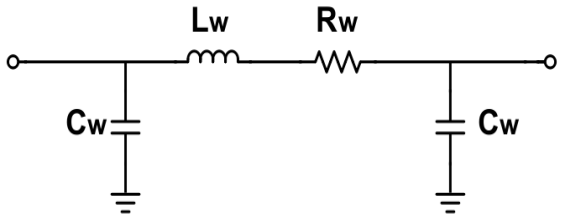

Fig. 7.3. Equivalent circuit of wire bonding.

Flip-chip and wire bonding are widely adopted techniques to interconnect chip and PCB board [10]. In flip-chip method, small solder bumps are employed in PCB board. Then the chip is inverted so that the metallized side facing the circuit board. Electrical connection is realized by reflow soldering process. Flip chip interconnects offer lower inductance however have some drawbacks including poor thermal dissipation to the PCB, and electromagnetic coupling to the PCB that may not have been taken into account during the chip design. In wire bonding, a small wire lead is used to connect the chip and board. This process is quite similar to the way that an integrated circuit is connected to its lead frame, but instead the chip is directly connected to circuit board. For higher frequencies, this interconnect leads to higher inductance values which makes the impedance matching difficult [11]. In this GaN rectenna design, wire bond interconnection is employed for connecting GaN chip on the circuit board. Wire bonding interconnect can be modeled by using an equivalent circuit as shown in Fig. 7.3. The equivalent circuit mainly consists of a series inductance (Lw) and series

resistance (Rw). Input and output capacitances (Cw) depict the electrical representation for the coupling to the substrate. As the operating frequency of the proposed design is 0.915 GHz, the major factor is the series inductance. In order to gain a better understanding of bond wire, the performance of the bond wire is analyzed using ADS software. Diameter of the bond wires in this design is considered as 30 um.

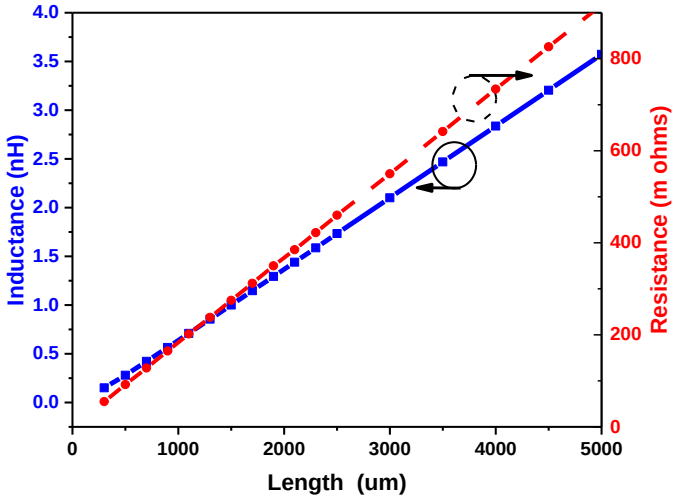

Fig. 7.4. Inductance (Lw) and resistance (Rw) versus bond wire length

Fig. 7.4 illustrates the variation in inductance and resistance value with respect to the bond wire length. It can be observed that the length of the bond wire is proportional to the inductance and resistance. Inductance is varying from 0.15 to 3.57 nH at 0.915 GHz whereas resistance varies from 0.055 to 0.9 ohms by changing bond wire length from 250 to 5000 um. The effect of input and output bond wire capacitance is considerably negligible at this frequency.

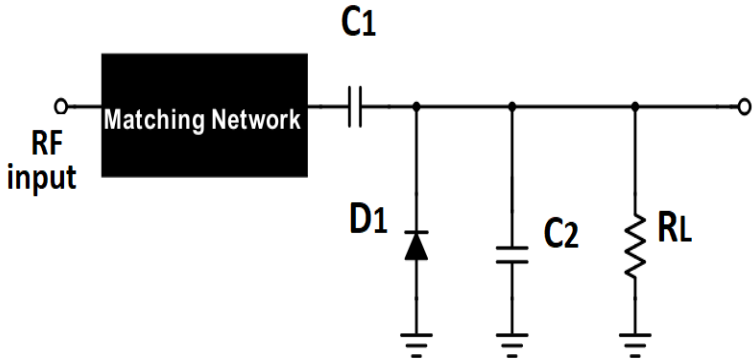

Fig. 7.5. Conventional shunt diode rectifier.

7.2.3. Impedance Matching and Rectifier Design

The topology of the rectifier is a crucial factor in determining the output power and efficiency of a rectifier. For maximum conversion efficiency, a shunt diode topology is selected in this design. A conventional shunt diode configuration is shown in Fig. 7.5. RF power is initially passed through a matching network for delivering the

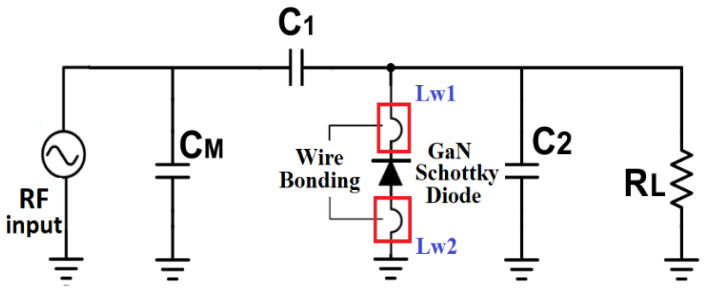

Fig. 7.6. Proposed high-power GaN rectifier.

maximum power. The negative half cycle of the wave is rectified by the shunt diode D1 and the energy is stored in C1. C2 along with load resistor RL acts as a DC pass filter to suppress the ripples from the rectified voltage. The impedance matching section in a rectifier has an important role in determining the losses of a rectifier. Due to the non-linearity of the Schottky diode, complex impedance matching circuits with lumped elements may act as the main source of loss and could affect the rectifier performance. To implement a high-power rectenna with high efficiency, it is necessary to reduce the losses accompanying the matching network as low as possible. Therefore, designing the impedance matching network with minimum components is essential to realize a high efficiency rectifier.

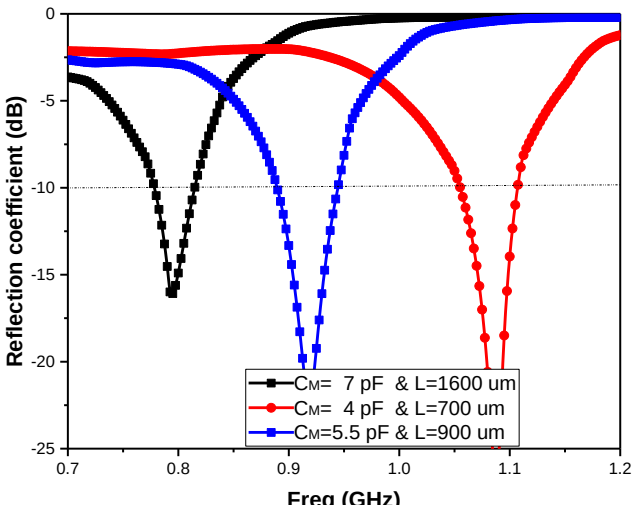

Fig. 7.7. Impedance tuning by shunt capacitor and bond wire.

For providing the electrical connection between chip and circuit board, wire bond is necessary. Hence, the proposed solution is to exploit the undesirable inductance effects of wire bonding in order to ease the impedance matching process. By properly estimating the length required for impedance matching, it is possible to avoid other lossy lumped inductors. Therefore, the unavoidable interconnecting bond wires for GaN chip can be effectively use with a capacitor for impedance matching. The schematic of the proposed high-power rectifier with a wire-bonding-based impedance matching network is shown in Fig. 7.6. The circuit includes the rectifying GaN HEMT based diode, matching capacitor C_M, energy storage element C_1, bond wires for attaching the chip to PCB, DC pass filter using capacitor C_2 and output load resistor. Instead of the conventional T-shaped or π-shaped impedance matching networks, a single shunt capacitor C_M is used in this proposed high-power rectifier along with the wire bonds for interconnection. L_{W1} and L_{W2} represents the length of wire bonds used for interconnection of GaN chip in circuit and also serves as inductors for impedance matching. For wireless energy harvesting applications, the expected RF input power from the antenna is in the range of 0 dBm (i.e., 1 mW). But in this design as we are aiming for high-power operation of rectifier, the rectifier is designed to perform well in the high-power region of 20 to 40 dBm. So, the designed high-power rectenna should have a maximum efficiency in this range of input power.

Fig. 7.7 represents the impedance tuning by employing shunt capacitor and bond wire length, L ($L=L_{W1}=L_{W2}$). It can be observed that by varying the capacitor value with accordance to the length of the wire bonds, it is possible to match the impedance properly at different frequencies. Therefore, the length of wire bond is taken as 900 um according to the simulation results. The diameter of the bond wire is initially fixed as 30 um based on the available fabrication facility. The proposed single shunt high-

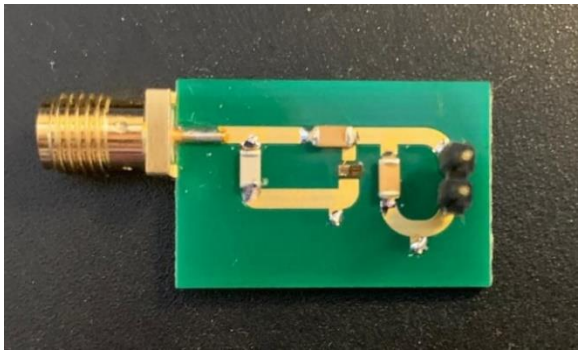

Fig. 7.8. Fabricated high-power GaN rectifier.

power rectifier is designed at 0.915 GHz on a 1.6 mm thick FR4 substrate (εr = 4.4, tan δ = 0.02). Rectifier layout is optimized to deliver maximum output DC power in the above-mentioned received antenna power. The final values of C_M and R_L have been determined through an optimization process performed with the commercial software Agilent ADS; both circuit analysis and full electromagnetic simulations have been carried out for improving results reliability. The load resistor value is selected based on the required DC voltage at the output of the rectifier. While designing the rectifier, the maximum conversion efficiency and maximum output DC power are enhanced based on the value of the load resistor. A 100 Ω resistor is selected as the load after careful design simulations. Final capacitors C_M, C_1 and C_2 are 5.1, 10000 and 10000 pF respectively. Capacitors are from Murata with model numbers GRM0335C1H5R1BA01D and GRM033R71A103KA01.

7.3. Rectifier Performance

The proposed microwave rectifier has been made and evaluated using the measurement setup shown in Fig. 7.9. A Keithley 2920 RF signal generator with an output power up to 13 dBm has been utilized to generate the RF signal at 0.915 GHz. A 40 dB power amplifier has been employed to amplify the signals for the testing of high-power rectifier. To protect the signal generator from any power surge and reflections, a 3-dB attenuator is connected between the signal generator and power amplifier. For analyzing and estimating the signal power from the power amplifier a Keithley signal analyzer together with a 20-dB attenuator is utilized. A digital multimeter has been used to measure the output voltage across the R_L resistor. The measurement setup has been appropriately calibrated considering all device losses to provide the most reliable results. Fig. 7.10 shows simulated and measured S-parameters of the designed high-power rectifier. The reflection coefficient is only measured at 0 dBm instead of the operating input power 30 dBm due to the limitations in the available measurement setup (VNA). Acceptable matching condition was confirmed under large signal S-parameters in the range of 30-40 dBm input power. Measured S-parameter has a good agreement with simulated value at 5 dBm power.

Fig. 7.11 shows the simulated and measured output DC voltage of the GaN rectifier. It can be observed that a maximum voltage of 24.5 V is obtained at 40 dBm input

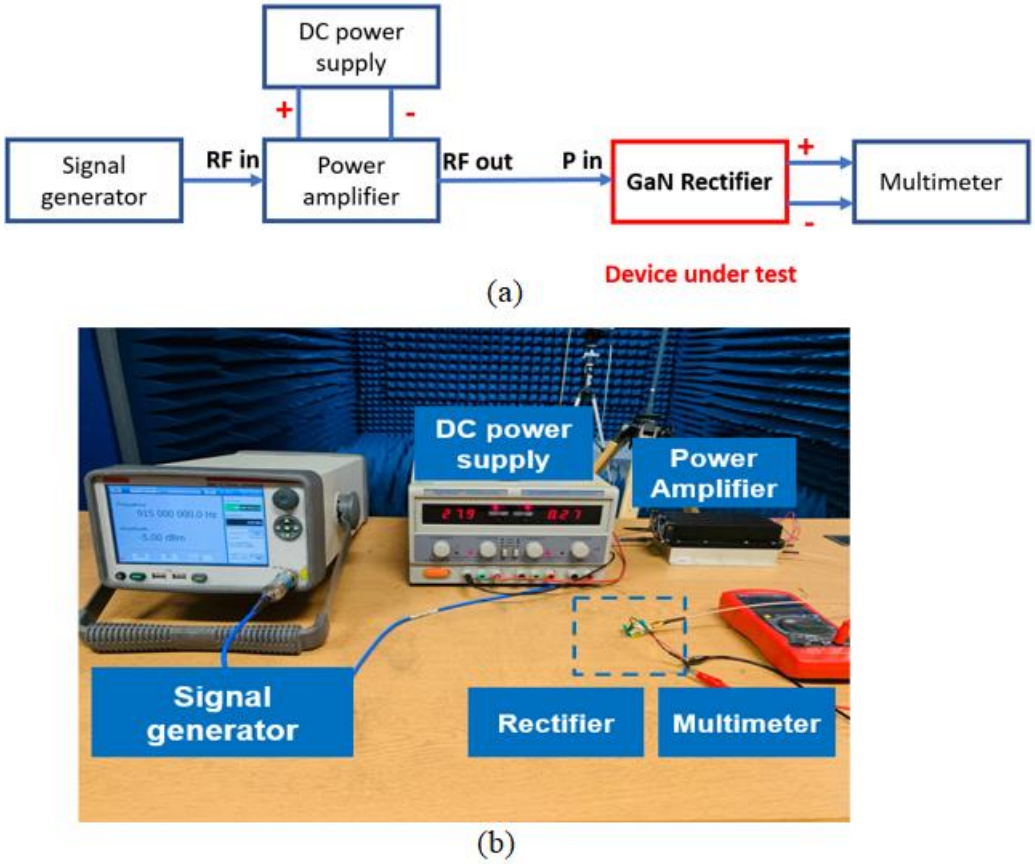

Fig. 7.9. (a) Block diagram of measurement setup (b) measurement setup of GaN rectifier.

power. Measured output voltage has good agreement with simulated values. The input power to the rectifier has been varied from 0 to 43 dBm, to measure the DC voltage across the load resistor. Input power is restricted to 43 dBm in order to ensure the safe

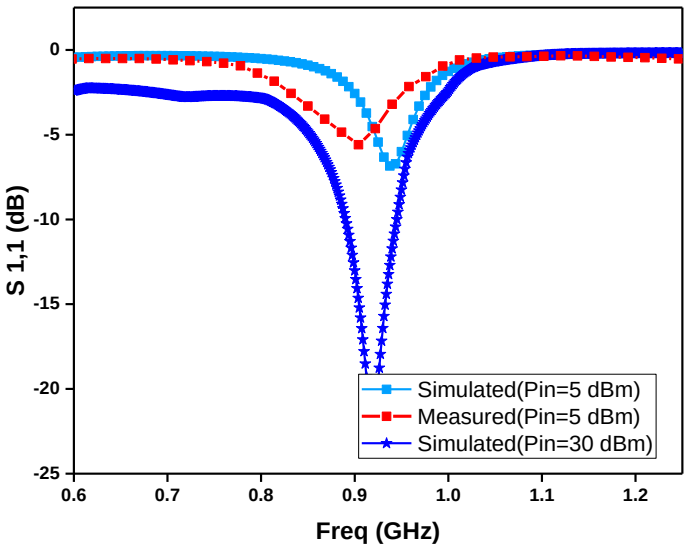

Fig. 7.10. Simulated and measured S1,1 of high-power GaN rectifier.

operation of GaN rectifier. The RF to DC conversion efficiency (η) of a microwave rectifier is calculated as the ratio of the rectified DC output power to the incident RF power, and it can be expressed as

$$\eta = {V_{out}^2}\Big/{R_L P_{in}} \times 100\ \% \tag{7.1}$$

where P_{in} is the input power and V_{out} is the DC output voltage across the load resistor R_L of the microwave rectifier.

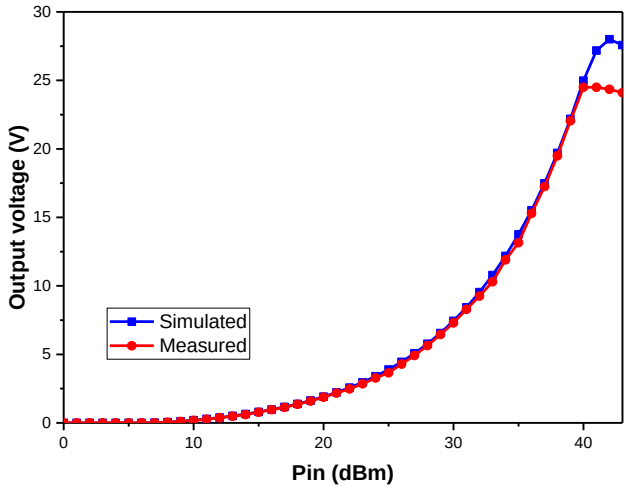

Fig. 7.11. Simulated and measured output voltage of high-power GaN rectifier.

Fig. 7.12 shows the simulated and measured conversion efficiencies of the proposed microwave rectifier as a function of input power. Maximum measured efficiency of 61.2 % is observed at 39 dBm. Efficiency is more than 50% from an input power of 28 dBm. The proposed GaN rectifier design has achieved high output power with high efficiency. Table 7.2 shows the comparison of high-power rectifiers for WPT

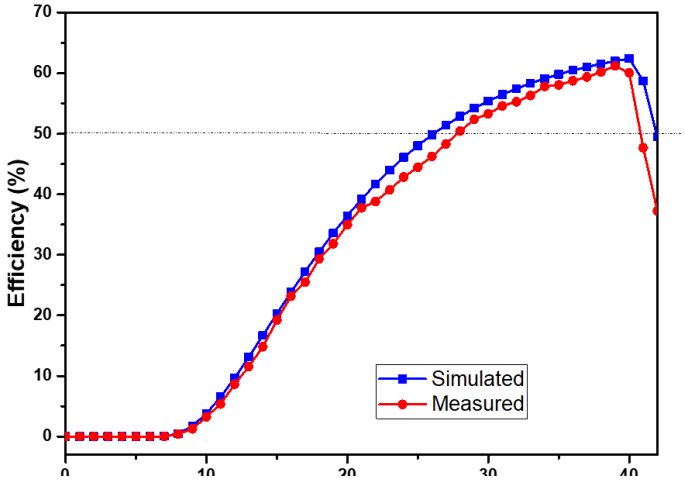

Fig. 7.12. Simulated and measured conversion efficiency of high power

application operating in similar frequency bands and input power conditions. It can be observed that our design can stand high input power of 39 dBm compared to the other published designs. For impedance matching, other designs utilized complex microstrip lines, whereas a single capacitor and interconnecting bond wires are utilized in our design. Although the measured results have shown that the proposed rectifier has a high output power, the overall dimension of our design is still the lowest due to the absence of complex and large matching networks. The proposed high-power rectifier is better than the other published designs in terms of the overall performance and size due to the novel wire bond matching, and thus is a very good candidate for future unmanned WPT applications.

Table 7.2. Comparison of the proposed rectifier with related rectifiers

Design	**[12]**	**[1]**	**[13]**	**[14]**	**[15]**	**This work**
Frequency (GHz)	0.915	2.45	0.915	2.45	0.915	**0.915**
Input power (dBm)	22	34	29	19	16	**39**
V_{out} (V)	4	15	-	5.2	5.5	**22.05**
Size (mm^2)	31 × 15.6 ($0.1\lambda_0$× $0.05\lambda_0$)	24 × 35 ($0.20\lambda_0$× $0.29\lambda_0$)	-	90 × 50 ($0.74\lambda_0$× $0.41\lambda_0$)	23 × 37 ($0.07\lambda_0$× $0.1\lambda_0$)	**16 × 22 ($0.05\lambda_0$ × $0.07\lambda_0$)**
Rectifying element	HSMS2850 and HSMS2860	HSMS 270 B	HSMS2822 and HSMS2852	HSMS 2862	HSMS2850 and GaAs pHEMT	**GaN**
Matching elements	FET transistor and microstrip lines	Three sections of microstrip lines	Microstrip lines	Double branch matching	Microstrip lines	**Single capacitor and bond wires**
Output power (Watts)	0.123	1.95	0.53	0.06	0.02	**4.9**

7.4. Summary

In this chapter, a novel high efficiency GaN rectifier for high-power WPT applications has been proposed. In order to realize high-power operations, a high breakdown voltage GaN Schottky diode is implemented from GaN HEMT. Chip on board technique is utilized to avoid the packaging losses and to reduce the size. A novel low loss impedance matching is proposed by exploiting the unavoidable inductance effects of bond wires used for providing the electrical connection between GaN chip and board. The microwave rectifier has been optimized for 0.915 GHz frequency and an input power of 39 dBm. The fabricated GaN rectifier achieved a maximum efficiency of 61.2% and a high output voltage of 22.05 V has been achieved at this optimized input power of 39 dBm. The proposed rectenna is better than other published designs in terms of the high-power operation as well as the peak voltage and power. The fabricated prototype has a compact size and exhibits high efficiency performance in high-power region, making it a good candidate for high-power electronics like future unmanned intelligent devices.

References

[1] F. Zhao, Z. Li, G. Wen, J. Li, D. Inserra and Y. Huang, “A compact high-efficiency watt-level microwave rectifier with a novel harmonic termination network,” *IEEE Microw. Wireless Compon. Lett.*, vol. 29, no. 6, pp. 418-420, June 2019.

[2] C. Song *et al*., “Novel compact and broadband frequency-selectable rectennas for a wide input-power and load impedance range,” *IEEE Trans. Antennas Propag*, vol. 66, no. 7, pp. 3306-3316, Jul. 2018.

[3] J. Zbitou, M. Latrach and S. Toutain, “Hybrid rectenna and monolithic integrated zero-bias microwave rectifier,” *IEEE Trans. Microw. Theory Techn.*, vol. 54, no. 1, pp. 147-152, Jan. 2006.

[4] Y. Xu and R. G. Bosisio, “Design of Multiway Power Divider by Using Stepped-Impedance Transformers,” *IEEE Trans. Microw. Theory Techn.*, vol. 60, no. 9, pp. 2781-2790, Sept. 2012.

[5] S. Kim, S. Jeon and J. Jeong, “Compact Two-Way and Four-Way Power Dividers Using Multi-Conductor Coupled Lines,” *IEEE Microw. Wireless Compon. Lett.*,

vol. 21, no. 3, pp. 130-132, March 2011.

[6] C. Liou, M. Lee, S. Huang and S. Mao, "High-Power and High-Efficiency RF Rectifiers Using Series and Parallel Power-Dividing Networks and Their Applications to Wirelessly Powered Devices," *IEEE Trans. Microw. Theory Techn.*, vol. 61, no. 1, pp. 616-624, Jan. 2013.

[7] U. Olgun, C. Chen and J. L. Volakis, "Investigation of Rectenna Array Configurations for Enhanced RF Power Harvesting," *IEEE Antennas Wireless Propag. Lett.*, vol. 10, pp. 262-265, 2011.

[8] H. T. Nia and V. Nayyeri, "A 0.85–5.4 GHz 25-W GaN Power Amplifier," *IEEE Microw. Wireless Compon. Lett.*, vol. 28, no. 3, pp. 251-253, March 2018.

[9] A. Hassan, Y. Savaria and M. Sawan, "GaN Integration Technology, an Ideal Candidate for High-Temperature Applications: A Review," *IEEE Access*, vol. 6, pp. 78790-78802, 2018.

[10] T. H. Hong *et al*., "Packaging Approach for Integrating 40/45-nm ELK Devices into Wire Bond and Flip-Chip Packages," *IEEE Trans. Compon. Packag. Manuf. Technol.*, vol. 1, no. 12, pp. 1923-1933, Dec. 2011.

[11] L. Lin *et al*., "Ruggedness Characterization of Bonding Wire Arrays in LDMOSFET-Based Power Amplifiers," *IEEE Trans. Compon. Packag. Manuf. Technol.*, vol. 8, no. 6, pp. 1032-1041, June 2018.

[12] A. M. Almohaimeed, M. C. E. Yagoub and R. E. Amaya, "A highly efficient power harvester with wide dynamic input power range for 900 MHz wireless power transfer applications," Proc. *MMS*, Abu Dhabi, 2016, pp. 1-4.

[13] M. Huang et al., "Single- and Dual-Band RF Rectifiers with Extended Input Power Range Using Automatic Impedance Transforming," *IEEE Trans. Microw. Theory Techn.*, vol. 67, no. 5, pp. 1974-1984, May 2019.

[14] Y. Cao, W. Hong, L. Deng, S. Li and L. Yin, "A 2.4 GHz Circular Polarization Rectenna with Harmonic Suppression for Microwave Power Transmission," *Proc. IEEE Int. Conf. Internet Things, IEEE Green Comput. Commun., IEEE Cyber, Phys. Social Comput., IEEE Smart Data*, Chengdu, 2016.

[15] Z. Liu, Z. Zhong and Y. Guo, "Enhanced Dual-Band Ambient RF Energy Harvesting with Ultra-Wide Power Range," *IEEE Microw. Wireless Compon. Lett.*, vol. 25, no. 9, pp. 630-632, Sept. 2015.

Chapter 8. High-Efficiency Wireless Power Transfer Using Duplexing Rectenna

In this chapter, a novel duplexing rectenna with harmonic feedback capability is proposed for efficient WPT (wireless power transfer) applications. The proposed duplexing rectenna can harvest the incoming RF energy efficiently and also make use of an inherent harmonic signal, which is sent back to the RF transmitter for positioning in order to guide the radiation patterns from transmitter antenna array for optimum wireless power transfer. A novel duplexing dipole antenna is designed based on the top loading and capacitive gap effects. It is used to receive RF power at fundamental frequency 0.915 GHz and transmit the second harmonic signals at 1.83 GHz as a feedback. Experimental validation of a complete WPT system with beam-scanning capability has been carried out. It is shown that the fabricated rectifier has realized a maximum RF-DC conversion efficiency of 71% (at 15 dBm input power) and a measured peak second harmonic power of -1 dBm. Thus, the proposed duplexing rectenna can form a closed-loop system by providing its location information for efficient WPT applications. One journal paper '*Second harmonic exploitation for high-efficiency wireless power transfer using duplexing rectenna'* has been published in *IEEE Trans. Microw. Theory Techn.*and one conference papers presented in *EuCAP 2020* based on this work.

8.1. Introduction

Conventionally, the rectenna for WEH and WPT is designed in a similar way, without considering the advantages of a dedicated RF source [5]. Therefore, the conventional rectennas for WEH and WPT can only offer a limited amount of dc power and normally do not have the location knowledge of the rectenna. To direct the microwave energy beam toward the desired rectenna and to enhance the incident

power level, several researchers proposed antenna arrays with beam steering capabilities [5]–[7]. Due to the use of antenna array for high gain performance, the radiation is very directive. Therefore, a slight misalignment can lead to a big drop in energy conversion efficiency and output dc power [8]. In this scenario, a feedback signal from the receiver (Rx) to the Tx can be used to overcome this problem [9]. However, it is challenging to create a passive and simple feedback signal from the Rx side where power is a critical issue.

Few studies were carried out by researchers to investigate the relation between harmonic effects in rectifiers and output dc power [12], [13]. In [14], an attempt to recycle and harvest the harmonics for improving the power conversion efficiency of the rectifier by rerectifying the harmonics. An energy harvesting passive UHF RFID relying on the exploitation of the power carried by the third harmonic signal generated by the RFID chip to provide dc power to an associated sensor while simultaneously communicating with the reader is reported in [15]. Thus, a promising technology is to use harmonics generated by the rectifying element as a feedback signal from the Rx for providing the knowledge about the Rx node [18]–[20].

In this chapter, we present the design of a novel duplexing rectenna with harmonic feedback capability for WPT applications and it offers the potential to track the Rx for effective and efficient WPT. Fig. 8.1 shows the proposed duplexing rectenna system with localization capability for WPT. At the WPT Tx side, the power from the microwave generator at the fundamental frequency (f_0) is amplified by a power amplifier. A set of phase shifters is used to control the radiation direction. In the Rx

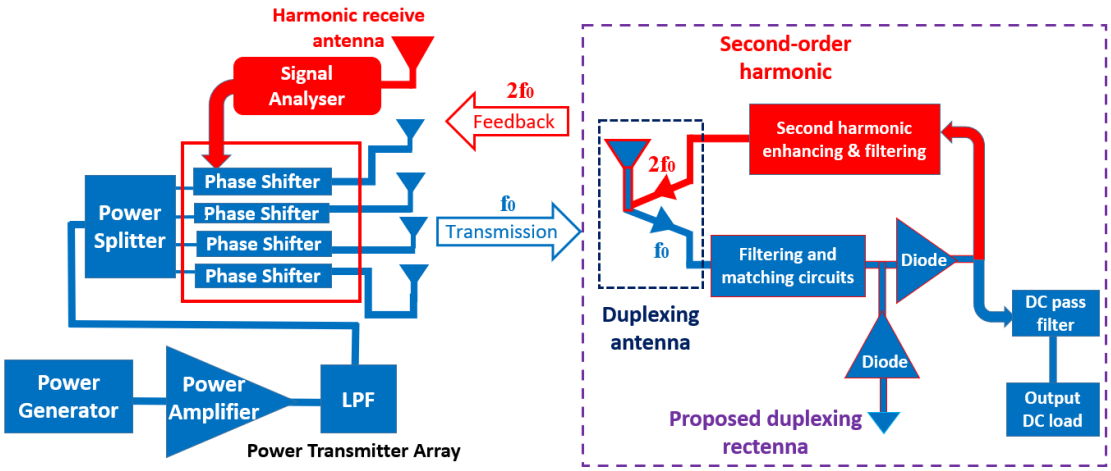

Fig. 8.1. Proposed duplexing rectenna system with harmonic feedback capability for localization in WPT.

side, a novel duplexing rectenna is designed to perform the WPT operation along with the feedback generation. More specifically, one antenna element can perform both harmonic feedback and WPT functions simultaneously. A harmonic receive antenna in the Tx side accepts the second harmonic signal ($2f_0$) from the duplexing antenna, based on which the maximum radiation direction can be determined. As the Tx antenna array has high gain and narrow beamwidth, the duplexing rectenna requires a wide beamwidth in horizontal angle for accepting the WPT power and to send the feedback even in angles for demonstrating the antenna misalignment property. Then by controlling the phase-shifters of array to the direction of maximum feedback power, targeted WPT becomes possible. The rest of this chapter is structured as follows. Section 8.2 explains the design and operation principle of the proposed duplexing antenna. The measured results are also explained in this section, Section 8.3 describes the design and performance of the harmonic feedback rectifier. Then, experimental validation of the complete WPT system including antenna array and duplexing rectenna is performed in Section 8.4. Finally, conclusions are drawn in Section 8.5 emphasizing the achievements of this research and future work directions.

8.2. Duplexing Antenna

8.2.1. Antenna Structure

The geometry of the proposed duplexing antenna is depicted in Fig. 8.2. In order to demonstrate the viability of this novel idea, we should select f_0 and $2f_0$ ideally from the license free ISM bands. Checking the ISM bands, we can see that 13.56 MHz and

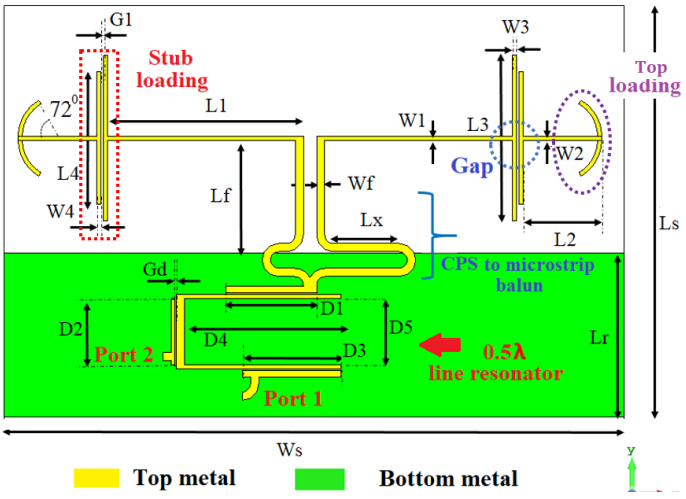

Fig. 8.2. Proposed duplexing antenna.

27.12 MHz, as well as 61.1 GHz and 122 GHz are the ISM bands available for both f0 and 2f0. However, in order to develop a demonstration system using a reasonably compact size and low loss, these frequencies are not selected on the basis of large wavelength (e.g., 13.56 MHz) and large attenuation (e.g., 61.1 GHz), at the end the ISM band frequency 0.915 GHz has been selected as the primary power transfer frequency for our optimized proof-of-concept prototype. Moreover, 915 MHz has been widely used for the studies and research in WPT applications as reported in [13], [18]. The proposed novel dipole antenna consists of a capacitive gap, a top loading and stub loading structure at each pole to realize as a compact dual-band dipole antenna which is printed on a Rogers RO4350B substrate with a relative permittivity of 3.48 and thickness of 1.52 mm. The capacitive gaps aided to generate the dual-band resonances at f0 and 2f0 frequencies and also to create similar radiation patterns in fundamental and harmonic band. Moreover, the proposed dual-band antenna is coupled to a λ microstrip line resonator for the duplexing action. Port 1 is used to excite the fundamental mode for receiving the 0.915 GHz signals to perform the WPT. Harmonic feedback is transmitted back through Port 2 at 1.83 GHz. All the physical dimensions of this antenna (after optimization to be discussed later) are tabulated in Table 8.1.

8.2.2. Evolution of Dual-Band Antenna Design

Dipole antennas are widely used in rectenna designs due to its broad beam width and structure simplicity. The target in this work is to design a half-wavelength dipole antenna that resonates at 0.915 GHz and 1.83 GHz for receiving RF power and sending feedback signals, respectively. The reason of choosing such frequencies is that the rectifier circuit generates a second harmonic signal which can be used for feedback radiation as will be discussed in detail in Section 8.3.

The conventional center-fed dipole can only excite odd-order modes [21]. Thus, a conventional half-wavelength dipole at 0.915 GHz is not good as its second odd mode is at 2.745 GHz, a new design for these two frequencies is required. The proposed dual-band antenna is evolved from three reference antennas as shown in Fig. 3. Initially, the Ref 1 half-wavelength dipole at 0.61 GHz with a length of 202 mm is selected. The second odd mode frequency in this case is at 1.83 GHz. The second reference design is a dipole antenna with capacitive gaps as in Fig. 8.3. Each arm of

the dipole is divided into two equal segments (x1 = x2 = 50.5 mm) by a gap width of 0.2 mm to provide a capacitive effect. The gap cuts off the flow of current and stores the electric field energy. According to the capacitive reactance X_C, relation with frequency and capacitance C in [22],

$$X_c = {}^{1}/_{\omega C} \tag{8.1}$$

Table 8.1. Parameters of the proposed antenna

Parameter	Value (mm)	Parameter	Value (mm)	Parameter	Value (mm)
L1	47.2	W1	0.8	Ar	25.4
L2	17	W2	0.5	Wr	1
L3	52	W3	1	Lf	37.2
L4	38	W4	1	Wf	2.5
Lm	7.5	Wm	9	G1	0.2
Lx	23	Wx	9	G2	0.2
D1	22	E1	1.6	D5	20
D2	19	E2	0.4	E5	1
D3	27	E3	1.5	Lr	43.3
D4	38	E4	0.5	Ls	114
Ws	150				

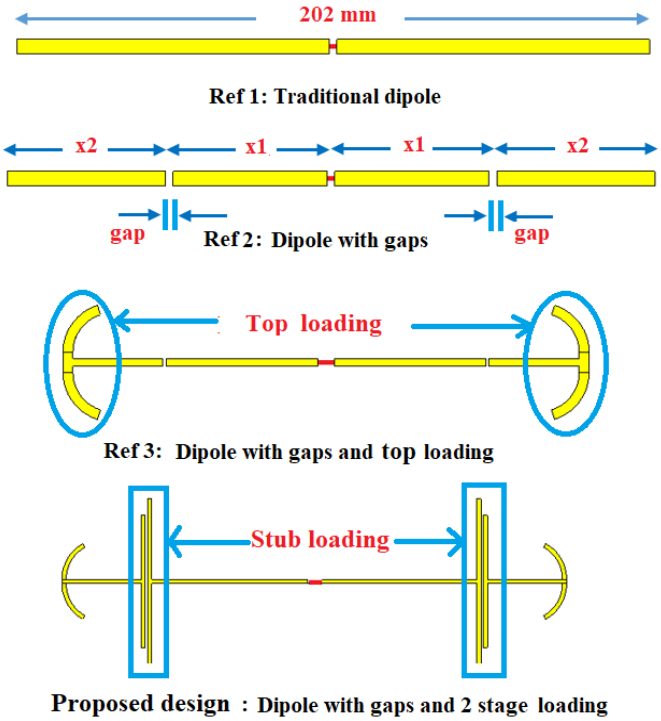

Fig. 8.3. Evolution of dual-band antenna design.

The capacitive gap reactance has much more influence on lower frequencies compared to higher frequencies. Furthermore, coupling becomes stronger with the decreasing gap width G1. Therefore, resonance of the fundamental frequency of Ref 2 antenna is shifted up to 0.915 GHz from the 0.61 GHz of Ref 1 design due to the capacitive gap effects as shown in Fig. 8.4. Fig. 8.5 (a) clearly reveals the frequency shift of fundamental mode.

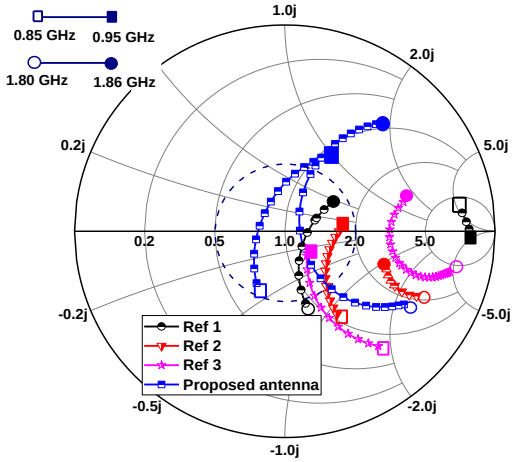

Fig. 8.4. Smith chart of the reference designs

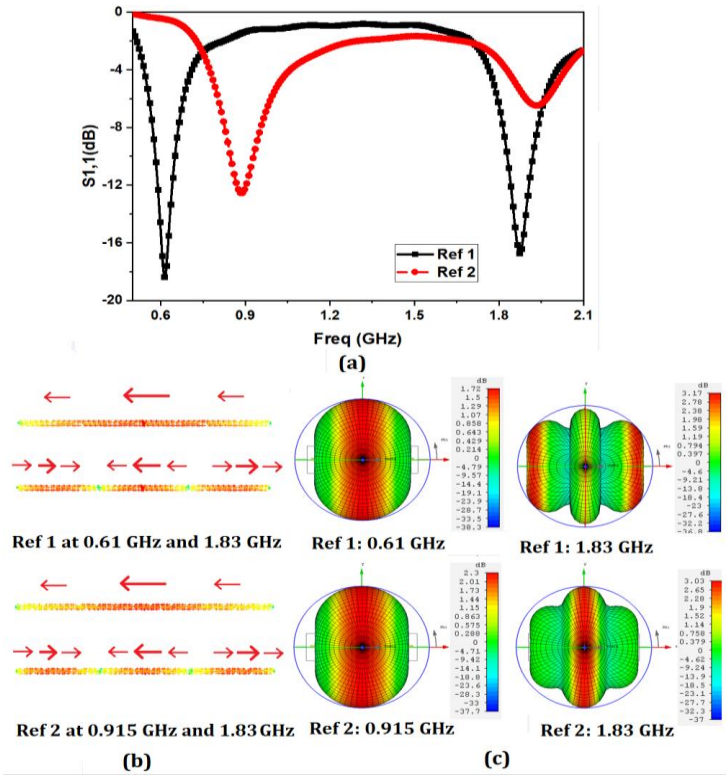

Fig. 8.5. (a) S1,1 of Ref 1 and Ref 2 (b)Surface current distribution of Ref 1 and Ref 2 (c) Radiation pattern of Ref 1 and Ref 2.

The current distributions of the two resonant modes of the Ref 1 and 2 designs are given in Fig. 8.5(b). It can be confirmed that the Ref 2 has the shifted fundamental mode at 0.915 GHz. Moreover, the capacitive gaps aided to enhance the central lobe and suppress the grating lobes in harmonic mode as depicted in Fig 8.5(c). Therefore, the two resonant modes in Ref 2 have similar omnidirectional radiation pattern. However, the second resonance is slightly shifted away from 1.83 GHz frequency. Thus, top loading is introduced in the Ref 3 design, by making circular arcs at the end of each dipole arms. The circular arcs help to reduce the second segment length of each dipole arm, but it maximizes the volume of antenna in the "kr" sphere ("k" is the wavenumber and "r" is the radius of the smallest sphere that encloses the antenna) [23]. For a half-wavelength dipole,

$$kr \approx 2\pi/\lambda \times \lambda/2 \approx \pi/2 \tag{8.2}$$

and the impedance bandwidth is far below the Wheeler–Chu limit [24]. Thus, the electrical size of the dipole can be reduced with a T-shaped top loading, while maintaining an impedance bandwidth similar to that of the λ/2 dipole. Hence, a kr of 1 is utilized to minimize the length of the antenna. Additionally, the resonance of the higher frequency band is shifted back to the 1.83 GHz due to the top loading. Unfortunately, this operation increases the real part of impedance due to the increase in overall length by the circular arcs. Further impedance matching is achieved in the proposed design by performing the stub loading in the gap region using the Smith chart analysis. Two stubs are used on either side of the gap in each dipole arm. This operation reduced the real part in the 1.83 GHz frequency band compared to Ref 3 and hence impedance matching becomes considerably simple. Dimensions of the stubs are optimized by analyzing the impedances in Smith chart with the aid of the Computer Simulation Technology (CST) software. Thus, an antenna is realized with pass bands at 0.915 GHz and 1.83 GHz. To integrate the proposed antenna with microstrip rectifier, a coplanar strip (CPS) to microstrip balun is utilized. A truncated metal ground is used in the bottom plane of the substrate. This ground plane acts as a metal reflector and helps to obtain a beam width of around 180^0 in the H-plane with increased gains.

8.2.3. Duplexing Antenna Design

A duplexer is a device that allows the use of the single antenna by both transmitter and receiver [25]. Some researchers have attempted to realize the antenna with

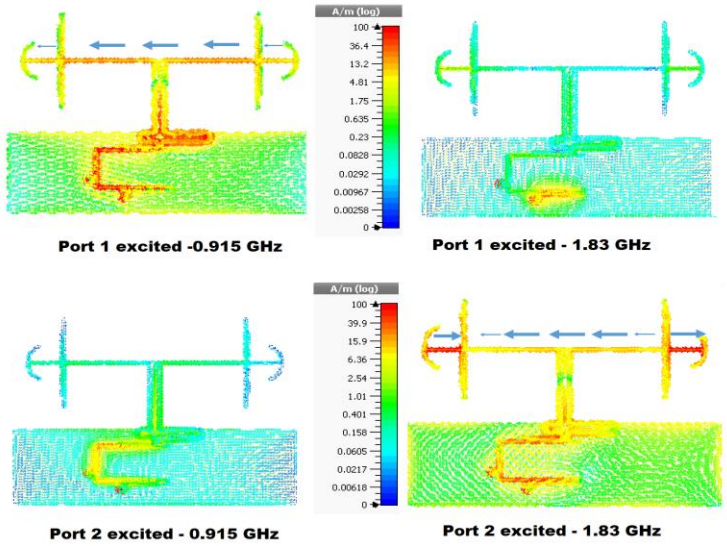

Fig. 8.6. Surface current distribution of the duplexing antenna

duplexing properties [25], [26]. A simple architecture of duplexing dipole antenna is implemented by using a 0.5λ microstrip line resonator coupled to the feed of the dual-band antenna as shown in Fig. 8.2. Two resonances of the microstrip line are designed to work at 0.915 GHz and 1.83 GHz. For receiving the 0.915 GHz signal, a coupled Port 1 is positioned at the end of 0.5λ microstrip line. Fine-tuning of the port placement is needed to achieve the maximum coupling of fundamental mode with a good consideration of harmonic signal isolation. Another coupled port is defined at the middle of the microstrip line for the harmonic signal. For the harmonic signal, 0.5λ microstrip line acts like a λ microstrip resonator. Therefore, at the line center the harmonic signal can be coupled with a zero-fundamental signal. The width of the line resonator and the coupled lines are adjusted to maximize the coupling of fundamental and harmonic signals with proper isolation. Thus, the simple 0.5λ microstrip line resonator can be used with dual-band antenna to form a duplexing antenna. Fig. 8.6 shows the surface current distribution of the duplexing antenna at different modes. Port 1 has the ability to excite the fundamental mode at 0.915 GHz and Port 2 deals with the harmonic mode excitation. Surface current distribution clearly reveals that Port 1 is completely isolated from the 1.83 GHz harmonic mode excitation and vice versa.

8.2.4. Duplexing Antenna Performance

To validate the predicted performance of this proposed duplexing antenna, a prototype was fabricated and measured. Fig. 8.7 shows the fabricated duplexing antenna. The proposed duplexing antenna has an overall dimension of 114 × 150 × 1.52 mm^3. Two SMA connectors are used to excite the two isolated bands of the fabricated antenna. Fig. 8.8 shows the simulated and measured S- parameter results of the duplexing antenna. A very good agreement between the measurements and simulations is achieved. The fundamental mode at 0.915 GHz is excited by Port 1. The measured bandwidth of the duplexing antenna is 60 MHz ranges from 0.895 GHz to 0.955 GHz in the fundamental band. Correspondingly, Port 2 can excite the harmonic mode with a bandwidth of 90 MHz which ranges from 1.815 GHz to 1.905 GHz. The isolation between the ports 1 and 2 in the fundamental band is around 13 dB. So, there is a very small leakage of WPT power at 0.915 GHz from the antenna to port 2. However, the port 2 is in the output side of the rectifier and does not affect the

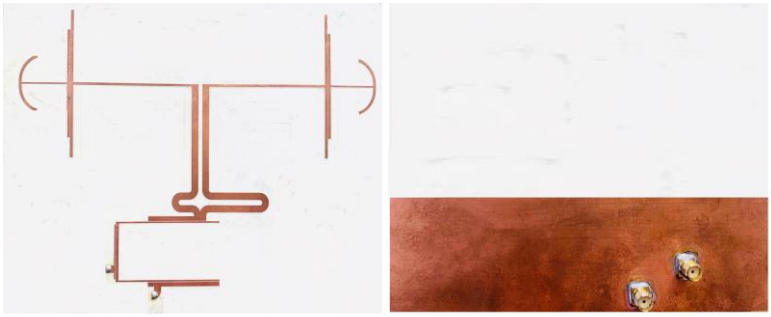

Fig. 8.7. Fabricated duplexing antenna (a) Front view (b) Back view.

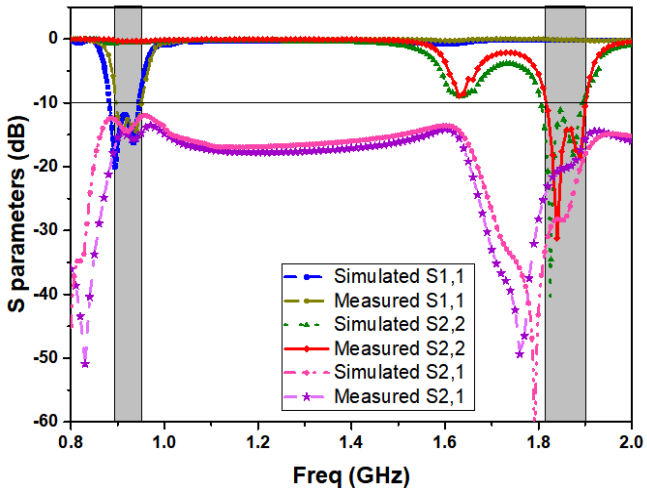

Fig. 8.8. Simulated and measured S parameters of the duplexing antenna

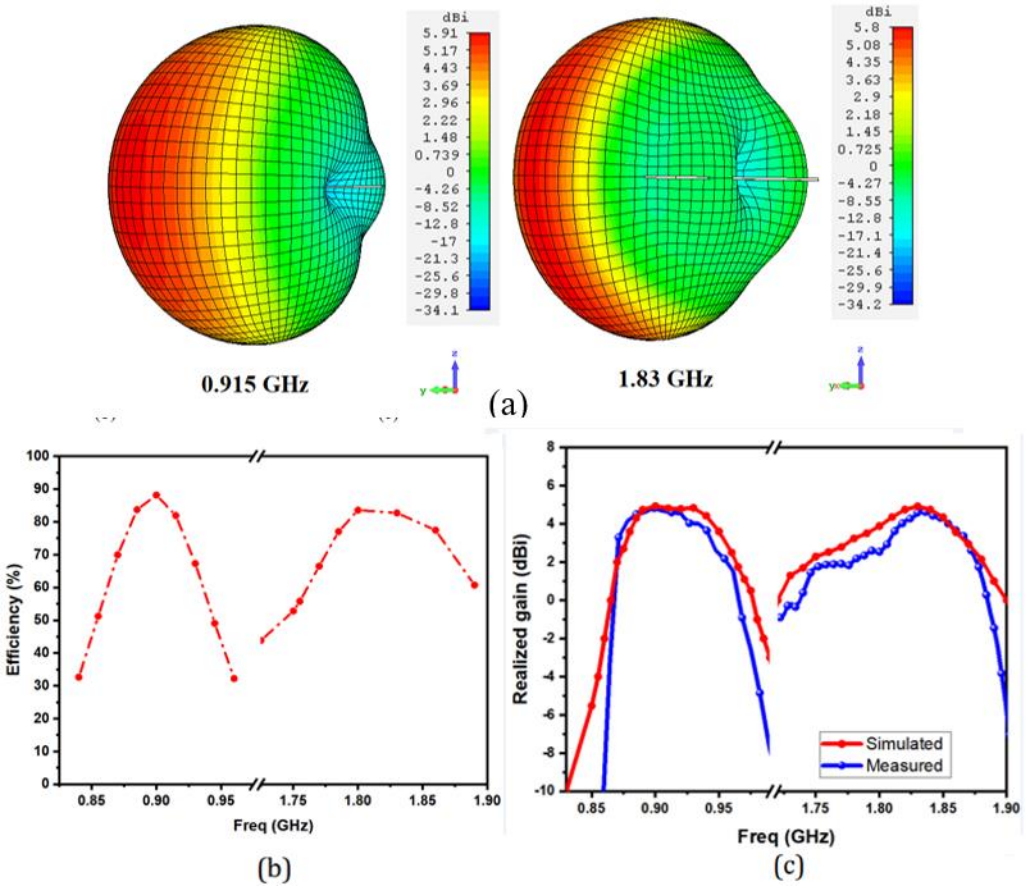

Fig. 8.9. (a) Simulated 3-D radiation patterns with excitation at Port 1 and Port 2 respectively (b) Simulated efficiency (c) Realized gain of duplexing antenna.

performance and conversion efficiency of the rectifier. While in the harmonic band where power is crucial, the isolation is around 20 dB as shown in Fig. 8.8. Consequently, the power leakage is extremely small, and it does not affect the feedback power from the rectifier to antenna. The simulated 3-D radiation patterns of the proposed antenna with excitation at Port 1 and Port 2 are shown in Fig. 8.9(a). The half-power beamwidth of the duplexing antenna is 150.50 at 0.915 GHz and 177.60 at 1.83 GHz. Fig. 8.9(b) depicts the simulated efficiency of the antenna. The duplexing antenna has achieved a total efficiency of 88% in fundamental band and 84% in harmonic band. Fig. 8.9(c) shows the simulated and measured realized gains of the antenna. Maximum measured gain of 4.83 dBi was obtained at 0.9 GHz. Similarly, 4.68 dBi was measured at 1.833 GHz. It is interesting to note that both frequency bands have similar gains and radiation patterns with good isolation, making it as a good duplexing dipole antenna.

8.3. Harmonic Feedback Rectifier

8.3.1. Analysis of Harmonic Generation

A conventional rectenna block diagram is shown in Fig. 8.10. The RF power received from the antenna is converted to DC power by the rectifying circuit after passing through a filtering and matching network. A matching network (or bandpass filter) ensures that the antenna is matched to the rectifier and the harmonics generated by the rectifying element are not radiated back into the environment through the antenna [27]. Schottky diodes can be used as the rectifying element. An accurate model of the diode is required with a low threshold voltage, a high reverse breakdown voltage, a low junction resistance, and a low junction capacitance [28]. Current-voltage relationship through the nonlinear diode can be expressed as

$$I(V) = I_s(\exp^{\left(\frac{qV}{nkT}\right)} - 1) \tag{8.3}$$

where q is the charge of an electron, k is Boltzmann's constant, T is temperature, n is the ideality factor, and Is is the saturation current [14]. Let a sinusoidal signal input to the rectifier be

$$V = V_s \cos(\omega_0 t) \tag{8.4}$$

where V_s is the amplitude and ω_0 is the frequency of the input signal. The output response of a nonlinear diode rectifier can be modelled as a Taylor series in terms of input signal voltage as

$$V_0 = x_0 + x_1 V + x_2 V^2 + x_3 V^3 + \cdots \tag{8.5}$$

where x_0, x_1, x_2,.. are the Taylor expansion coefficients [29]. For sinusoidal input in (8.4), Taylor series can be expanded as

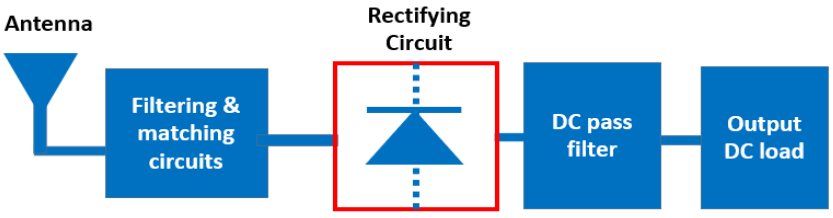

Fig. 8.10. Block diagram of a conventional rectifier

$$V_0 = x_0 + x_1 V_s \cos(\omega_0 t) + x_2 [V_s \cos(\omega_0 t)]^2 + x_3 [V_s \cos(\omega_0 t)]^3 + \cdots \quad (8.6)$$

Since,

$$cos^2(\theta) = \frac{1}{2}(1 + \cos(2\theta)) \quad (8.7)$$

and

$$cos^3(\theta) = \frac{3}{4}\cos(\theta) + \frac{1}{4}\cos(3\theta) \quad (8.8)$$

$$V_0 = x_0 + x_1 V_s \cos(\omega_0 t) + \frac{x_2}{2} {V_s}^2 + \frac{x_2}{2} {V_s}^2 \cos(2\omega_0 t) + \frac{3x_3}{4} {V_s}^3 \cos(\omega_0 t) + \frac{x_3}{4} {V_s}^3 \cos(3\omega_0 t) + \cdots \quad (8.9)$$

Thus, the output voltage contains DC rectified output and AC signals of frequency ω_0, $2\omega_0$ and $3\omega_0$ (as well as higher order harmonics), which are usually filtered out with a simple low-pass filter. Moreover, the second and third order harmonics increases with increase in incident RF power. The second and third harmonics generated from the rectifier can be expressed as

$$V_{2\omega_0} = \frac{x_2}{2} V_s^2 \cos(2\omega_0 t) \quad (8.10)$$

$$V_{3\omega_0} = \frac{x_3}{4} V_s^3 \cos(3\omega_0 t) \quad (8.11)$$

In conventional rectenna design, a DC pass filter is used to obtain a ripple free DC signal by suppressing the fundamental and harmonic frequencies from the rectified output. DC pass filter also has a key role in determining the output impedance for maximizing the DC power. An important concern in the design of feedback rectifier is to ensure the efficient operation of primary function i.e., wireless power transfer. So, it is necessary to design the rectifier with high DC output power. Another essential consideration is to avoid the use of external power or a part of rectified DC power [18]. As (8.10) reveals that the second harmonic power increases with rectifier input power and has higher value than third harmonic, this work proposed a second harmonic feedback rectifier.

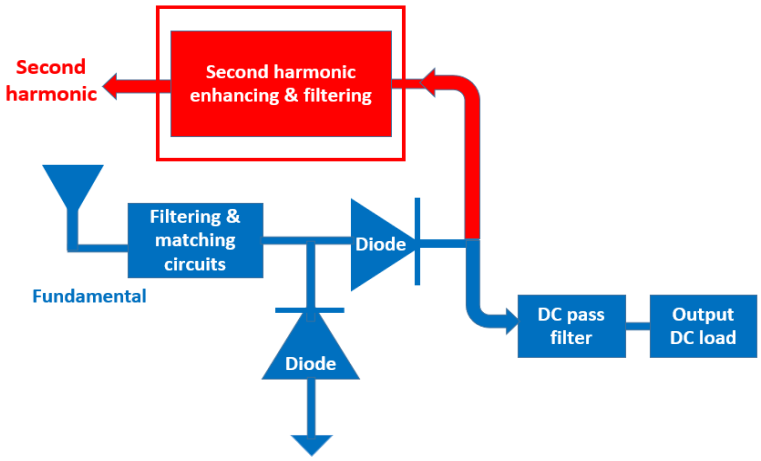

Fig. 8.11. Proposed block diagram of harmonic feedback rectifier.

Fig. 8.11 represents the proposed block diagram of the harmonic feedback rectifier. It demonstrates the RF to DC power rectification process and channelling the second harmonic from the rectifier output by enhancing and matching. A voltage doubler circuit is adopted for the design of this harmonic feedback rectifier. A second harmonic enhancing, and filtering part is commenced from the output side of diodes, before the DC pass filter. The power of the second harmonic is very crucial as it acts as a feedback signal. Therefore, great care is needed to enhance and match the impedance to the output feedback port.

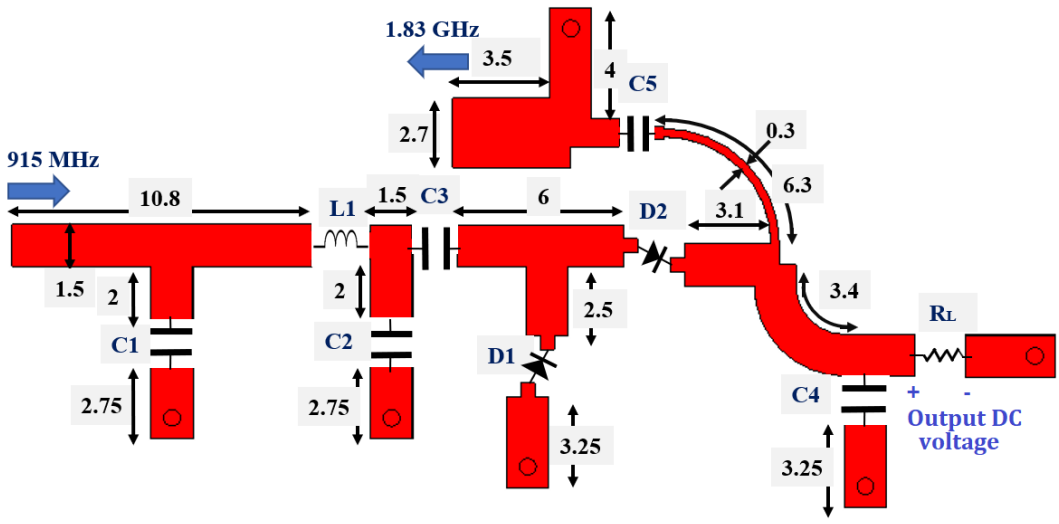

Fig. 8.12. Layout of harmonic feedback rectifier. (dimensions in mm)

8.3.2. Harmonic Feedback Rectifier Design

A novel harmonic feedback rectifier is designed based on the above-mentioned requirements. The final layout is shown in Fig. 8.12. The harmonic feedback rectifier is designed to operate at 0.915 GHz which is printed on a Rogers RO4350B substrate with a relative permittivity of 3.48 and thickness of 1.52 mm. The design flow of the rectifier starts with determining the operating power level and expected output power. The operating input power for WPT application is typically 5 to 15 dBm [5]. Therefore, Schottky diode HSMS 2860B from Avago has been selected in the design. Moreover, the low junction capacitance and series resistance of this Schottky diode are also favorable for a high output DC power. In order to realize a high output voltage rectifier, a voltage doubler topology and a load resistance of 1000 Ω are selected. The Large Signal S-parameter (LSSP) and Harmonic Balance (HB) simulations are used to analyze the input impedance for impedance matching and conversion efficiency of the rectifier structure. A π- network of lumped components is used for filtering and matching of the fundamental frequency. It consists of two capacitors *C1*, *C2* and an inductor *L1* with values 1.1 pF, 0.3 pF and 15 nH, respectively, aiming to get the circuit matched at 0.915 GHz. Capacitors *C3* and *C4* have the function of storing the energy rectified by the rectifying elements *D1* and *D2*. Despite of this energy storage function, *C3* works along with the input band pass filter in the sense that it acts as a DC block. Similarly, *C4* in shunt with load resistor R_L acts as the output low pass filter with a f_{cutoff}, cutoff frequency $1/(2\pi R_L C4)$. Initially, both capacitor *C3* and *C4* are assigned to have a value of 20 pF to serve as a DC block filter. The chip capacitors and inductors

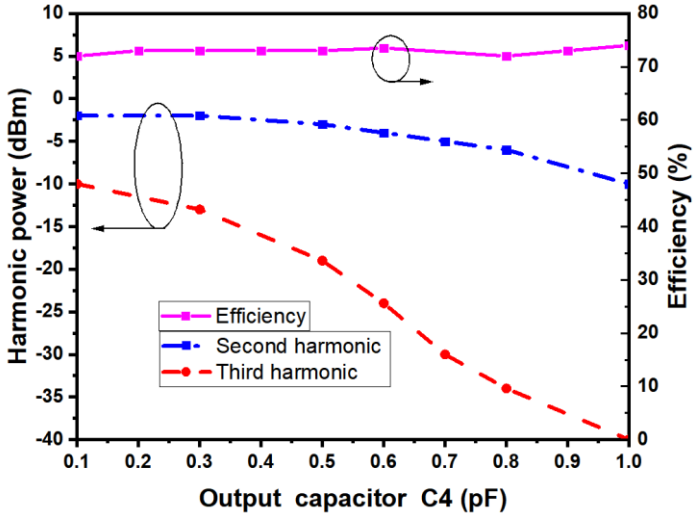

Fig. 8.13. Effect of output capacitor C4 in harmonic power and efficiency.

are modeled using S-parameter files provided by Murata and Coil craft. After the rectifier performance is optimized for required output voltage and power, the next step is to design the harmonic extraction from the output of voltage doubler. The DC pass filter on the output side is critical in this design because it has an important role in determining the second harmonic power [17]. The output capacitor *C4* has significant role in controlling the ripples and smoothing the output DC voltage. Normally *C4* with higher values can be directly used with R_L for realizing the output low-pass filter to reduce the ripples in output voltage, by bypassing the harmonics to ground. But, in harmonic feedback rectifier the load resistance, R_L and *C4* can tune the power of harmonic signals. Variations of harmonic power and conversion efficiency as a function of capacitor *C4* are shown in Fig. 8.13. By providing an input power of 10 dBm to the rectifier, second harmonic power of -2 dBm can be observed with an output DC pass capacitor of 0.1 pF whereas third harmonic power is only -10 dBm which is about 8 dB smaller than the second harmonic. Furthermore, the propagation loss for higher modes is also more compared to lower frequencies. Therefore, second harmonic will be better as the feedback signal, as it is having more power. In the designed rectifier, output capacitor has a very low impact on the input impedance of the rectifier. Moreover, the rectifier is designed for moderately wide bandwidth. Thus, it is having relatively stable performance and good impedance matching for a change of C4 from 0.1 to 1 pF. Efficiency is almost constant over 70 % for different output DC pass capacitor values. So, it provides the opportunity to tune the capacitor C4 for a better second harmonic power without disturbing the output power significantly. For realizing the harmonic feedback system, the second harmonic signal at the output of the rectifier is required to be enhanced and matched to the second port of the antenna.

Table 8.2. Circuit components used in the rectifier design

Component name	Nominal value	Part number and supplier
C1	1.1 pF chip capacitor	GRM0335C2A1R1CA01,Murata
C2	0.3 pF chip capacitor	GRM0335C2AR30BA01, Murata
C3	20 pF chip capacitor	GRM0335C2A200JA01, Murata
C4	0.5 pF chip capacitor	GRM0335C2AR50BA01, Murata
C5	1.5 pF chip capacitor	GRM0335C2A1R5CA01, Murata
L1	15 nH chip inductor	0402HP-15NX_E_, Coilcraft

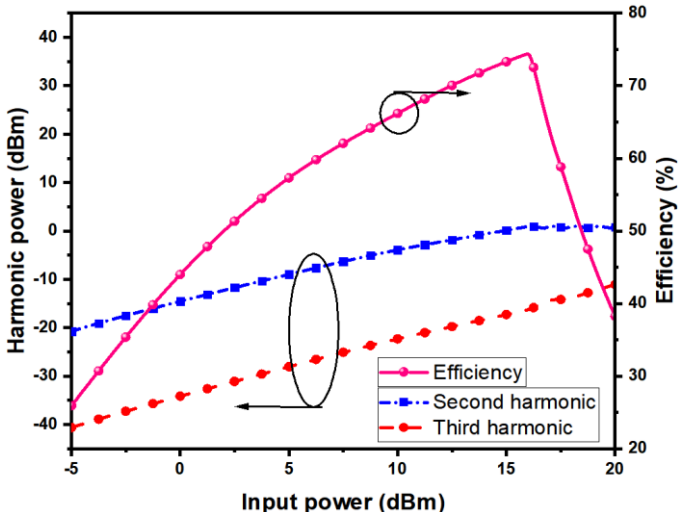

Fig. 8.14. Effect of harmonic power and conversion efficiency with respect to input power level.

Capacitor C5 has the functions of blocking the rectified DC and allowing the impedance matching of the second harmonic signal. Through proper tuning of the output capacitor C4, bypass capacitor C5 and the shorted stub length, the feedback signal is constructively directed to the harmonic port of the rectifier. These operations in the feedback signal branch do not impair the power conversion efficiency of the rectifier. In this design, after careful optimization a 0.5 pF Murata capacitor is chosen as C4 and 1.5 pF as C5. This value can provide a good conversion efficiency and second harmonic power with less ripples in the output DC voltage. The values and part numbers of the circuit components are given in Table 8.2. Fig. 8.14 shows the effect of harmonic power and conversion efficiency as a function of input power. It can be clearly observed that the second and third harmonic power are increasing with input power and the second harmonic has higher power than third. As the capacitors C4 and C5 are tuned to enhance the second harmonic, it can be observed that the third harmonic is not increasing at a higher rate as in normal rectifiers. Layout level simulations are performed using electromagnetic (EM) simulator Momentum in ADS.

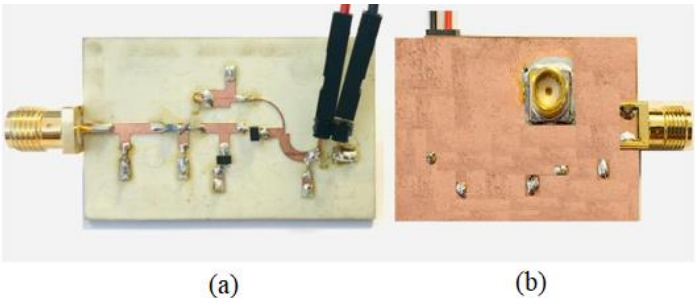

Fig. 8.15. Fabricated harmonic feedback rectifier (a) Front view (b) Back view

8.3.3. Harmonic Feedback Rectifier Performance.

For evaluating the performance of harmonic feedback rectifier, a prototype is fabricated. A fundamental signal port is placed on the edge of the circuit board while the second connector for harmonic power is connected through the substrate. The overall dimension of harmonic feedback rectifier is 25 × 40 mm^2. The fabricated prototype is shown in Fig. 8.15. The experimental setup for rectifier measurement is illustrated in Fig. 8.16(). The reflection coefficient of the designed rectifier is depicted in Fig. 8.17. The impedance bandwidth of the harmonic feedback rectifier is 390 MHz ranges from 680 MHz to 1070 MHz at 5 dBm input power. A fundamental reflected

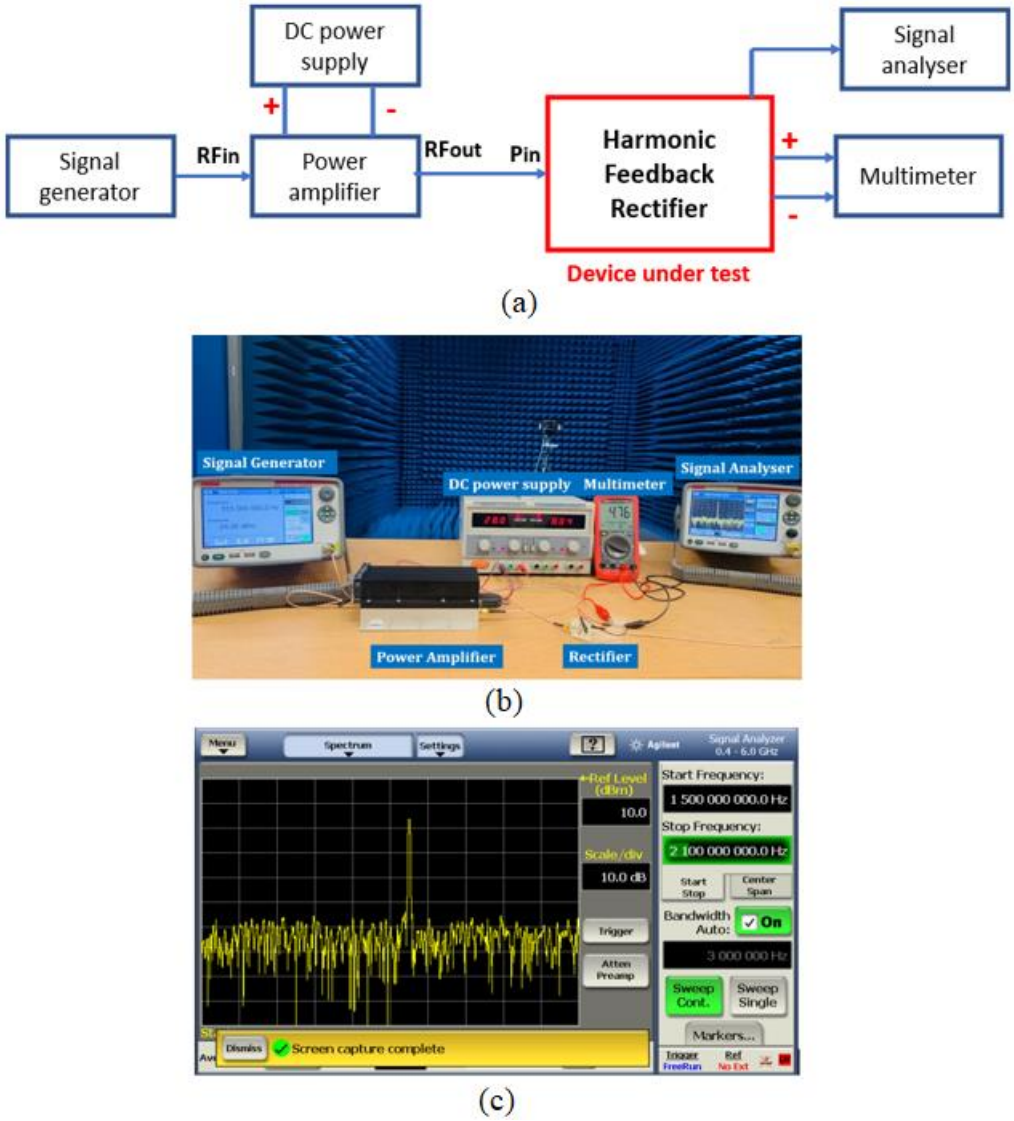

Fig. 8.16. (a) Block diagram of measurement setup (b) experimental setup for rectifier measurement (c) Harmonic spectrum at 12 dBm

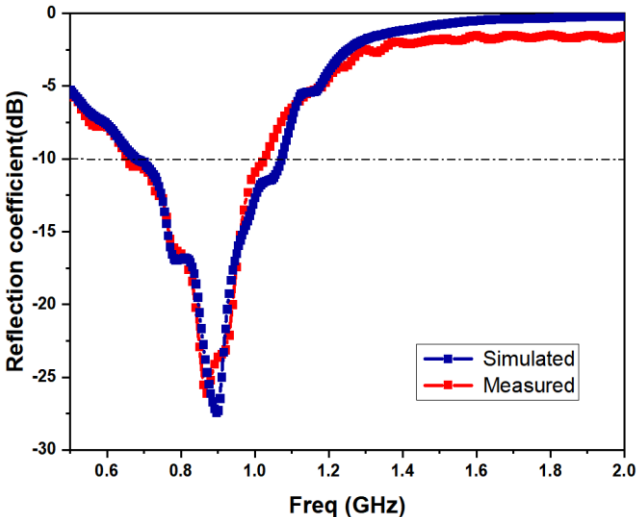

Fig. 8.17. Reflection coefficient of the harmonic feedback rectifier.

power of -23 dBm is observed with an input power of 5 dBm at the input of rectifier. Reflected power of fundamental is 8 dB lower compared to the extracted second harmonic power (-15 dBm). A Keithley 2920 RF signal generator is used for signal generation at 0.915 GHz. The signal generator can provide a maximum output power of 13 dBm. Thus, a 40-dB power amplifier is used to amplify the signals for having complete access of the input power. The output power of the signal generator is varied from -41.5 to -19.5 dBm. A 3-dB attenuator is connected between the signal generator and power amplifier to protect the signal generator from any power surge and reflections. The input power from the power amplifier is estimated using a Keithley signal analyzer. After considering the 3-dB attenuator and the loss in cables, the power from the amplifier is estimated to be from -5 dBm to 17 dBm. The output voltage and second harmonic power are measured by varying the input power. Second harmonic power is measured using the Keithley signal analyzer. Fig. 8.18(a) plots the output voltage variation with the input power. The maximum output voltage of 5.2 V is obtained at 17 dBm with a 1000 Ω load resistor. Second harmonic power is linearly increasing with input power and reaches at -1 dBm for an input power of 16 dBm as in Fig. 8.18(b). It can be observed that the simulated and measured conversion efficiency has a difference in low power region around -5 dBm. The measured one achieved only 12% while the simulated is around 25% at -5 dBm. A similar difference can be observed in the harmonic signal also. These differences in low input power are due to the inherent property of the diode to work well in high input power (5-15 dBm)

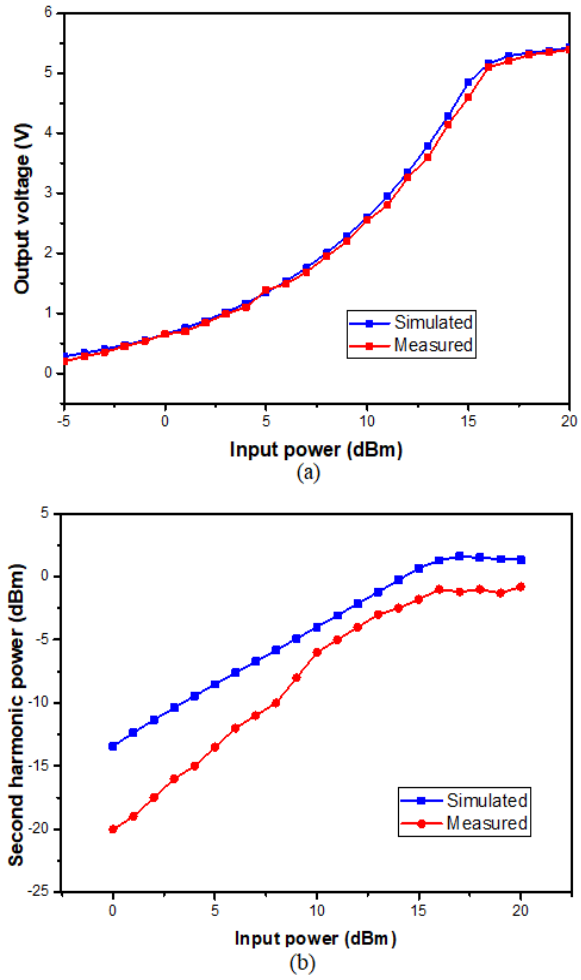

Fig. 8.18. Performance of rectifier as a function of input power (a) Output voltage (b) Second harmonic power.

and partially due to the impedance mismatch at lower input powers. Moreover, the parasitic behavior of the SMD components used in the circuit and the fabrication errors are also contributed to the slight differences in simulated and measured second harmonic power. The rectifier RF to DC conversion efficiency is defined as

$$\eta = {V_{out}^2}\Big/{R_L P_{in}} \times 100\ \% \tag{8.12}$$

where V_{out} is the DC voltage across the load resistor R_L, P_{in} is the RF input power. Fig. 8.19 shows the simulated and measured conversion efficiency for various input power. The harmonic feedback rectifier achieved a peak conversion efficiency of 71% at 15 dBm input power.

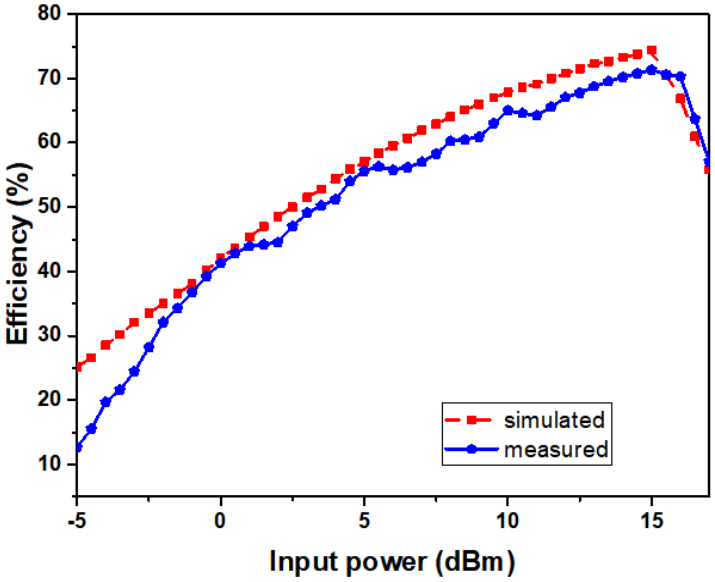

Fig. 8.19. RF to DC conversion efficiency versus input power.

8.4. Experimental Validation

A prototype of the proposed rectenna is fabricated after careful co-simulation of the duplexing antenna and harmonic feedback rectifier. The rectenna is fabricated on a 1.52 mm Rogers RO4350B substrate as shown in Fig. 8.20. A 4-element transmitter (Tx) antenna array is utilized with an overall width of 60 cm, to transmit the RF signal at 0.915 GHz. The array is fed by a 4-way power divider which is fed by a 40-dB gain microwave GaN power amplifier, which amplifies the power generated by the signal

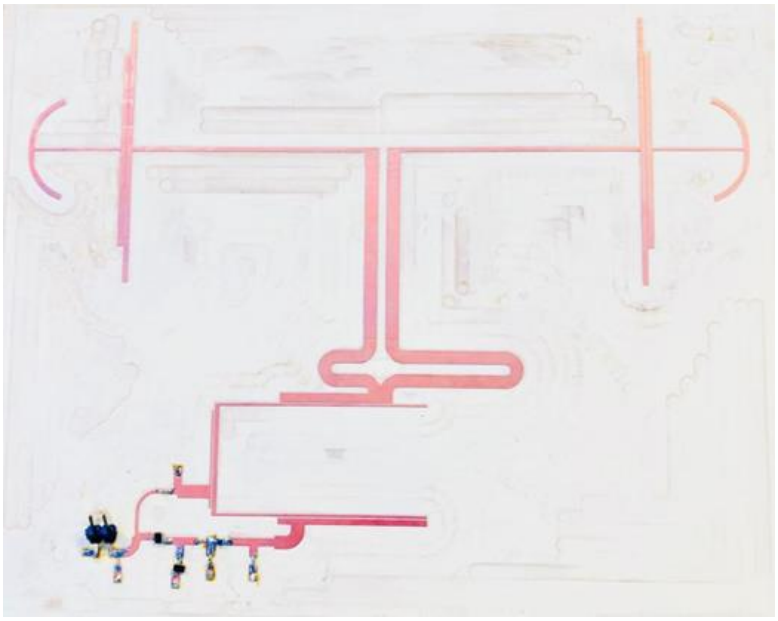

Fig. 8.20. Fabricated duplexing rectenna.

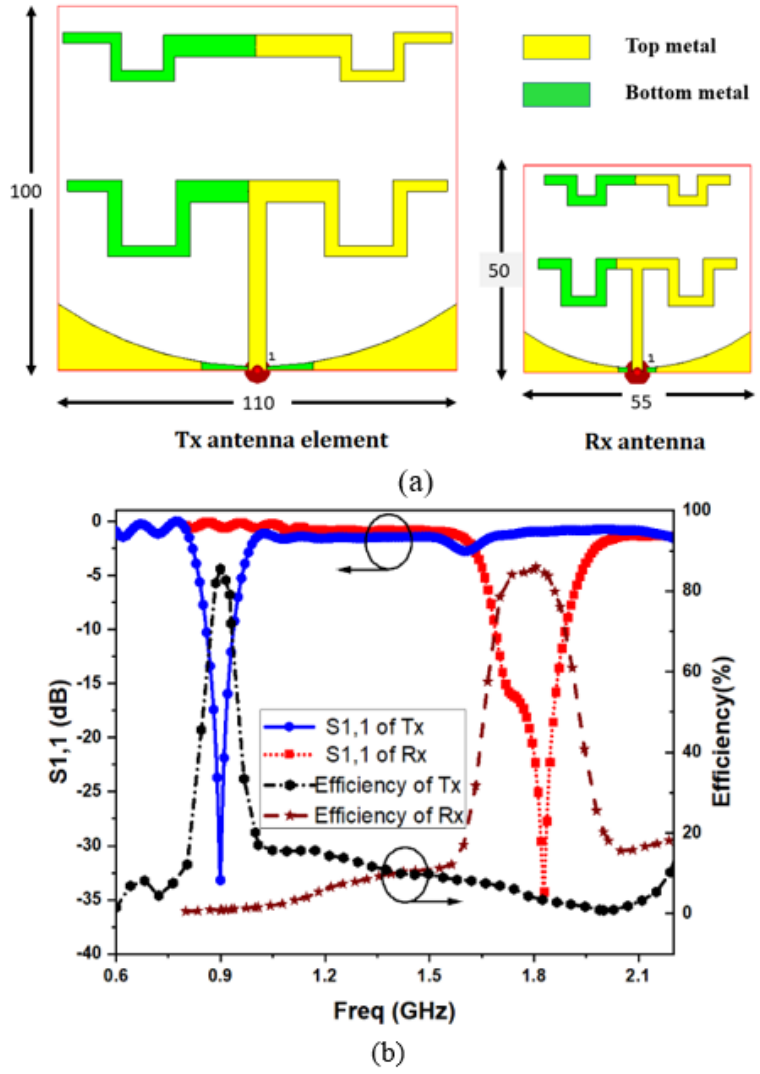

Fig. 8.21. (a) Layout of Tx antenna element and Rx antenna (b) Reflection coefficient and efficiency of Tx and Rx antennas.

generator. A harmonic feedback receives antenna (Rx) with a beamwidth of 155° is placed below the antenna array with a spacing of 15 cm to receive the second harmonic feedback signal from the duplexing rectenna at 1.83 GHz. Fig. 8.21(a) shows the layout of the Tx antenna array element and Rx antenna. Reflection coefficient and efficiency of Tx antenna element and Rx antenna are depicted in Fig. 8.21(b). The design is the same but for different frequencies. They are Yagi-Uda antennas with a meandered dipole and director, and curved reflector. Both antennas are fabricated on FR4 substrate with a thickness 1.52 mm. Simulated radiation patterns of the Tx antenna array (at various beam-scanning angles) and Rx antenna are shown in Fig. 8.22. The Tx antenna array has a gain of 12.5 dBi and the Rx antenna has a gain of 5.6 dBi.

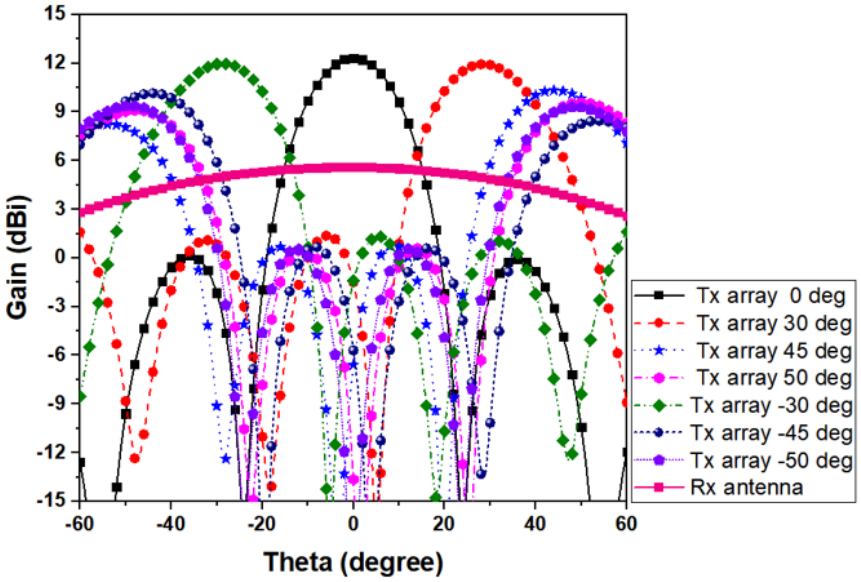

Fig. 8.22. Simulated radiation patterns of Tx antenna array (at various beam-scanning angles) and Rx antenna.

As explained in Section 8.3, a Keithley 2920 RF signal generator is utilized to generate the signal at 0.915 GHz, which fed to the power amplifier through a 3-dB

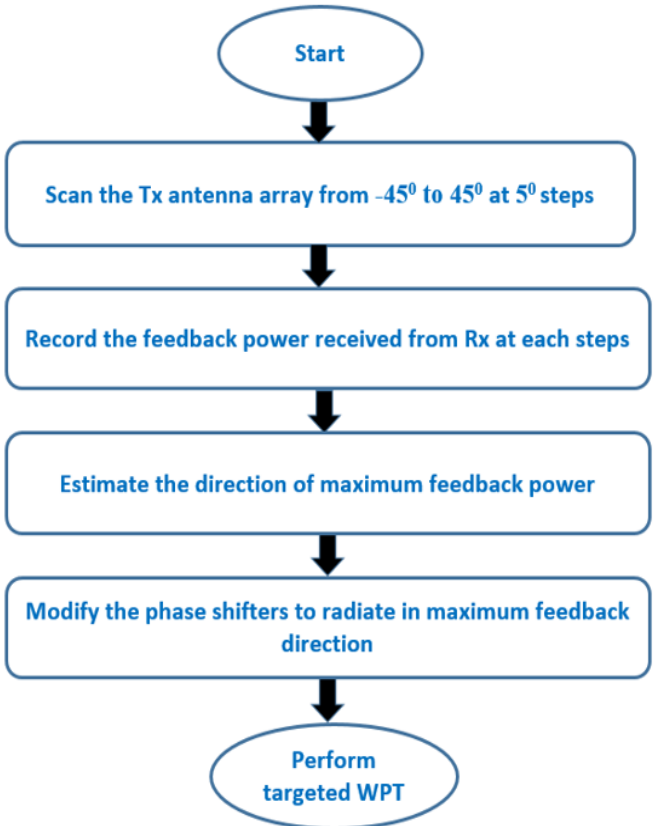

Fig. 8.23. Flow chart of operations for targeted WPT using feedback power

attenuator. The power from the 40-dB power amplifier is estimated to be from 20 dBm to 37 dBm. Then, the power is fed to the 4-way power splitter (6 dB loss) through the low pass filter. A maximum second harmonic power of -43.5 dBm from the Tx array was observed in the Rx antenna, with a maximum input power of 29 dBm. Thus, a low pass filter VLF1000 having high attenuation in stop band is utilized to reduce the second harmonic power to a very low power around -86.5 dBm (noise floor). The cable losses in the transmitter side and the insertion loss of low pass filter are estimated as 2 dB. Finally, the RF signal with power in the range of 12 to 29 dBm is fed to the Tx antenna array elements. Thus, the maximum EIRP is in the range of 41.5 dBm. In this measurement, distance R is set to be greater than 2.2 m, which satisfies the far field

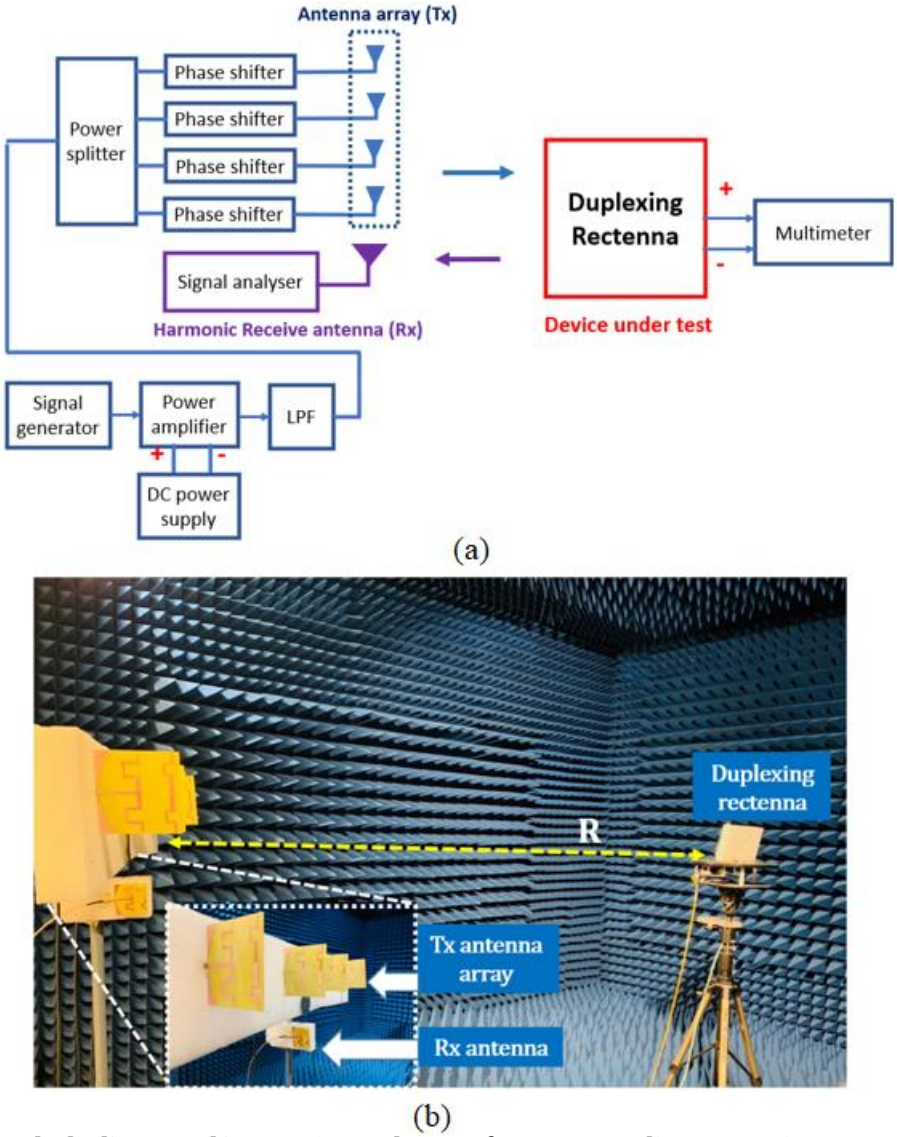

Fig. 8.24. (a) Block diagram (b) Experimental setup for antenna alignment using second harmonic feedback signal.

condition at 0.915 GHz. The transmitted continuous wave high-power signals in these experiments are only used as a demonstration in laboratory conditions, rather than real world application. In real world scenario, to meet the EIRP safety levels, it is possible to use modulated signals or multi-carrier signals to reduce the peak power levels. Fig. 8.24 illustrates the experimental setup for antenna alignment using second harmonic feedback signal. The DC output voltage is measured as a function of the received power derived by Friis' formula [30]. The power received in rectenna is therefore:

$$P_r = P_t G_t G_r \left({\lambda_0}/{4\pi R}\right)^2 \tag{8.13}$$

where P_t is the transmitted power, P_r is the received power, Gt is the transmitter antenna array's gain, Gr is the receiver antenna gain, λ0 is the free space wavelength and R is the distance between the transmitter and the rectenna. The received power in the duplexing rectenna is in the range of -12 to 7 dBm. Fig. 8.23 describes the flowchart of operations for targeted WPT using feedback power. As observed in Section 8.3, the output DC power from the rectenna is proportional to the received feedback signal, it is possible to evaluate antenna misalignment by analyzing the feedback signal power. Thus, this duplexing rectenna based WPT system can determine the rectenna position by sweeping the Tx antenna array beam from-45^0 to 45^0 by controlling the phase shifters and analyzing the feedback power received by the Rx antenna at each beam positions. Initially, if the duplexing rectenna is misaligned with the Tx antenna array, the incident power on the rectenna will be low. Thus, a low feedback power will be recorded by the Rx antenna. Then, the Tx antenna array beam sweeping will record the corresponding relative feedback power at different beam directions. The peak value of the feedback power will be the position of the duplexing rectenna and hence the Tx antenna array and duplexing rectenna can align for maximum power transfer. Even though the Rx antenna is for the second harmonic, at the output of Rx antenna a maximum fundamental power of -36 dBm is observed. However, we have used the second harmonic power and neglected the fundamental power for the antenna alignment application by using a VBF-1840 bandpass filter centered around second harmonic. Fig. 8.25 shows the received second harmonic power and DC voltage measured at two different distance from the Tx antenna array and rectenna. The experiment was conducted in multiple times to improve the accuracy of results and to analyze the uncertainties. The measured harmonic feedback powers and output DC

voltages are shown in Figs. 8.25, 8.26 and 8.27 with error bars. Output DC voltage has a small error while repeating the experiments for accuracy. However, at low received feedback power conditions slightly more fluctuations can be observed at the output of Rx antenna output. As the received power in rectenna is increasing, the received second harmonic power and output voltage are also increasing. The maximum output voltage measured at R = 2.5 m is 1.65 V, which is limited by the input power applied to the antenna array to protect the low pass filter power rating. Feedback power of -51.06 dBm is observed at R = 2.5 m, while at 3.5 m distance -56.95 dBm is measured.

For analyzing the feedback power from rectenna as a function of horizontal antenna misalignment angle (between the transmitter antenna array and rectenna), the deviation angle β is varied in steps of 50. R is kept as 2.5 m with a fixed transmitted power of 28 dBm is fed to the Tx array elements. Fig 8.26 shows the measured feedback power in Rx antenna and DC voltage from rectenna for β values ranging from -45^0 to 45^0. It can be observed that the maximum received second harmonic power -52 dBm and the maximum output voltage 1.4 V are achieved when β approaches 0°. Thus, the maximum feedback power from harmonic receives antenna and peak DC output voltage occur simultaneously at the angle corresponding to the position of the rectenna. To improve the robustness of the proposed system, a fixed phase shifter is used to tilt the antenna beam to 30^0 from the initial direction. Then, deviation angle βis varied to analyze the received feedback power at different rectenna positions.

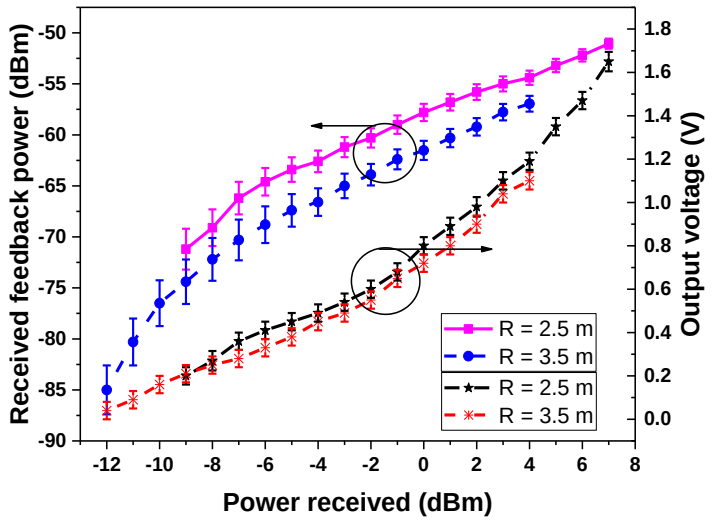

Fig. 8.25. Measured feedback power and DC voltage at R = 2.5 m and 3.5 m.

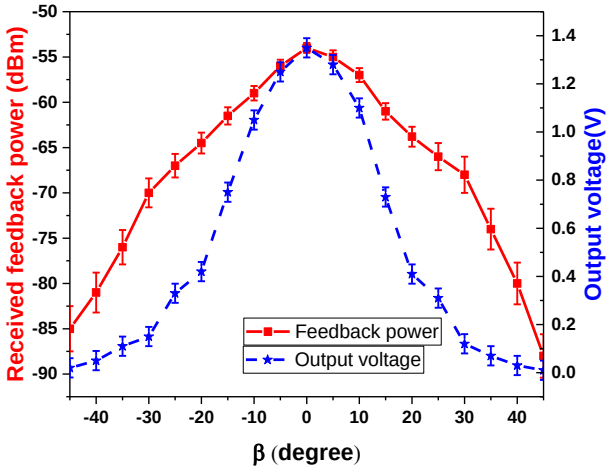

Fig. 8.26. Measured feedback power and DC voltage as a function of β.

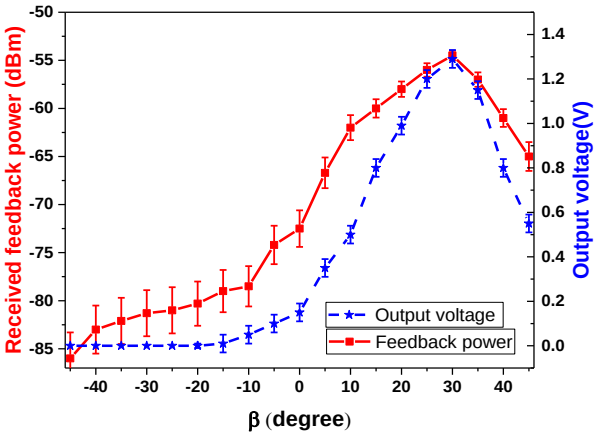

Fig. 8.27. Measured feedback power and DC voltage with a 30^0 phase shifter as a function of deviation angle β.

Fig. 8.27 shows the plot of measured feedback and DC voltage with a 30^0 phase shifter as a function of deviation angle β. It shows that the maximum second harmonic power as well as the output voltage can be achieved when the deviation angle and the beam direction coincide. Harmonic feedback power of -54.5 dBm is observed from the harmonic receive antenna output while $\beta = 30^0$. A maximum output voltage of 1.29 V is also observed in this specific β value. Therefore, it is possible to conclude that by scanning the Tx array and detecting the maximum feedback power received by the Rx antenna, the direction of rectenna can be determined. A comparison between our duplexing rectenna and some harmonic feedback rectenna designs is given in Table 8.3.

Table 8.3. Comparison of the proposed rectenna and related designs

Ref	[9]	[18]	[19]	[20]	**Proposed Rectenna**
Frequency (GHz)	2.45	0.915	2.45	2.6	**0.915**
Rectenna elements studied	Rectifier only	Rectifier and amplifier	Rectifier only	Rectifier only	**Duplexing rectenna (Rectifier+antenna)**
Extra antenna for harmonic feedback	Yes	No	No	Yes	**No**
Harmonic feedback type	Third - feedback	Second-feedback	Third - feedback	Second-feedback	Second- feedback
RF to DC conversion efficiency (%) at 10 dBm input power level	NA	30	59	NA	**65**
Harmonic power measured (dBm) at 10 dBm input power level	NA	-33	-26	NA	**-6**
Maximum measured conversion efficiency (%)	76	30	70.6	49.5	**71**
Maximum harmonic power measured in rectifier (dBm) at input power (dBm)	-21 at 7	-33 at 10	-12 at 20	-20 at 0	**-1 at 17**
Feedback power measured in transmitter side (dBm) at distance (m)	-53 at 0.5	-	-65 at 0.3	-49 at 1	**-51.06 at 2.5**
Distance coverage of feedback power	Medium	Low	Low	Medium	**High**

Our integrated duplexing rectenna uses one antenna element to perform both harmonic feedback and WPT functions simultaneously. At a typical WPT power level of 10 dBm, the proposed duplexing rectenna can provide high RF to DC conversion efficiency with a reasonable feedback power. Moreover, the measured harmonic power of -1 dBm in rectifier is relatively high compared to other rectifier works. Thus, it is evident that our single antenna based rectenna can send desired feedback signals over a relatively long distance with a considerably high-power conversion efficiency. Therefore, this duplexing-antenna based harmonic feedback rectenna can work as a standalone system which can provide a feedback signal for rectenna alignment to achieve efficient WPT.

8.5. Summary

A novel duplexing rectenna with a harmonic feedback capability has been proposed for efficient WPT applications with the antenna alignment. The proposed duplexing rectenna can efficiently convert the incident RF power at 0.915 GHz to DC and also send a reasonable harmonic signal back to the RF transmitter at 1.83 GHz for tracking the position of rectenna to improve power transfer efficiency without the need of another antenna and transmitters. The fabricated novel duplexing antenna exhibited dual-band operation with similar radiation pattern for RF power reception and sending the harmonic feedback signals simultaneously. A harmonic feedback rectifier with a maximum measured conversion efficiency of 71% and a peak second harmonic power of -1 dBm at 17 dBm has been proposed. The proposed duplexing rectenna is better than other published feedback rectenna designs in terms of the overall conversion efficiency as well as the harmonic feedback power at a typical WPT power level of 10 dBm. Experimental demonstration of rectenna alignment for optimum power transfer has been carried out by determining the maximum received feedback power. Thus, this complete WPT system based on a duplexing rectenna with feedback property is a very promising solution for future efficient WPT applications.

References

[1] M. Zorzi, A. Gluhak, S. Lange, and A. Bassi, “From today’s INTRAnet of things to a future INTERnet of things: A wireless-and mobility-related view,” *IEEE Wireless Commun.*, vol. 17, no. 6, pp. 44-51, Dec. 2010.

[2] M. Tabesh, N. Dolatsha, A. Arbabian, and A. Niknejad, “A power-harvesting pad-less millimeter-sized radio,” *IEEE J. Solid-State Circuits*, vol. 50, no. 4, pp. 962-977, Apr. 2015.

[3] M. Pinuela, P. D. Mitcheson, and S. Lucyszyn, “Ambient RF energy harvesting in urban and semi-urban environments,” *IEEE Trans. Microw. Theory Techn.*, vol. 61, no. 7, pp. 2715-2726, Jul. 2013.

[4] C. Song, Y. Huang, J. Zhou, J. Zhang, S. Yuan, and P. Carter, “A High-Efficiency Broadband Rectenna for Ambient Wireless Energy Harvesting,” *IEEE Trans. Antennas Propag.*, vol. 63, no. 8, pp. 3486-3495, Aug. 2015.

[5] S. Ladan, A. B. Guntupalli, and W. Ke, "A high-efficiency 24 GHz rectenna development towards millimeter-wave energy harvesting and wireless power transmission," *IEEE Trans. Circuits Syst. I Reg. Papers*, vol. 61, no. 12, pp. 3358-3366, Dec. 2014.

[6] S. D. Joseph, Y. Huang, S. Hsu, M. Stanley, and C. Song, "A novel dual-polarized millimeter-wave antenna array with harmonic rejection for wireless power transmission," *Proc. Eur. Conf. Antennas Propag.,* London, 2018, pp. 1-3.

[7] D. Masotti, A. Costanzo, M. Del Prete, and V. Rizzoli, "Time-modulation of linear arrays for real-time reconfigurable wireless power transmission," *IEEE Trans. Microw. Theory Techn.*, vol. 64, no. 2, pp. 331-342, Feb. 2016.

[8] Z. A. Pour, L. Shafai, and B. Tabachnick, "A practical approach to locate offset reflector focal point and antenna misalignment using vectorial representation of far-field radiation patterns," *IEEE Trans. Antennas Propag*., vol. 62, no. 2, pp. 991–996, Feb. 2014.

[9] H. Zhang, Y. X. Guo, S. P. Gao, and W. Wu, "Wireless power transfer antenna alignment using third harmonic," *IEEE Microw. Wireless Compon. Lett*., vol. 28, no. 6, pp. 536–538, Jun. 2018.

[10] S. N. Daskalakis, J. Kimionis, A. Collado, G. Goussetis, M. M. Tentzeris, and A. Georgiadis, "Ambient backscatters using FM broadcasting for low cost and low power wireless application," *IEEE Trans. Microw. Theory Techn*., vol. 65, no.2, Dec 2017.

[11] T. H. Lin, J. Bito, J. G. D. Hester, J. Kimionis, R. A. Bahr, and M. M. Tentzeris, "On-body long-range wireless backscattering sensing system using inkjet/3D-printed flexible ambient RF energy harvesters capable of simultaneous DC and harmonics generation," *IEEE Trans. Microw. Theory Techn.*, vol. 65, no.2, Dec 2017.

[12] M. Roberg, T. Reveyrand, I. Ramos, E. A. Falkenstein, and Z. Popović, "High-efficiency harmonically terminated diode and transistor rectifiers," *IEEE Trans. Microw. Theory Techn*., vol. 60, no. 12, pp. 4043–4052, Dec. 2012.

[13] J. Guo, H. Zhang, and X. Zhu, "Theoretical analysis of RF-DC conversion efficiency for class-F rectifiers," *IEEE Trans. Microw. Theory Techn*., vol. 62, no. 4, pp. 977–985, Apr. 2014.

[14] S. Ladan and K. Wu, "Nonlinear modeling and harmonic recycling of millimeter-wave rectifier circuit," *IEEE Trans. Microw. Theory Techn*., vol. 63, no. 3, pp. 937–944, Mar. 2015.

[15] D. Allane, G. A. Vera, Y. Duroc, R. Touhami, and S. Tedjini, "Harmonic power harvesting system for passive RFID sensor tags," *IEEE Trans. Microw. Theory Techn*., vol. 64, no. 7, pp. 2347–2356, Jul. 2016.

[16] T. Mitani, S. Kawashima, and N. Shinohara, "Experimental Study on a Retrodirective System Utilizing Harmonic Reradiation from Rectenna, " *IEICE Trans. Electron*., vol. E102.C, no. 10, pp. 666-672, Oct. 2019.

[17] N. Decarli, M. Del Prete, D. Masotti, D. Dardari, and A. Costanzo, "High-accuracy localization of passive tags with multisine excitations," *IEEE Trans. Microw. Theory Techn*., vol. 66, no. 12, pp. 5894–5908, Dec. 2018.

[18] C. J. Peng, S. F. Yang, A. C. Huang, T. H. Huang, P. J. Chung, and F. M. Wu, "Harmonic enhanced location detection technique for energy harvesting receiver with resonator coupling design," *Proc. IEEE Wireless Power Transf. Conf. (WPTC)*, May 2017, pp. 1–3.

[19] H. Zhang, Y. X. Guo, S. P. Gao, Z. Zhong, and W. Wu, "Exploiting third harmonic of differential charge pump for wireless power transfer antenna alignment," *IEEE Microw. Wireless Compon. Lett*., vol. 29, no. 1, pp. 71–73, Jan. 2019.

[20] T. Ngo, and T. Yang, "Harmonic-recycling Rectifier Design for Localization and Power Tuning," *Proc. IEEE Wireless Power Transf. Conf. (WPTC)*, Montreal, QC, Canada, 2018, pp. 1-4.

[21] C. A. Balanis, "*Antenna Theory: Analysis, and Design, 3rd ed*," Hoboken, NJ, USA: Wiley, 2005.

[22] R. Ludwig and P. Bretchko, "*RF Circuit Design: Theory and Applications*," Englewood Cliffs, NJ, USA: Prentice-Hall, 2000, pp. 210–220.

[23] J. Chen, J. Ludwig, and S. Lim, "Design of a compact log-periodic dipole array using T-shaped top loadings," *IEEE Antennas Wireless Propag. Lett*., vol. 16, pp. 1585–1588, 2017.

[24] D. F. Sievenpiper et al., "Experimental validation of performance limits and design guidelines for small antennas," *IEEE Trans. Antennas Propag*., vol. 60, no. 1, pp. 8–19, Jan. 2012.

[25] C. X. Mao, S. Gao, Y. Wang, F. Qin and Q. X. Chu, "Compact highly integrated planar duplex antenna for wireless communications," *IEEE Trans. Microw. Theory Techn.*, vol. 64, no. 7, pp. 2006–2013, Jul. 2016.

[26] C. X. Mao, S. Gao and Y. Wang, "Dual-Band Full-Duplex Tx/Rx Antennas for Vehicular Communications," *IEEE Trans. Veh. Technol.*, vol. 67, no. 5, pp. 4059–4070, May.2018.

[27] R. Ibrahim *et al*., "Novel design for a rectenna to collect pulse waves at 2.4 GHz," *IEEE Trans. Microw. Theory Techn*., vol. 66, no. 1, pp. 357-365, Jan. 2018.

[28] C. R. Valenta and G. D. Durgin, "Harvesting wireless power: Survey of energy-harvester conversion efficiency in far-field wireless power transfer systems," *IEEE Microw. Mag*., vol. 15, no. 4, pp. 108-120, Jun. 2014.

[29] D. M. Pozar, *Microwave Engineering*. Hoboken, NJ, USA: Wiley, 2009.

[30] Y. Suh and K. Chang, "A high-efficiency dual-frequency rectenna for 2.45- and 5.8-GHz wireless power transmission," *IEEE Trans. Microw. Theory Techn*., vol. 50, no. 7, pp. 1784-1789, July 2002.

Chapter 9. Conclusions and Future Work

This thesis has been mainly divided into two parts with the first part focused on developing rectennas for ambient energy harvesting and the second part focused on developing rectennas for wireless power transfer. The antenna and rectifier requirements for both applications are different and hence the challenges associated with them are different.

An overview on the current state of the art of the rectenna designs has been introduced in the beginning. This had been followed by a brief familiarisation of rectenna for ambient energy harvesting and wireless power transfer in Chapter 2. Motivated by the potential of creating energy-harvesting enabled self-sustainable wireless sensors and low power electronic devices, wireless energy harvesting from ambient EM fields has becoming an emerging technology and has attracted an upsurge of research interests during the past ten years. However, nonlinear effects in rectennas are an important factor affecting the performance of ambient WEH systems. In WPT systems, available rectenna designs are not making use of the advantages of a dedicated RF transmitter. As a consequence, there are very few rectennas reported with good performance for the target applications.

Although some of the designs discussed in this thesis are not completely suitable for implementation, the idea and the knowledge gained from these designs will still be useful for practical design guidance.

9.1. Key Contributions

In this thesis, six main contributions for ambient energy harvesting and wireless power transfer have been achieved. Some results of this thesis have been peer reviewed by many top scientists and researchers in this field. The major contributions of this thesis are outlined in the following six sub-sections.

9.1.1. Broadband Rectenna

In Chapter 2, the lack of broadband rectenna designs for harvesting energy from a large spectrum had been discussed. Considering the factors and the challenges, a novel broadband rectenna for wireless energy harvesting has been proposed in Chapter 3. A novel broadband Yagi-Uda antenna with a transmission lines-based broadband rectifier has been demonstrated. A highly compact broadband antenna with constant enhanced gain has been realized using curved reflectors, meandered dipoles and director. The novel three-stage transmission lines-based impedance matching technique has successfully demonstrated an improved conversion efficiency of more than 50% over a wide bandwidth of 1.12-2.43 GHz (FBW = 74%). The proposed design outperformed the existing designs in terms of frequency coverage and overall size under similar operating conditions. One journal paper has been published in *IEEE ACCESS* and two conference papers were presented in *EuCAP 2018* and *AWPT 2019* based on this work.

9.1.2. Highly Sensitive Dual-Band Rectenna

A highly sensitive rectenna with omnidirectional radiation is a desirable feature for ambient energy harvesting. In addition, a simple rectenna with compact size and minimum matching elements was also desired for the ease of fabrication and lower cost. Considering these factors, a novel dual-band rectenna was proposed in Chapter 4, combining a dipole antenna with folded stubs and a high sensitivity rectifier. An important contribution in this work is that we have developed a novel dual-mode dipole antenna with folded stubs. By introducing these stubs in the dipole antenna, the effective electrical length for the third-order mode has been increased, which shifts the third-harmonic frequency down and results in a dual-mode antenna with a wideband characteristic. A stable omnidirectional radiation pattern was achieved over the entire operating band from 2.95 to 4.75 GHz. Thus, the proposed broadband dipole antenna with a compact size ($0.45\boldsymbol{\lambda}_0 \times 0.15\boldsymbol{\lambda}_0$), is a promising solution for future wideband applications. A dual-band antenna has been demonstrated to cover the 0.915 GHz and 2.45 GHz based on the proposed dual-mode technique. Another major contribution is that we have developed a novel single external inductor-based highly sensitive rectifier for very low power ambient energy harvesting. Based on the rectifier design, a dual-

band rectifier has successfully proposed. Finally, this design has demonstrated very high conversion efficiencies of 53% and 40% at a low input power of -15 dBm. It is the first dual-band rectenna design with high conversion efficiency at ambient environments. One journal paper on *IET Microwave Antennas & Propagation* currently has been submitted based on this work.

9.1.3. High Efficiency RF Energy Harvester

The motivation and the recent developments of IoT systems have been discussed in Section 5.1. Considering the power requirements for these IoT sensors, a high efficiency RF harvester has been proposed in Chapter 5. Instead of the conventional wideband antenna based rectenna, a novel combined harvesting topology has been proposed in this Chapter, where several dual-band and broadband antennas were utilized to harvest RF energy and fed to different RF branch. The DC output from each RF branch was initially connected in parallel and then, DC output from each rectenna was combined serially to produce maximum output DC voltage. The fabricated high sensitivity and high efficiency RF energy harvesting system comprised of five antenna elements to cover the ambient RF energy in 915-960 MHz, 1.8-2.7 GHz, and 3.4-3.7 GHz frequency bands. Since many previous rectenna designs have focused on high input powers that are not suitable for energy harvesting from the real ambient environments. Five highly efficient dual branch rectifiers have successfully demonstrated an improved conversion efficiency at very low ambient power conditions. Under the similar condition, the overall efficiency and output power of this design were much higher than that of other designs reported in the literature.

9.1.4. SWIPT Rectenna With AWEH Capability for WSN Nodes

Wireless sensor networks require an uninterrupted power supply for powering the WSN nodes in order to perform data acquisition and communication with other nodes. Considering these aspects, a novel communication rectenna solution has been introduced to provide effective data and power transfer in wireless sensor nodes. The proposed design demonstrated simultaneous wireless information and power transfer along with the AWEH capability for facilitating uninterrupted power supply and data

transfer of WSN nodes. The proposed compact rectenna system has been designed with a dual polarized 2×1 square patch antenna array and a multisection bended broadband monopole antenna for performing SWIPT and AWEH. Fabricated multibranch broadband rectifier demonstrated a fractional bandwidth (FBW) of 85% (from 1.49 to 3.73 GHz) and a power conversion efficiency of more than 50% at a 0 dBm input power level. Thus, the proposed communication rectenna array with ambient energy harvesting can be a promising candidate for future wireless sensor nodes.

9.1.5. High Power GaN Rectifier

Future unmanned and smart devices require a wireless power technique to supply actuators or wireless sensors. In Chapter 7, a novel GaN Schottky diode based high-power microwave rectifier has been proposed. A GaN HEMT was converted to a Schottky diode by shorting the source and drain to make the cathode and gate as the anode. A novel low loss impedance matching has been proposed by exploiting the unavoidable inductance effects of bond wires used for providing the electrical connection between GaN chip and board. The fabricated GaN rectifier demonstrated a maximum efficiency of 61.2% and a high output voltage of 22.05 V at the optimized input power of 39 dBm. The proposed rectenna is better than other published designs in terms of the high-power operation as well as the peak voltage and power. One journal paper has been published in *IEEE ACCESS* based on this work.

9.1.6. Duplexing Rectenna With Harmonic Feedback Capability

A novel duplexing rectenna with a harmonic feedback capability for efficient WPT applications with the antenna alignment has been proposed in this chapter. Unlike the conventional WPT rectenna, this duplexing rectenna can efficiently convert the incident RF power at 0.915 GHz to DC and also send a reasonable harmonic signal back to the RF transmitter at 1.83 GHz for tracking the position of rectenna to improve power transfer efficiency without the need of another antenna and transmitters. The fabricated harmonic feedback rectifier has successfully demonstrated a maximum measured conversion efficiency of 71% and a peak second harmonic power of -1 dBm

at 17 dBm input power. Experimental demonstration of rectenna alignment for optimum power transfer has been carried out by determining the maximum received feedback power. It is the first duplexing rectenna design that can work as a standalone system to provide a feedback signal for rectenna alignment to achieve high efficiency WPT. Thus, this complete WPT system based on a duplexing rectenna with feedback property is a very promising solution for future efficient WPT applications. One journal paper has been published in *IEEE Transactions on Microwave Theory and Techniques* and one conference paper has been published in *EuCAP 2020*.

9.2. Future Work

Based on the conclusions drawn and the limitations of the work presented, future work can be carried out in the following areas.

- Development of new Schottky diodes with a lower loss, a smaller series resistance and a much higher saturation is an important future research direction in WEH and WPT applications. As discussed in Chapter 5, the high forward bias voltage, high series resistance and high junction capacitance of the diode limits the power sensitivity of the rectenna at the ambient power levels. Moreover, the relatively large parasitic capacitances in state-of-the-art semiconductor diodes lead to a strong nonlinearity and impedance matching difficulty. In the literature, zero-biased antimonite-based heterojunction backward diodes (Sb-HBDs) are shown to have extremely low junction parameters and superior I-V characteristics when the input power is very low. Furthermore, zero bias resistance in the rectification process of the spin-diodes could improve the rectification efficiency even at a very low-power level. Utilization of these diodes in the presented broadband rectenna designs in this thesis may significantly improve the energy captured from the ambient low power environments.
- Frequency Selective Surfaces (FSS) for ambient energy harvesting is a major research direction. The excellent absorption characteristics of FSS is quite interesting. However, FSS designs have narrow bandwidth and also it uses rectifiers in every unit cell, which meant a considerable part of the collected

power was dissipated at the diodes. Therefore, FSS with high efficiency performance over broad spectrum is a promising research area.

- MIMO WPT is another interesting possibility for optimized simultaneous wireless information and wireless power transfer in multipath communication channels. Recently, some fascinating studies were performed for the design of MIMO WPT via radio waves in multipass circumstances. Target detection is a major challenge in MIMO WPT. The retrodirective target-detecting method in the multipass circumstances is a possible technology for MIMO WPT.
- Optical nano-rectennas for visible and infrared light energy harvesting is a latest research topic. Optical rectennas are fundamentally similar to microwave rectennas, however it is more difficult in practice to make an optical rectenna. Rectifying diodes operating in terahertz frequencies for visible light are only a few types of specialized diodes. As the operating frequency is high, optical antenna requires a challenging nanotechnology fabrication process. Moreover, an optical antenna typically absorbs very little power due to small size, and therefore works with low efficiency. Due to these challenges, optical rectennas have so far been restricted to laboratory demonstrations, typically with intense focused laser light producing a tiny but measurable amount of power.
- Until now, the RF energy harvesting system using rectennas has not been commercialized by large companies. The reason is that the energy captured from the ambient EM fields is too low for a typical application, as mentioned in Chapter 1. Therefore, hybrid energy harvester has a considerable significance, which can harvest energy from vibration, solar, thermal and RF (ambient and/or dedicated) energies simultaneously. By selecting the optimal energy source from the ambience, the devices and sensors will become truly self-sustainable and standalone which is very important for smart home and IoT-related applications.

The future work in rectenna design is not limited to the works proposed in this thesis. WPT is one of the most beneficial wireless technologies that have ever been developed. However, it will make a significant impact on every area where wireless transmission is inevitable.

Appendix

Agilent - HSMS 285X

Agilent HSMS-285x Series Surface Mount Zero Bias Schottky Detector Diodes

Data Sheet

Description

Agilent's HSMS-285x family of zero bias Schottky detector diodes has been designed and optimized for use in small signal (P_{in} <-20 dBm) applications at frequencies below 1.5 GHz. They are ideal for RF/ID and RF Tag applications where primary (DC bias) power is not available.

Important Note: For detector applications with input power levels greater than –20 dBm, use the HSMS-282x series at frequencies below 4.0 GHz, and the HSMS-286x series at frequencies above 4.0 GHz. The HSMS-285x series IS NOT RECOMMENDED for these higher power level applications.

Available in various package configurations, these detector diodes provide low cost solutions to a wide variety of design problems. Agilent's manufacturing techniques assure that when two diodes are mounted into a single package, they are taken from adjacent sites on the wafer, assuring the highest possible degree of match.

Pin Connections and Package Marking

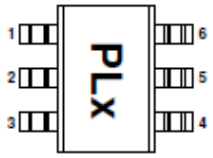

Notes:
1. Package marking provides orientation and identification.
2. See "Electrical Specifications" for appropriate package marking.

SOT-23/SOT-143 Package Lead Code Identification (top view)

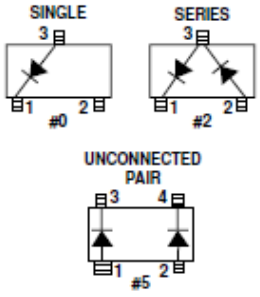

SOT-363 Package Lead Code Identification (top view)

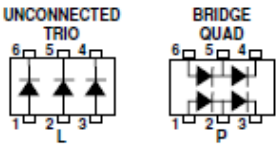

SOT-323 Package Lead Code Identification (top view)

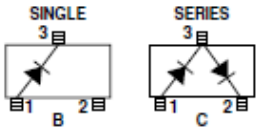

Features

- **Surface Mount SOT-23/ SOT-143 Packages**
- **Miniature SOT-323 and SOT-363 Packages**
- **High Detection Sensitivity:** up to 50 mV/µW at 915 MHz
- **Low Flicker Noise:** -162 dBV/Hz at 100 Hz
- **Low FIT (Failure in Time) Rate***
- **Tape and Reel Options Available**
- **Matched Diodes for Consistent Performance**
- **Better Thermal Conductivity for Higher Power Dissipation**
- **Lead-free Option Available**

* For more information see the Surface Mount Schottky Reliability Data Sheet.

Attention: Observe precautions for handling electrostatic sensitive devices.

ESD Machine Model (Class A)

ESD Human Body Model (Class 0)

Refer to Agilent Application Note A004R: Electrostatic Discharge Damage and Control.

Agilent Technologies

Agilent - HSMS 285X

SOT-23/SOT-143 DC Electrical Specifications, T_C = +25°C, Single Diode

Part Number HSMS-	Package Marking Code	Lead Code	Configuration	Maximum Forward Voltage V_F (mV)		Maximum Reverse Leakage, IR (μA)	Typical Capacitance C_T (pF)
2850 2852 2855	P0 P2 P5	0 2 5	Single Series Pair[1,2] Unconnected Pair[1,2]	150	250	175	0.30
Test Conditions				I_F = 0.1 mA	I_F = 1.0 mA	VR=2V	V_R = –0.5 V to –1.0V f = 1 MHz

Notes:
1. ΔV_F for diodes in pairs is 15.0 mV maximum at 1.0 mA.
2. ΔC_T for diodes in pairs is 0.05 pF maximum at –0.5 V.

SOT-323/SOT-363 DC Electrical Specifications, T_C = +25°C, Single Diode

Part Number HSMS-	Package Marking Code	Lead Code	Configuration	Maximum Forward Voltage V_F (mV)		Maximum Reverse Leakage, IR (μA)	Typical Capacitance C_T (pF)
285B 285C 285L 285P	P0 P2 PL PP	B C L P	Single Series Pair Unconnected Trio Bridge Quad	150	250	175	0.30
Test Conditions				I_F = 0.1 mA	I_F = 1.0 mA	VR=2V	V_R = 0.5 V to –1.0V f = 1 MHz

Notes:
1. ΔV_F for diodes in pairs is 15.0 mV maximum at 1.0 mA.
2. ΔC_T for diodes in pairs is 0.05 pF maximum at –0.5 V.

RF Electrical Specifications, T_C = +25°C, Single Diode

Part Number HSMS-	Typical Tangential Sensitivity TSS (dBm) @ f = 915 MHz	Typical Voltage Sensitivity γ (mV/μW) @ f = 915 MHz	Typical Video Resistance RV (KΩ)
2850 2852 2855 285B 285C 285L 285P	–57	40	8.0
Test Conditions	Video Bandwidth = 2 MHz Zero Bias	Power In = –40 dBm R_L = 100 KΩ, Zero Bias	Zero Bias

Agilent - HSMS 285X

Absolute Maximum Ratings, T_C = +25°C, Single Diode

Symbol	Parameter	Unit	Absolute Maximum[1]	
			SOT-23/143	SOT-323/363
P_{IV}	Peak Inverse Voltage	V	2.0	2.0
T_J	Junction Temperature	°C	150	150
T_{STG}	Storage Temperature	°C	-65 to 150	-65 to 150
T_{OP}	Operating Temperature	°C	-65 to 150	-65 to 150
θ_{jc}	Thermal Resistance[2]	°C/W	500	150

ESD WARNING:
Handling Precautions Should Be Taken To Avoid Static Discharge.

Notes:
1. Operation in excess of any one of these conditions may result in permanent damage to the device.
2. T_C = +25°C, where T_C is defined to be the temperature at the package pins where contact is made to the circuit board.

Equivalent Linear Circuit Model

HSMS-285x chip

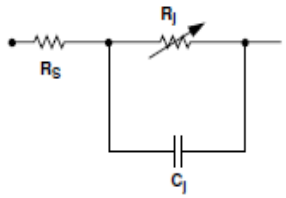

R_S = series resistance (see Table of SPICE parameters)

C_j = junction capacitance (see Table of SPICE parameters)

$$R_j = \frac{8.33 \times 10^{-5}\, nT}{I_b + I_s}$$

where
I_b = externally applied bias current in amps
I_s = saturation current (see table of SPICE parameters)
T = temperature, °K
n = ideality factor (see table of SPICE parameters)

Note:
To effectively model the packaged HSMS-285x product, please refer to Application Note AN1124.

SPICE Parameters

Parameter	Units	HSMS-285x
B_V	V	3.8
C_{J0}	pF	0.18
E_G	eV	0.69
I_{BV}	A	3 E-4
I_S	A	3 E-6
N		1.06
R_S	Ω	25
P_B (V_J)	V	0.35
P_T (XTI)		2
M		0.5

Murata Capacitor - GRM0335C2A101GA01

muRata INNOVATOR IN ELECTRONICS Product Search Data Sheet

GRM0335C2A101GA01#

Note: This datasheet may be out of date.
Please download the latest datasheet of GRM0335C2A101GA01# from the official website of Murata Manufacturing Co., Ltd.

"#" indicates a package specification code.

Specifications

Length	0.6±0.03mm
Width	0.3±0.03mm
Thickness	0.3±0.03mm
Capacitance	100pF ±2%
Distance between external terminals g	0.2mm min.
External terminal size e	0.1 to 0.2mm
Operating Temperature Range	-55℃ to 125℃
Rated Voltage	100Vdc
Size code in inch(mm)	0201 (0603M)
TC	0±30ppm/℃
Temperature characteristics (complied standard)	C0G(EIA)
Temperature range of temperature characteristics	25℃ to 125℃

Murata Capacitor - GRM0335C2A220JA01

muRata INNOVATOR IN ELECTRONICS Product Search Data Sheet

GRM0335C2A220JA01#

Note: This datasheet may be out of date.
Please download the latest datasheet of GRM0335C2A220JA01# from the official website of Murata Manufacturing Co., Ltd.

http://www.murata.com/en-us/products/productdetail?partno=GRM0335C2A220JA01%23

"#" indicates a package specification code.

Specifications

Length	0.6±0.03mm
Width	0.3±0.03mm
Thickness	0.3±0.03mm
Capacitance	22pF ±5%
Distance between external terminals g	0.2mm min.
External terminal size e	0.1 to 0.2mm
Operating Temperature Range	-55℃ to 125℃
Rated Voltage	100Vdc
Size code in inch(mm)	0201 (0603M)
TC	0±30ppm/℃
Temperature characteristics (complied standard)	C0G(EIA)
Temperature range of temperature characteristics	25℃ to 125℃

Skyworks- SMS 7630

SKYWORKS®

DATA SHEET

Surface Mount Mixer and Detector Schottky Diodes

Applications

- Sensitive RF and microwave detector circuits
- Sampling and mixer circuits
- High-volume wireless
- WiFi and mobile
- Low-noise receivers in high-sensitivity ID tags
- Radio designs

Features

- Tight parameter distribution
- Available as singles, pairs, and dual pairs
- Packages rated MSL1, 260 °C per JEDEC J-STD-020)

Skyworks Green™ products are compliant with all applicable legislation and are halogen-free. For additional information, refer to *Skyworks Definition of Green™*, document number SQ04-0074.

Description

These low-cost, surface mountable, plastic packaged silicon mixer Schottky diodes are designed for RF and microwave mixers and detectors. They include low barrier diodes and zero-bias detectors that combine Skyworks advanced semiconductor technology with low-cost packaging techniques. All diodes are 100 percent DC tested and deliver tight parameter distribution, which minimizes performance variability.

These diodes are available in SOD-882, SC-70, SC-79, SC-88, SOD-323, SOT-23, SOT-143, and Molded Interconnect System (MIS) packages. Wiring configurations include singles, common cathode, series pairs, unconnected pairs, and dual series pairs. They may be used at frequencies up to 24 GHz.

Table 1 describes the various packages and marking of the mixer and detector Schottky diodes.

Skyworks- SMS 7630

DATA SHEET • MIXER AND DETECTOR SCHOTTKY DIODES

Table 1. Schottky Diode Packaging and Marking

				
Single	Single	Single	Common Cathode	Series Pair
SC-79 Green™	SOD-323 Green™	SOT-23	SOT-23	SOT-23
				SMS1546-005LF Green™ Marking: XG2
		SMS7621-001 Marking: SH1		♦**SMS7621-005** Marking: SH2
♦**SMS7621-079LF** Marking: Cathode		**SMS7621-001LF** Green™ Marking: XH1		♦**SMS7621-005LF** Green™ Marking: XH2
		SMS7630-001 Marking: SD1		**SMS7630-005** Marking: SD2
♦**SMS7630-079LF** Marking: Anode	**SMS7630-011LF** Marking: XD	**SMS7630-001LF** Green™ Marking: XD1		**SMS7630-005LF** Green™ Marking: XD2
L_S = 0.7 nH	L_S = 1.5 nH	L_S = 1.5 nH		L_S = 1.5 nH
			SC-70	SC-70
			SMS7621-074 Marking: SH3	**SMS7621-075** Marking: SH2
			SMS7621-074LF Green™ Marking: XH3	**SMS7621-075LF** Green™ Marking: XH2
			L_S = 1.4 nH	L_S = 1.4 nH

					
Reverse Series Pair	Unconnected Pair	Reverse Unconnected Pair	Unconnected Pair	Dual Series Pair	Single
SOT-23	SOT-143	SOT-143	MIS Green™	SC-88 Green™	SOD-882 Green™
♦**SMS7621-006** Marking: SH8	**SMS7621-015** Marking: SH7		**SMS7621-517** Marking: H Pb-Free		
♦**SMS7621-006LF** Green™ Marking: XH8	**SMS7621-015LF** Marking: XH7			**SMS7621-081LF** Marking: XHQ	**SMS7621-040LF** Marking: E
♦**SMS7630-006** Marking: SD8		♦**SMS7630-020** Marking: SD0	**SMS7630-517** Marking: D Pb-Free		
♦**SMS7630-006LF** Green™ Marking: XD8		♦**SMS7630-020LF** Marking: XD0			**SMS7630-040LF** Marking: P
L_S = 1.5 nH	L_S = 1.5 nH	L_S = 1.5 nH	L_S = 0.6 nH	L_S = 1.8 nH	L_S = 0.45 nH

The Pb-free symbol or "LF" in the part number denotes a lead-free, RoHS-compliant package unless otherwise noted as Green™. Tin/lead (Sn/Pb) packaging is not recommended for new designs.

Innovation to Go™
Select Linear Products (indicated by ♦) now available for purchase online.

Skyworks- SMS 7630

Electrical and Mechanical Specifications

The absolute maximum ratings of the mixer and detector Schottky diodes are provided in Table 2. Electrical specifications are provided in Tables 3 and 4. The associated SPICE model parameters are provided in Table 5. A typical detector schematic diagram is shown in Figure 1.

A pinout and equivalent circuit diagram for the dual series pair Schottky diode (SMS7621-081LF) is shown in Figure 2. Typical performance characteristics are illustrated in Figures 3 and 4. Package dimensions are shown in Figures 5 to 19 (odd numbers), and tape and reel dimensions are provided in Figures 6 to 20 (even numbers).

Otherwise, problems related to moisture absorption may occur when the part is subjected to high temperature during solder assembly.

The mixer and detector Schottky diodes are rated to Moisture Sensitivity Level 1 (MSL1) at 260 °C for 5 seconds. They can be used for lead or lead-free soldering. For additional information, refer to the Skyworks Application Note, *Solder Reflow Information*, document number 200164.

Care must be taken when attaching this product, whether it is done manually or in a production solder reflow environment. Production quantities of this product are shipped in a standard tape and reel format.

Package and Handling Information

Instructions on the shipping container label regarding exposure to moisture after the container seal is broken must be followed.

Table 2. Surface Mount Mixer and Detector Diodes Absolute Maximum Ratings

Parameter	Symbol	Minimum	Maximum	Units
Reverse voltage	V_R		Rated V_R	V
Forward current, steady state	I_F		50	mA
Power dissipation	P_D		75	mW
Storage temperature	T_{STG}	–65	+150	°C
Operating temperature	T_A	–65	+150	°C
Junction temperature	T_J		+150	°C

Note: Exposure to maximum rating conditions for extended periods may reduce device reliability. There is no damage to device with only one parameter set at the limit and all other parameters set at or below their nominal value. Exceeding any of the limits listed here may result in permanent damage to the device.

CAUTION: *Although this device is designed to be as robust as possible, Electrostatic Discharge (ESD) can damage this device. This device must be protected at all times from ESD. Static charges may easily produce potentials of several kilovolts on the human body or equipment, which can discharge without detection. Industry-standard ESD precautions should be used at all times.*

Table 3. Surface Mount Mixer and Detector Diodes Electrical Specifications (Note 1)
(T_A = +25 °C Per Junction, Unless Otherwise Noted)

Part Number	Barrier	Minimum V_R @ 10 µA (V)	Typical C_T @ 0 V (pF)	V_F @ 1 mA (mV)	Maximum Pair Configuration ΔV_F @ 1 mA (mV)	Maximum R_T (Note 2) (Ω)
SMS1546 series	Low	2	0.50	200 to 270	10	8 @ 10 mA
SMS7621 series	Low	2	0.25	260 to 320	10	18 @ 5 mA

Note 1: Performance is guaranteed only under the conditions listed in this Table.
Note 2: R_T is the slope resistance.

Skyworks- SMS 7630

Table 4. Surface Mount Mixer and Detector Diodes Electrical Specifications (Note 1)
(T_A = +25 °C Per Junction, Unless Otherwise Noted)

Part Number	Minimum V_B @ 100 µA (V)	Typical C_T @ 0.15 V (pF)	V_F @ 0.1 mA (mV)	V_F @ 1 mA (mV)	Maximum Pair Configuration ΔV_F @ 1 mA (mV)	Typical R_V (Ω)
SMS7630 series	1	0.3	60 to 120	135 to 240	10	5000

Note 1: Performance is guaranteed only under the conditions listed in this Table.

Table 5. SPICE Model Parameters (Per Junction)

Parameter	Units	SMS1546 Series	SMS7621 Series	SMS7630 Series
Is	A	3E-7	4E-8	5E-6
Rs	Ω	4	12	20
N	–	1.04	1.05	1.05
TT	sec	1E-11	1E-11	1E-11
CJ0	pF	0.38	0.1	0.14
M	–	0.36	0.35	0.40
Eg	eV	0.69	0.69	0.69
XTI	–	2	2	2
Fc	–	0.5	0.5	0.5
Bv	V	3	3	2
Ibv	A	1E-5	1E-5	1E-4
VJ	V	0.51	0.51	0.34

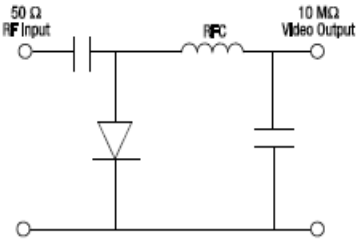

Figure 1. Typical Detector Circuit

Coilcraft inductor: 0402HP series

Web page | Sample & buy | Tools & software | Support & FAQ | Document 526-1

Chip Inductors - 0402HP Series (1005)

RoHS/REACH COMPLIANT

Halogen Free

- Higher Q and lower DCR than other 0402 inductors
- Very high SRF values – as high as 16 GHz
- Excellent current handling capability – up to 2300 mA
- 54 inductance values from 1.0 to 220 nH

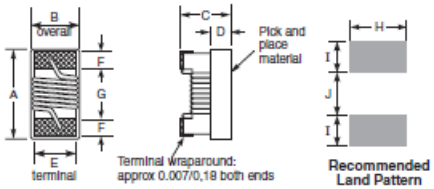

	A max[2]	B (min – max)	C max[3]	
0402HP	0.043	0.020 – 0.028	0.024	inches
	1,09	0,51 – 0,71	0,61	mm

	A max[2]	B	C max[3]	
0402HPH	0.044	0.026 ±0.002	0.026	inches
	1,12	0,66 ±0,051	0,66	mm

D ref	E	F	G	H	I	J	
0.010	0.020	0.008	0.024	0.026	0.014	0.020	inches
0,25	0,51	0,20	0,61	0,66	0,36	0,51	mm

Notes: 1. Unless otherwise indicated, all dimensions are nominal.
2. Length dimension (A) is before optional solder application. Maximum dimension including solder is 0.045 in / 1.143 mm.
3. Height dimension (C) is before optional solder application. For maximum height dimension including solder, add 0.006 in / 0,152 mm.

Core material Ceramic
Environmental RoHS compliant, halogen free
Terminations Silver-palladium-platinum-glass frit. Other terminations available at additional cost.
Weight 0.7 – 1.0 mg
Ambient temperature –40°C to +125°C with Irms current
Maximum part temperature +140°C (ambient + temp rise).
Storage temperature Component: –40°C to +140°C. Tape and reel packaging: –40°C to +80°C
Resistance to soldering heat Max three 40 second reflows at +260°C, parts cooled to room temperature between cycles
Temperature Coefficient of Inductance (TCL) +25 to +125 ppm/°C
Moisture Sensitivity Level (MSL) 1 (unlimited floor life at <30°C / 85% relative humidity)
Failures in Time (FIT) / Mean Time Between Failures (MTBF) One per billion hours / one billion hours, calculated per Telcordia SR-332
Packaging 2000 or 5000 per 7" reel. Paper tape: 8 mm wide, 0.66 mm thick, 2 mm pocket spacing
PCB washing Tested to MIL-STD-202 Method 215 plus an additional aqueous wash. See Doc787_PCB_Washing.pdf.

Typical L vs Frequency

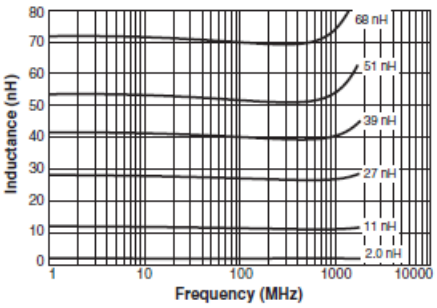

Typical Q vs Frequency

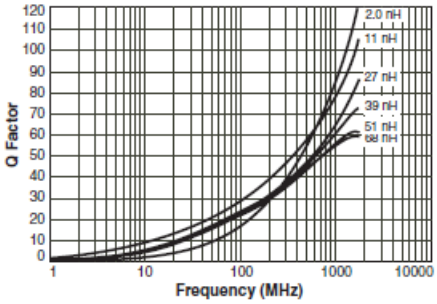

Coilcraft
www.coilcraft.com

US +1-847-639-6400 sales@coilcraft.com
UK +44-1236-730595 sales@coilcraft-europe.com
Taiwan +886-2-2264 3646 sales@coilcraft.com.tw
China +86-21-6218 8074 sales@coilcraft.com.cn
Singapore + 65-6484 8412 sales@coilcraft.com.sg

Document 526-1 Revised 03/12/20

Coilcraft inductor: 0402HP series

Document 526-2

RoHS/ REACH COMPLIANT

Halogen Free

0402HP Series (1005)

Designer's Kit C403 contains 20 each of 5% values
Designer's Kit C403-2 contains 20 each of 2% values

Part number[1]	Inductance[2] (nH)	Percent tolerance[3]	Test freq (MHz)	900 MHz L typ	900 MHz Q typ[4]	1.7 GHz L typ	1.7 GHz Q typ[4]	SRF typ[5] (GHz)	DCR max[6] (Ohms)	Irms[7] (mA)
0402HP-1N0XJE_	1.0	**5**	250	0.97	46	0.99	72	16.0	0.030	2300
0402HP-2N0XJE_	2.0	**5**	250	1.96	58	1.98	85	15.2	0.038	2100
0402HP-2N2XJE_	2.2	**5**	250	2.17	60	2.17	86	15.1	0.038	2100
0402HP-2N4X_E_	2.4	**5,3,2**	250	2.37	60	2.38	83	14.0	0.042	2000
0402HP-2N7X_E_	2.7	**5,3,2**	250	2.66	62	2.68	85	13.0	0.085	1500
0402HP-3N3X_E_	3.3	**5,3,2**	250	3.26	66	3.28	95	12.8	0.045	1700
0402HP-3N6X_E_	3.6	**5,3,2**	250	3.56	65	3.58	94	11.7	0.045	1700
0402HP-3N9X_E_	3.9	**5,3,2**	250	3.87	64	3.91	98	9.50	0.045	1700
0402HP-4N3X_E_	4.3	**5,3,2**	250	4.26	63	4.33	90	7.15	0.050	1600
0402HP-4N7X_E_	4.7	**5,3,2**	250	4.67	58	4.74	83	6.85	0.075	1500
0402HP-5N1X_E_	5.1	**5,3,2**	250	5.07	54	5.16	76	6.80	0.125	1200
0402HP-5N6X_E_	5.6	**5,3,2**	250	5.56	73	5.66	105	6.50	0.055	1600
0402HP-6N2X_E_	6.2	**5,3,2**	250	6.18	73	6.25	100	5.80	0.055	1600
0402HP-6N8X_E_	6.8	**5,3,2**	250	6.78	68	6.97	94	5.80	0.070	1500
0402HP-7N5X_E_	7.5	**5,3,2**	250	7.49	60	7.77	82	5.40	0.100	1400
0402HP-8N2X_E_	8.2	**5,3,2**	250	8.10	68	8.40	95	5.40	0.065	1500
0402HP-8N7X_E_	8.7	**5,3,2**	250	8.73	66	9.04	95	5.00	0.070	1500
0402HP-9N0X_E_	9.0	**5,3,2**	250	8.99	67	9.21	92	5.00	0.080	1400
0402HP-9N5X_E_	9.5	**5,3,2**	250	9.52	64	9.97	90	4.70	0.090	1400
0402HP-10NX_E_	10	**5,3,2**	250	9.98	62	10.4	90	4.70	0.110	1300
0402HP-11NX_E_	11	**5,3,2**	250	11.0	68	11.6	98	4.70	0.065	1400
0402HP-12NX_E_	12	**5,3,2**	250	12.0	66	12.6	100	4.40	0.100	1200
0402HP-13NX_E_	13	**5,3,2**	250	13.1	62	13.9	82	4.20	0.155	870
0402HP-15NX_E_	15	**5,3,2**	250	15.1	62	16.0	85	3.90	0.115	1100
0402HP-16NX_E_	16	**5,3,2**	250	16.2	57	17.3	77	3.70	0.150	850
0402HP-17NX_E_	17	**5,3,2**	250	17.2	51	18.7	64	3.70	0.230	650
0402HP-18NX_E_	18	**5,3,2**	250	18.2	58	19.5	74	3.55	0.120	900
0402HP-19NX_E_	19	**5,3,2**	250	19.2	61	20.7	88	3.50	0.145	850
0402HP-20NX_E_	20	**5,3,2**	250	20.3	58	22.0	76	3.50	0.185	780
0402HP-21NX_E_	21	**5,3,2**	250	21.3	48	23.2	62	1.70	0.460	450
0402HP-22NX_E_	22	**5,3,2**	250	22.3	60	24.4	74	3.30	0.160	800
0402HP-23NX_E_	23	**5,3,2**	250	23.3	60	25.5	77	3.30	0.160	800
0402HP-24NX_E_	24	**5,3,2**	250	24.5	55	27.1	71	3.15	0.210	700
0402HP-25NX_E_	25	**5,3,2**	250	25.5	57	28.3	73	3.15	0.260	700
0402HP-26NX_E_	26	**5,3,2**	250	26.6	56	29.3	74	3.15	0.290	700
0402HP-27NX_E_	27	**5,3,2**	250	27.3	62	29.5	86	3.20	0.350	450
0402HP-30NX_E_	30	**5,3,2**	250	30.8	61	35.0	87	2.90	0.350	450
0402HP-33NX_E_	33	**5,3,2**	250	34.0	61	38.3	80	2.80	0.330	490
0402HP-36NX_E_	36	**5,3,2**	250	37.1	59	42.2	76	2.80	0.390	480
0402HP-37NX_E_	37	**5,3,2**	250	38.2	57	44.0	72	2.70	0.480	470
0402HP-39NX_E_	39	**5,3,2**	250	40.5	56	47.0	84	2.60	0.430	450
0402HP-40NX_E_	40	**5,3,2**	250	41.3	56	47.4	75	2.60	0.430	450
0402HP-43NX_E_	43	**5,3,2**	250	45.0	52	54.1	68	2.50	0.520	450
0402HP-47NX_E_	47	**5,3,2**	250	49.0	48	58.9	62	2.40	0.580	420
0402HP-51NX_E_	51	**5,3,2**	250	49.1	52	58.8	59	2.30	0.700	360
0402HPH-56NX_E_	56	**5,3,2**	250	58.8	56	72.2	64	2.07	0.900	330
0402HPH-68NX_E_	68	**5,3,2**	250	72.2	56	91.4	64	1.84	1.00	320
0402HPH-82NX_E_	82	**5,3,2**	250	89.7	52	–	–	1.75	1.10	315
0402HPH-R10X_E_	100	**5,3,2**	250	–	–	–	–	1.58	1.20	310
0402HPH-R12X_E_	120	**5,3,2**	250	–	–	–	–	1.25	1.20	310
0402HPH-R15X_E_	150	**5,3,2**	100	–	–	–	–	1.14	2.0	240
0402HPH-R16X_E_	160	**5,3,2**	100	–	–	–	–	1.65	2.0	240
0402HPH-R18X_E_	180	**5,3,2**	100	–	–	–	–	1.08	2.1	240
0402HPH-R22X_E_	220	**5,3,2**	100	–	–	–	–	0.96	3.1	160

1. When ordering, specify **tolerance**, **termination** and **packaging** codes:

0402HP-82NXJEW

Tolerance: **G** = 2% **H** = 3% **J** = 5%
(Table shows stock tolerances in bold.)

Termination: **E** = Halogen free component. RoHS compliant silver-palladium-platinum-glass frit terminations.
L = RoHS compliant, not halogen-free. Silver-palladium-platinum-glass frit terminations.
R = RoHS compliant matte tin over nickel over silver-platinum-glass frit.
Special order: **T** = RoHS tin-silver-copper (95.5/4/0.5) or **S** = non-RoHS tin-lead (63/37).

Packaging: **W** = 7" machine-ready reel. EIA-481 punched paper tape (2000 parts per full reel). Quantities less than full reel available: in tape (not machine ready) or with leader and trailer ($25 charge).
Q = 7" machine-ready reel. EIA-481 punched paper tape (5000 parts per full reel). Quantities less than full reel available: in tape (not machine ready) or with leader and trailer ($25 charge).
U = Less than full reel. In an effort to simplify our part numbering system, Coilcraft is eliminating the need for multiple packaging codes. When ordering, simply change the last letter of your part number from U to W.

2. Inductance measured at test frequency using a Coilcraft SMD-F fixture in an Agilent/HP 4286 impedance analyzer with Coilcraft-provided correlation pieces.
3. Tolerances in bold are stocked for immediate shipment.
4. Q measured using an Agilent/HP 4287A with an Agilent/HP 16197 test fixture.
5. SRF measured using an Agilent/HP 8722ES network analyzer and a Coilcraft SMD-D test fixture.
6. DCR measured on a micro-ohmmeter and a Coilcraft CCF858 test fixture.
7. Current that causes a 15°C temperature rise from 25°C ambient. This information is for reference only and does not represent absolute maximum ratings.
8. Electrical specifications at 25°C.

Refer to Doc 362 "Soldering Surface Mount Components" before soldering.

Coilcraft
www.coilcraft.com

US +1-847-639-6400 sales@coilcraft.com
UK +44-1236-730595 sales@coilcraft-europe.com
Taiwan +886-2-2264 3646 sales@coilcraft.com.tw
China +86-21-6218 8074 sales@coilcraft.com.cn
Singapore + 65-6484 8412 sales@coilcraft.com.sg

Document 526-2 Revised 03/12/20

Murata Capacitor - GRM0335C2A1R0CA01

muRata Product Search Data Sheet
INNOVATOR IN ELECTRONICS

GRM0335C2A1R0CA01#

Note: This datasheet may be out of date.
Please download the latest datasheet of GRM0335C2A1R0CA01# from the official website of Murata Manufacturing Co., Ltd.

http://www.murata.com/en/products/productdata/lfpartno=GRM0335C2A1R0CA01%23

"#" indicates a package specification code.

Specifications

Length	0.6±0.03mm
Width	0.3±0.03mm
Thickness	0.3±0.03mm
Capacitance	1.0pF ±0.25pF
Distance between external terminals g	0.2mm min.
External terminal size e	0.1 to 0.2mm
Operating Temperature Range	-55℃ to 125℃
Rated Voltage	100Vdc
Size code in inch(mm)	0201 (0603M)
TC	0±30ppm/℃
Temperature characteristics (compiled standard)	C0G(EIA)
Temperature range of temperature characteristics	25℃ to 125℃

Murata Capacitor - GRM0335C2AR70BA01

muRata INNOVATOR IN ELECTRONICS Product Search Data Sheet

Note: This datasheet may be out of date.
Please download the latest datasheet of GRM0335C2AR70BA01# from the official website of Murata Manufacturing Co., Ltd.

http://www.murata.com/en-gb/products/productdetail?partno=GRM0335C2AR70BA01%23

GRM0335C2AR70BA01#

"#" indicates a package specification code.

Specifications

Length	0.6±0.03mm
Width	0.3±0.03mm
Thickness	0.3±0.03mm
Capacitance	0.70pF ±0.1pF
Distance between external terminals g	0.2mm min.
External terminal size e	0.1 to 0.2mm
Operating Temperature Range	-55℃ to 125℃
Rated Voltage	100Vdc
Size code in inch(mm)	0201 (0603M)
TC	0±30ppm/℃
Temperature characteristics (complied standard)	C0G(EIA)
Temperature range of temperature characteristics	25℃ to 125℃

Murata Capacitor - GRM0335C1H5R1BA01

muRata Product Search Data Sheet
INNOVATOR IN ELECTRONICS

Note: This datasheet may be out of date.
Please download the latest datasheet of GRM0335C1H5R1BA01# from the official website of Murata Manufacturing Co., Ltd.

http://www.murata.com/en/products/productdata/lfpartno=GRM0335C1H5R1BA01%23

GRM0335C1H5R1BA01#

"#" indicates a package specification code.

Specifications

Length	0.6±0.03mm
Width	0.3±0.03mm
Thickness	0.3±0.03mm
Capacitance	5.1pF ±0.1pF
Distance between external terminals g	0.2mm min.
External terminal size e	0.1 to 0.2mm
Operating Temperature Range	-55℃ to 125℃
Rated Voltage	50Vdc
Size code in inch(mm)	0201 (0603M)
TC	0±30ppm/℃
Temperature characteristics (complied standard)	C0G(EIA)
Temperature range of temperature characteristics	25℃ to 125℃

Murata Capacitor - GRM033R71A103KA01

muRata INNOVATOR IN ELECTRONICS Product Search Data Sheet

GRM033R71A103KA01#

Note: This datasheet may be out of date.
Please download the latest datasheet of GRM033R71A103KA01# from the official website of Murata Manufacturing Co., Ltd.

http://www.murata.com/en-gb/products/productdetail?partno=GRM033R71A103KA01%23

"#" indicates a package specification code.

Specifications

Length	0.6±0.03mm
Width	0.3±0.03mm
Thickness	0.3±0.03mm
Capacitance	10000pF ±10%
Distance between external terminals g	0.2mm min.
External terminal size e	0.1 to 0.2mm
Operating Temperature Range	-55℃ to 125℃
Rated Voltage	10Vdc
Size code in inch(mm)	0201 (0603M)
Capacitance change rate	±15.0%
Temperature characteristics (complied standard)	X7R(EIA)
Temperature range of temperature characteristics	-55℃ to 125℃

Murata Capacitor - GRM0335C2A1R1CA01

Product Search Data Sheet

GRM0335C2A1R1CA01#

Note: This datasheet may be out of date.
Please download the latest datasheet of GRM0335C2A1R1CA01# from the official website of Murata Manufacturing Co., Ltd.

http://www.murata.com/en/products/productdata/lfpartno=GRM0335C2A1R1CA01%23

"#" indicates a package specification code.

Specifications

Length	0.6±0.03mm
Width	0.3±0.03mm
Thickness	0.3±0.03mm
Capacitance	1.1pF ±0.25pF
Distance between external terminals g	0.2mm min.
External terminal size e	0.1 to 0.2mm
Operating Temperature Range	-55℃ to 125℃
Rated Voltage	100Vdc
Size code in inch(mm)	0201 (0603M)
TC	0±30ppm/℃
Temperature characteristics (compiled standard)	C0G(EIA)
Temperature range of temperature characteristics	25℃ to 125℃

Murata Capacitor - GRM0335C2AR30BA01

muRata INNOVATOR IN ELECTRONICS Product Search Data Sheet

Note: This datasheet may be out of date.
Please download the latest datasheet of GRM0335C2AR30BA01# from the official website of Murata Manufacturing Co., Ltd.

http://www.murata.com/en-gb/products/productdetail?partno=GRM0335C2AR30BA01%23

GRM0335C2AR30BA01#

"#" indicates a package specification code.

Specifications

Length	0.6±0.03mm
Width	0.3±0.03mm
Thickness	0.3±0.03mm
Capacitance	0.30pF ±0.1pF
Distance between external terminals g	0.2mm min.
External terminal size e	0.1 to 0.2mm
Operating Temperature Range	-55℃ to 125℃
Rated Voltage	100Vdc
Size code in inch(mm)	0201 (0603M)
TC	0±30ppm/℃
Temperature characteristics (complied standard)	C0G(EIA)
Temperature range of temperature characteristics	25℃ to 125℃

Murata Capacitor - GRM0335C2A200JA01

muRata INNOVATOR IN ELECTRONICS Product Search Data Sheet

GRM0335C2A200JA01#

Note: This datasheet may be out of date.
Please download the latest datasheet of GRM0335C2A200JA01# from the official website of Murata Manufacturing Co., Ltd.

http://www.murata.com/en-gb/products/productdetail?partno=GRM0335C2A200JA01%23

"#" indicates a package specification code.

Specifications

Length	0.6±0.03mm
Width	0.3±0.03mm
Thickness	0.3±0.03mm
Capacitance	20pF ±5%
Distance between external terminals g	0.2mm min.
External terminal size e	0.1 to 0.2mm
Operating Temperature Range	-55℃ to 125℃
Rated Voltage	100Vdc
Size code in inch(mm)	0201 (0603M)
TC	0±30ppm/℃
Temperature characteristics (compliled standard)	C0G(EIA)
Temperature range of temperature characteristics	25℃ to 125℃

Murata Capacitor - GRM0335C2AR50BA01

muRata INNOVATOR IN ELECTRONICS Product Search Data Sheet

Note: This datasheet may be out of date.
Please download the latest datasheet of GRM0335C2AR50BAD1# from the official website of Murata Manufacturing Co., Ltd.

http://www.murata.com/en-gb/products/productdetail?partno=GRM0335C2AR50BA01%23

GRM0335C2AR50BA01#

"#" indicates a package specification code.

Specifications

Length	0.6±0.03mm
Width	0.3±0.03mm
Thickness	0.3±0.03mm
Capacitance	0.50pF ±0.1pF
Distance between external terminals g	0.2mm min.
External terminal size e	0.1 to 0.2mm
Operating Temperature Range	-55℃ to 125℃
Rated Voltage	100Vdc
Size code in inch(mm)	0201 (0603M)
TC	0±30ppm/℃
Temperature characteristics (complied standard)	C0G(EIA)
Temperature range of temperature characteristics	25℃ to 125℃

Murata Capacitor - GRM0335C2A1R5CA01

muRata INNOVATOR IN ELECTRONICS Product Search Data Sheet

Note: This datasheet may be out of date.
Please download the latest datasheet of GRM0335C2A1R5CA01# from the official website of Murata Manufacturing Co., Ltd.

http://www.murata.com/en-gb/products/productdetail?partno=GRM0335C2A1R5CA01%23

GRM0335C2A1R5CA01#

"#" indicates a package specification code.

Specifications

Length	0.6±0.03mm
Width	0.3±0.03mm
Thickness	0.3±0.03mm
Capacitance	1.5pF ±0.25pF
Distance between external terminals g	0.2mm min.
External terminal size e	0.1 to 0.2mm
Operating Temperature Range	-55℃ to 125℃
Rated Voltage	100Vdc
Size code in inch(mm)	0201 (0603M)
TC	0±30ppm/℃
Temperature characteristics (complied standard)	C0G(EIA)
Temperature range of temperature characteristics	25℃ to 125℃

Avago - HSMS 286X

HSMS-286x Series
Surface Mount Microwave Schottky Detector Diodes

AVAGO TECHNOLOGIES

Data Sheet

Lead (Pb) Free
RoHS 6 fully compliant

Description

Avago's HSMS-286x family of DC biased detector diodes have been designed and optimized for use from 915 MHz to 5.8 GHz. They are ideal for RF/ID and RF Tag applications as well as large signal detection, modulation, RF to DC conversion or voltage doubling.

Available in various package configurations, this family of detector diodes provides low cost solutions to a wide variety of design problems. Avago's manufacturing techniques assure that when two or more diodes are mounted into a single surface mount package, they are taken from adjacent sites on the wafer, assuring the highest possible degree of match.

Pin Connections and Package Marking

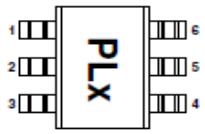

Notes:
1. Package marking provides orientation and identification.
2. The first two characters are the package marking code. The third character is the date code.

SOT-23/SOT-143 Package Lead Code Identification (top view)

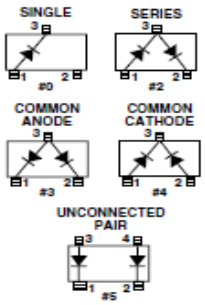

Features

- Surface Mount SOT-23/SOT-143 Packages
- Miniature SOT-323 and SOT-363 Packages
- High Detection Sensitivity:
  up to 50 mV/µW at 915 MHz
  up to 35 mV/µW at 2.45 GHz
  up to 25 mV/µW at 5.80 GHz
- Low FIT (Failure in Time) Rate*
- Tape and Reel Options Available
- Unique Configurations in Surface Mount SOT-363 Package
  – increase flexibility
  – save board space
  – reduce cost
- HSMS-286K Grounded Center Leads Provide up to 10 dB Higher Isolation
- Matched Diodes for Consistent Performance
- Better Thermal Conductivity for Higher Power Dissipation
- Lead-free

* For more information see the Surface Mount Schottky Reliability Data Sheet.

SOT-323 Package Lead Code Identification (top view)

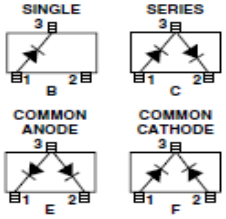

SOT-363 Package Lead Code Identification (top view)

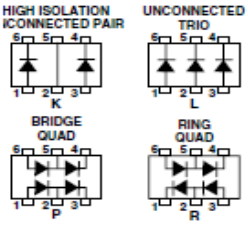

Avago - HSMS 286X

SOT-23/SOT-143 DC Electrical Specifications, T_C = +25°C, Single Diode

Part Number HSMS-	Package Marking Code	Lead Code	Configuration	Forward Voltage V_F (mV)		Typical Capacitance C_T (pF)
2860	T0	0	Single	250 Min.	350 Max.	0.30
2862	T2	2	Series Pair[1,2]			
2863	T3	3	Common Anode[1,2]			
2864	T4	4	Common Cathode[1,2]			
2865	T5	5	Unconnected Pair[1,2]			
Test Conditions				I_F = 1.0 mA		V_R = 0 V, f = 1 MHz

Notes:
1. ΔVF for diodes in pairs is 15.0 mV maximum at 1.0 mA.
2. ΔCT for diodes in pairs is 0.05 pF maximum at –0.5V.

SOT-323/SOT-363 DC Electrical Specifications, T_C = +25°C, Single Diode

Part Number HSMS-	Package Marking Code	Lead Code	Configuration	Forward Voltage V_F (mV)		Typical Capacitance C_T (pF)
286B	T0	B	Single	250 Min.	350 Max.	0.25
286C	T2	C	Series Pair[1,2]			
286E	T3	E	Common Anode[1,2]			
286F	T4	F	Common Cathode[1,2]			
286K	TK	K	High Isolation Unconnected Pair			
286L	TL	L	Unconnected Trio			
286P	TP	P	Bridge Quad			
286R	ZZ	R	Ring Quad			
Test Conditions				I_F = 1.0 mA		V_R = 0 V, f = 1 MHz

Notes:
1. ΔVF for diodes in pairs is 15.0 mV maximum at 1.0 mA.
2. ΔCT for diodes in pairs is 0.05 pF maximum at –0.5V.

Avago - HSMS 286X

RF Electrical Specifications, T_C = +25°C, Single Diode

Part Number HSMS-	Typical Tangential Sensitivity TSS (dBm) @ f = 915 MHz	2.45 GHz	5.8 GHz	Typical Voltage Sensitivity g (mV/µW) @ f = 915 MHz	2.45 GHz	5.8 GHz	Typical Video Resistance RV (KΩ)
2860	–57	–56	–55	50	35	25	5.0
2862							
2863							
2864							
2865							
286B							
286C							
286E							
286F							
286K							
286L							
286P							
286R							
Test Conditions	Video Bandwidth = 2 MHz I_b = 5 µA			Power in = –40 dBm R_L = 100 KΩ, I_b = 5 µA			I_b = 5 µA

Absolute Maximum Ratings, T_C = +25°C, Single Diode

Symbol	Parameter	Unit	Absolute Maximum[1] SOT-23/143	SOT-323/363
P_{IV}	Peak Inverse Voltage	V	4.0	4.0
T_J	Junction Temperature	°C	150	150
T_{STG}	Storage Temperature	°C	-65 to 150	-65 to 150
T_{OP}	Operating Temperature	°C	-65 to 150	-65 to 150
θ_{jc}	Thermal Resistance[2]	°C/W	500	150

Notes:
1. Operation in excess of any one of these conditions may result in permanent damage to the device.
2. T_C = +25°C, where T_C is defined to be the temperature at the package pins where contact is made to the circuit board.

Attention:
Observe precautions for handling electrostatic sensitive devices.

ESD Machine Model (Class A)

ESD Human Body Model (Class 0)

Refer to Avago Application Note A004R: Electrostatic Discharge Damage and Control.

Avago - HSMS 286X

Equivalent Linear Circuit Model, Diode chip

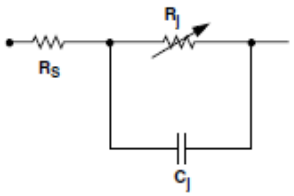

R_S = series resistance (see Table of SPICE parameters)

C_J = junction capacitance (see Table of SPICE parameters)

$$R_J = \frac{8.33 \times 10^{-5}\, nT}{I_b + I_s}$$

where

I_b = externally applied bias current in amps

I_s = saturation current (see table of SPICE parameters)

T = temperature, °K

n = ideality factor (see table of SPICE parameters)

Note:
To effectively model the packaged HSMS-286x product, please refer to Application Note AN1124.

SPICE Parameters

Parameter	Units	Value
B_V	V	7.0
C_{J0}	pF	0.18
E_G	eV	0.69
I_{BV}	A	1 E - 5
I_S	A	5 E - 8
N		1.08
R_S	Ω	6.0
P_B (VJ)	V	0.65
P_T (XTI)		2
M		0.5